ornl

OAK RIDGE NATIONAL LABORATORY

LOCKHEED MARTIN

ORNL-6902

Fossil Energy Program Annual Progress Report for April 1995 Through March 1996

R. R. Judkins
Program Manager

Fossil Energy Program

MANAGED AND OPERATED BY
LOCKHEED MARTIN ENERGY RESEARCH CORPORATION
FOR THE UNITED STATES
DEPARTMENT OF ENERGY

ORNL-27 (3-96)

ORNL-6902

Fossil Energy Program

Fossil Energy Program Annual Progress Report for April 1995 Through March 1996

R. R. Judkins
Program Manager

June 1996

Prepared for the
DOE Office of Fossil Energy
(AA, AB, AC, AW, AZ, SA)

Prepared by the
OAK RIDGE NATIONAL LABORATORY
Oak Ridge, Tennessee 37831-6285
Managed by
LOCKHEED MARTIN ENERGY RESEARCH CORP.
for the
U.S. DEPARTMENT OF ENERGY
under Contract DE-AC05-96OR22464

CONTENTS

FOSSIL ENERGY PROGRAM ANNUAL PROGRESS REPORT FOR APRIL 1995 THROUGH MARCH 1996[1]

R. R. Judkins, Program Manager

ABSTRACT

This report covers progress made during the period April 1, 1995, through March 31, 1996, for research and development projects that contribute to the advancement of various fossil energy technologies. Projects on the Fossil Energy Program are supported by the DOE Office of Fossil Energy, the DOE Morgantown Energy Technology Center, the DOE Pittsburgh Energy Technology Center, the DOE Fossil Energy Clean Coal Technology Program, the DOE Bartlesville Project Office, and the DOE Fossil Energy Office of Strategic Petroleum Reserve.

---

1. INTRODUCTION

Paul T. Carlson

The Oak Ridge National Laboratory (ORNL) Fossil Energy Program research and development activities, performed for the Department of Energy (DOE) Assistant Secretary for Fossil Energy, cover the areas of coal, clean coal technology, gas, petroleum, and support to the Strategic Petroleum Reserve. The coal activities include materials research and development; environmental analysis support; bioprocessing of coal to produce liquid or gaseous fuels; and coal combustion research. The work in support of gas technologies includes activities on the Advanced Turbine Systems Program, primarily in the materials and manufacturing aspects. Several activities are contributing to petroleum technologies in the areas of computational tools for seismic analysis and the use of bioconversion for the removal of impurities from heavy oils.

The Fossil Energy Program has projects in several ORNL divisions. Included as part of the Fossil Energy Program is the technical management of all activities on the DOE Fossil Energy Advanced Research and Technology Development (AR&TD) Materials Program. The AR&TD

---

[1]Research sponsored by the U.S. Department of Energy, Office of Fossil Energy, under contract DE-AC05-96OR22464 with Lockheed Martin Energy Research Corp.

Materials Program includes research at other DOE and government laboratories, at universities, and at industrial organizations.

1.1 MATERIALS RESEARCH AND DEVELOPMENT

Materials research and development activities at Oak Ridge National Laboratory include development of ceramic composites for high temperature applications; new alloys with unique mechanical properties for advanced fossil energy systems; development of functional materials, such as ceramic filters, ceramic membranes, and carbon materials; and corrosion research to understand the behavior of materials in coal processing environments. The transfer of technology developed on this program is enhanced through interactions with industry and joint research programs with those interested in using the technology. Transfer to industry of the technology developed on the program has been an important activity this year, and this commitment to technology transfer is reflected in an active CRADA involvement.

1.2 ENVIRONMENTAL ANALYSIS SUPPORT

Activities in environmental analysis support included assistance to the Morgantown and Pittsburgh Energy Technology Centers (METC and PETC) in reviewing and preparing documents required by the National Environmental Policy Act (NEPA) for projects selected for the Clean Coal Technology (CCT) Program. An important activity was the preparation for METC of a final Environmental Assessment (EA) for the proposed Externally Fired Combined Cycle (EFCC) Project in Warren, Pennsylvania. In addition, a post-project environmental analysis was prepared for PETC to evaluate the Demonstration of Advanced Combustion Techniques for a Tangentially-Fired Boiler in Lynn Haven, Florida.

1.3 BIOPROCESSING RESEARCH

Work on the Fossil Energy Bioprocessing Research Program includes fundamental research for coal applications that investigates advanced reactor design for conversion of coal and coal liquids, the use of enzymes in pure organic media, and development of biological processes for the conversion of coal residuum. In addition, the program includes studies on advanced

bioreactor systems for the treatment of gaseous substrates and the conversion to liquid fuels, removal of heteroatoms from heavy oils, renewable hydrogen production, remediation of oil containing soils. The program also includes natural gas and oil technology partnership support.

1.4 COAL COMBUSTION RESEARCH

It is known that fossil energy combustion devices, such as fluidized beds and pulsed combustors, can exhibit characteristic features of deterministic chaos. The ability to measure and describe chaotic components will contribute to greatly improved methods for characterizing, modeling, designing, and controlling commercial fossil energy processes such as combustion, coal gasification, hot-gas cleanup, and oil retorting. The Fossil Energy Program is involved in the evaluation of chaotic components in data from fluidized beds and other coal combustion processes.

1.5 FOSSIL FUEL SUPPLIES MODELING AND RESEARCH

The Strategic Petroleum Reserve (SPR) is a government-owned stockpile of crude oil intended to serve as a buffer against possible oil market disruptions. The overall purpose of this project is to develop and apply improved models and tools for SPR management. Current project efforts emphasize developing new modeling tools to explicitly and flexibly portray oil market uncertainty and SPR planning risk. Another task in this program area is the development of advanced computational tools for three-dimensional seismic analysis.

1.6 ADVANCED TURBINE SYSTEMS

The DOE Offices of Fossil Energy and Energy Efficiency and Renewable Energy have initiated a program to develop advanced turbine systems for power generation. The objective of the Advanced Turbine Systems (ATS) Program is to develop ultra-high efficiency, environmentally superior, and cost competitive gas turbine systems for utility and industrial applications. One of the supporting elements of the ATS Program is the Materials/Manufacturing Technologies Task. The objective of this element is to address the critical materials and manufacturing issues for both industrial and utility gas turbines.

2. MATERIALS RESEARCH AND DEVELOPMENT

N. C. Cole

Materials research and development activities at Oak Ridge National Laboratory include development of ceramic composites for high temperature applications; new alloys with unique mechanical properties for advanced fossil energy systems; development of functional materials, such as ceramic filters, ceramic membranes, and carbon materials; and corrosion research to understand the behavior of materials in coal processing environments. The transfer of technology developed on this program is enhanced through interactions with industry and joint research programs with those interested in using the technology, as well as an active CRADA involvement.

2.1 FABRICATION OF FIBER-REINFORCED COMPOSITES BY CHEMICAL VAPOR INFILTRATION

T. M. Besmann, W. M. Matlin, D. P. Stinton, and P. K. Liaw

ABSTRACT

Processing equipment for the infiltration of fiber-reinforced composite tubes is being designed that incorporates improvements over the equipment used to infiltrate disks. A computer-controlled machine-man interface is being developed to allow for total control of all processing variables. Additionally, several improvements are being made to the furnace that will reduce the complexity and cost of the process. These improvements include the incorporation of free standing preforms, cast mandrels, and simpler graphite heating elements.

INTRODUCTION

Fiber-reinforced silicon carbide matrix composites are a candidate for a number of high temperature applications due to their high temperature strength, light weight, thermal shock resistance and damage tolerance. However, in the current commercial isothermal, isobaric chemical vapor infiltration process, thick parts are difficult to density. A leading alternative process is forced chemical vapor infiltration (FCVI). In FCVI, a preform is placed in a reactor, where one side is heated and the other side is cooled, resulting in a thermal gradient across the preform. As the reactant gases pass through the preform they undergo a surface reaction, resulting in the formation of a ceramic matrix and an effluent gas. In the case of SiC deposited from chlorosilanes, the effluent gas has a poisoning effect on the reaction rate. This poisoning, combined with the depletion of the reactant, tends to slow down the deposition rate. However, since the gases are traveling toward the hot side of the preform their temperature increases, resulting in faster deposition rates due to the Arrhenius behavior of the deposition reaction. Control over deposition can thus be maintained by using the increase in temperature to offset reactant depletion and effluent gas buildup.

Work at the Oak Ridge National Laboratory (ORNL) has shown that the time to infiltrate 4.45 cm diameter disks 1.27 cm thick can be reduced from 24 hours to less than 15 hours by utilization of a two-step process [1]. This reduction in processing time is expected to result in lower processing cost, thereby making the process more industrially feasible [2]. Additionally, ORNL researchers have investigated the production of more industrially relevant shapes such as

tubes. Initially, 2.54 cm diameter tubes were made using furnaces originally designed for the production of disks [3]. Based on the initial successes of the 2.54-cm inner diameter, 0.64-cm wall thickness tubes, a larger furnace was designed exclusively for the fabrication of tubes (Fig. 1). This furnace is designed to process tubes up to 10 cm in diameter and 30 cm in length. The new furnace, as well, will incorporate a number of improvements based on the experience of processing numerous disks and a few initial tubes.

DISCUSSION OF CURRENT ACTIVITIES

Process Optimization Through the Continual Control of Processing Variables

As demonstrated in the two-step FCVI process, significant time savings can be achieved through the proper control of thermal gradient, reactant concentration, total gas flow, and pressure. The two-step process does not represent the end of process optimization, but an initial step. In the ideal case, processing conditions would be varied continuously in response to the continually changing pore structure within the preform. A LabView™-based process control system is being designed that will allow for the complete control of reactant and carrier gas flow rates as well as preform hot-side temperature. Each of these variables can be controlled as a function of time, thereby allowing the investigation of more complex process optimization schemes. Figure 2 is a schematic of the FCVI system and controls.

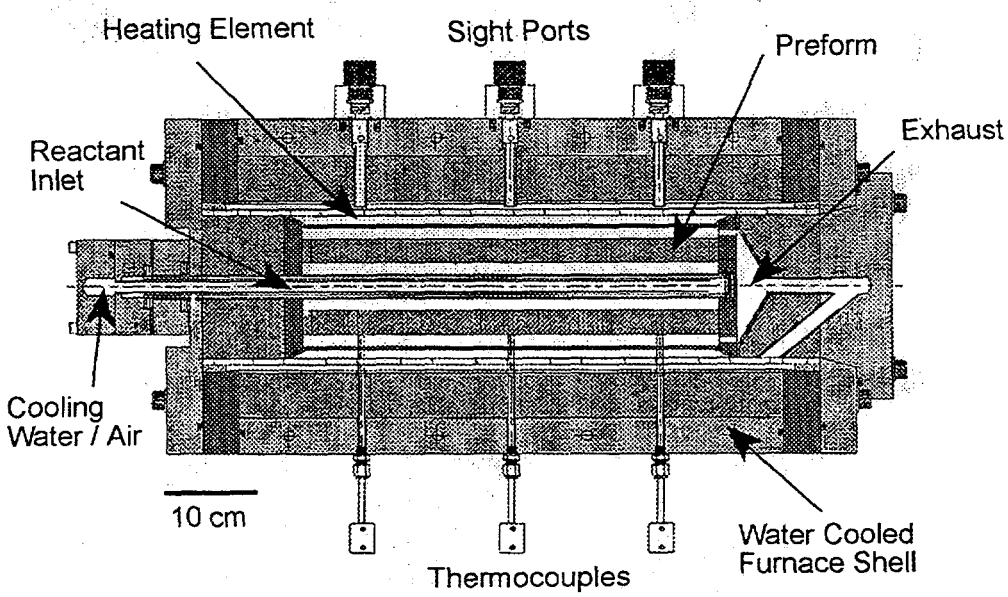

Figure 1. Scale-up furnace for the fabrication of tubular composites.

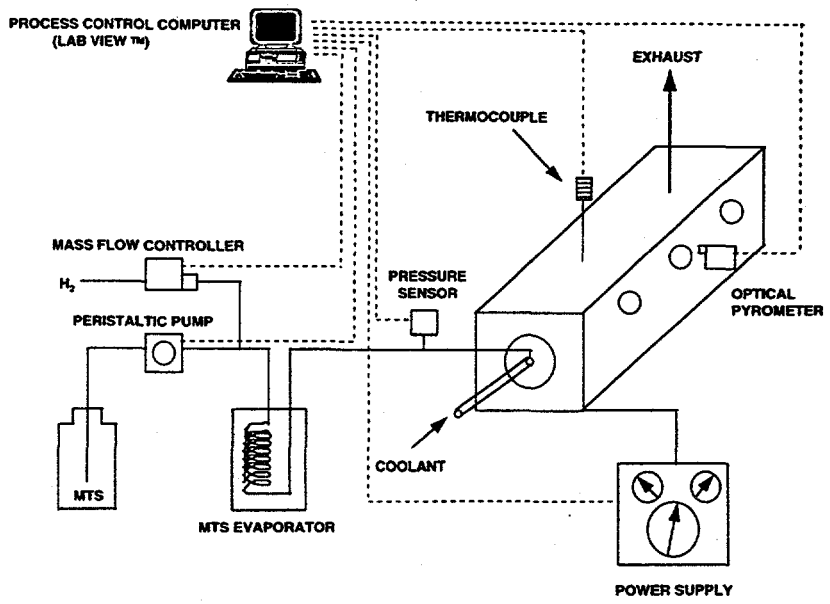

Figure 2. Flow diagram and controls for the scale-up FCVI system for preparing tubular composites.

At the heart of the system is a Power Macintosh 7100/80 containing a four port serial card and a Lab - NB data acquisition card running LabView 3.1.1. Carrier gas flow is controlled through the use of a serial connection between the LabView computer and mass flow controllers. Liquid methyltrichlorosilane (CH_3SiCl_3 or MTS), at room temperature and pressure is pumped from a storage container to a vaporizer using a peristaltic pump. In a manner similar to the control of the carrier gas, LabView is used to send a set point to the peristaltic pump thereby controlling the flow of reactant into the system. As an additional method of control the MTS container is placed on a electronic balance with a serial port. In this way an accurate measurement of reactant flow can be maintained by continually monitoring the reduction in container weight using LabView.

The final area of control is preform temperature. The system has two methods for controlling preform temperature. The first method is through the use of an Ircon Modline Plus optical pyrometer. Additional monitoring of preform temperature can be accomplished through a thermocouple which can be placed on the cool side of the preform to monitor the thermal gradient.

Improvements in the Tube Furnace Design

The transition from processing relatively simple shape preforms such as disks to more complicated shapes such as tubes requires alternate design furnace internals. In order to effectively infiltrate composites using FCVI, four criteria must be met; a pressure differential must be established across the preform, a thermal gradient must be established across the preform, reactant and carrier gases must be introduced to the high pressure, cool-side of the preform, and effluent gases must be removed from the low pressure hot side of the preform.

The pressure differential in the disk furnace is achieved by allowing a water-cooled injector to be pressed against the bottom of the preform holder. A graphite foil gasket is placed between the holder and the injector to ensure a relatively gas-tight seal. The holder is held in place by ridges inside the coating chamber. In addition to positioning the preform within the furnace, the coating chamber also serves to protect the heating element, which resides outside the coating chamber, from overcoating by SiC. A preform hot side temperature can be measured and controlled by sighting an optical pyrometer down the inside of the coating chamber and focusing on the top of the preform. Once the correct preform hot-side temperature is established the correct thermal gradient can be fixed by varying the materials and distance between the preform and the water-cooled injector. The further away from the injector and the lower the thermal conductivity of the spacer material the higher the cool-side temperature. Finally, the reactant gases are directed to the cool-side of the preform by flowing them through the inside of the water-cooled injector.

Since this furnace design served the production of disks so well it was adapted for the production of tubes. However, the first tube infiltration revealed a number of areas which required improvement. In the production of disks the graphite holder became bonded by deposited SiC to the preform during the FCVI process. At completion, the holder must be machined from the part. While this works well in the case of disks where the preform is surrounded by the holder, it does not work as easily with tubes since the mandrel is surrounded by the preform. It is also difficult to form a gas-tight seal between the mandrel and the cooled injector. Without such a seal a pressure differential can not be imposed across the preform. Lack of a tight seal has two negative results. It becomes impossible to achieve high final preform densities and there is a large loss of reactant through deposition on the inner walls of the furnace and through exhaust from the furnace.

As a solution to these difficulties, methods of removing the graphite mandrel were investigated. Initially, the use of more easily machinable mandrel material, such as carbon bonded carbon fiber were investigated. However, it was recognized that the ideal situation would being able to process the preform without the use of a mandrel. With the assistance , of researchers at the 3M Company's Research and Development Center, a process for rigidizing tubular preforms was adapted for the current system. While originally developed as a method to rigidize thin, hot gas filter preforms, the method works equally well for thicker preforms. In the 3M process, the preform is immersed in a dilute phenolic resin solution. The impregnated tube is then removed from the solution, dried, and cured, resulting in a rigid preform. When fired to FCVI process temperatures, 800°C - 1200°C, the phenolic resin pyrolyzes, leaving a thin carbon layer. It is speculated that this carbon layer bonds the individual fibers together where the fibers contact each other, thereby explaining the limited strength of the after fired tubes.

Without the use of a mandrel, another approach to forming of a gas tight seal is needed. Casting the preform to the cooled injector was attempted since it was simple, inexpensive, and likely effective. In this method a high-alumina castable refractory was used to fix the preform directly to the injector, thereby positioning the preform a specific distance from the injector and creating a gas tight seal. Tailoring the thermal gradient can still be achieved by positioning an insulating sleeve of material between the injector and the preform.

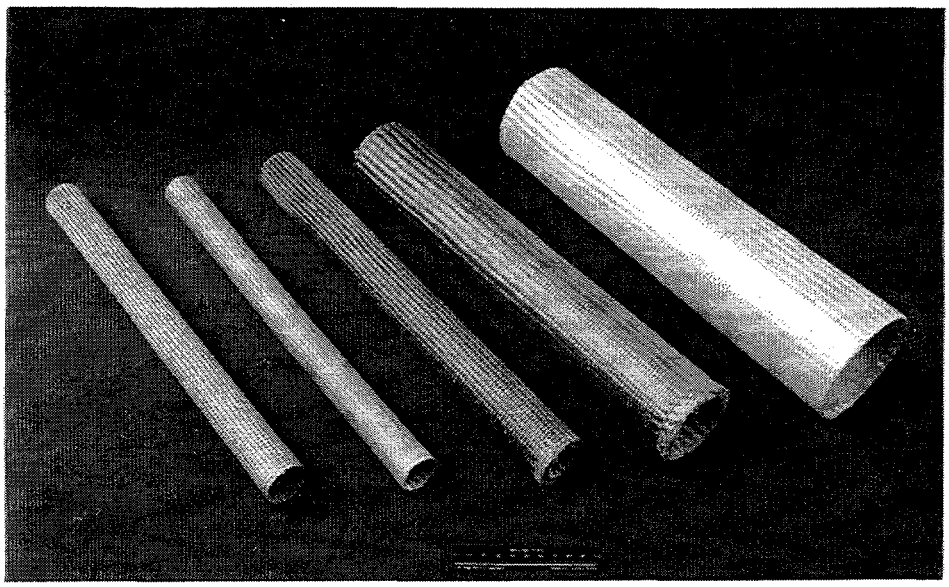

Figure 3. Various Nextel™ fiber tubes rigidized with phenolic resin.

Rather than supplying reactant to the cool-side of the preform by running the gases inside the injector, as is done in the smaller units for preparing disks, penetrations through the cast end caps were used to allow the reactant gases to be routed to the inside of the preform. This method greatly simplifies the injector design and eliminates any welds from being exposed to the highly corrosive environment within the furnace.

Finally, one of the most critical process parameters in FCVI is the thermal gradient, and therefore the cool- and hot-side temperatures. Hot-side temperatures are relatively easily controlled via power to the furnace. Cool-side temperature control is more problematic. Current efforts to improve control of the cool-side temperature in the scale-up tube furnace involve variability in the injector coolant. The injector system has been designed to allow for water, high-temperature oil (silicone), or air cooling. Previous experience in the smaller tube fabrication systems has indicated that maintaining a sufficiently high inner diameter temperature is difficult. It is thus expected that alternate cooling media will allow greater control over the thermal gradient and allow higher inner diameter temperatures to be used.

REFERENCES

1. W.M. Matlin, D.P. Stinton, and T.M. Besmann, "Fabrication of Fiber-Reinforced Composites by Chemical Vapor Infiltration", Proceedings of the Ninth Annual Conference on Fossil Energy Materials, Oak Ridge National Laboratory Report ORNL/FMP-95/1, pp 157-165, (1995)

2. Y.G. Roman, D.P. Stinton, "The Preparation and Economics of Silicon Carbide Matrix Composites by Chemical Vapor Infiltration"; in Mat. Res. Soc. Symp. Proc. Vol. 365 Edited by R.A. Lowden, M.K. Ferber, J.R. Hellman, K.K. Chawla, S.G. DiPietro, Materials Research Society, Pittsburg, PA, pp. 343-350 (1994)

3. D.P. Stinton, T.M. Besmann, W.M. Matlin, T.L. Starr, and W.A. Curtin, "Forced Chemical Vapor Infiltration of Tublar Geometries: Modeling, Design, and Scale-Up"; in Mat. Res. Soc. Symp. Proc. Vol. 365 Edited by R.A. Lowden, M.K. Ferber, J.R. Hellman, K.K. Chawla, S.G. DiPietro, Materials Research Society, Pittsburg, PA, pp. 317-324 (1994)

2.2 INTERACTION OF LOW-EXPANSION NZP CERAMICS WITH Na_2SO_4 AT 1000°C

W.Y. Lee, D. P. Stinton, and D. L. Joslin

ABSTRACT

The interaction between several low-expansion NZP materials and Na_2SO_4 at 1000°C in pure O_2 was studied. $Ba_{1.25}Zr_4P_{5.5}Si_{0.5}O_{24}$ experienced extensive cracking and delamination upon reaction with Na_2SO_4. On the other hand, $Ca_{0.5}Sr_{0.5}Zr_4P_6O_{24}$ remained intact in terms of visual appearance, and had no significant weight loss or gain. However, the ion exchange between Na^+ ions and Ca^{+2} ions was observed to be sufficiently rapid to allow the penetration of the Na^+ ions into the test specimens in 100 h. The segregation of Ca to the specimen surface was observed due to the ion exchange. $Ca_{0.6}Mg_{0.4}Zr_4P_6O_{24}$ was also tested, but its stability could not properly be assessed because the as-received specimens contained a significant amount of $MgZr_4P_6O_{24}$ as an impurity phase.

INTRODUCTION

A new class of ceramic materials with low and tailorable thermal expansion characteristics has been developed for potential use in a variety of high temperature applications [1-3]. They are commonly referred to as NZP and named after the parent composition ($NaZr_2P_3O_{12}$) which was discovered to exhibit high cationic conductivity and low-expansion characteristics. Although the thermal expansion behavior of most NZP materials is generally anisotropic, some NZP compositions such as $Ba_{1+x}Zr_4P_{6-2x}Si_{2x}O_{24}$ (where $0 \leq x \leq 1$), $Ca_{1-x}Sr_xZr_4P_6O_{24}$, and $Ca_{1-x}Mg_xZr_4P_6O_{24}$ can be tailored to obtain isotropic expansion characteristics [2-4]. The Young's modulus of these NZP materials is reported to be rather low for a ceramic (~70 GPa) [3]. Another interesting property of these materials is their low thermal conductivity (~1 W/mK for slip-cast materials [3]) which is essentially as low as that of air plasma sprayed yttria stabilized zirconia coatings currently used as thermal barrier coatings in advanced gas turbines.

In addition to their potential use as bulk materials, the NZP ceramics could also be considered for thermal barrier and corrosion resistant coating applications. For example, Si-based materials such as Si_3N_4 and SiC are known to be susceptible to major strength reduction in certain corrosive environments containing condensible deposits such as Na_2SO_4 and Na_2CO_3 [5,6]. Thus, the need for developing a coating system which protects the surface of the Si-based materials from

the corrosive environments has been recognized [7,8]. Unfortunately, progress in developing such a coating system has been limited because of many challenging thermochemical and thermomechanical requirements. From a thermomechanical point of view, the use of the NZP materials as protective coatings for Si-based ceramics may be advantageous because of the low thermal expansion and compliance of the NZP materials relative to most Si-based materials. However, the thermochemical stability of these complex material systems has not been explored except for the recent work of Li et al. [9]. They prepared a thin $Ca_{0.6}Mg_{0.4}Zr_4P_6O_{24}$ coating on Si_3N_4 and SiC substrates using a sol-gel method. The coated substrates were exposed to several environments containing Na_2CO_3 at 1000°C for 50 h, and yet no major change in the flexural strength of the Si_3N_4 substrates was observed. This suggested that the coating was effective in protecting the Si_3N_4 substrates from the corrosive environments. In order to further assess the potential of NZP materials for use as corrosion-resistant coatings, the present study is aimed at examining the intrinsic stability of several NZP bulk forms in a Na_2SO_4-containing atmosphere.

DISCUSSION OF CURRENT ACTIVITIES

Experimental

Three slip-cast NZP materials were evaluated: $Ba_{1.25}Zr_4P_{5.5}Si_{0.5}O_{24}$ (BS25, x=0.25, LoTEC, Salt Lake City, UT), $Ca_{0.6}Mg_{0.4}Zr_4P_6O_{24}$ (CM40, x=0.4, Golden Technologies, Golden, CO), and $Ca_{0.5}Sr_{0.5}Zr_4P_6O_{24}$ (CS50, x=0.5, LoTEC). These particular compositions were chosen because they possess high strength while exhibiting low thermal expansion anisotropy and hysterisis [2,3]. Two specimens (1 cm x 0.4 cm x 0.3 cm) were tested for each material. The specimens were typically loaded with about 5 to 10 mg/cm^2 Na_2SO_4 of using a procedure described elsewhere [8]. Prior to applying the layer of Na_2SO_4, the specimens were cleaned with distilled water, methanol, and acetone. The Na_2SO_4 loaded specimens were placed on an Al_2O_3 holder and exposed for 100 h to a flowing oxygen environment (200 cm^3/min) at 101 kPa in a quartz tube heated to 1000°C using an electric resistance furnace. It is noted that Na_2SO_4 has a relatively low rate of evaporation at these temperature and pressure conditions (~ 0.016 mg/cm^2/h) [10]. Thus, the premature loss of Na_2SO_4 due to evaporation was not expected to occur for the test duration used in this study. Each NZP composition was tested in separate batches to avoid any sample cross-contamination. A Scintag V X-ray diffractometer (XRD) and a JEOL Superprobe 733 electron microprobe analyzer (EMPA) were used for characterization. Both as-received and reacted specimens were mounted in epoxy and polished using kerosene as a lubricant to examine the formation of any reaction products and

resulting surface microstructures. One of the two specimens exposed to the reaction treatment was washed in warm water using an ultrasonic bath to remove any water-soluble or weakly bonded phase(s) from the reacted surface.

Results

Table 1 shows that BS25 lost significant weight after reacting with Na_2SO_4 for 100 h. In reference to the initial weight before Na_2SO_4 loading, Sample #BS25-1 lost 33.7 mg (or 27.2 mg/cm^2) after the reaction and washing steps. It was visually evident that both unwashed and washed BS25 specimens were structurally disintegrated. Severe surface recession due to cracking and delamination were observed particularly along the corners and edges of the specimens' top surface. The formation of $NaZr_2P_3O_{12}$ was detected by XRD as a minor phase in both unwashed and washed specimens. In addition, the BS25 diffraction peaks were observed to be somewhat randomly shifted by small amounts as a result of the reaction step.

Table 1. Weight (g) of low-expansion ceramic specimens (dimensions; 1 cm x 0.4 cm x 0.3 cm) measured after Na_2SO_4 loading, reaction, and washing in warm water. Net weight change (Æm) = Final weight after washing - Initial sample weight. CM40 specimens could not be washed because they were fractured into pieces after reaction.

Sample	Initial	Na_2SO_4	Reacted	Washed	Æm
BS25-1	0.3745	0.3859	0.3644	0.3414	-0.0337
BS25-2	0.3519	0.3652	0.3087	-	-
CM40-1	0.3875	0.3945	0.3725	-	-
CM40-2	0.3774	0.3879	-	-	-
CS50-1	0.3151	0.3203	0.3162	0.3145	-0.0006
CS50-2	0.3225	0.3308	0.3242	-	-

CM40 specimens also significantly cracked, and were actually fractured into several pieces after reacting with Na_2SO_4. However, it appeared from the XRD analysis that the as-received CM40 specimens contained a significant amount of $MgZr_4P_6O_{24}$ as an impurity phase. The XRD pattern of the reacted specimens indicated the formation of $NaZr_2P_3O_{12}$ and/or $CaZr_4P_6O_{24}$ along with an unknown phase(s). Note that $NaZr_2P_3O_{12}$ and $CaZr_4P_6O_{24}$ are difficult to distinguish by XRD because of their similar lattice parameters.

Unlike the BS25 and CM40 samples, the weight of the CS50 specimens decreased only slightly after the reaction and washing steps (0.5 mg/cm^2 for Sample #CS50-1 in Table I). No significant recession due to cracking and delamination was visually detected. However, as shown in Figure 1, an EMPA analysis of the polished cross-section of the reacted specimen (Sample #CS50-1) shows that the ion exchange between Na^+ ions from Na_2SO_4 and Ca^{+2} ions from CS50 was fairly extensive during the 100-h reaction period. The presence of Na was observed throughout the entire cross-section of the reacted sample. In contrast, as-received CS50 samples did not contain any Na detectable to the EMPA technique. The segregation of Ca toward the surface was observed as shown in Figure 1. It appeared that the Ca-enriched surface layer was weak since it was somewhat damaged by polishing as evidenced by some delamination in this region. There was no apparent change in the Ca-enriched surface layer after washing. The presence of sulfur was not detected by the EMPA technique in the reacted and washed samples. In comparing the XRD patterns of the as-received, corroded, and washed samples, the appearance of some new, unindexable diffraction peaks was observed after the reaction step. The new peaks did not disappear after the specimen was washed.

Discussion

The experimental observations suggested that the BS25 specimens became structurally as well as chemically unstable when reacted with Na_2SO_4 at 1000°C for 100 h in O_2. The formation of the $NaZr_2P_3O_{12}$ phase was observed as a reaction product from the BS25 samples. The $NaZr_2P_3O_{12}$ phase is known to exhibit highly anisotropic thermal expansion behavior, and consequently microcracks extensively. Also, the formation of $NaZr_2P_3O_{12}$ can induce undesired volume changes since the unit-cell volume of $NaZr_2P_3O_{12}$ (1527.83 Å^3) is smaller than that of BS25 (1559.94 Å^3 [11]). Therefore, the formation of the $NaZr_2P_3O_{12}$ phase appears to be responsible for the observed cracking and delamination of the reacted BS25 samples.

The stability of CM40 with respect to Na_2SO_4 could not be assessed from this study, because the starting material contained a significant amount of $MgZr_4P_6O_{24}$ as an impurity phase.

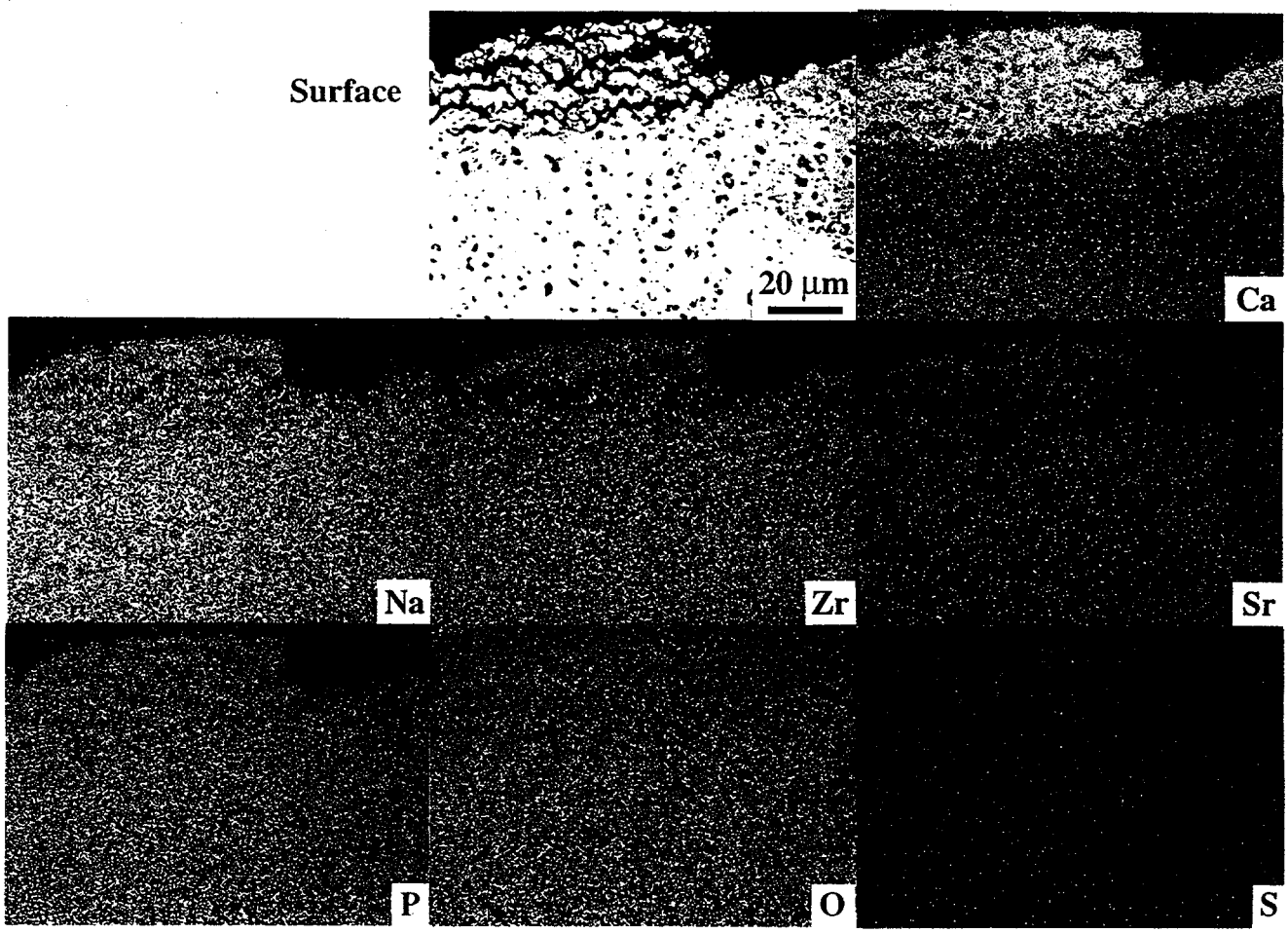

Fig. 1. Backscattered image and X-ray elemental maps of CS50 after reaction with Na_2SO_4 at 1000°C for 100 h in pure O_2.

Nevertheless, the observed cracking and delamination of these specimens after reaction with Na_2SO_4 could be explained by the relatively large volume change anticipated from the transition of $MgZr_4P_6O_{24}$ to $NaZr_2P_3O_{12}$ and/or $CaZr_4P_6O_{24}$. The unit-cell volume of monoclinic $MgZr_4P_6O_{24}$ (977.52 Å^3) is considerably smaller than that of rhomobehedral $NaZr_2P_3O_{12}$ and $CaZr_4P_6O_{24}$ (1527.83 and 1516.01 Å^3, respectively). Because of the $MgZr_4P_6O_{24}$ impurity phase, the results from this study could not directly be compared to those reported by Li et al. [9]. As mentioned earlier, Si_3N_4 substrates coated with a sol-gel CM40 coating did not show any strength degradation after exposure to several corrosive environments containing Na_2CO_3 at 1000°C for 50 h. In future work, pure CM40 specimens are needed to determine their intrinsic stability in the corrosive environments.

In terms of visual appearance and weight loss, the CS50 samples appeared to have remained relatively intact after reaction with Na_2SO_4. However, at a microscopic level, the EMPA results clearly indicated that the ion exchange between the Na^+ and Ca^{+2} ions was sufficiently rapid for the Na^+ ions to penetrate the entire CS50 specimens during the 100-h exposure. The presence of sulfur was not detected at least within the sensitivity of the EMPA technique. Therefore, it seems that the CS50 material promotes the dissociation of Na_2SO_4 while releasing SO_3 and/or SO_2 as gaseous byproducts. The significance of these observations relative to the potential of the CS50 material as a corrosion resistant coating for Si-based ceramics is not yet clear. A further study is needed to assess the effects of Na penetration through a CS50 coating structure in protecting Si-based substrates. Also, the thermochemical compatibility between the CS50 and Si-based ceramics must be addressed.

Acknowledgments

The authors acknowledge their gratitude to Santosh Limaye for providing the BS25 and CS50 samples, Kevin Cooley for performing the Na_2SO_4 reaction experiments, Tom Geer for metallography, Y. W. Bae for X-ray diffraction, and Ted Besmann, Dane Wilson and Ian Wright for reviewing this manuscript.

References

1. C.-Y. Huang, D.K. Agrawal, H.A. McKinstry, and S.Y. Limaye, "Synthesis and Thermal Expansion Behavior of $Ba_{1+x}Zr_4P_{6-2x}Si_{2x}O_{24}$ and $Sr_{1+x}Zr_4P_{6-2x}Si_{2x}O_{24}$ systems," J. Mater. Res., **9**, 2005 (1994).

2. D.A. Hirschfeld, S.M. VanAken, T.K. Li, Y.P. Yang, and J.J. Brown, "Development of Ultra-Low-Expansion Ceramics: Synthesis, Thermal Expansion, and Thermal Conductivity of $(Ca_{1-x},Mg_x)Zr_4(PO_4)_6$," pp. 239-244 in the Proceedings of the Annual Automotive Technology Development Contractors' Meeting, Dearborn, MI, October 22-25, 1990. Published by the Society of Automotive Engineers, Inc., Warrendale, PA, 1991.

3. S.Y. Limaye and R. Nageswaran, "Development of NZP Ceramic Based "Cast-In-Place" Diesel Engine Port Liners," Final Report, LoTEC, Inc., West Valley City, UT, November 1994.

4. T.B. Jackson, S.Y. Limaye, and W.D. Porter, "The Effects of Thermal Cycling on the Physical and Mechanical Properties of [NZP] Ceramics," pp. 63-80 in Ceramics Transactions Vol. 52; Low-Expansion Materials. Edited by D.P. Stinton and S.Y. Limaye, The American Ceramic Society, Westerville, OH, 1995.

5. N.S. Jacobson, "Corrosion of Silicon-Based Ceramics in Combustion Environments," J. Am. Ceram. Soc., **76**, 3 (1993).

6. T.E. Strangman and D.S. Fox, "Resistance of Silicon Nitride Turbine Components to Erosion and Hot Corrosion/Oxidation Attack," p. 36-1 in Proceedings of Advisory Group for Aerospace and Research & Development Symposium on Erosion, Corrosion, and Foreign Object Damage Effects in Gas Turbines, Printed by Canada Communication Group, Quebec, Canada, November 1994.

7. K.N. Lee, N.S. Jacobson, and R.A. Miller, "Refractory Oxide Coatings on SiC Ceramics," MRS Bulletin, 35, (October 1994).

8. W.Y. Lee, Y.W. Bae, and D.P. Stinton, "Na_2SO_4 Induced Corrosion of Si_3N_4 Coated with Chemically Vapor Deposited Ta_2O_5," J. Am. Ceram. Soc., **78**, 1927 (1995).

9. T.K. Li, D.A. Hirschfeld, and J.J. Brown, "Thin Film Coatings of $(Ca_{1-x},Mg_x)Zr_4(PO_4)_6$ on Si_3N_4 and SiC," J. Mater. Res., **9**, 2014 (1994).

10. N.S. Jacobson and D.S. Fox, "Molten-Salt Corrosion of Silicon Nitride: II, Sodium Sulfate," J. Am. Ceram. Soc., **71**, 139 (1988).

11. S. Shanmugham, D.P. Stinton, O.B. Calvin, C.R. Hubbard, and S.Y. Limaye, "Synthesis and Cell Refinement of $Ba_{0.5+x/2}Zr_2P_{3-x}Si_xO_{12}$ with x=0.25 and x=0.375," J. Mater. Sci. Lett., **13**, 1326 (1994).

2.3 OXIDATION-RESISTANT INTERFACE COATINGS FOR SiC/SiC COMPOSITES

D. P. Stinton, E. R. Kupp, J. W. Hurley, R. A. Lowden, S. Shanmugham and P. K. Liaw

ABSTRACT

The characteristics of the fiber-matrix interfaces in ceramic matrix composites control the mechanical behavior of these composites. Finite element modeling (FEM) was performed to examine the effect of interface coating modulus and coefficient of thermal expansion on composite behavior. Oxide interface coatings (mullite and alumina-titania) produced by a sol-gel method were chosen for study as a result of the FEM results. Amorphous silicon carbide deposited by chemical vapor deposition (CVD) is also being investigated for interface coatings in SiC-matrix composites. Processing routes for depositing coatings of these materials were developed. Composites with these interfaces were produced and tested in flexure both as-processed and after oxidation to examine the suitability of these materials as interface coatings for SiC/SiC composites in fossil energy applications.

INTRODUCTION

Continuous fiber ceramic matrix composites require fiber/matrix interfaces which allow load transfer from the matrix to the fibers when the composite materials are stressed. Crack deflection and fiber pullout are also necessary components of the mechanical behavior of composites. Fiber/matrix interfaces are currently on of the weak links in continuous fiber ceramic matrix composites materials for applications in the oxidative environments which are typical of fossil energy applications. Pyrolytic carbon performs well as an interfacial coating for Nicalon fiber-reinforced silicon carbide-matrix composites, however it's use in fossil energy applications may be limited because of its poor oxidation resistance. If stressed above the point where the matrix cracks, air can penetrate into the composites and oxidize the fiber/matrix interfaces. After very short times the composite's mechanical properties suffer and eventually the material becomes brittle.[1] Alternate interface coatings need to be developed that are chemically stable with respect to the fiber and matrix materials, and thermally stable and oxidation resistant at use temperatures.

Shanmugham et al[2] conducted FEM analysis and reported that a low modulus interfacial coating will be effective in reducing the radial stresses that result on cooling to room temperature from processing temperature. Further, for interfacial materials with the same modulus, a material with a higher thermal expansion coefficient than that of the fiber and the matrix may be more effective in reducing the radial stresses than a material with a lower thermal expansion coefficient. These FEM results were similar to the analytical modeling results of Hsueh et al[3]. In order to investigate the above hypothesis, mullite and aluminum titanate were chosen as candidate interface materials for further study.

Another approach being investigated is to deposit a modified form of SiC in the interface. This idea was described previously by Lowden et al[4]. In a SiC fiber/SiC matrix composite, such an interface would be chemically and mechanically stable and as thermally stable as the other components of the composite. The modified SiC, amorphous in this case, would have a relatively low modulus to encourage crack propagation at the fiber/matrix interface.

EXPERIMENTAL PROCEDURE

Composite preforms were prepared by stacking discs of ceramic-grade Nicalon™ plain-weave cloth (Nippon Carbon Company, Tokyo, Japan) in a 0/30/60 sequence in graphite holders. After immersing the preforms in acetone to remove the fiber sizing they were ready for interface coating deposition. The oxide interface coatings were deposited by a sol-gel process described previously[5]. Thin CVD carbon films were deposited on most samples on the fibers and/or on the interface coating prior to matrix infiltration. These films were not thick enough to act as effective interface coatings, but their purpose is simply to protect the samples from the corrosive CVD environment. Carbon deposition conditions were:

Temperature: 1100°C
Pressure: ~1-2 kPa
Time: 15 min
Gas flows: 25 cm^3/min C_3H_6
500 cm^3/min Ar.

The amorphous SiC interface coatings were also deposited by CVD, but at varying conditions. Only the pressure was held constant, at atmospheric pressure (101 kPa). The reaction gases in this case were methane (CH_4), methylsilane (CH_3SiH_3) and Ar.

The composites were infiltrated using forced flow chemical vapor infiltration. In this process, described in detail by Stinton et al[6], the gases are forced to flow through the preform under temperature and pressure gradients. When the pressure gradient reaches 200 kPa, the furnace automatically shuts off and the gas flows are stopped. The reactants used are 0.3 cm^3/min methyltrichlorosilane (MTS, CH_3SiCl_3) and 500 cm^3/min hydrogen. The top temperature of the preform holder is maintained at 1200°C and the pressure downstream of the part is 101 kPa.

RESULTS AND DISCUSSION

Sol-Gel Oxide Interface Coatings

Mullite and aluminum titanate precursor sols were developed for coating applications. The high temperature X-ray diffraction (HTXRD) study conducted on the precursor gels revealed that mullite and aluminum titanate formed at 1050°C and 1400°C, respectively. Based on the HTXRD

results, it could be concluded that the aluminum titanate formation temperature is too high and would degrade Nicalon fibers. Since mullite forms at 1050°C, it was predicted that a mullite coating could be obtained on Nicalon fibers without damaging the fibers.

The developed mullite and aluminum titanate precursor sols were utilized for coating Nicalon tows and fabrics. Nicalon tows dipcoated in the mullite precursor sol and heat treated at 1000°C for 10 h, and cooled to room temperature broke easily during handling. In contrast, Nicalon tows dipcoated in the aluminum titanate precursor sol and heat treated similarly were relatively easy to handle. It should be noted that only an alumina and titania mixture would form on Nicalon fibers at 1000°C. Since alumina-titania did not damage the Nicalon fibers, it was considered as an interface material for further investigation.

A Nicalon/SiC composite with a mullite interface was fabricated, with the mullite (50 nm thick) interface deposited by a sol-gel process. However, the composite exhibited brittle fracture, and this could be attributed to the degradation of the Nicalon fibers during the sol-gel processing of mullite. In order to avoid damage to the fibers during the sol-gel processing of the oxide, the need to apply a thin carbon coating (inner carbon layer) prior to the deposition of an oxide coating deposition was recognized. Thermodynamic modeling studies indicated that oxide coatings would be attacked by HCl, a by-product of the SiC matrix formation reaction. It was surmised that a thin carbon coating (outer carbon layer) deposited on the oxide coating prior to the SiC matrix infiltration may help prevent the HCl attack. It should be noted that these carbon coatings are too thin to act as effective interfaces on their own.

In order to get a better understanding of the type of interface that would be appropriate to pursue, Nicalon/SiC composites with the following interfaces were considered: An oxide/C interface and a C/oxide/C interface. The composite with an oxide/C interface would identify the degradation of Nicalon fibers, if any, that might occur during the sol-gel processing of the oxide, because the oxide coating is directly applied on the fibers in this case. The composite with a C/oxide/C interface is likely to have better mechanical properties than a composite with a C/oxide interface, since the likelihood of the fiber degradation taking place during the sol-gel processing of the oxide is reduced due to an inner carbon layer.

The flexure strength results of Nicalon/SiC composites with four different interfaces are summarized in Table 1. The standard deviation of the flexure strength measurements for all the cases was less than 25%. For the first two cases, it should be noted that there was no inner carbon layer, while the last two composites had an inner carbon layer between the fiber and the oxide. Twenty four flexure bars of approximately 2.5 x 3.0 x >33 mm dimensions were cut from each of the composites. The four-point bend testing was conducted either with inner and outer spans of 10 mm and 20 mm, or 10 mm and 30 mm, respectively. Twelve flexure bars of each of the composites were tested in the as-processed condition. For composites with low strength (< 150 MPa) in the as-processed condition, the remaining 12 bars were oxidized at 1000°C for 24 h in air, and subsequently tested at room

temperature. In the case of composites with moderate or high strength (> 225 MPa) in the as-fabricated condition, the remaining 12 bars were oxidized at 1000°C in air as follows: 6 bars for 24 h, 3 bars for 200 h, and 3 bars for 500 h.

From Table 1, it is evident that composites with out an inner carbon layer had low flexure strength (< 122 MPa). The composite with a mullite/C interface had low flexure strengths (< 80 MPa) both in the as-processed and oxidized condition, and underwent brittle failure (no damage-tolerance). In contrast, the composite with an Al_2O_3-TiO_2/C interface had an average flexure strength of 122 MPa in the as-processed condition, and did not undergo any significant strength reduction on oxidation. Morevoer, it displayed damage-tolerant behavior in both the cases.

Table 1. Flexure strength results of Nicalon/SiC composites with four different interfaces

ID#	Interface	Strength (MPa)‡				Fracture Type
		As Processed	Oxidized at 1000°C in air 24 h	200 h	500 h	
1	Mullite/C	64	80	-**	-	Brittle
2	AT*/C	122	112	-	-	Composite
3	C/Mullite/C	304	286	221	217	Composite
4	C/AT/C	255	189	TBT***	TBT	Composite

‡ standard deviation < 25 % AT* - Al_2O_3-TiO_2 -** - not tested TBT***- to be tested

The composite with a C/mullite/C interface had a moderate flexure strength of around 304 MPa as-processed condition and did not have any significant strength reduction after 24 h oxidation. However, the strength dropped to 221 MPa after 200 h oxidation and remained at that level even after 500 h oxidation. In contrast to a composite without an inner carbon layer (mullite/C interface), this composite (with an inner carbon layer) had damage-tolerant behavior in the as-processed condition and sustained this characteristic even after 500 h oxidation. Fig. 1 shows the load vs displacement curve for samples in the as-processed and after 200 h oxidation for a composite with a C/mullite/C interface. It is evident from the figure that even after 200 h oxidation, the sample displayed a non-catastrophic mode of failure.

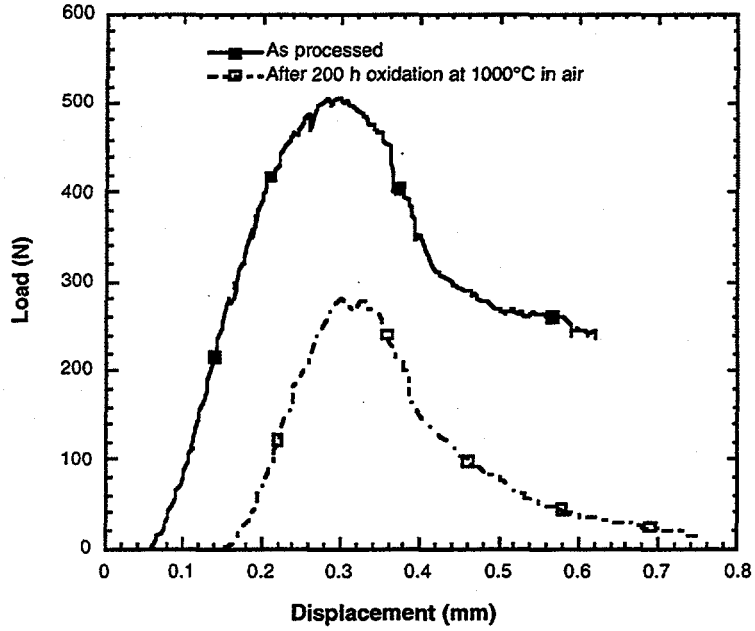

Figure 1. Composite with a Nicalon/C/mullite/C interface exhibit damage-tolerant behavior even after 200 h oxidation at 1000°C in air, but with reduced flexure strength

In the as-fabricated condition, the composite with a C/Al_2O_3-TiO_2/C interface had a higher flexure strength (255 MPa) than the composite with an Al_2O_3-TiO_2/C interface (120 MPa). This situation prevailed even after oxidation for 24 h (200 h and 500 h oxidized samples are to be tested). Similar to the composite with an Al_2O_3-TiO_2/C interface, this composite also exhibited non-catastrophic failure.

Preliminary fracture surface examination revealed that the composite which underwent catastrophic failure showed very little pullout. In contrast, the samples which displayed non-catastrophic failure showed considerable amount of pullout. Scanning auger spectrometer analysis is underway and should identify where the debonding occurred (fiber-coating interface or coating-matrix interface) and the interface coating thickness.

Amorphous SiC Interface Coatings

Previous work with a modified SiC interface coating in SiC/SiC composites yielded promising oxidation-resistance, but the coatings were generally non-uniform within the part. The primary goal of much of the recent work involving this interface material was to optimize the

interface deposition uniformity. Other objectives were to repeat promising processing conditions to assess the reproducibility of the process and run longer term oxidation tests to further assess the stability of the materials in high temperature oxidative environments.

A series of experiments was performed in which the amorhpous SiC deposition temperature was varied from 880 to 1000°C. The intent of these runs was to increase the interface coating uniformity by lowering the thermal gradient across the preform. The results of these tests were inconclusive since the flexure strengths were not statistically different in samples coated at different temperatures (see Table 2), although the variability in strengths was generally decreased as the temperature decreased. The load-displacement curves were indicative of materials showing good composite behavior in all cases. Another matrix of experiments was initiated at a deposition temperature of 1000°C in which the total flow of gases as well as the methylsilane and methane concentrations were varied to study their effects on composite uniformity. Increasing the total gas flow and/or concentrations of CH_3SiH_3 and CH_4 appeared to produce composites with less uniform coatings (high standard deviations for strengths and densities). At low flow/low concentration conditions, the composite properties (density, flexure strength and graceful failures) were promising. Strength retention after exposure to air for 24 hours at 1000°C was also good.

Table 2. Density and flexure strength data for composites with amorphous SiC interfaces deposited at temperatures between 880 and 1000°C.

Sample	Deposition Temperature (°C)	Density (g/cc)			Flexure Strength (MPa)		
		Top	Middle	Bottom	Top	Middle	Bottom
CVI947	880	2.63	2.58	2.36	144.2±28.5	334.3±22.1	248.1±35.4
CVI946	925	2.56	2.46	2.25	164.2±71.7	207.9±90.4	221.3±10.3
CVI950	1000	2.60	2.56	1.84	123.1±5.4	229.7±75.8	98.4±4.3

The following set of processing conditions was determined to be optimum after further refinement of the process, combining the best conditions from each set of experiments and additional tests of deposition time:

Temperature - 900°C
Pressure - 101 kPa
Time - 1 hr
Gas flows - 40 cm^3/min CH_3SiH_3
500 cm^3/min CH_4
500 cm^3/min Ar

The optimization was based on the magnitudes and uniformity of density, coating thickness and mechanical behavior (flexure strength and load-displacement curve shape) throughout the parts. Density is a measure of the degree of infiltration, which may be affected by the distribution of the interface coating. Non-uniform distribution may lead to portions of the part sealing before they are fully dense. Flexure testing is used not only as an assessment of the strength and damage tolerance of a material, but also to determine the extent of damage caused by oxidation. The flexure behavior of samples with an amorphous SiC interface coating deposited using the above conditions is illustrated in Figure 2. The composite retained 75% of its strength after being exposed to air at 1000°C for 100 hours. Some of the damage tolerance, or composite-like behavior, was lost during oxidation as evidenced by a faster decline in load-bearing cability past the peak load (i.e. the tail of the curve drops over a smaller displacement). In addition to the optimization of properties at this set of deposition conditions, the composite characteristics were reproducible using these conditions.

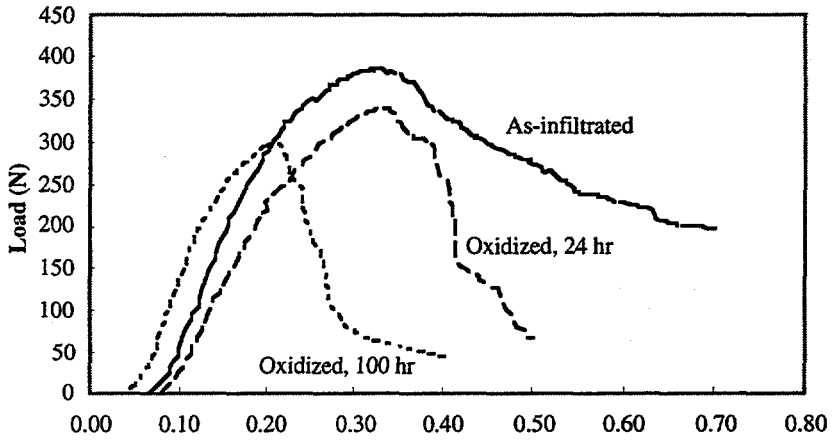

Figure 2. Flexure curves for a SiC/SiC composite (CVI993), with an amorphous SiC interface coating, as-processed and after oxidation for 24 and 100 hours at 1000°C in air.

Additional evidence that the SiC interface coating is effective even after oxidation is seen in Figure 3. This figure contains micrographs of the fracture surfaces of as-infiltrated and oxidized composite samples. Considerable pullout is apparent in both images, indicating that the interface coating is still acting as the weak point and crack deflection is occuring at the interface.

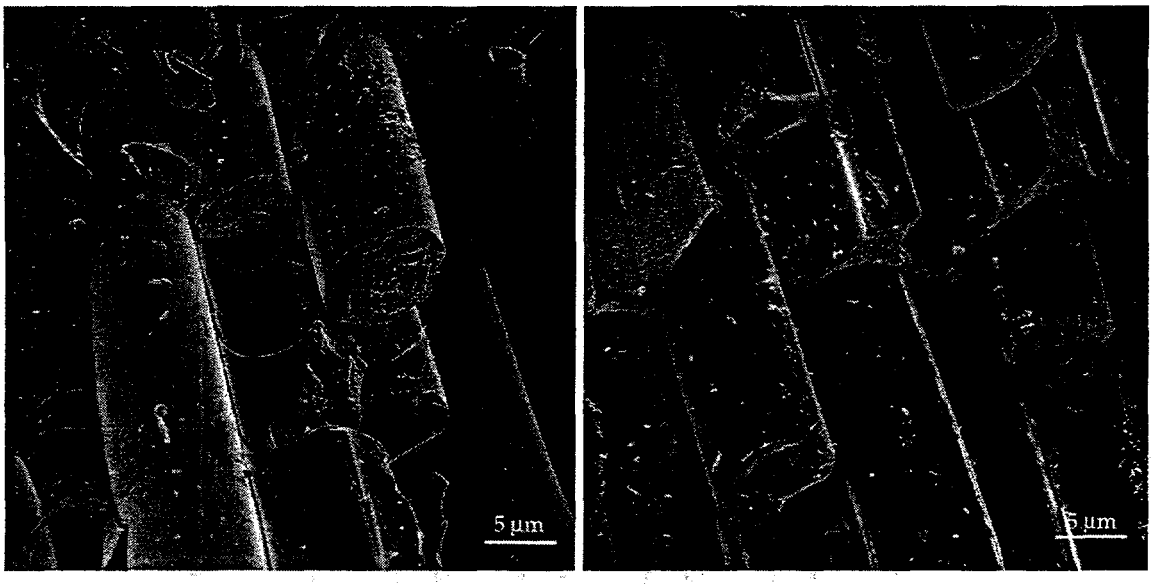

(a) (b)

Figure 3. Scanning electron micrographs of a SiC/SiC composite with an amorphous SiC interface coating showing extensive pullout in both (a) as-infiltrated and (b) oxidized (100 hr, air, 1000°C) states.

CONCLUSIONS

Composites with C/oxide/C interfaces exhibited higher flexure strengths than those of composites with oxide/C interfaces. Among the composites investigated, the composite with a C/mullite/C interface had the highest flexure strength and retained damage tolerant behavior even after 500 h oxidation. Both C/mullite/C and C/Al_2O_3-TiO_2/C interfaces have good potential as interface materials for Nicalon/SiC composites and long-term oxidation tests need to be conducted to ascertain their potential.

Amorphous SiC also shows potential as an oxidation-resistant interface material in SiC/SiC composites. The deposition process has been optimized to yield a composite that is fairly uniform from top to bottom in terms of density and mechanical behavior. Flexure strengths of 350-400 MPa have been achieved. These materials also exhibit graceful failures characteristic of composite behavior even after oxidation, although a portion of the strength and damage tolerance are lost during oxidation.

REFERENCES

1. P. F. Tortorelli, S. Nijhawan, L. Riester and R. A. Lowden, "Influence of Fiber Coatings on the Oxidation of Fiber-Reinforced SiC Composites," Ceram. Eng. Sci. Proc., 14 [7-8], 358-366 (1993).

2. S. Shanmugham, D. P. Stinton, F. Rebillat, A. Bleier, T. M. Besmann, E. Lara-Curzio, and P. K. Liaw, "Oxidation-Resistant Interfacial Coatings for Continuous Fiber Ceramic Composites," Ceram. Eng. Sci. Proc., 16 [4], 389-99 (1995).

3. C. H. Hsueh, P. F. Becher, and P. Angelini, "Effects of Interfacial Films on Thermal Stresses in Whisker-Reinforced Ceramics," J. Am. Ceram. Soc., 71 [11], 929-33 (1988).

4. R. A. Lowden, O. J. Schwarz and D. P. Stinton, "Development of Oxidation-Resistant Interface Coatings," pp. 105-116 in the Proceedings of the Eighth Annual Conference on Fossil Energy Materials, ed. by N. C. Cole and R. R. Judkins, Oak Ridge, TN, May 10-12, 1994.

5. S. Shanmugham, P. K. Liaw, D. P. Stinton, T. M. Besmann, K. L. More, A. Bleier, W. D. Porter and S. T. Misture, "Development of Sol-Gel Derived Coatings for Nicalon™/SiC Composites," to be published in Ceram. Eng. Sci. Proc., 17 (1996).

6. D. P. Stinton, A. J. Caputo and R. A. Lowden, "Synthesis of Fiber-Reinforced SiC Composites by Chemical Vapor Infiltration," Amer. Ceram. Soc. Bull., 65 [2], 347-350 (1986).

2.4 CERAMIC FIBER FILTER TECHNOLOGY

Brenda. L. Holmes and Mark A. Janney

INTRODUCTION

Fibrous filters have been used for centuries to protect individuals from dust, disease, smoke, and other gases or particulates [1]. In the 1970s and 1980s ceramic filters were developed for filtration of hot exhaust gases from diesel engines[2-4]. Tubular, or candle, filters have been made to remove particles from gases in pressurized fluidized-bed combustion and gasification-combined-cycle power plants [5]. Very efficient filtration is necessary in power plants to protect the turbine blades. The limited lifespan of ceramic candle filters has been a major obstacle in their development.

The present work is focused on forming fibrous ceramic filters using a papermaking technique. These filters are highly porous and therefore very lightweight. The papermaking process consists of filtering a slurry of ceramic fibers through a steel screen to form paper. Papermaking and the selection of materials will be discussed, as well as preliminary results describing the geometry of papers and relative strengths.

EXPERIMENTAL

Four classes of materials were used in making ceramic filters. These were the ceramic fiber, an organic binder fiber to hold the paper together and provide strength before firing, a bulking fiber to maintain an open, porous structure, and the ceramic bond phase. The ceramic fibers evaluated were Saffil ®, Nextel 312®, fused quartz fibers (QPC 300¤ and QPC 125 ®), fiberglass, and two aluminosilicate fibers with

alumina to silica ratios of 60%:40% and 87%:13%. The composition, diameter, and use temperature of the ceramic fibers are summarized in Table I. The QPC quartz fibers were heated to remove sizing prior to paper forming. All fibers were used in chopped form.

Table I. Summary of Ceramic Fibers

Fiber	Composition	Diameter	Continuous Use Temp (iC)	Producer
Saffil¤	Al_2O_3	3 micron diam.	1600	ICI
Nextel 312¤	62% Al_2O_3: 24% SiO_2: 14% B2O3	10 - 12 micron diam.	1200	3M
QPC 300¤	SiO_2	9 micron diam. (3 mm long)	1000	Quartz Products Company
QPC 125¤	SiO_2	14 micron diam. (13 mm long)	1000	Quartz Products Company
Al_2O_3:SiO_2	60% Al_2O_3: 40% SiO_2	20 micron diam.	1300	Zircar
Al_2O_3:SiO_2	87% Al_2O_3: 13% SiO_2	8 micron diam.	1600	Zircar
Fiberglass	SiO_2	33 micron diam.	400	Zircar

Polyethylene†, polyester §, polypropylene ‡, cellulose acetate¤, cellulose#, and fibrillated acrylic ¶ were tested as binder fibers. Cellulose* and Crestbrook pine+ were examined as bulking fiber. Colloidal silica ◊ and four particulate alkali glasses¥ were used for

ceramic bond phase. Table II summarizes selected properties of the glasses. The sintering temperature of the colloidal silica was experimentally determined to be 1200ßC.

Table II. Glass Bond Phases

Glass	Composi-tion	Diameter	Softening Temp. (°C)	Sintering Temp. (°C)
7052	Alkali Barium Borosilicate	9.4 micron	712	770
7056	Alkali Borosilicate	7.6 micron	718	770
7070	Lithia Potash Borosilicate	17.0 micron	Not Available	770
9013	Alkali Barium	10.7 micron	656	670

The ceramic filters were formed using a papermaking technique. It was determined that 9 grams of fibers were sufficient to form a paper approximately 20 cm x 20 cm x 0.1 cm. The total fiber weight was comprised of 75% ceramic fiber, 15% binder fiber, and 10% bulking fiber. The fibers were mixed in a blender in one liter of water. This slurry was poured into a Williams Standard Handsheet Mold** and further diluted with water to a volume of 5 liters. Upon draining the water from the handsheet mold, the fibers formed a paper on a stainless steel screen. This paper could be easily removed from the screen and handled after drying. Ceramic bond phase was incorporated into the paper either by direct addition to the slurry or

by dip coating the dried paper in a suspension of bond phase in water.

Comparison of papers formed with the various ceramic fibers and binder fibers was accomplished by determining the average relative strength of papers in tensile tests. Strips of paper 2.5 cm x 0.6 cm (1 inch x 0.25 inch) were loaded axially along the length of the sample to determine the breaking strength of the paper. Results from this test were used to select model systems for further study. Once ceramic fibers and binder fibers were chosen, the ceramic bond phases were compared using a biaxial loading test. Discs 5.8 cm (2.3 inch) in diameter were cut from fired papers. These discs were place on a supporting ring of the same diameter, a load was applied in the center of the disc at 7.9×10^{-3} cm/minute (0.02 inch/minute), and the breaking load and displacement were recorded. In this way, the different ceramic bond phases could be compared, and the amount of bond phase necessary to obtain acceptable strength could be evaluated.

RESULTS AND DISCUSSION

Fiber Evaluation

The relative strength of papers made with the different binder fibers was measured for papers which included Saffil¤ as the ceramic fiber and cellulose as the bulking fiber. The results are shown in Figure 1. Papers formed with the acrylic fiber were significantly stronger in tension than papers made with the other binder fibers. The acrylic fiber is highly branched, or fibrillated, with large numbers of long fibrils. These fibrils are very efficient at mechanically bonding particles or other fibers. The acrylic was the only one of the binder

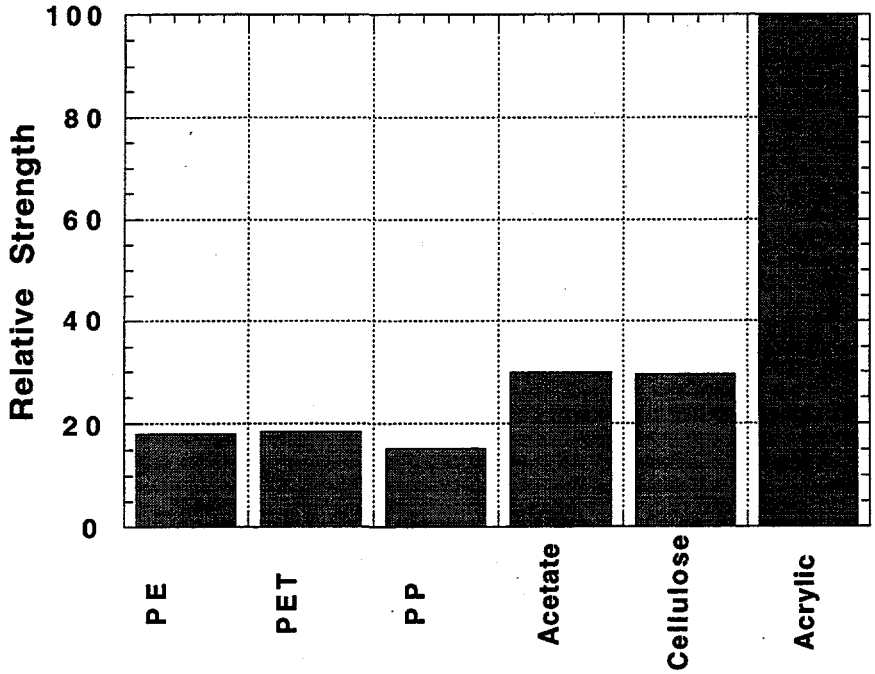

Figure 1. Relative strengths of Saffil® green papers made with various binder fibers.

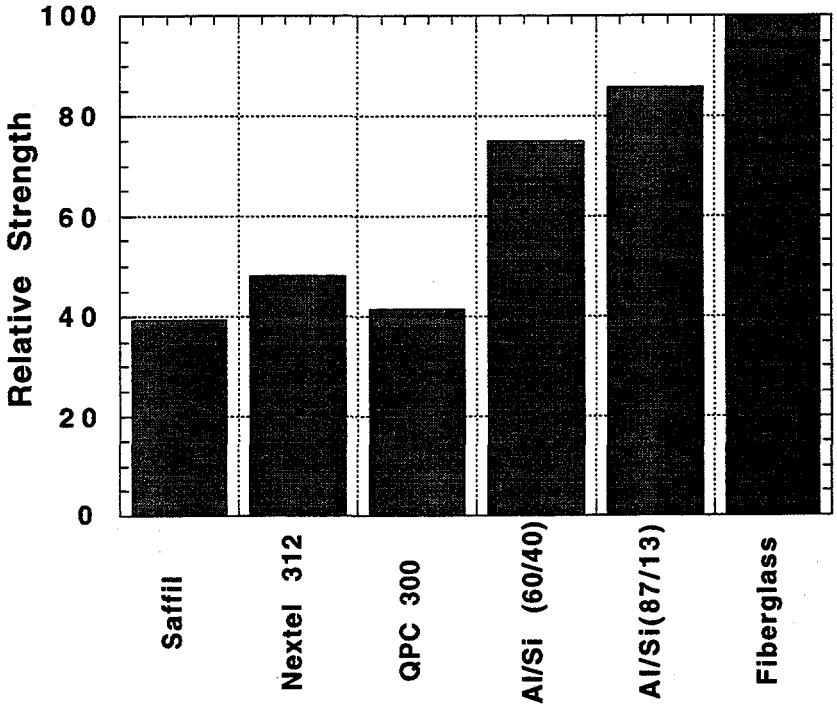

Figure 2. Relative strengths of green papers made with various ceramic fibers.

fibers tested which was fibrillated. Its high degree of fibrillation makes this fiber an excellent binder fiber for paper.

A similar test was conducted to select appropriate ceramic fibers. The results obtained from as formed, unfired papers made with cellulose acetate binder fiber and cellulose bulking fiber are provided in Figure 2. The goal of this test was to make a filter similar to Whatman ® analytical filters, and therefore strength alone was not a sufficient criterion to determine which ceramic fibers to study. Qualitative criteria such as brittleness, ease of tearing, the ability to be folded and hold a pleat, and ease of handling were noted and are summarized in Table III. Fiberglass filters proved to be the strongest samples, however papers containing this fiber were very brittle and difficult to handle. The two aluminosilicates performed well in the tensile test, yet resulted in very thin papers which tore easily when removed from the stainless steel screen. Papers made from the Saffil®, Nextel 312 ®, and quartz (QPC®) fibers were similar in relative strength. Papers made with Nextel 312® ceramic fibers were susceptible to tearing and showed no ability to fold or be formed into simple shapes such as pleats. The Saffil ® and QPC 300® fibers resulted in the most satisfactory papers overall, based on the criteria in Figure 2 and Table III, and were selected as the ceramic fibers to study further.

Bond Phase Particle Capture

One method of incorporating the particulate ceramic bond phase into the paper is to add it to the fiber slurry before the paper is formed. When using this method, it is desirable to know the distribution of the particles in the paper. To model the distribution of

Table III. Summary of Papers Made with Various Ceramic Fibers

Ceramic Fiber	Brittleness	Ability to Fold	Ease of Tearing	Ease of Handling
Saffil®	not brittle	very good	high	excellent
Nextel 312®	not brittle	poor	low	very good
QPC 300®	not brittle	very good	high	excellent
Al_2O_3:SiO_2 (60%:40%)	not brittle	very good	high	poor
Al_2O_3:SiO_2 (87%:13%)	not brittle	very good	high	poor
Fiberglass	very brittle	poor	low	moderate
Whatman¤ filter	not brittle	very good	low	excellent

particulate glass bond phase, one gram of silicon carbide particles of known size was used. The black silicon carbide particles were easily seen under an optical microscope, as opposed to the white glass particles. The silicon carbide particles could be counted to determine the number of particles per area of paper as a function of particle size and the specific region of the paper being studied, i.e. the center or the edge. Silicon carbide particles of 14.5, 23, and 50 micron diameter were used. Using an optical microscope, the number of particles observed in a known area were counted. A hole punch was used to remove samples from the outer edge and middle of the paper. Observations were made on both the top and bottom surfaces of each

sample. Specimens were then peeled apart to make observations on the inside of the paper.

When Saffil® was used as the ceramic fiber the distribution of particles showed some dependence on the particle size. In these instances, the 50 micron silicon carbide particles were more numerous in the middle of the paper than along the edge, while the opposite was true of 14.5 micron particles. The 23 micron particles resulted in the most uniform distribution between the edge and middle of the paper. When QPC 300® fibers were used the particle distribution was much more uniform across the paper, independent of the particle size used. For all samples, it was observed that more particles were captured in the inner layers of the papers than the outer surfaces, independent of the ceramic fiber used.

The average number of particles per area for several papers is shown in Figure 3. Blends of QPC 300 ® and QPC 125® (80%:20% and 50%:50%) were used to study the effect of fiber length (Table I) in particulate bond phase capture. As seen in Figure 3, the QPC ® fibers were slightly more efficient at capturing bond phase than the smaller Saffil® fibers. More small particles (14.5 and 23 micron) were captured in papers made of QPC 125 ® ceramic fiber than QPC 300®. The papers studied to obtain the results in Figure 3 contained fibrillated acrylic binder fiber and Crestbrook pine bulking fiber. As discussed previously, the fibrillation of the acrylic makes this fiber very efficient at capturing particles. To determine the particle capture caused only by the ceramic fibers and remove any effect due to the fibrillated acrylic, the experiment was repeated with papers which did not contain acrylic fiber. These papers retained only two particles/mm^2, regardless of the ceramic fiber used. To determine how

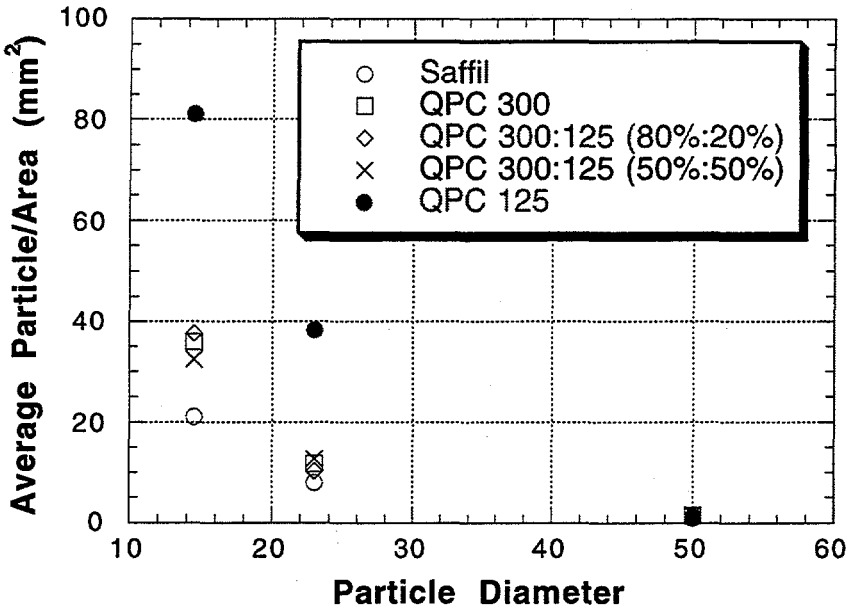

Figure 3. The number of particles of glass bond phase captured per unit area varied with the ceramic fiber used.

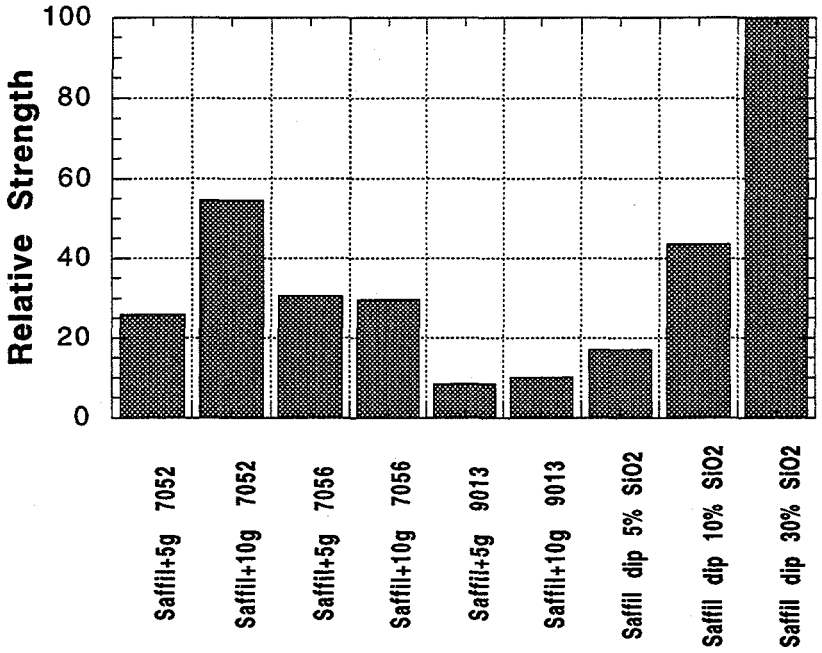

Figure 4. Relative compressive strength of fired papers.

much bond phase was present in a paper which was formed with acrylic, and subsequently subjected to binder burnout, the papers used in Figure 3 were heated to 800°C and the silicon carbide particles recounted. When compared to the data in Figure 3, no significant change in the number of particles present was noted.

Biaxial Load Test

Samples from fired papers containing one of four ceramic bond phases were tested using a biaxial load test. Glass bond phases 7052, 7056, and 9013 were added to slurries of Saffil® paper in 5 and 10 gram quantities. The colloidal silica bond phase was incorporated into papers by dipping Saffil® papers in 5%, 10%, or 30% aqueous colloidal silica solutions prior to firing. These papers contained approximately 0.4 g, 0.7 g, and 2.2 g of silica, respectively. The relative breaking loads for all samples are presented in Figure 4. Papers containing 5 grams of 7052 glass bond phase were half as strong as papers containing 10 grams of 7052. The relative strengths of papers containing colloidal silica increased in the ratio 1:3:6.5 as the amount of silica in the paper increased in the ratio 1:2:6. These examples indicate that increasing the amount of bond phase results in an increase in the number of bonds between fibers in the paper, thereby increasing the strength of the paper proportionally. The strength of papers made with 7056 and 9013 glass bond phases did not increase with the amount of bond phase added. This could be due to insufficient wetting of the bond phase on the fibers, possibly caused by surface chemistry problems or a firing temperature which was not high enough. The displacement observed during loading was approximately 50% greater for the papers made with glass bond phase

than for those made with colloidal silica. Papers made with glass or colloidal silica bond phase showed strain-tolerant behavior during testing, and exhibited graceful rather than catastrophic failure.

SUMMARY

Filter papers were made using Saffil ® and fused quartz ceramic fibers, acrylic binder fibers, bulking fiber, and ceramic bond phase. The fibers used were selected by tensile testing of papers made with several different ceramic and organic fibers. Glass and colloidal silica were used as the ceramic bond phase and were incorporated into the papers by addition to the fiber slurry or by dip coating prior to firing. Firing temperatures were determined experimentally. Silicon carbide particles of known size were used to model the distribution of particulate bond phase in the papers. The number of particles in a known area were counted under an optical microscope. More particles were captured in the inner layers of paper than the top or bottom surfaces. The particle distribution in the edge and center of the papers showed some dependence on particle size. As the ceramic fiber increased in length and diameter the calculated distance between particles decreased. The calculated number of particles per unit area showed good agreement with the observed number of particles per unit area. Fired papers were subjected to biaxial load tests. The strength of papers made with 7052 glass and colloidal silica showed a dependence on the amount of bond phase included in the paper. All samples exhibited strain-tolerant behavior.

† Polyethylene, Dupont Co., Wilmington, DE

§ Polyester, Schuller International, Denver, CO

‡ Polypropylene, Hercules, Passaic, NJ

¤ Cellulose Acetate, Hoescht-Celanese, Somerville, NJ

Cellulose (high alpha), Rayonier, Stamford, CT

¶ Fibrillated Acrylic (114-3), Cytec Industries Inc., Stamford, CT

* Kimwipe, Kimberly-Clark Corp., Roswell, GA

+ Crestbrook pine pulp, Buckeye Cellulose Corp., Memphis, TN

◊ Colloidal Silica, Matheson, Coleman, and Bell, Cincinnati, OH

¥ Sealing Glasses, Corning, Corning, NY

** Williams Standard Handsheet Mold, Testing Machines Inc., Amityville, NY

REFERENCES

1. C. N. Davies, Air Filtration, Academic Press, London, 1973.

2. M. Tomita, S. Tadagi, Method for Producing a Ceramic Filter for Cleaning Exhaust Gases from a Diesel Engine , U. S. Pat. 4540535 (1985).

3. J. Abthoff, H. D. Schuster, G. Loose, B. Jokl, Exhaust Gas Filter for Diesel Engine , U. S. Pat. 4704863 (1987).

4. Exhaust Gas Filter , U. S. Pat. 1498130 (1978).

5. H. P. Schiffer, S. Laux, U. Renz, High Temperature Gas Filtration ,GS-6489, Research Project 1336-07, Electric Power Research Institute, Palo-Alto, CA, (1992).

2.5 DEVELOPMENT OF MICROWAVE-HEATED DIESEL PARTICULATE FILTERS

Mark A. Janney and David P. Stinton
Oak Ridge National Laboratory

Thomas M. Yonushonis, A. Carl McDonald, and P. D. Wiczynski
Cummins Engine Company, Inc.

William C. Haberkamp
Fleetguard, Inc.

INTRODUCTION

Diesel engines are a prime mover of freight in the United States. Because of legislated reductions in diesel engine emissions, considerable research has been focused on the reduction of these emissions while maintaining the durability, reliability, and fuel economy of diesel engines.

The Environmental Protection Agency (EPA) has found that particulate exhaust from diesel powered vehicles represents a potential heath hazard. As a result, regulations have been promulgated limiting the allowable amounts of particulate from those vehicles. The 0.1 g/bhp/hr (gram per brake horsepower per hour) particulate standard that applies to heavy-duty diesels became effective in 1994. Engine manufacturers have met those requirements with engine modifications and/or oxidation catalysts. EPA has established more stringent standards for diesel-powered urban buses because of health concerns in densely populated urban areas.

Particulate traps have been shown to significantly reduce carbon particulate emissions from diesel engines. However, current particulate trap systems are expensive and unreliable. Demonstration of a fiber

based particulate trap coupled with a novel microwave energy regeneration system which address reliability and cost issues would greatly accelerate the introduction of this filtration technology into diesel engines.

A Cooperative Research and Development Agreement (CRADA No. ORNL93-0172) between Lockheed Marietta Energy Research (LMER) and the Cummins Engine Company is in place that supports this work. ORNL has unique capabilities in microwave technology and chemical vapor deposition that are critical to this effort. Cummins and Fleetguard (a subsidiary of Cummins) have unique capabilities in diesel engine technology and filter technology. The combination of all of these talents provided a basis for a successful project. The Department of Energy (DOE) CRADA monies came from both the Fossil Energy AR&TD Materials Program and the Energy Efficiency and Renewable Energy Office of Transportation Technologies (EE-OTT), Heavy Duty Transport Program.

FILTER DEVELOPMENT

An exhaust filter or diesel particulate trap must be designed to remove particles or soot in the 0.1 to 1.0 micrometer in size. Experience with fiber-based filter media has shown that fiber based systems are more effective than porous structures such as membranes or ceramic monoliths in terms of the efficiency and particulate trapping capacity.

Alumina fiber (Saffil¤, ICI Americas) was chosen to produce filter media for the diesel particulate filter. Formulation work was accomplished by making small (30.4 cm by 30.4 cm) samples cast in a

laboratory hand sheet mold. A fiber formulation was dispersed in water and then drained rapidly through a forming fabric or screen. Additional difficulties with Saffil fiber were encountered at this point. Saffil is very weak in both wet web and dry strength and on its own has very high air resistance. To increase the permeability of Saffil¤ fiber and add strength, other 'fugitive' fibers were required. Approximately 20-25% fugitive materials were incorporated to add strength and improve the porosity of the media. Various binder fibers that are highly fibrillated and provide strength through entanglement in the web have been examined. Chemical resins to aid formation and wet strength were also tested. In order for the paper samples to have good 'fired' strength, a thermosetting phenolic coating was added to maintain geometry during the coating process.

Candidate samples of the filter material were coated by chemical vapor deposition (CDV) at the Oak Ridge National Laboratory. A CVD silicon carbide coating of about 1 to 2 micrometers was deposited on the filter material. It was found that the coating did not significantly alter the porosity or pore structure of the media. The CVD coating effectively replaced the fugitive material producing samples with filtration characteristics similar to the original paper.

Pilot paper machine trials have been conducted on a laboratory machine capable of making continuous Saffil¤ paper. The goal was to produce sufficient amounts of Saffil¤ papers for building filter prototypes. Additions were incorporated with the Saffil¤ fiber to develop the green strength and porosity required for the particulate filter application.

Packaging density of the filter media is a primary concern since the filter must reside within a microwave cavity. The basic filter shape is a cylinder 15.2 cm in diameter and 15.2 cm in length. The construction considered is that of a single face corrugated or pleated media to be spiral wound. This geometry requires the ceramic paper be either formed into a sinusoidal or pleated arrangement and then alternately sealed between flat layers of material as it is wound.

Media properties will affect the ability to produce an element of ideal geometry. The samples, fabricated by Fleetguard, have used the pleated design with triangular cells of approximately 6 mm on each side and a material thickness of 1.6 mm. The estimated area is 1 square meter. Work is underway to improve the base paper, making it thinner and allowing for smaller pleats or possible fluting. This will give an increase in the packing density of 2 to 3 fold. The immediate goal is to reach the original target of 2 square meters with 1 mm thick media and a 3 mm pleat.

With the pleated or corrugated configuration, it is necessary to seal the alternating ends of the cells to create a flow path. Ideally, one edge would be sealed as the pleated and flat sheets are combined and then the opposing end sealed as the element is wound. This requires a sealant that will withstand the chemical vapor processing without opening up the flow path. A sealant composed of milled Saffil¤, vinyl acetate and powdered phenolic resin has been tested with some success.

The weight of the ceramic paper filter element is much lower than the extruded ceramic traps currently available and provides more rapid heating. The elements are also resilient although not extremely strong at this point in the development. As completed filters of better

geometry become available, strength and durability testing will commence. A typical SiC-coated filter element is shown in Figure 1.

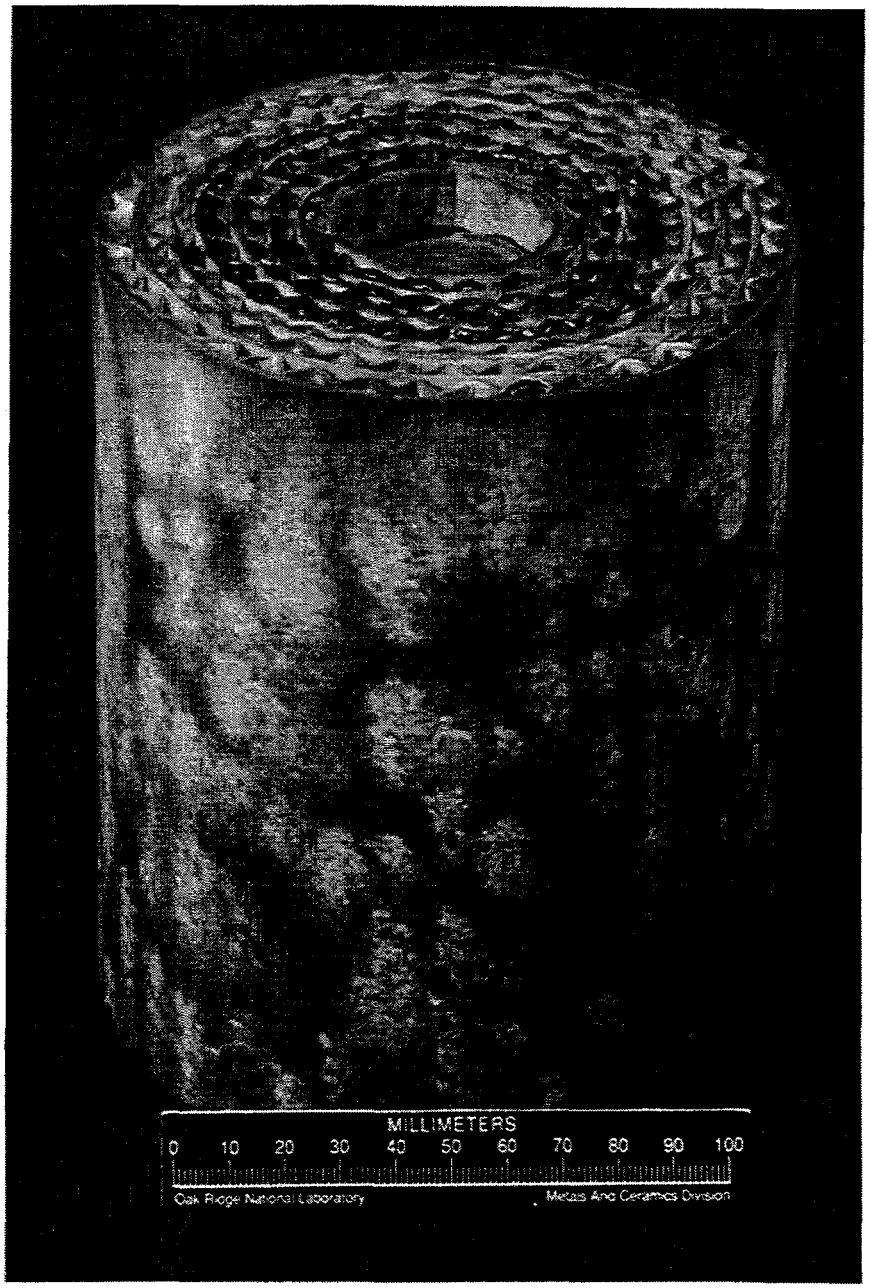

Figure 1. SiC coated Saffil® diesel exhaust particulate filter.

SYSTEM EVALUATION

Testing of the microwave regeneration method with a carbon-loaded filter under engine conditions was conducted in a test cell at the Cummins Technical Center. The filter was put into a stainless steel "can" following current exhaust system practices in the diesel engine industry. To validate laboratory results, a proof of concept evaluation was planned for the microwave filter system. The primary objective of the evaluation was to learn if a microwave filter could oxidize carbon particulates from a diesel engine (thus regenerating the filter). Two distinct evaluations were conducted to assess the regeneration capability of the microwave system.

Two methods were used to detect regeneration: 1) temperature, and 2) exhaust manifold back pressure. Thermocouples inserted into the filter recorded the temperature of the system during the regeneration cycle. Although temperature measurements provided adequate indication that the particulate carbon was being burned, back pressure measurements provided more useful information. Back pressure readings can signal when to start the regeneration process and can also signal the effectiveness of regeneration. We initiated regeneration once the back pressure rose to two times its starting value under the same operating conditions. The 2X rule allowed collection of sufficient carbon particulate matter to produce a measurable event without producing an extreme exotherm associated with oxidation of carbon.

The first evaluation assessed regeneration capabilities without exhaust gas flowing through the filter. The engine was operated for ten hours at 1500 rpm producing 17.2 kW of power. After the filter

had been loaded with carbon from the engine exhaust, the engine was switched off and power to the magnetron was engaged.

Testing without exhaust flow proved that it was possible to heat a filter system to the temperatures necessary for regeneration bymicrowaves. Time and temperature history of the three thermocouples, Figure 2, show the center region achieved temperatures

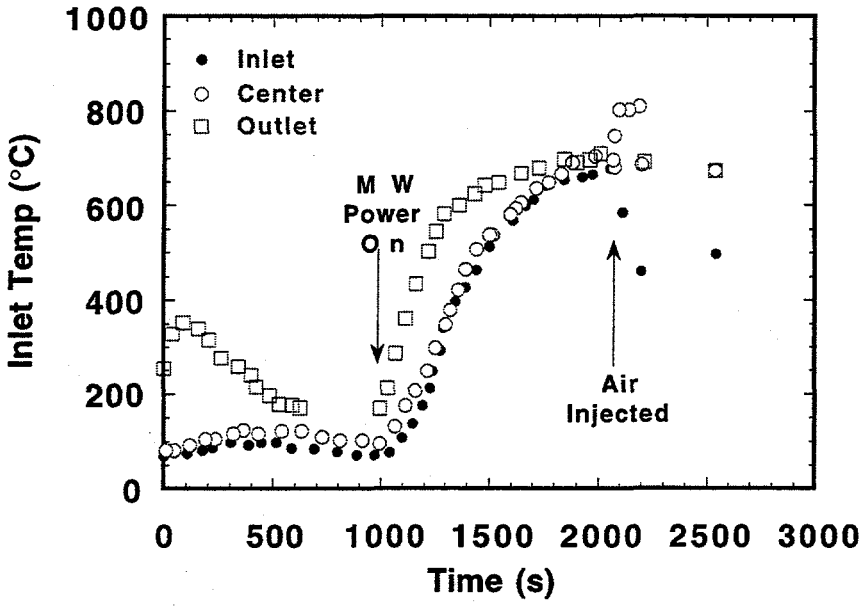

Figure 2. Carbon burnoff in regenerable filter system under "no flow" conditions.

necessary to oxidize carbon. The temperature fluctuations during the first one thousand seconds reflect system integrity evaluation and leak check using partial power. After applying full magnetron power, temperatures increased rapidly to 600¡C and began leveling, an indication of insufficient oxygen being available for combustion. Stopping the exhaust flow had decreased the supply of air to the filter. An injection of ambient air into the system resulted in a

temperature spike to 760¡C; the sudden increase suggested carbon oxidation.

The second evaluation measured the system's ability to regenerate while the engine continued to operate. Once the build up of carbon had increased the back pressure by a factor of two, engine operation was set to idle (800 RPM) and the magnetron was turned on.

Attempting to regenerate in the presence of exhaust flow gave results that were very positive. Figure 3 details the time history of both temperature and engine back pressure. Prior to dropping the engine to low idle, the back pressure measured 18 kPa and temperature readings exceeded 425¡C. Cooler exhaust temperatures, associated with idling, slightly decreased filter temperatures. However, within seconds of switching on the microwave power, the temperature of the center region increased to 760¡C. The exhaust back pressure decreased by 50% immediately after the temperature spike.

SUMMARY

A composite diesel particulate filter was developed which was heated using microwave energy. Temperature measurements suggest that the temperatures achieved were sufficient to oxidize diesel particulates without exhaust flow. Back pressure and temperature data strongly suggest the occurrence of regeneration during a low idle operation. A key concern is the detection of the regeneration event. Back pressure and to a lesser degree temperature readings are indicators of the regeneration event. However, localized heating in the filter may go undetected. Improved methods of detecting regeneration of the filter are required for development purposes.

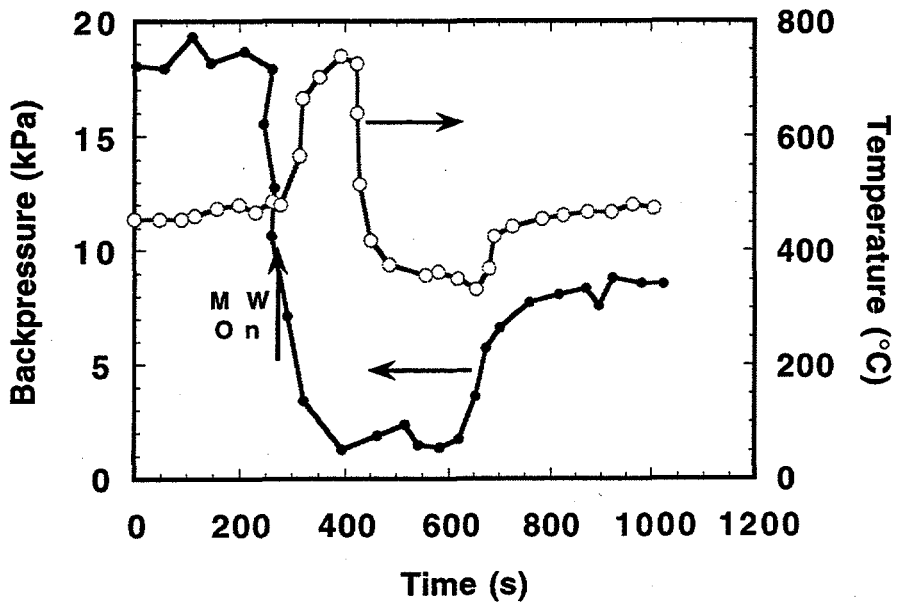

Figure 3. Carbon burnoff in regenerable filter system under "idle" conditions.

2.6 CARBON FIBER COMPOSITE MOLECULAR SIEVES

T. D. Burchell, M. R. Rogers, and A. M. Williams

INTRODUCTION

The removal of CO_2 is of significance in several energy applications. The combustion of fossil fuels, such as coal or natural gas, releases large volumes of CO_2 to the environment. Several options exist to reduce CO_2 emissions, including substitution of nuclear power for fossil fuels, increasing the efficiency of fossil plants and capturing the CO_2 prior to emission to the environment. All of these techniques have the attractive feature of limiting the amount of CO_2 emitted to the atmosphere, but each has economic, technical, or societal limitations. In the production of natural gas, the feed stream from the well frequently contains contaminants and diluents which must be removed before the gas can enter the pipeline distribution system. Notable amongst these diluent gasses is CO_2, which has no calorific value. Currently, the pipeline specification calls for <2 mol % CO_2 in the gas. Gas separation is thus a relevant technology in the field of energy production. A novel separation system based on a parametric swing process has been developed that utilizes the unique combination of properties exhibited by our carbon fiber composite molecular sieve (CFCMS).

The CFCMS is a monolithic activated carbon composed of petroleum pitch-derived carbon fiber and a phenolic resin-derived binder[1-3]. Routinely, micropore volumes and surface areas >1000 m^2/g are obtained using pitch fibers. The binder phase content is quite low and provides a monolithic structure by bonding the fibers at contact points only, thus rendering the CFCMS macroporous. The CFCMS offers, therefore, a highly adsorbent material with very little resistance to bulk gas flow. Experiments conducted at ORNL have shown the CFCMS to have a high affinity for carbon dioxide compared to zeolites and conventional granular activated carbons. The CFCMS also allows certain equipment variations not possible with granular materials. It can be molded into almost any shape, i.e., shape is constrained only by the ability to fabricate molds, where constraints appear to be minimal. The CFCMS can be machined by skilled operators using conventional tooling. These features permit the activated carbon to be formed to a desired shape to meet process equipment constraints as opposed to conventional filling of vertically oriented vessels with granular carbon. Granular carbon systems are also subject to attrition due to abrasive

wear in service, and channeling of the gas being processed as a result of inhomogeneous packing in the beds. Use of the CFCMS would permit the employment of, for example, horizontally-oriented vessels with controlled flow of the natural gas with the contaminants/diluents to be adsorbed through the adsorbent without risk of channeling and bypass flows.

The CFCMS is, as a result of the continuity of the fiber-matrix unit, electrically conductive. Advantage has been taken of this property to develop a novel desorption process we have termed electrical (or voltage) swing adsorption. On saturation of the CFCMS with, for example, carbon dioxide, immediate desorption can be accomplished by application of very low voltages (in our experiments we have used 0.5-1 volt) across the adsorbent. There are many important operational implications of this desorption process. The system pressure and temperature do not have to be altered as they do in other parametric swing processes such as pressure swing adsorption (PSA) or temperature swing adsorption (TSA). The electrical swing adsorption process is extremely fast in comparison to PSA or TSA. It is an inherently low energy process compared to the energy requirements of PSA or TSA processes. All of these features suggest a great deal of system and operational simplicity. We present below the results of several experiments which demonstrate the performance of the CFCMS and the electrical swing adsorption process.

EXPERIMENTAL

The carbon fiber composite molecular sieve (CFCMS) material used in this study was fabricated using a process initially developed by the U. S. Department of Energy (USDOE) for the production of thermal insulators for NASA space missions[4]. The CFCMS synthesis route is illustrated in Fig.1. Isotropic pitch derived carbon fibers are mixed with powdered phenolic resin to form a water slurry. The slurry is transferred to a molding tank and the water drawn through a porous screen under vacuum. The resultant green artifact is dried, cured at 60°C in air, and stripped from the mold screen. The composite is cured at ~150°C in air prior to carbonization at 650°C in an inert gas. The final synthesis stage involves activation of the composite in moisture saturated He in the temperature range 800-950°C.

Porosity characterization was performed using nitrogen adsorption and mercury intrusion. Nitrogen adsorption isotherms were measured at 77 K using our Autosorb-1 instrument.

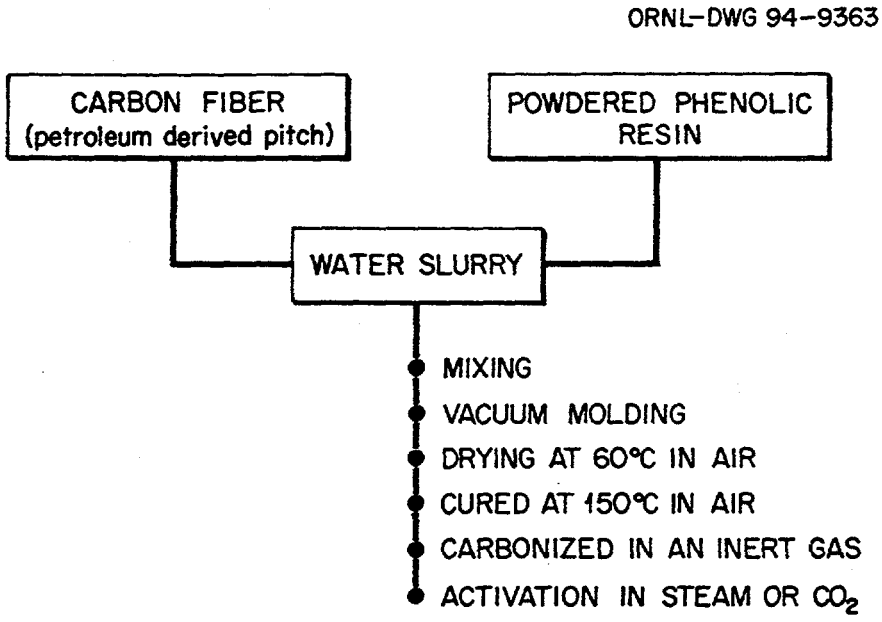

Fig. 1. The CFCMS synthesis route.

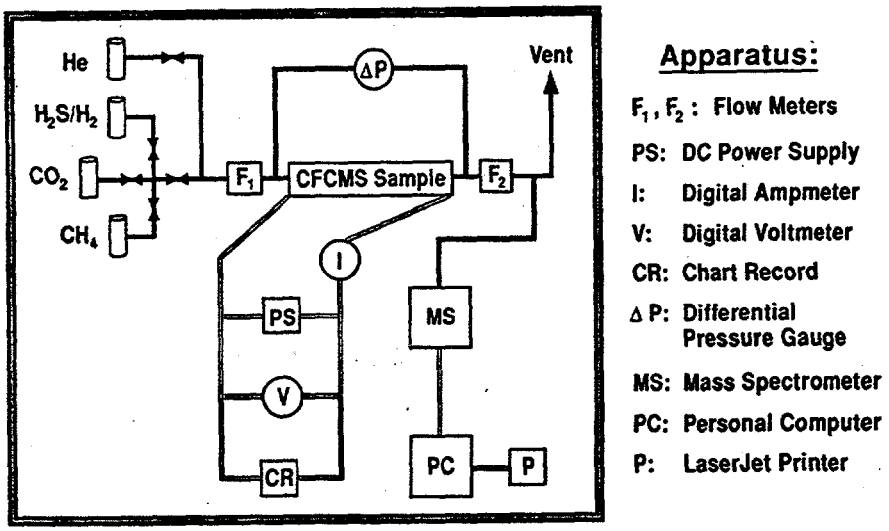

Fig. 2. Schematic drawing of our experimental breakthrough apparatus.

Micropore size analysis used a variety of methods, including the Brunauer, Emmett, and Teller (BET)[5] method for surface area and the Dubinin-Astakhov (DA)[6] method for micropore radius and the t-method for micro-pore volume. CO_2 and CH_4 adsorption isotherms for CFCMS were also obtained using the Autosorb-1 apparatus over the pressure range 0.1 to 760 mm Hg and at temperatures of 30, 60, and 100 °C. High pressure CO_2 and CH_4 adsorption data (850 psi max.) were obtained using a gravimetric apparatus, courtesy of Westvaco Corporation.

CFCMS is, as a result of the continuity of the fiber-matrix unit, electrically conductive. Advantage has been taken of this property to develop a novel desorption process, which we have termed electrical (or voltage) swing adsorption. On saturation of the CFCMS with, for example, carbon dioxide, immediate desorption can be accomplished by application of very low voltages (in our experiments we have used 0.5-1 volt) across the adsorbent. A schematic diagram of our experimental breakthrough apparatus is shown in Fig. 2. The feed gas flows through a CFCMS sample (25.4-mm diameter and 76.2-mm long) to a vent. A sample of the downstream gas is fed to a mass spectrometer allowing on-line monitoring of the exit gas composition. Flowmeters (F1 & F2) are positioned either side of the CFCMS sample. Electrical leads are connected to each end of the sample creating an electric circuit through the sample which allows an electric current to flow.

RESULTS AND DISCUSSION

Our previous gravimetric studies of CO_2 adsorption indicated that at 25°C and atmospheric pressure CFCMS can adsorb >100 mg of CO_2 per gram of CFCMS[7,8]. Here we report the extension of our CO_2 adsorption data to higher temperatures and pressures. Moreover, breakthrough experiments were conducted to determine the efficacy of CFCMS at separating CO_2 from CH_4.

Micropore Structure Analysis

A series of CFCMS cylinders was prepared and activated to burn-offs ranging from 9 to 36% and the BET surface area and micropore size/volume determined from the N_2 adsorption isotherms. Table 1 reports the mass and average burn-off for each of the four cylinders (25-mm diameter x 75-mm length), and their BET surface area, micropore volume (t-method), and mean micropore radius (DA method). Samples were taken from the top (T) and bottom (B) of each

cylinder for analysis. Where the measured BET surface areas were widely different between the top and bottom of the cylinders a repeat measurement was performed.

Table 1. Micropore analysis data for activated CFCMS samples.

Specimen	Mass (g)	Burn-off (%)	BET Area (m^2/g)	Pore Volume [t-method] (cm^3/g)	DA Pore Radius (nm)
21-11 T	11.96	9	485	-	0.70
21-11 B	11.96	9	540	0.212	0.65
21-2B T	11.01	18	770	0.282	0.72
21-2B B	11.01	18	1725	0.603	0.70
21-2B B (repeat)	11.01	18	961	0.328	0.71
21-2D T	9.86	27	939	0.305	0.75
21-2D B	9.86	27	2470	0.866	0.75
21-2D B (repeat)	9.86	27	2477	0.791	0.75
21-2C T	8.86	36	923	0.235	0.87
21-2C B	8.86	36	2323	0.723	0.75
21-2C B (repeat)	8.86	36	856	0.270	0.75

At high burn-offs there was a tendency for one end of the cylinder to exhibit higher BET surface areas than the other end. The activation fixture used in this work was designed to distribute the saturated He along the length of the CFCMS cylinder. Despite this, activation to high burn-off does result in a non-uniform activation as indicated by the BET data. The BET surface area increases with burn-off, approaching 2500 m^2/g at >25% burn-off (Fig. 3). The micropore size (DA pore radius) is apparently less sensitive to burn-off (Table 1) and increases only slightly over the weight loss range reported here (Fig. 4). The pore volume (t-method) varies with the BET surface area, increasing with burn-off (Fig. 5). The observed variations in BET surface area and micropore volume and radius are in agreement with our previous data[8]. In

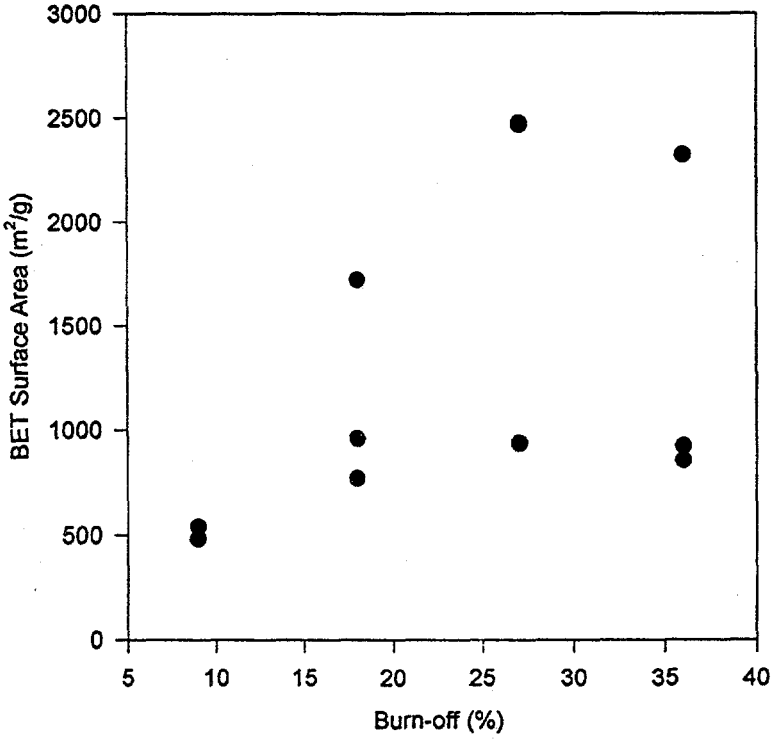

Fig. 3. The variation of BET surface area with burn-off for CFCMS.

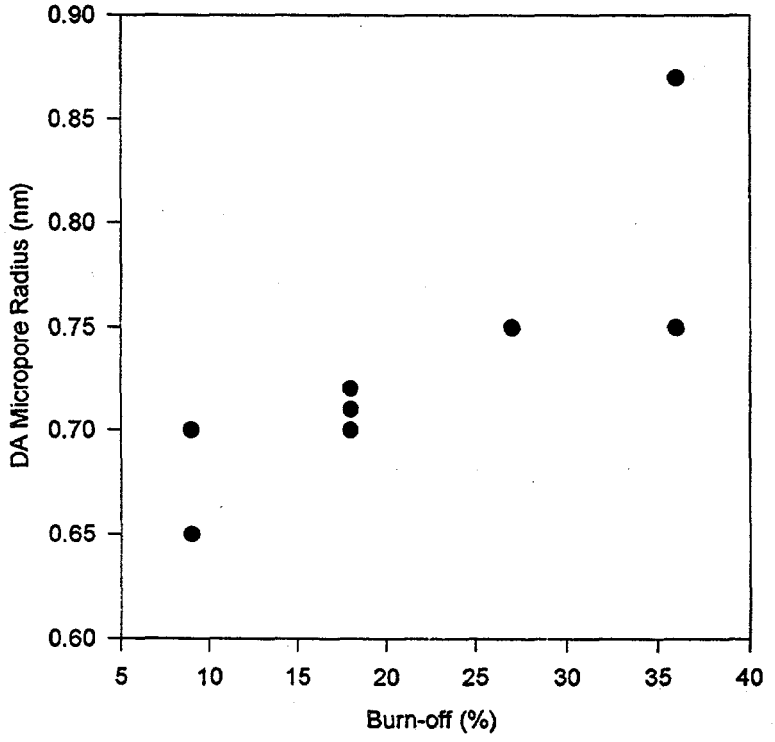

Fig. 4. The variation of DA micropore radius with burn-off for CFCMS.

addition to the data reported above, a density function theory (DFT) analysis was performed on the N_2 adsorption isotherm for sample 21-11B. The isotherm (Fig. 6) is a "type I" isotherm[9], as were all the isotherms obtained for our CFCMS materials. Fig. 7 shows the DFT analysis results, which indicate a micropore (<2-nm width) distribution centered at approximately 0.4-0.5-nm radius. This value is somewhat smaller than DA pore radii reported in Table 1, but agrees well with our previously published DR method pore width data for CFCMS with similar burn-offs[8]. The pore volume attributable to the micropores is also shown in Fig. 7. Summing the volume elements for pore half widths <10Å yields a micropore volume of approximately 0.16 cm^3/g, which is in reasonable agreement with the "t-method" micropore volume data in Table 1 for CFCMS samples 21-11 B and T.

CO_2/CH_4 Adsorption Studies

Adsorption isotherms were obtained at temperatures of 30, 60, and 100°C at presures up to one atmosphere for CO_2 (Figs. 8 and 9) and CH_4 (Figs. 10 and 11). Both of the CFCMS samples analyzed adsorbed less CO_2 at 60 and 100°C than at 30°C (Figs. 8 and 9). At 100°C the amount of CO_2 adsorbed was approximately one third that adsorbed at 30°C. Both CFCMS specimens displayed similar trends with respect to CH_4 adsorption (Figs. 10 and 11). CFCMS has a greater uptake of CO_2 compared to CH_4 at all of the temperatures studied here. For example, at 30°C approximately 50 cm^3/g of CO_2 was adsorbed whereas only approximately 27 cm^3/g of CH_4 was adsorbed at one atmosphere pressure. The data reported in Figs. 8-11 are for CFCMS specimens 22-11 and 22-2B which had burn-offs of 9 and 18% respectively. The uptakes of CO_2 at one atmosphere for specimen 21-11 and 21-2B were 54.6 and 47.9 cm^3/g respectively, indicating a lower burn-off may be preferable for CO_2 adsorption. Moreover, specimen 21-2B (18% burn-off) adsorbed slightly more CH_4 (28.9 cf. 27.5 cm^3/g) than specimen 21-11 (9% burn-off), indicating that CO_2 selectivity may diminish at higher burn-offs. Figure 12 shows the variation of the amount of gas adsorbed (CO_2 or CH_4) at one atmosphere pressure with temperature for our two CFCMS specimens. The greater selectivity of specimen 21-11 at 30°C is apparent. However, the selectivity of the two specimens is very similar at 60 and 100°C.

Figure 13 shows CO_2 adsorption isotherms for CFCMS specimens 21-11 and 21-2B over the pressure range 0.5-59 bar (8-850 psi), and Fig. 14 shows CH_4 adsorption isotherms for the same specimens over the pressure range 0.5-39 bar (8-560 psi). The measured volumetric

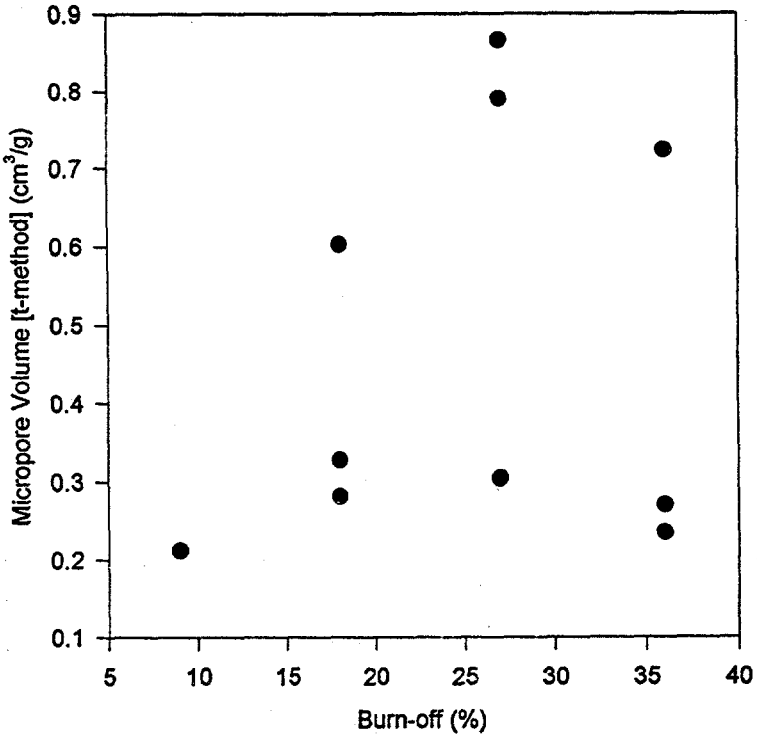

Fig. 5. The variation of pore volume (t-method) with burn-off for CFCMS.

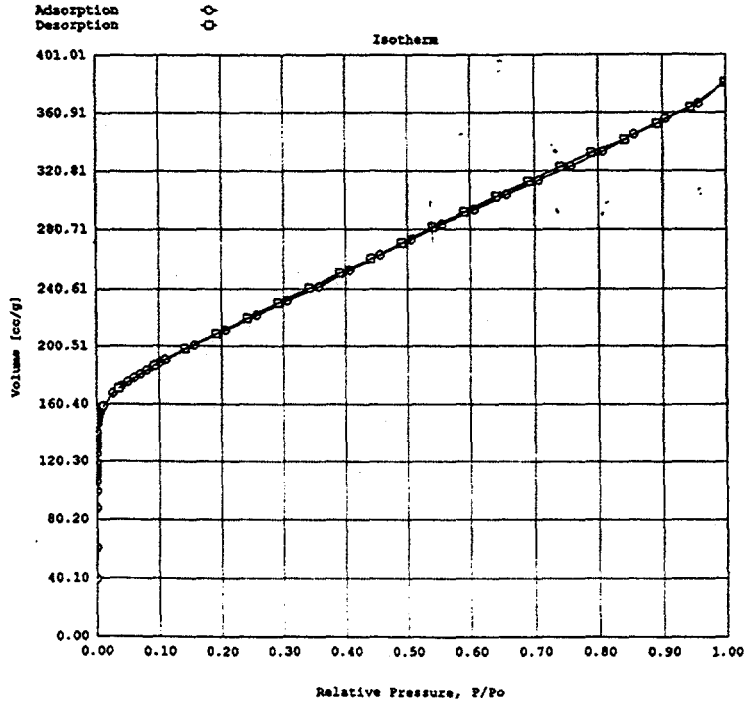

Fig. 6. Nitrogen adsorption isotherm at 77K on CFCMS activated to 9% burn-off.

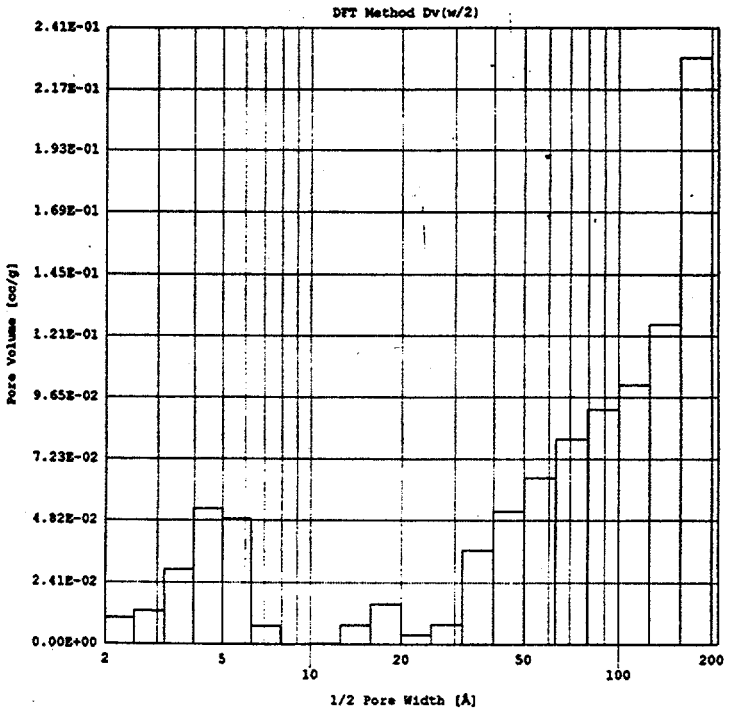

Fig. 7. DFT micropore size analysis of nitrogen adsorption isotherm at 77K on CFCMS (9% burn-off).

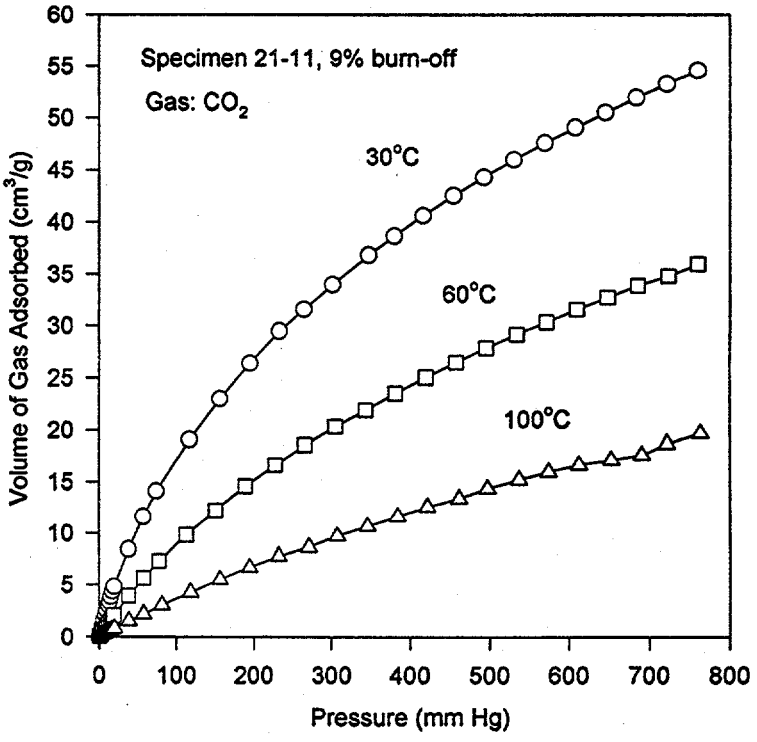

Fig. 8. Carbon dioxide adsorption isotherms at 30, 60, and 100°C on CFCMS (9% burn-off).

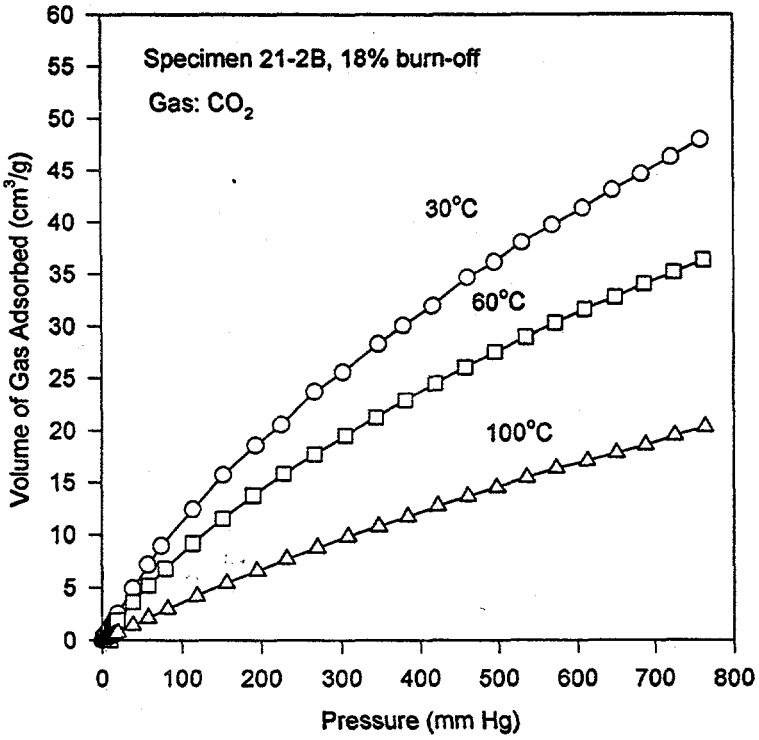

Fig. 9. Carbon dioxide adsorption isotherms at 30, 60, and 100°C on CFCMS (18% burn-off).

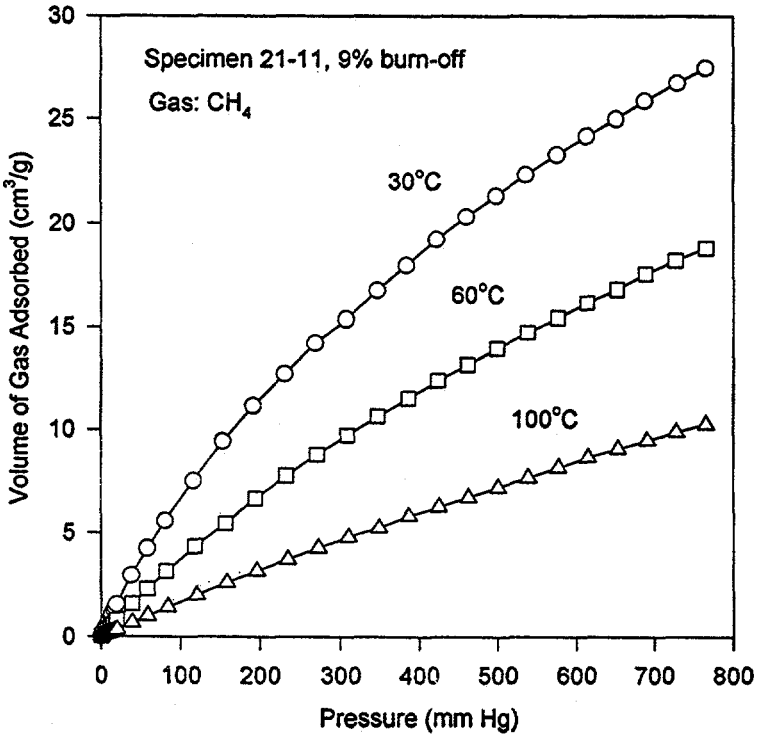

Fig. 10. Methane adsorption isotherms at 30, 60, and 100°C on CFCMS (9% burn-off).

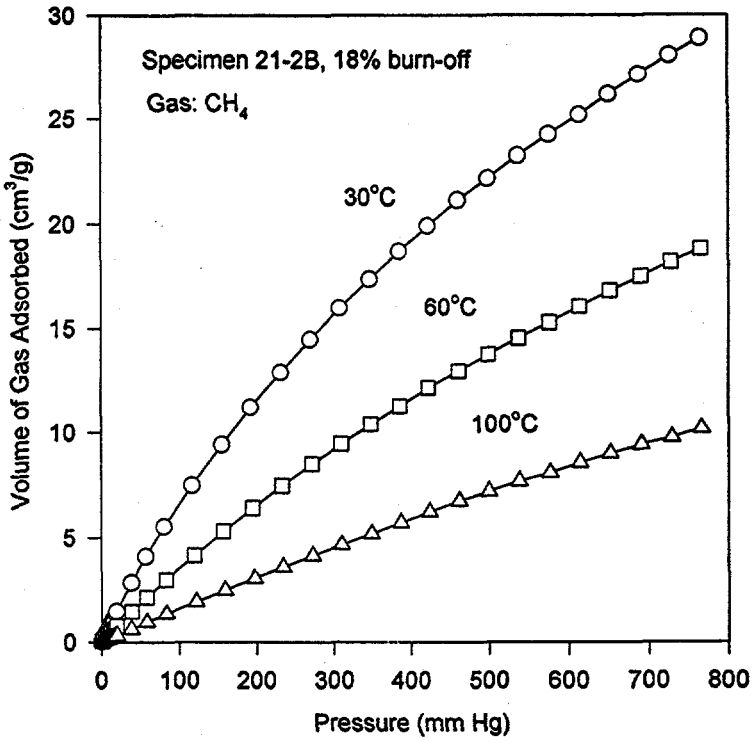

Fig. 11. Methane adsorption isotherms at 30, 60, and 100°C on CFCMS (18% burn-off).

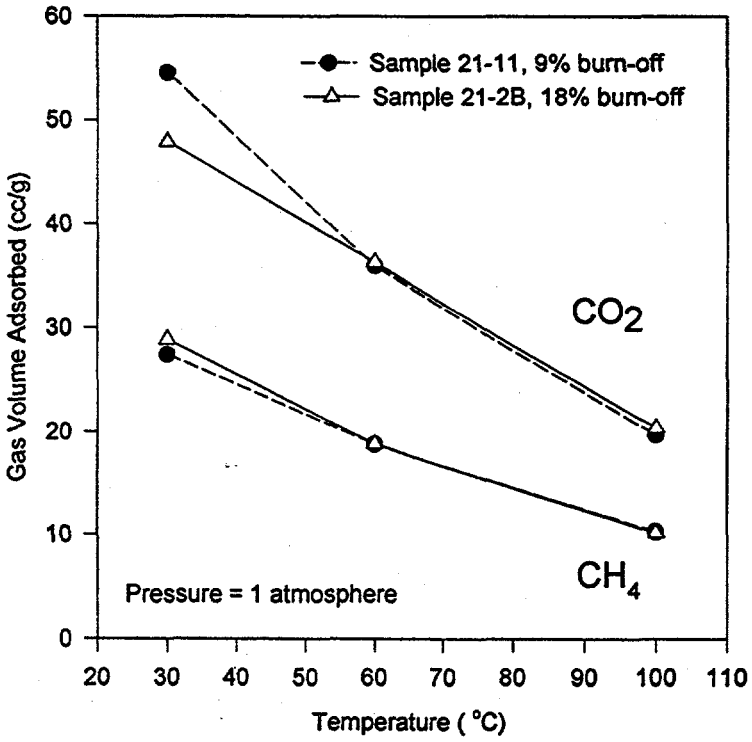

Fig. 12. A comparison of CO_2 and CH_4 gas adsorption for CFCMS at different burn-offs as a function of adsorption temperature.

(Fig. 12) and gravimetric (Figs. 13 and 14) adsorption capacities at one atmosphere for both CH_4 and CO_2 are in good agreement for the CFCMS specimens. At one atmosphere, approximately 100 mg of CO_2 per g of CFCMS and approximately 19 mg of CH_4 per g of CFCMS was adsorbed. The quantities of gas adsorbed rose to >490 mg/g (CO_2 on specimen 21-2B) and >67 mg/g (CH_4 on specimen 21-2B). Moreover, the CO_2 isotherms are still increasing with pressure whereas the CH_4 isotherms have flattened (i.e., the CFCMS has become saturated with CH_4). However, the data in Figs. 13, 14, and 15 clearly shows that CFCMS exhibits selective adsorption of CO_2 over CH_4.

The CO_2 adsorption data discussed above suggests that CFCMS might provide for the effective separation of CO_2 from CH_4. To determine the efficacy of CFCMS for this purpose, several steam activated samples were tested in the breakthrough apparatus (Fig. 2) described previously. Figure 16 shows a breakthrough plot for CO_2 on CFCMS specimen 21-11. Initially the CFCMS sample is purged with helium to drive out any entrained air. The input gas is then switched to CO_2 at a flow of 0.1 standard liters per minute (slpm) and the He concentration falls to zero. The CO_2 concentration stays constant at a low level because the CO_2 is adsorbed. After approximately nine minutes the CO_2 concentration begins to rise as the CFCMS becomes saturated with CO_2 (i.e., breakthrough occurs). The CO_2 adsorption capacity can thus be calculated from the gas flow rate and the breakthrough time. In this instance, specimen 21-11 adsorbed 0.9 liters of CO_2. A typical breakthrough plot for a CH_4/CO_2 mixture is shown in Fig. 17. Any entrained air is initially driven out with a He purge. The input gas is then switched to a 2:1 mixture of CH_4/CO_2 at a flow rate of 0.33 slpm. The outlet stream He concentration decreases and the CH_4 concentration increases rapidly (i.e., CH_4 breaks through). Adsorption of CO_2 occurs and therefore the CO_2 concentration remains constant at a low level for approximately six minutes before the CO_2 concentration begins to increase, i.e., "breakthrough" occurs. Table 2 reports data from our preliminary study of CO_2 separation. CO_2 capacities are reported as determined from pure CO_2 and CO_2/CH_4 mixtures on each specimen examined. The reported CO_2 capacities are the means of several repeats of the breakthrough experiments, and the BET surface areas are the means of the data reported in Table 1. Two of the CFCMS samples (lowest burn-off) had CO_2 adsorption capacities of almost one liter on 0.037 liters of adsorbent, and only a small capacity reduction was observed in the CO_2/CH_4 gas mixture. The CO_2 adsorption capacity decreases with increasing burn-off, in agreement with the isotherm data.

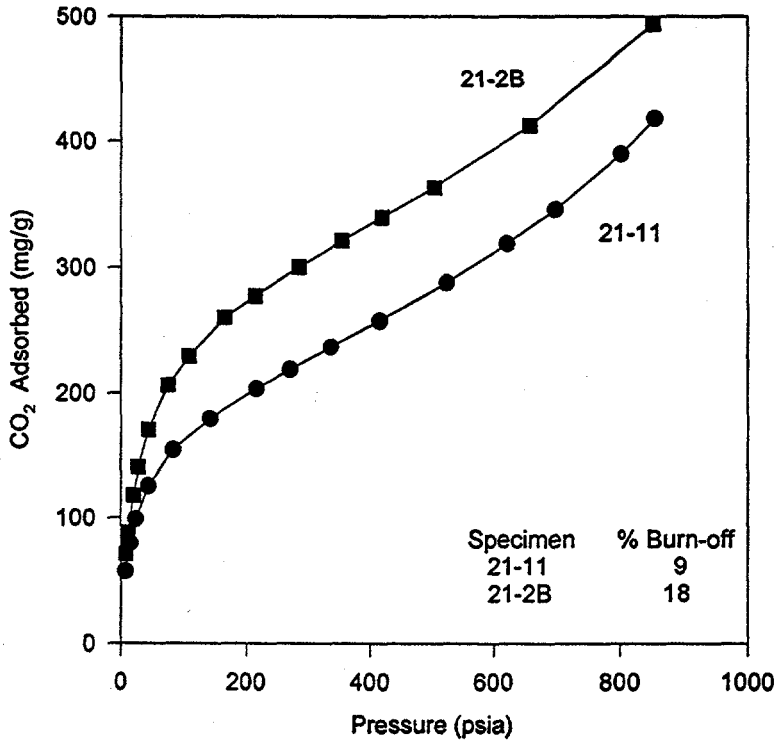

Fig. 13. Carbon dioxide isotherms at 298K on CFCMS activated to different burn-offs (9 and 18%).

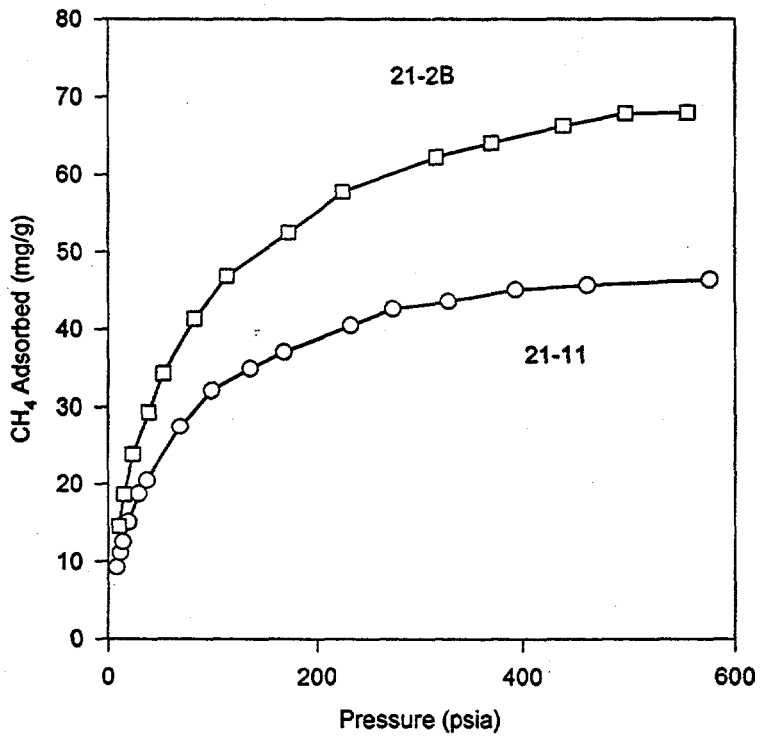

Fig. 14. Methane isotherms at 298K on CFCMS activated to different burn-offs (9 and 18%).

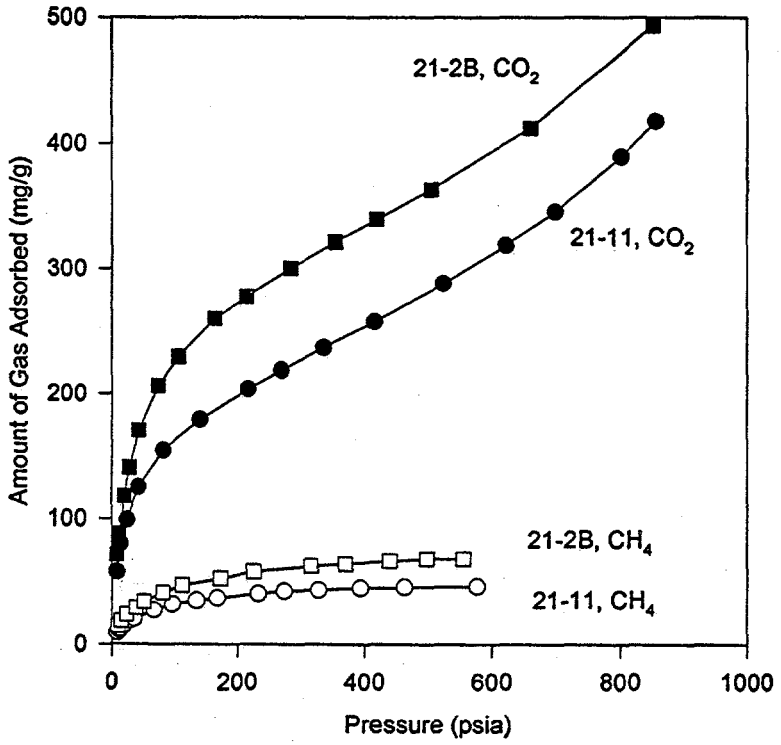

Fig. 15. A summary plot of high pressure CO_2 and CH_4 adsorption isotherms on CFCMS.

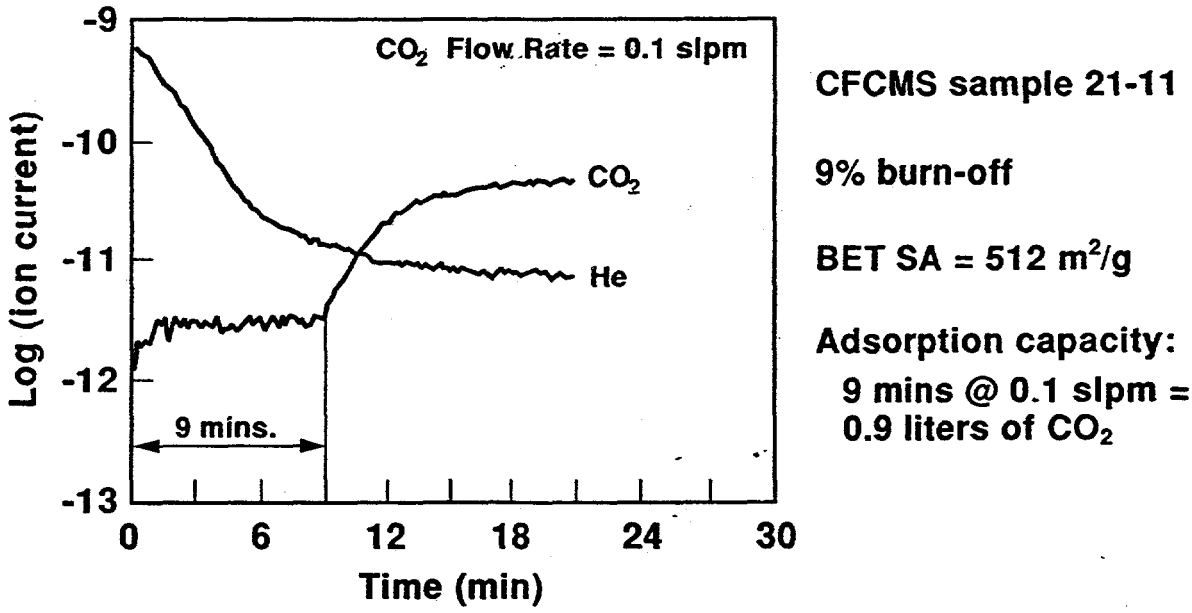

Fig. 16. Typical CO_2 breakthrough plot on CFCMS sample 21-11 (9% burn-off).

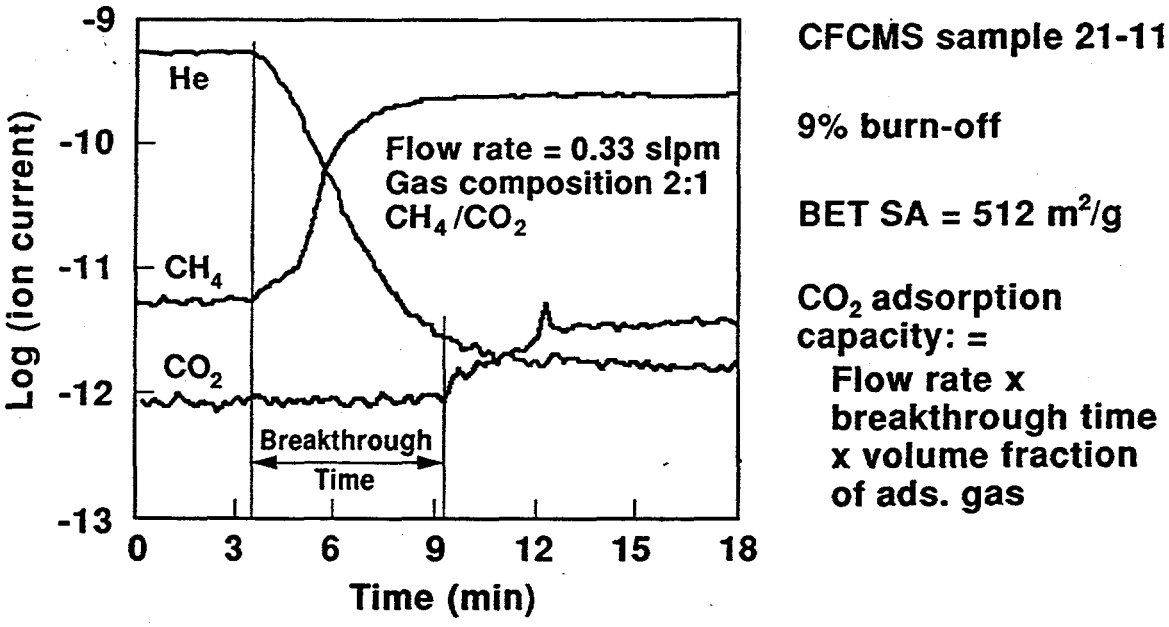

Fig. 17. Typical CO_2/CH_4 breakthrough plots on CFCMS sample 21-11 (9% burn-off).

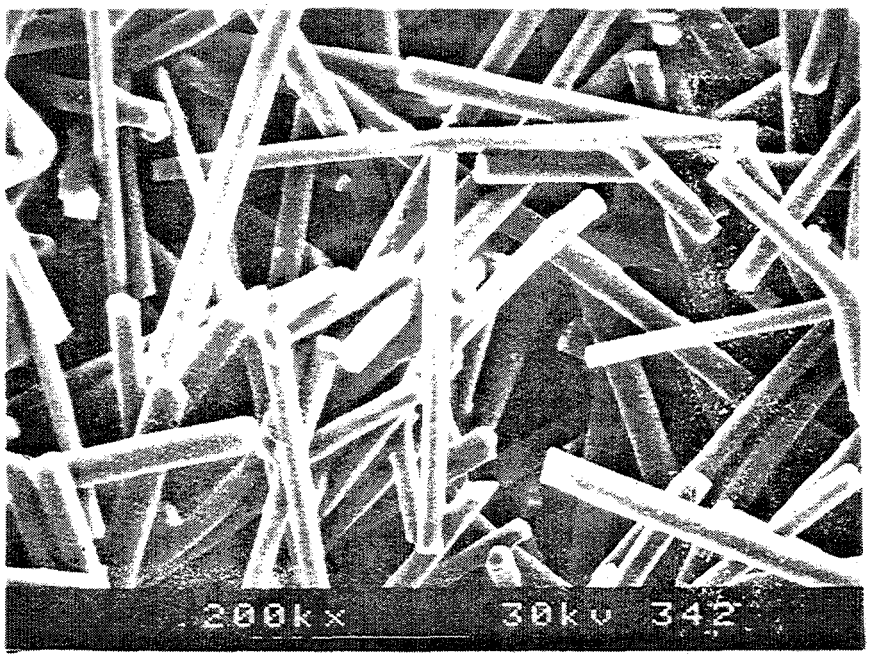

Fig. 18. SEM photomicrograph of CFCMS revealing its continuous carbon skeleton structure.

Table 2. CO_2 separation data from our CO_2 and CO_2/CH_4 breakthrough experiments.

Specimen No.	Burn-off (%)	BET Surface Area (m^2/g)	CO_2 Capacity (Liters)	
			CO_2/CH_4	CO_2 only
21-11	9	512	0.73	0.97
21-2B	18	1152	0.45	0.98
21-2D	27	1962	0.39	0.80
21-2C	36	1367	0.35	0.80

A Novel Gas Separation System

CFCMS has a continuous carbon skeleton (Fig. 18) which imparts electrical conductivity to the material. The carbon fibers used in the synthesis of CFCMS have, according to their manufacturer, an electrical resistivity of 5 milliohm.cm. Figure 19 is a plot of the current-voltage characteristics of a 2.5-cm diameter, 7.5-cm long CFCMS cylinder. The plot is linear, indicating that in CFCMS electrical conduction obeys ohm's Law. At an applied d.c. potential of one volt, approximately 5 amps flows through the CFCMS. The CFCMS samples electrical resistance is thus 0.2 Ohm and the resistivity is 131 milliohm.cm. This resistivity is considerably greater than that of the fibers, and is attributed to contact resistance and the lower electrical conductivity of the phenolic resin derived carbon binder. A consequence of the passage of an electric current through the CFCMS is a heating effect, which causes the CFCMS to increase in temperature to approximately 50-60°C.

We have utilized the electrical properties of CFCMS to effect a rapid desorption of adsorbed gases in our breakthrough apparatus. The process has been named electrically enhanced desorption, and the benefit of this technique is shown in Fig. 20 where the CO_2 and CH_4 gas concentrations in the outlet gas stream of our breakthrough apparatus (Fig. 2) are shown as a function of time. Three adsorption/desorption cycles are shown in Fig. 20. In the first and second cycles (A and B in Fig. 20) desorption is caused by the combined effect of an applied voltage (1 volt) and a He purge gas. In the third cycle (C in Fig. 20) desorption is caused only by the He purge gas. A comparison of cycles B and C indicated that the applied voltage reduces the desorption time to less than one third of that for the He purge gas alone (cycle C). Clearly,

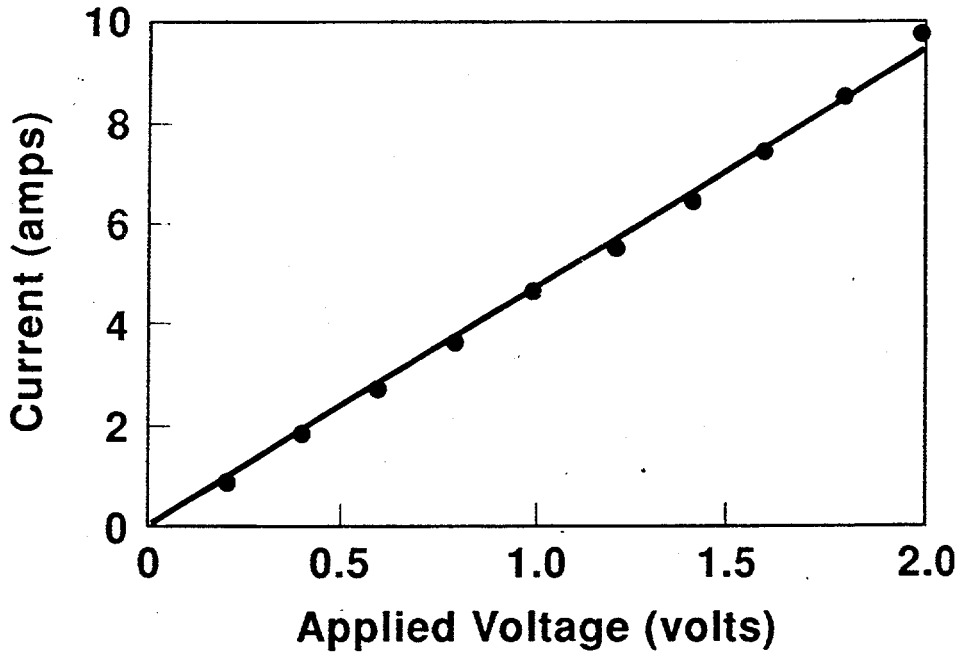

Fig. 19. The current-voltage relationship for CFCMS (sample 21-2B, 18% burn-off, 25-mm diameter x 76-mm length).

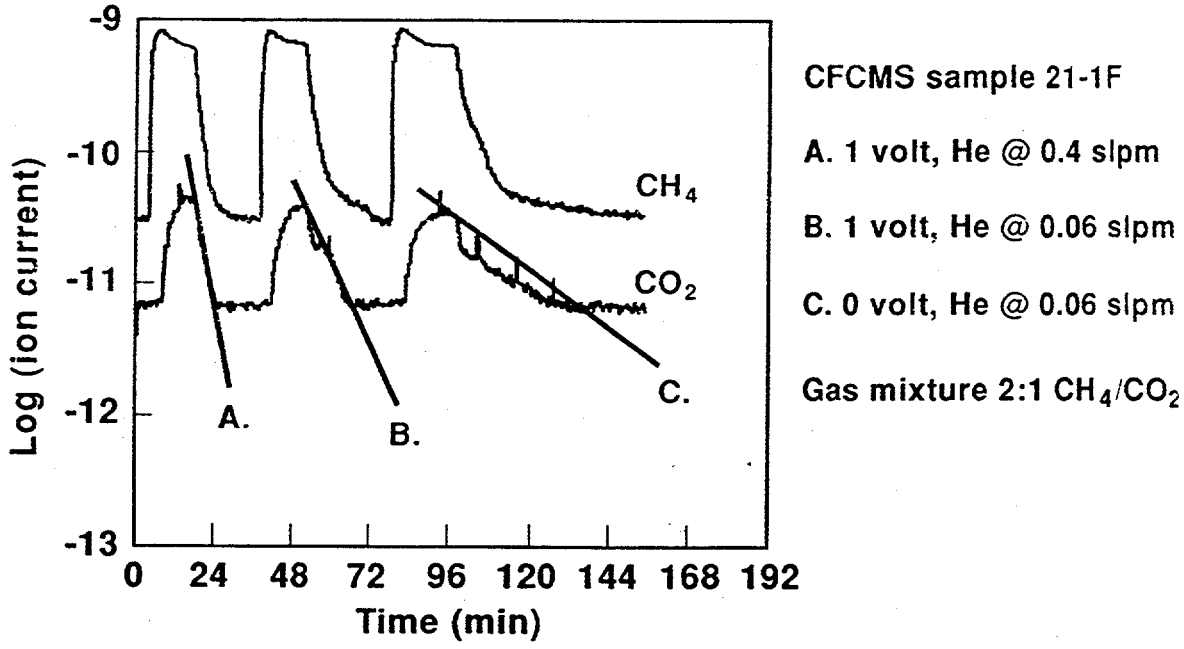

Fig. 20. CO_2/CH_4 breakthrough plots on CFCMS showing the benefit of electrically enhanced desorption.

the desorption of adsorbed CO_2 can be rapidly induced by the application of an electric potential. We postulate two explanations for this effect. First, the passage of an electric current through the CFCMS causes an increase in the materials temperature, which in turn thermally excites the adsorbed gas, effecting the desorption. Second, the flow of electrons through the CFCMS disrupts the weak dispersion or polar attractive forces which bind the gas in the micropores.

The ability of CFCMS to selectively adsorb CO_2 from a CH_4/CO_2 mixture, combined with the electrically enhanced desorption of the CO_2 allow for a gas separation system where the separation is effected by electrical swing, rather than the more conventional pressure or temperature swings. A preliminary system concept for upgrading of natural gas through electrical swing adsorption is shown schematically in Fig. 21. The sketch shows three vessels as an example and, of course, the actual arrangement and number of vessels will depend on many factors such as volume of gas to be treated, etc. The system as depicted in Fig. 21 provides for alternating between the three vessels with adsorption occurring in one vessel, desorption in another, and the third in an intermediate stage of the cycle being readied for adsorption. In operation, subquality natural gas feed, F, flows through valve A_1 into vessel V_1, which is filled with CFCMS, and the carbon dioxide and hydrogen sulfide (and perhaps other contaminants/diluents) are adsorbed on the activated carbon fibers. Pipeline quality methane exits vessel V_1 through valve B_1 and is directed to the gas pipeline, P, either directly or through a reservoir system. At saturation of the adsorbent in V_1, valves A_1 and B_1 are closed, and the natural gas feed is directed to vessel V_2 to begin the adsorption cycle in that vessel. A power source is activated and a voltage applied across the CFCMS resulting in current flow through the CFCMS, desorption of carbon dioxide and hydrogen sulfide, and flow of the desorbed gases through check valve, CV_1, where they are vented to the atmosphere or collected in a reservoir for future disposition. As the adsorption-desorption cycle proceeds, vessel V_1 is readied for the adsorption phase of the cycle by opening valves A_1 and C_1 to purge the vessel and assure a pure product stream is being produced. Then valve C_1 is closed and valve B_1 is opened as before. This cycle is repeated to maintain a flow of product gas that accommodates the desired feed flow.

Before a system such as that described above can be constructed much work must be accomplished. Specifically, several issues directly applicable to natural gas production systems which yield subquality gas must be addressed. Currently at ORNL we are constructing a gas flow loop (breakthrough system) which will be operated at relevant conditions of natural gas

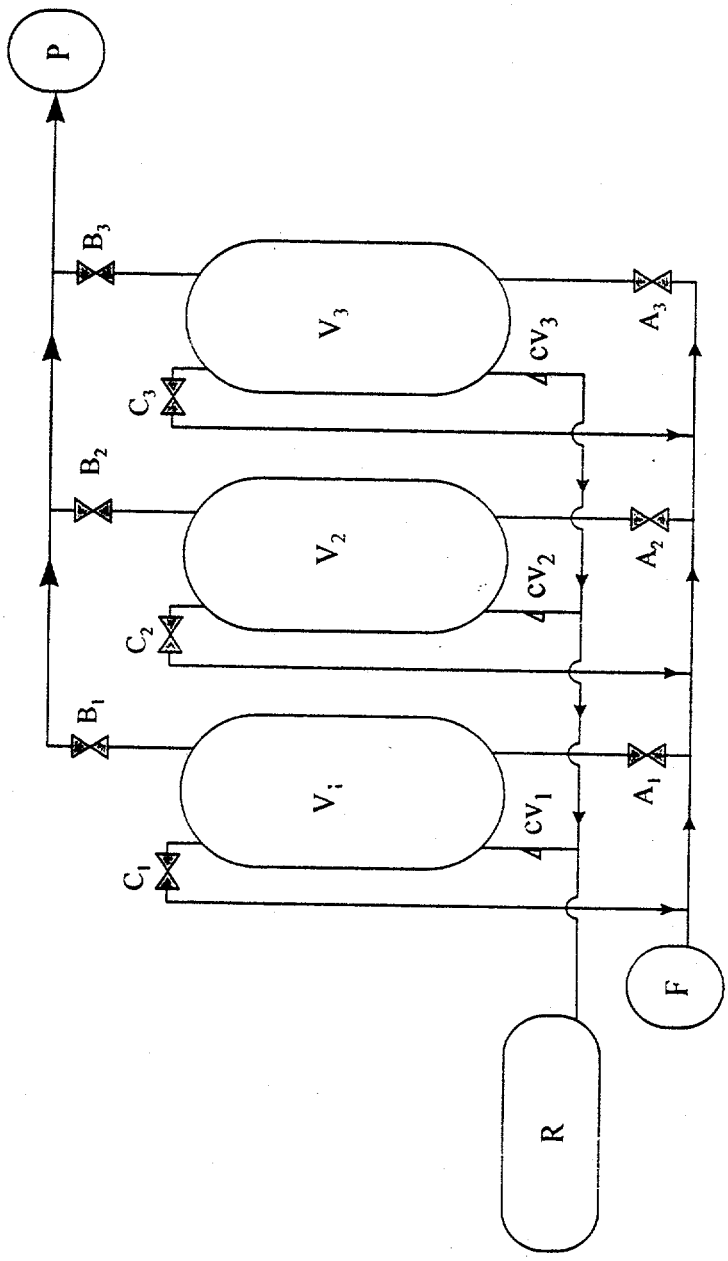

Fig. 21. A schematic diagram of an electrical swing adsorption system.

production. Issues of multiple contaminant/diluent removal, effects of moisture, high pressure operation, purge gas options, and cyclic operations can then be addressed.

CONCLUSIONS

A porous monolithic activated carbon material (CFCMS) has been developed that is strong, rigid and which overcomes problems associated with operation using granular adsorbents. The open structure of CFCMS results in a permeable material which offers little resistance to the free-flow of fluids. The material has a unique combination of properties, including reasonable compressive strength, electrical conductivity and a large micropore volume.

CO_2 and CH_4 isotherms have been obtained for samples of CFCMS both volumetrically and gravimetrically. The CFCMS material has a CO_2 uptake of >50 cm^3/g (>100 mg/g) at 30°C and atmospheric pressure. The CO_2 uptake is reduced at elevated temperature, and falls to approximately 20 cm^2/g (40 mg/g) at 100°C. However, the adsorption of CO_2 increases with increasing pressure such that at 58 bar the mass of CO_2 adsorbed increases to >490 mg/g. Similar trends were observed for CH_4 adsorption on CFCMS, except that the adsorption capacity was much less.

A series of breakthrough experiments was performed on CFCMS specimens and their ability to selectively remove CO_2 demonstrated. The unique combination of properties of CFCMS has been exploited to effect the rapid desorption of CO_2 from the materials. It has been shown that for adsorbent configuration reported here a 4-5 amp current flowing under an applied dc voltage of one volt causes a rapid desorption of the CO_2. A preliminary design of an "electrical swing adsorption" system was outlined and its use for the cleanup of subquality natural gas advocated.

REFERENCES

1. T. D. Burchell. Carbon Fiber Composite Molecular Sieves, In *Proceedings of Eighth Annual Conference on Fossil Energy Materials*, Oak Ridge, Tennessee, U.S.A., May 1994. ORNL/FMP-94/1, CONF-9405143, pp. 63-70. Pub. Oak Ridge National Lab, U.S.A., August 1994.

2. T. D. Burchell, C. E. Weaver, F. Derbyshire, Y. Q. Fei and M. Jagtoyen. Carbon Fiber Composite Molecular Sieves: Synthesis and Characterization, In *Poc. Carbon '94*, Granada, Spain, July 3-8, 1994. Pub. Spanish Carbon Group, July 1994.

3. F. Derbyshire, Y. Q. Fei, M. Jagtoyen, G. Kimber, M. Matheny and T. Burchell, Carbon Fiber Composite Molecular Sieve for Gas Separation. *"New Horizons for Materials". Advances in Science and Technology, 4.* P. Vincenzini (Ed.), pp. 411-417 (1995). Pub. Techna Srl, Faenza, Italy, 1995.

4. G. C. Wei and JM Robbins, Carbon-Bonded Carbon Fiber Insulation for Radioisotope Space Power Systems, *Ceramic Bulletin*, Vol. 64, No. 5, p. 691 (1985).

5. S. Brunauer, P. H. Emmett and E. Teller, *J. Am. Chem. Soc.*, Vol. 60, p. 309 (1938).

6. R. C. Bansal, J-B Donnet and F. Stoeckli, *Active Carbon*, Pub. Marcell Dekker, Inc., New York (1988).

7. T. D. Burchell, J. W. Klett and C. E. Weaver, A Novel Carbon Fiber Based Porous Carbon Monoltih, In *Proceedings of Ninth Annual Conference on Fossil Energy Materials*, Oak Ridge, Tennessee, U.S.A., May 1995. ORNL/FMP-95/1, CONF-9505204, pp. 447-456. Pub. Oak Ridge National Lab, U.S.A., August 1995.

8. T. D. Burchell and R. R. Judkins, *Energy Convers. Mgmt* Vol. 37, Nos 6-8, pp. 947-954, 1996.

9. S. J. Gregg and K. S. W. Sing, *Adsorption, Surface Area and Porosity, 2nd Edition,* Pub. Academic Press, San Diego, CA (1982).

2.7 INVESTIGATION OF AUSTENITIC ALLOYS FOR ADVANCED HEAT RECOVERY AND HOT GAS CLEANUP SYSTEMS

R. W. Swindeman and W. Ren

INTRODUCTION

The objective of the research is to provide databases and design criteria to assist in the selection of optimum alloys for construction of components needed to contain process streams in advanced heat recovery and hot-gas cleanup systems. Typical components include: steam line piping and superheater tubing for low emission boilers (600 to 700°C), heat exchanger tubing for advanced steam cycles and topping cycle systems (650 to 800°C), foil materials for recuperators on advanced turbine systems (700 to 750°C), and tubesheets for barrier filters, liners for piping, cyclones, and blowback system tubing for hot-gas cleanup systems (850 to 1000°C). The materials being examined fall into several classes, depending on which of the advanced heat recovery concepts is of concern. These classes include martensitic steels for service to 650°C, lean stainless steels and modified 20Cr-30Ni steels for service to 700°C, modified 25Cr-20Ni steels for service to 900°C, and high Ni-Cr-Fe or Ni-Cr-Co-Fe alloys for service to 1000°C.

DISCUSSION OF CURRENT ACTIVITIES

The efforts in FY 1996-1996 have included work on materials for all of the systems mentioned above: (1) low emission boilers, (2) advanced steam cycles, (3) recuperators, and (4) hot-gas cleanup systems.

Steels for Low Emission Boilers

Vanadium-modified 2 1/4 Cr, 9Cr, and 12Cr steels are candidates for the construction of piping, headers, and tubing in the low emission boiler (LEB) project supported by the Pittsburgh Energy Technology Center[1]. However, these steels exhibit a complex metallurgical constitution that is not fully understood. Issues related to the effects of fabrication variables on strength and ductility have arisen as components are being fabricated for advanced plants, and construction code groups in the U.S. and Europe have requested research to resolve these issues. Concerns exist about long-term

embrittlement due to Laves phase precipitation, degradation of weldments due to Type IV cracking, and softening under cyclic loading. Methods for on-line damage assessment are needed as an assurance against component failures, so a small effort continues at ORNL to examine damage accumulation in bainitic and martensitic steels. This effort uses 9Cr-1Mo-V steel as a model material and examines isostress methods for estimating residual life of exposed samples. Specimens exposed up to 75,000 h have been tested, and procedures have been developed for estimating the influence of exposure on subsequent life. In a supplementary project, supported by Wright Patterson Air Force Base, research on 9Cr-1Mo-V steel has been expanded to include variable stress and temperature testing, compression creep tests, and multiaxial stress tests. Data from these tests are being used for the development of constitutive equations related to deformation and damage accumulation.

Steels for Advanced Steam Cycles

In advanced steam cycles, austenitic stainless steel tubing will be used in the hotter sections of the superheater and reheater. Steels that are being investigated for these applications include high-strength 14Cr-15Ni stainless steels, fine-grained 347 stainless steel, niobium-modified 310 stainless steel, and titanium-zirconium-modified 20Cr-25Ni-Nb stainless steel. These steels are limited to approximately 730°C but they could be suitable for tubing in an advanced LEB and as heat exchanger tubing in an advanced topping cycle[2].

Long-time testing was continued on samples machined from modified 14Cr-15Ni and modified 20Cr-30Ni stainless steel tubing. Times exceed 30,000 h and temperatures are in the range of 650 to 700°C. Cross-weld specimens have been in test for times to beyond 30,000 h. These steels were observed to perform quite well in the cold and warm worked condition, and rupture ductilities remained high.

The modified 310 stainless steels were tested to beyond 10,000 h. The microstructures in these steels were examined and found to be very sensitive to testing temperatures. Various carbides, nitrides, and intermetallic phases were observed, and indications were that the steels were more sensitive to cold work than the steels containing 20% chromium. Two service failures occurred in the niobium-modified 310 stainless steel, suggesting the need for an improved understanding of the limitations of the steel. The modified 20Cr-25Ni-Nb stainless steel was observed to be more ductile and exhibited better cross weld strength and ductility.

Steels for Recuperators

An activity was begun to support Solar Turbines, Inc. in the selection of a suitable material to fabricate a recuperator capable of sustained operation at 700°C and above. The component requires a foil product, approximately 0.11-mm thick, that is fabricable, oxidation resistant, and has good strength. The current material of choice is 347H stainless steel, but its use is limited to 650°C. Nickel-base alloys have suitable properties above 650°C, but are expensive. Modified 25Cr-20Ni and 20Cr-25Ni-Nb stainless steels are being examined as alternative materials. Small heats of experimental steels were supplied by Solar Turbines, and these were fabricated to plate, sheet, and foil product forms. The foils were heat-treated at ORNL and Solar Turbines, Inc. to establish optimum fabrication schedules. Oxidation testing of foils was begun.

Alloys for Hot-Gas Cleanup Systems

Some structural components in advanced combined-cycle systems are expected to experience temperatures above 800°C where damage due to creep, fatigue, thermal-fatigue, and creep-fatigue is significant[3]. To assist designers, exploratory research on creep, creep-fatigue, fatigue, and crack-growth of several candidate alloys has been in progress. Early research involved studies of alloy 333, which was the tubesheet material used in pressurized fluidized bed (PFBC) hot-gas cleanup system at the Tidd plant[4]. Materials with higher strength were required for scale-up applications, and little information was found regarding the performance of these materials in the severe operating conditions of the hot-gas clean-up systems. Techniques for creep- and fatigue-crack growth measurements were developed for temperatures to 950°C using alloy 160. These methods were then applied to investigate alloy 120, which is new material being used to fabricate the tubesheet for a hot-gas cleanup system on the PFBC located at the Southern Services, Inc. facility at Wilsonville, Alabama. A cut-out from the tubesheet was provided to ORNL by Westinghouse Electric Company. Creep and tensile testing was performed on the alloy 120 to characterize the material relative to the manufacturers database. Exploratory low-cycle fatigue tests were completed at 870°C, and crack-growth experiments were started. Except for the tubesheet, the structural components in the dirty side of the hot-gas cleanup system at Wilsonville were fabricated from 310 stainless steel. In the Tidd plant, this steel was found to distort and embrittle under the severe thermal/mechanical loading. A possible replacement material could be one of the modified 310 stainless steels. Testing of a tantalum modified 310 stainless steel is in progress at temperatures above 800°C. The material appears to have twice the strength of standard 310 stainless steel, and has been in test for 30,000 h at 870°C.

SUMMARY

An effort continued to assist in the resolution of issues related to the fabrication and performance of high-strength martensitic steels as tubing and piping in low emission boilers.

High-performance austenitic stainless steels were examined for applications in advanced steam cycle systems and recuperators operating in the temperature range 650 to 800°C. Testing times to beyond 10,000 h were achieved, and metallurgical investigation of microstructures was started.

Testing continued on alloys for use as structural components in hot-gas cleanup vessels. Work on alloy 120 was started to assist in the performance evaluation of the tubesheet operating above 800°C, and creep testing of a modified 310 stainless steel was continued to beyond 30,000 h at 870°C.

REFERENCES

(1) J. N. Darguzas, G. W. Vandervoort, D. G. Sloat, R. Beittel, and D. P. Kalmanovitch, "Material Selection for the Low Emission Boiler System Design for DOE's Combustion 2000 Program," paper presented at the Fossil Energy Materials Conference, Oak Ridge, TN, May 11, 1994.

(2) T. E. Duffy and C. S. Knox, *High-Temperature Steam Topping Cycle Study*, Report No. TR-102059, Electric Power Research Institute, Palo Alto, CA, February 1993.

(3) R. W. Swindeman and D. L. Marriott, "Criteria for Design with Structural Materials in Combined-Cycle Applications above 815°C," *J. Engineering for Gas Turbines and Power*, **116**, 352-59 (April, 1994).

(4) R. H. Manjoine, J. M. Thompson, and R. W. Swindeman, "Experience with Conventional Inelastic Analysis Procedures in Very High Temperature Applications," pp. 167 to 174 in *Fatigue, Fracture, and Risk 1991*, ASME PVP-Vol. 216, American Society of Mechanical Engineers, 1991.

2.8 CERAMIC TUBESHEET DESIGN ANALYSIS

R. H. Mallett and R. W. Swindeman

INTRODUCTION

A transport combustor is being commissioned at the Southern Services facility in Wilsonville, Alabama to provide a gaseous product for the assessment of hot-gas filtering systems. One of the barrier filters incorporates a ceramic tubesheet to support candle filters. The ceramic tubesheet, designed and manufactured by Industrial Filter and Pump Manufacturing Company (IF&PM), is unique and offers distinct advantages over metallic systems in terms of density, resistance to corrosion, and resistance to creep at operating temperatures above 815°C (1500°F). Nevertheless, the operational requirements of the ceramic tubesheet are severe. The tubesheet is almost 1.5 m in (55 in.) in diameter, has many penetrations, and must support the weight of the ceramic filters, coal ash accumulation, and a pressure drop (one atmosphere). Further, thermal stresses related to steady state and transient conditions will occur. To gain a better understanding of the structural performance limitations, a contract was placed with Mallett Technology, Inc. to perform a thermal and structural analysis of the tubesheet design. The design analysis specification[1] and a preliminary design analysis[2] were completed in the early part of 1995. The analyses indicated that modifications to the design were necessary to reduce thermal stress, and it was necessary to complete the redesign before the final thermal/mechanical analysis could be undertaken[3]. The preliminary analysis identified the need to confirm that the physical and mechanical properties data used in the design were representative of the material in the tubesheet. Subsequently, few exploratory tests were performed at ORNL to evaluate the ceramic structural material.

DISCUSSION OF CURRENT ACTIVITIES

The tubesheet material supplied to ORNL was an aluminosilicate composite of relatively low density and strength. Test bars were provided to ORNL for the determination of thermal expansion, thermal conductivity, thermal diffusivity, elastic modulus, Poisson's ratio, and modulus of rupture in the longitudinal (X) and through-thickness (Y) directions of the composite plate material.

The thermal expansion was observed to be similar in the X and Y directions to 815°C (1500°F) but above this temperature densification of the composite occurred, and shrinkage in the Y direction was greater than in the X direction. The thermal expansion coefficient of the composite was similar to the value assumed for the preliminary thermal/mechanical analysis.

The thermal conductivity was measured in the X direction to 815°C (1500°F) and found to be double the values assumed in the thermal analysis. Thermal diffusivity was measured in the X direction to 815°C (1500°F) but no comparative values were available from the material supplier. The specific heat was measured to 1000°C (1830°F) and found to be slightly less than the specific heat of Mullite. The Mullite properties were assumed in the thermal analysis.

The Young's modulus was measured in the X and Y directions by two methods. Only room temperature measurements were made. The modulus in the X direction was found to be significantly greater than the modulus in the Y direction. Data were similar for the ultrasonic and vibratory methods and more-or-less agreed with values assumed for the preliminary analysis. Poisson's ratio values were estimated from the vibratory modulus data and found to agree with the assumed values.

The modulus of rupture was determined at room temperature and 760°C (1400°). Again, strength data were in the range assumed in the thermal/mechanical analysis.

SUMMARY

Physical and mechanical properties were gathered for a ceramic composite tubesheet material. Data verified the properties that were assumed in a preliminary thermal mechanical/analysis of the tube sheet design. A redesign of the tubesheet was undertaken to reduce thermal and mechanical loads.

REFERENCES

1. R. H. Mallett, *Design Analysis Specification for Filter Vessel Ceramic Tubesheet*, Mallett Technology Report MTI-TR-825, February 3, 1995.

2. R. H. Mallett, *Preliminary Design Analysis for a Filter Vessel Ceramic Tubesheet*, Mallett Technology Report MTI-TR-845, February 6, 1995.

1. R. H. Mallett, *Stress Estimates for a Filter Vessel Ceramic Tubesheet Using Bonded Ceramic Layer Construction*, Mallett Technology Report MTI-TR-855, April 7, 1995.

2.9 APPLICATION OF ADVANCED AUSTENITIC ALLOYS TO FOSSIL POWER SYSTEM COMPONENTS

R. W. Swindeman

INTRODUCTION

Most power and recovery boilers operating in the U. S. produce steam at temperatures below 565°C (1050°F) and pressures below 24 MPa (3500 psi). For these operating conditions, carbon steels and low alloy steels may be used for the construction of most of the boiler components. Austenitic stainless steels often are used for superheater/reheater tubing when these components are expected to experience temperatures above 565°C (1050°·F) or when the environment is too corrosive for low alloys steels. The austenitic stainless steels typically used are the 304H, 321H, and 347H grades. New ferritic steels such as T91 and T92 are now being introduced to replace austenitic stainless steels in aging fossil power plants. Generally, these high-strength ferritic steels are more expensive to fabricate than austenitic stainless steels because the ferritic steels have more stringent heat treating requirements. Now, annealing requirements are being considered for the stabilized grades of austenitic stainless steels when they receive more than 5% cold work, and these requirements would increase significantly the cost of fabrication of boiler components where bending strains often exceed 15%. It has been shown, however, that advanced stainless steels developed at ORNL greatly benefit from cold work, and these steels could provide an alternative to either conventional stainless steels or high-strength ferritic steels. The purpose of the activities reported here is to examine the potential of advanced stainless steels for construction of tubular components in power boilers. The work is being carried out with collaboration of a commercial boiler manufacturer.

DISCUSSION OF CURRENT ACTIVITIES

The efforts in FY 1995-1996 have focused on four technology needs: (1) a compilation of information to assess the effect of cold work on the high temperature strength and ductility of 304H and 347H stainless steels; (2) the construction of high temperature tube testing facilities, (3) exploratory testing of uniaxial specimens for comparison to tubing performance, and (4) fabrication and testing of cold worked tubes and tube bends.

The compilation of creep-rupture data bearing on cold work effects in austenitic stainless steels has been completed, and a draft report is being prepared. Instances of premature and low-ductility creep-ruptures around 650°C (1200°F) were found for virtually all the austenitic stainless steels. The stabilized grades were not the only steels to undergo degradation[1-4].

Facilities to perform eight pressurized tubes were constructed, and the final evaluation prior to testing is in progress. Some tubular specimens have been prepared. A system to test full U-bend tubes has been designed.

Exploratory testing of uniaxial specimens machined from tubes was begun for temperatures around 650°C (1200°F). Tests at higher temperatures were completed on specimens from butt welds in 304H tubes. Tests of specimens from butt welds in advanced stainless steel tubes are in progress, and some testing times have exceeded 30,000 h.

Cold formed tubes of the advanced stainless steels have been provided to the industrial partner and are ready for cold bends.

SUMMARY

Work is proceeding on the investigation of advanced alloys for superheater tubing at temperatures around 650°C (1200°F). Indications are that the advanced steels will meet the performance requirements, but commercial fabrication methods have yet to be established.

REFERENCES

1. B. Mitchell, "High-Temperature Materials for Electrical Power Generation," pp. 540-560 in *High-Temperature Properties of Steels*, The Iron and Steel Institute, London, 1966.

2. D. D'Angelo, E. Evangelista, S. Spigarelli, L. Kloc, and A. Rosen, "Creep of Cold Deformed AISI 347 Stainless Steel," pp. 127-133 in *Creep: Characterization, Damage, and Life Assessment*, ASM International, Materials Park, Ohio, 1992.

3. L. Bernard, E. Campo, and S. Quaranta, "Creep behavior of AISI 304 and 316 Stainless Steels and Influence of Cold Working," pp. 35-40 in *Stainless Steels for Nuclear Applications*, The Institute of Metals, London, 1985.

4. M. Gold, W. E. Leyda, and R. H. Zeisloft, "The Effect of Varying Degrees of Cold Work on the Stress-Rupture Properties of Type 304 Stainless Steel. *J. Eng. Mater. Tech.*, October, 1975, 305-312.

2.10 Cr_2Nb-BASED ALLOY DEVELOPMENT

C. T. Liu, P. F. Tortorelli, J. A. Horton, D. S. Easton, and L. Heatherly

INTRODUCTION

The objective of this work is to develop a new generation of structural materials based on intermetallic alloys for use at high temperatures in advanced fossil energy conversion systems. Target applications of such ultrahigh strength alloys include hot components (for example, air heat exchangers) in advanced energy conversion systems and heat engines. However, these materials may also find use as wear-resistant parts in coal handling systems (for example, nozzles), drill bits for oil/gas wells, and valve guides in diesel engines.

One potential class of such alloys is that based on Cr-Cr_2Nb alloys. The intermetallic phase, Cr_2Nb, with a complex cubic structure (C-15)[1,2] has been selected for initial development because of its high melting point (1770°C),[2-4] relatively low material density (7.7 g/cm^2),[5] and excellent high-temperature strength (at 1000 to 1250°C).[6,7] This intermetallic phase, like many other Laves phases, has a wide range of compositional homogeneity[2,4] suggesting the possibility of improving its mechanical and metallurgical properties by alloying additions.

The major engineering concern with Cr_2Nb and other A_2B Laves phases is their poor fracture toughness and fracture resistance at ambient temperatures.[3,6-9] The single-phase Cr_2Nb is very hard (~800 DPH) and brittle at room temperature.[9] Because of this brittleness, the development effort has concentrated on two-phase structures containing the hard intermetallic phase Cr_2Nb and the softer Cr-rich solid solution phase. Previous studies indicate that the two-phase Cr-Cr_2Nb alloys (CN) exhibited significant plastic deformation prior to fracture under compressive tests at room temperature.[6,7,9] The alloys showed excellent compressive strength at room and elevated temperatures, with the yield strength much superior to nickel-base superalloys and Ni_3Al alloys at and above 1000°C. The CN alloys, however, showed poor fracture strength in tension at ambient temperatures. Because tensile properties were sensitive to defects, efforts aimed at reducing as-cast defects and refining the cast Cr-Cr_2Nb eutectic structure led to improved ductility.[10] A room-temperature fracture strength of 548 MPa and an ultimate tensile strength of 388 MPa, and 23% elongation, at 1200°C were achieved, while another CN alloy showed a fracture toughness of 7.6 MPa$\sqrt{m}$ at room temperature and 24.4 MPa$\sqrt{m}$ at 1000°C.[10]

Current studies are focused on enhancement of fracture resistance in tension at ambient temperatures and oxidation resistance above 1000°C. This report summarizes recent progress on controlling microstructure and improving the mechanical and metallurgical properties and the high-temperature corrosion behavior of Cr-Cr_2Nb alloys through alloying additions, material processing, and heat treatment.

ALLOY PREPARATION AND PROCESSING

CN alloys weighing 430 g were prepared by arc melting and drop casting in a copper mold (2.5 cm diam x 7.6 cm long) preheated to 200°C. High-purity niobium, chromium, and other metal chips were used as charge materials. The cast alloy ingots with the compositions listed in Table 1 generally contained oxide inclusions and cast porosity ranging in size from a few to several hundred microns. The cast alloys also exhibited a coarse eutectic structure with interconnected Cr_2Nb plates, which adversely affect mechanical properties.[8] In order to minimize the cast defects and to refine the eutectic structure, selected alloy ingots were clad inside Mo billets and hot extruded at 1480°C at an extrusion ratio of 4:1. Most alloys were successfully hot extruded into 1.3 cm bar stock.

The CN alloys were also prepared by a powder metallurgy (P/M) route. In this case, elemental powders in ratios chosen to give the correct alloy compositions were mixed thoroughly in an inert environment and then placed inside molybdenum cans. The filled cans

Table 1. Tensile Properties of Cr-Nb Base Alloys Fabricated by Hot Extrusion at 1480°C

Alloy No.	Alloy Composition (at. %)[a]	Tensile Fracture Strength (MPa)	Yield Strength (MPa)	Elongation (%)
	Room Temperature			
CN-80	12Nb-6Mo-1.5Al	548		
CN-90	6Nb-5Mo-4X2-2X3-1.5Al	435		
CN-104	10Nb-6Mo-4X2-0.5X3	293		
CN-112	6Nb-5Mo-2X2-1X3-1X4-1.5Al	508		
CN-113	6Nb-5Mo-2X2-1X3-2X4-1.5Al	374		
	1200°C			
CN-80		388	290	23.0
CN-90		384	302	13.4
CN-104		473	371	25.7
CN-112		440	345	30.1
CN-113		414	330	26.4

[a]Balance is Cr.

Table 2. Tensile Properties of Cr-Zr Base Alloys Fabricated by Hot Extrusion

Alloy No.	Alloy Composition (at. %)	Tensile Fracture Strength (MPa)	Yield Strength (MPa)	Elongation (%)
		Room Temperature		
CN-107	Cr-12Zr	304		
CN-114	Cr-8Zr	240		
CN-115	Cr-8Zr-5X1	413		
CN-116	Cr-8Zr-5X1-4X2	443		
CN-117	Cr-8Zr-5X1-4X2-2X3	393		
		1200°C		
CN-107				
CN-114		138	108	112
CN-115		267	203	46.3
CN-116		386	281	87.7
CN-117		485	344	28.8

were then degassed in a vacuum chamber and sealed by electron-beam welding. As above, they were hot extruded at 1480°C to produce CN alloys. All the alloys were successfully hot extruded into bar stock without difficulty.

Within the past year, a series of alloys based on Cr-Cr_2Zr were also prepared by melting and casting. The advantage of these alloys is that they are more resistant to cast and thermally induced cracking because, unlike the Cr-Cr_2Nb system, there is a reasonable match between the coefficient of thermal expansion of the second phase and that of the matrix. The alloys with the compositions listed in Table 2 were all successfully fabricated into rod stock by hot extrusion in the same way as the Cr-Cr_2Nb alloys.

MICROSTRUCTURAL ANALYSIS

Alloying additions, heat treatment, and material processing all strongly affect the microstructure of the CN alloys. Examination of the microstructure produced by hot extrusion revealed micro-porosity and foreign particles in the P/M products. Energy dispersive x-ray spectroscopic (EDS) analysis indicated that these particles were mainly oxides of aluminum or niobium that formed during materials processing. Apparently, this contamination could not be simply eliminated even though the alloy powders were carefully processed in an inert

atmosphere. Mechanical tests indicated that the P/M CN alloys had poor fracture resistance at room and elevated temperatures.

Figure 1 shows the optical microstructures of the ingot-processed CN-104 alloy with and without hot extrusion at 1480°C. It, as well as the other alloys listed in Table 1, was given a final heat treatment of 1 d at 1200°C for control of Cr_2Nb precipitation in the Cr-rich phase. The hot extrusion was effective in breaking up the interconnected coarse Cr_2Nb phase in the eutectic structure. In fact, it became difficult to distinguish the primary and secondary Cr_2Nb particles in the alloy after this processing step.

Figure 2 compares the optical microstructures of cast CN-114 and CN-115 fabricated by hot extrusion at 1480°C. Both alloys are based on the Cr-Cr_2Zr composition containing 8 at. % Zr (see Table 2). Alloy CN-114 is a binary alloy, while CN-115 is a ternary alloy containing 5 % of element X1. The comparison of the microstructures indicates that 5% of X1 is quite effective in breaking up the interconnected Cr_2Zr phase into blocky particles. All the alloys were also given a final heat treatment of 1 d at 1200°C. It is important to note that, unlike the Cr-Cr_2Nb system, no precipitation of Cr_2Zr particles was found in the primary Cr-rich patches. This is consistent with the Cr-Zr phase diagram which shows a very low solubility of Zr in the Cr-rich solid solution phase.[4]

Specimens of the Cr-Nb alloy, CN-90, and the binary Cr-Zr alloy, CN-107, were examined by transmission electron microscopy and energy dispersive spectroscopy (EDS). Both specimens were hot extruded at 1480°C and annealed for 1 d at 1200°C. The matrix of the CN-90 alloy contained a very high density of dislocations while the Cr_2Nb-based second phase showed fewer dislocations but some faulting (Fig. 3a). In the CN-107 alloy, (Cr-12% Zr) both the matrix and most of the second phase showed a high density of dislocations even after the 1 d anneal at 1200°C (Fig. 3b). Chemical analyses were performed on very thin areas with the precipitate intersecting the hole and on slightly thicker regions. The analysis of CN-90 showed that the Nb, X2, and X3, elements partitioned strongly to the Cr_2Nb precipitates, while the molybdenum level in the precipitate matched the matrix. In CN-107, the composition of the precipitate was determined to be 68% Cr - 32% Zr, indicating the expected formation of Cr_2Zr. Virtually no zirconium remained in solution. Table 3 summarizes the average compositions determined by EDS.

TENSILE PROPERTIES

Button-type tensile specimens with gage dimensions 0.31 diam x 0.95 cm long were machined by electro-discharge machining, followed by grinding and polishing with "0"

(a)

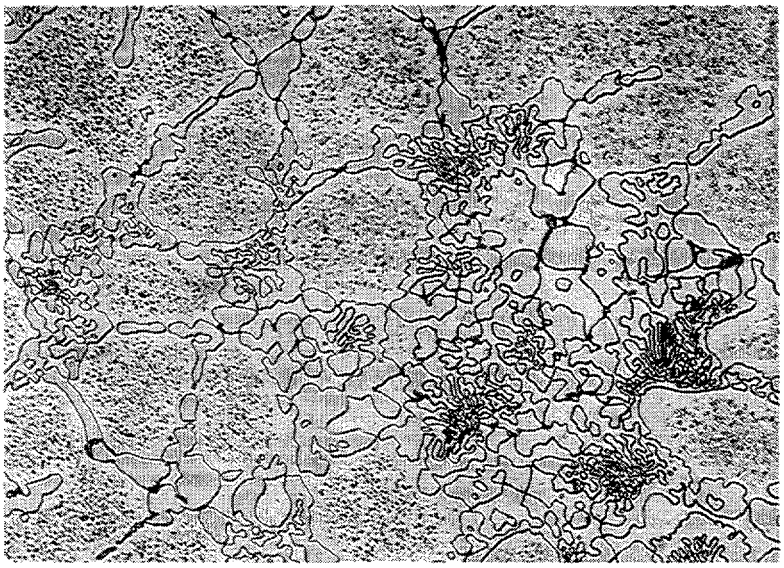

(b)

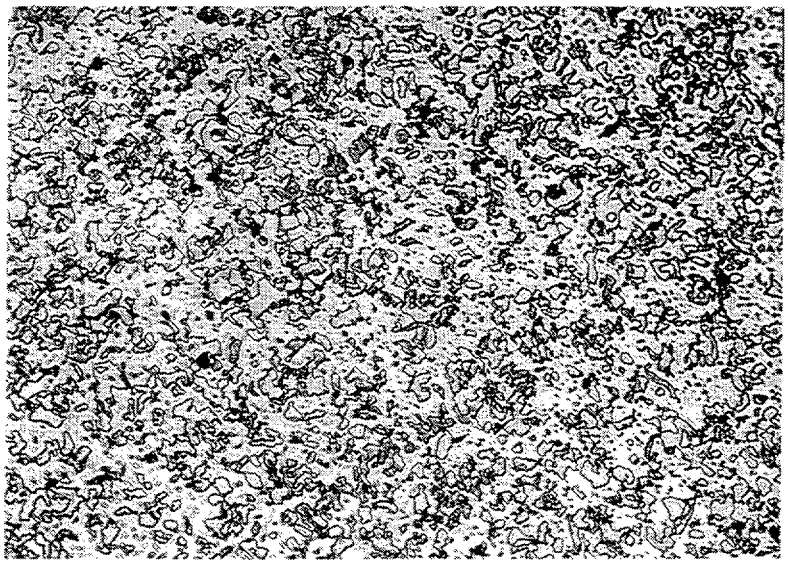

Fig. 1. Optical micrographs of CN-104: (a) as-cast plus annealed for 1 d at 1200°C and (b) hot-extruded at 1480°C plus annealed for 1 d at 1200°C; 625X.

(a)

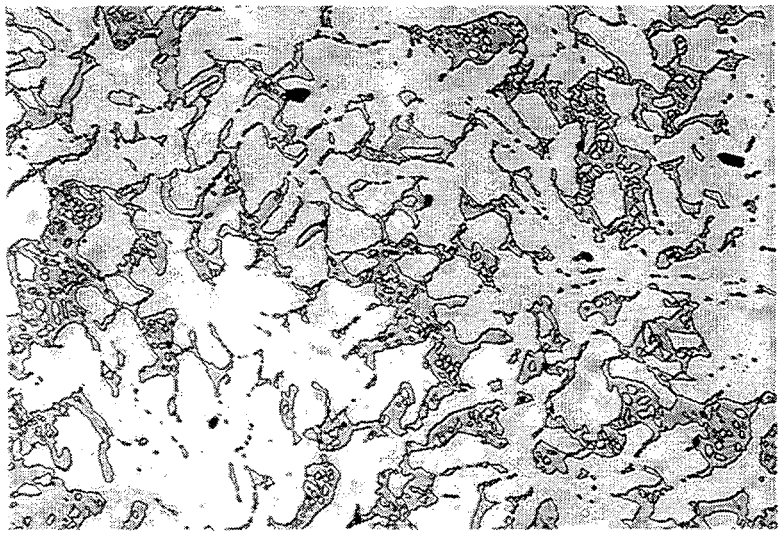

(b)

Fig. 2. Micrographs of CN alloys produced by hot extrusion at 1480°C and annealed for 1 d at 1200°C. (a) CN-114 and (b) CN-115; 625X.

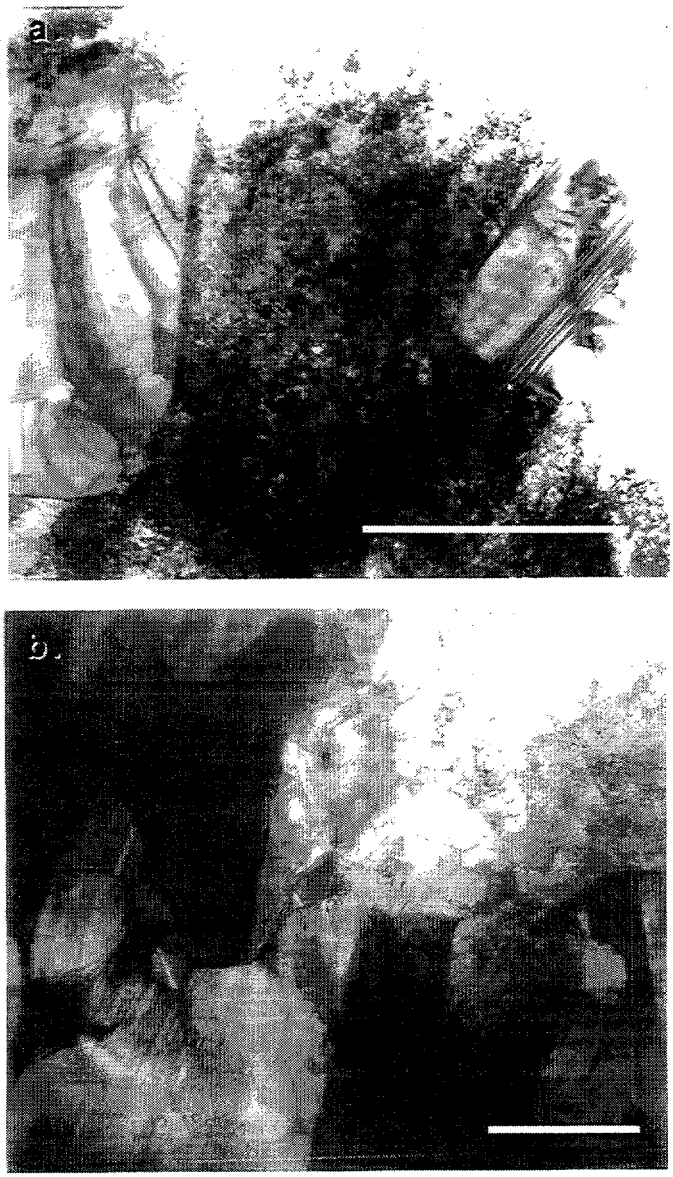

Fig. 3. TEM micrographs of (a) CN 90 and (b) CN 107 showing a high dislocation density present after extrusion at 1480°C and an anneal for 1 d at 1200°C. The Cr_2Nb-based second phase in (a) has few dislocations while the Cr_2Zr second phase in (b) has a higher location density. Bar is 1 μm long.

Table 3. Chemical Analysis of CN-90 and CN-107 (in at. %)

CN-90	Al	X2	X3	Cr	Nb	Mo
Average matrix	1	1	1	90	1	6
Average ppt	0.5	11	4	52	25	7
nominal	1.5	4	2	81.5	6	5

CN-107	Cr	Zr
Average matrix	99	1
Average ppt	68	32
nominal	88	12

Emery paper. The tensile specimens were tested in an Instron Testing Machine at room temperature in air and at 1200°C in vacuum. Since the tensile properties of brittle materials are sensitive to microstructure and defects in materials, the CN alloys were tested at room temperature for different fabrication conditions. Table 4 compares the tensile properties of CN-90 processed in different ways. The P/M material, fabricated by hot pressing and isothermal forging of the power compact, had the lowest fracture strength, while the material fabricated by hot extrusion of the cast ingot showed the highest value. As mentioned previously, the low fracture strength of the P/M material is associated with interstitial contamination and the formation of oxide/nitride particles.

Table 1 summarizes the tensile properties of Cr-Nb base alloys fabricated by hot extrusion of cast materials. The CN alloys showed no microscopic yielding prior to fracture, and the two alloys CN-80 and -112 exhibited the best room-temperature fracture strength, >500 MPa. At 1200°C, the CN alloys were very strong and ductile. Yield and ultimate tensile strengths were above 340 MPa (50 ksi) and 420 MPa (60 ksi), respectively, for both CN-104 and 112. These values are among the highest ever measured for alloys and meet the strength goal of this alloy development program. Alloy CN-112 appeared to have the best combined properties at room temperature and 1200°C. All the alloys except CN-90 had more than 20% elongation at 1200°C.

Table 2 summarizes the tensile properties of the Cr-Zr base alloys fabricated by hot

Table 4. Room-Temperature Tensile Properties of CN-90[a]

Alloy Preparation and Fabrication	Fracture Strength (MPa)
Hot pressing and forging elemental powders at 1480°C	140
Induction melted ingot	169
Hot extrusion of ingot at 1480°C	435

[a]All materials were given a final heat treatment of 1 d at 1200°C.

extrusion. Both binary alloys had a low fracture strength, compared to the more highly alloyed compositions. Among all the alloys, CN-116 had the best tensile fracture strength at room temperature. Both yield and ultimate tensile strengths increased substantially with alloying additions, and the alloy CN-117 had the best strength at 1200°C. All the alloys are ductile at 1200°C, with tensile elongation more than 25%. Alloy CN-117 had the best combination of strengths at room temperature and 1200°C.

HIGH-TEMPERATURE OXIDATION BEHAVIOR

It has been previously demonstrated that the addition of element X2 to Cr-Cr_2Nb alloys improves oxidation resistance under isothermal and thermal cycling conditions.[10,11] The beneficial influence of X2 was attributed to improvement in the oxidation resistance of the Cr-rich regions (despite its partitioning to the Cr_2Nb phase),[11] which otherwise showed preferential susceptibility to degradation upon exposure to high-temperature air.[12] However, despite improvements in the oxidation resistance of Cr-Cr_2Nb alloys, such materials cannot be used in an uncoated condition in oxidizing environments at the very high temperatures where the superior strength of the CN compositions can be exploited (>1100°C). At these temperatures, thermally grown oxides on Cr-Cr_2Nb alloys are not protective because chromia volatilizes at a significant rate. Oxidation protection will therefore involve the use of coatings. In this regard, silicide coatings applied by a pack cementation process can substantially improve the oxidation resistance of Cr-Cr_2Nb alloys.[10,13,14] Such coatings can also protect these alloys against high-temperature sulfidation. As indicated by the data in Fig. 4, which shows specimen weight gain as a function of isothermal exposure time in a highly-reducing H_2S-H_2-H_2O-Ar gas mixture ($p_{O2} = 10^{-22}$ atm, $p_{S2} = 10^{-6}$), a Cr-12% Nb binary alloy was very susceptible to sulfidation, but a Cr-8% Nb composition (CN-87) coated with a Cr-Si layer produced by pack cementation exhibited very low weight gains. The resistance of the coated alloy was comparable to Fe_3Al alloys containing > 2% Cr, which are considered to have very good sulfidation resistance compared to stainless steels and FeCrAl-type alloys.[15]

Figure 5 compares the isothermal oxidation rate of two more recent Cr-Cr_2Nb compositions, CN-90 (see Table 1) and CN-100 (8% Nb-6% Mo-4% X2-2% X3), with that of CN-87, which heretofore showed the best oxidation resistance of the CN alloys.[10,11] (Isothermal air oxidation at 950°C has traditionally served as the initial baseline evaluation of oxidation resistance of the CN alloys.) All three compositions shown in Fig. 5 include the same concentration of X2, which, as noted above, has been shown to significantly improve oxidation resistance.[10] Despite this, CN-90 showed a significantly higher oxidation rate. The reason for this is unknown; all of the alloying elements in this alloy are present in comparable

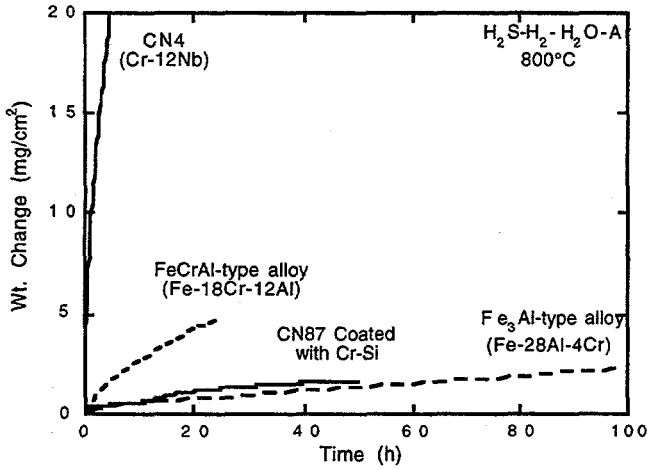

Fig. 4. Weight change as a function of time for alloys isothermally exposed to H_2S-H_2-H_2O-Ar at 950°C. The CN87 alloy consisted of Cr-20%Fe-5%Mo-4%X2-1.5%Al and was coated by a pack cementation process (see ref. 13). Compositions shown are in at.%.

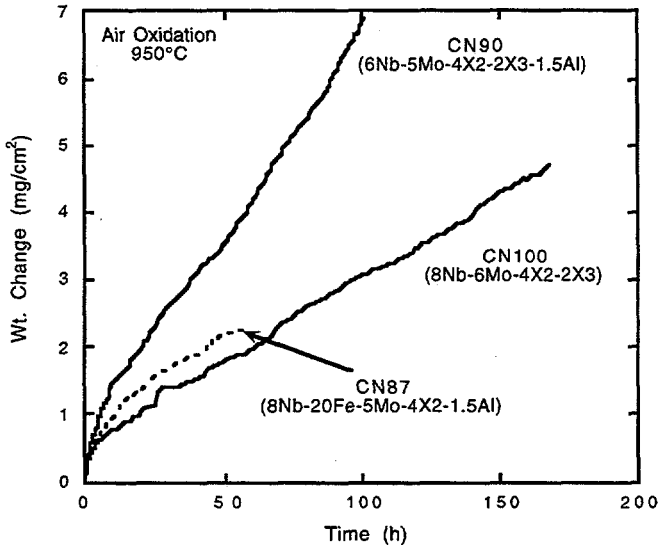

Fig. 5. Weight change as a function of time for Cr-Cr_2Nb alloys during isothermal exposure to dry air at 950°C. Compositions shown are in at.%.

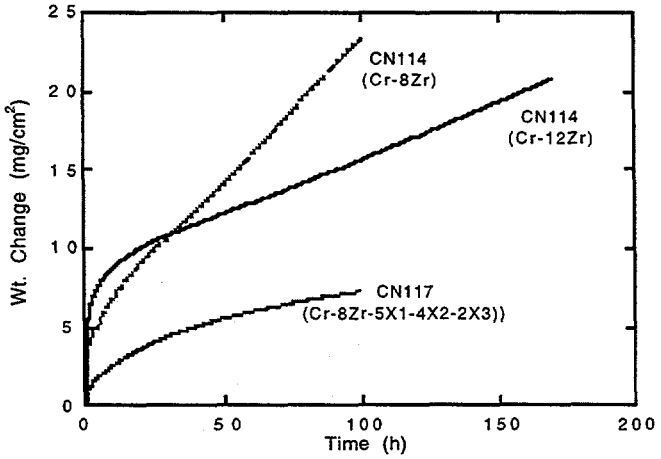

Fig. 6. Weight change as a function of time for Cr-Cr_2Zr alloys during isothermal exposure to dry air at 950°C. Compositions shown are in at.%.

concentrations in CN-87 and/or CN-100, which had similar rates of weight gain that were less than that of CN-90. It is possible that the lower Nb concentration of CN-90, and the accompanying distribution of the matrix and eutectic phases, contributes to its higher oxidation rate as such a trend has been established previously,[12] but a definite explanation awaits chemical and microstructural analyses of these specimens. Examination of the data in Fig. 5 and the respective compositions of CN-87, -90, and -100 indicates that iron and element X3 don't have substantial effects on macroscopic oxidation behavior at 950°C.

Alloys based on Cr-Zr will be susceptible to high-temperature oxidation as Zr forms a very stable oxide that grows very rapidly.[16] It is therefore not surprising that the measured weight changes during isothermal oxidation exposures of alloys CN-107 and -114 (Fig. 6) are significantly higher than what is expected for reactions solely controlled by the growth of Cr_2O_3 (ref. 16) and than what is measured for certain Cr-Cr_2Nb alloys (Fig. 5). Interestingly, the addition of alloying elements substantially reduced the weight gains and oxidation rate over those measured for the binary compositions - see the results for CN-117 in Fig. 6. There are at least two possible reasons for the observed beneficial effect of alloying. Element X2 may improve oxidation resistance in a similar manner to its effect in the Cr-Nb system.[11] Secondly, as noted above, element X1 effectively breaks up the network of interconnected Cr_2Zr (Fig. 2). As this phase is much more susceptible to oxidation than the Cr matrix, creation of a finer distribution of Cr_2Zr may act to reduce the overall oxidation rate. Experiments specifically designed to examine the effects of volume fraction and distribution of Cr_2Zr, in the context of all the possible processes by which oxide products can grow on two-phase alloys at high temperatures,[17] can best address the validity of this hypothesis.

FUTURE WORK

The development work on the Cr-Nb system indicates that the alloy CN-112 (Cr-6Nb-5Mo-2X2-1X3-1X4-1.5 Al, at.%) is close to an optimum composition and meets the strength goal of this project. Further studies are required to learn how to scavenge interstitials from the Cr-rich phase in order to achieve good tensile ductility at ambient temperatures. While Cr-Zr alloys show little as-fabricated cracking, there is a need to strengthen the Cr-rich phase by either solid-solution hardening or second-phase precipitation. Oxidation-resistant coatings are needed for the Cr-Zr alloys.

The Cr-rich phase has a limited ductility and fracture resistance at room temperature. In order to significantly improve the room-temperature ductility, the Cr-rich solid solution matrix phase must be substantially modified. Recently, ternary phase diagrams based on the Cr-Nb-X system have been reviewed and new compositions have been identified for alloy development

based on a strategy of avoiding as-fabricated cracking and improving the ductility of the matrix in the presence of a Laves phase, which confers the unique high-temperature strength.

SUMMARY

Alloys of Cr-Cr_2Nb with exceptionally high strength at 1200°C have been developed. However, these compositions suffer from limited ductility and toughness at room temperature. Despite improvements from processing modifications, as-fabricated defects still limit room temperature mechanical behavior. Alloys based on Cr-Cr_2Zr show good fabricability because there is only a small mismatch of the coefficients of thermal expansion of the two phases. However, these alloys are generally weaker than Cr-Cr_2Nb compositions at high temperatures and have poor oxidation resistance. Silicide coatings can provide high-temperature oxidation and sulfidation protection of this alloys. Improvements in room temperature mechanical properties of Laves-phase-strengthened alloys will come from increasing the ductile of the matrix phase by impurity control and compositional modifications.

ACKNOWLEDGMENTS

The authors thank D. F. Wilson and C. G. McKamey for their reviews of the manuscript. This research was sponsored by the Fossil Energy Advanced Research and Technology Development (AR&TD) Materials Program, U S. Department of Energy, under contract DE-AC05-96OR22464 with Lockheed Martin Energy Research Corporation.

REFERENCES

1. F. Laves, p. 124 in Theory of Alloy Phases, American Society for Metals, Metals Park, OH, 1956, .

2. D. J. Thoma and J. H. Perepezko, Mat. Sci. and Eng. A156 (1992) 97.

3. H. J. Goldschmidt and J. A. Brand, J. Less-Common Met. 3 (1961) 44.

4. T. B. Massalski, J. L. Murray, L. H. Bennett, and H. Baker (eds.), Binary Alloy Phase Diagram, American Society for Metals, Metals Park, OH, 1986.

5. A. I. Taub and R. L. Fleischer, Science 243 (1989) 616.

6. C. T. Liu, pp. 375-383 in *Proc. 6th Annual Conf. Fossil Energy Materials*, N. C. Cole and R. R. Judkins (comp.), U. S. Department of Energy, July 1992.

7. C. T. Liu, J. A. Horton, and C. A. Carmichael, pp. 297-307, in *Proc. 7th Annual Conf. on Fossil Energy Materials*, N. C. Cole and R. R. Judkins (comp.), U. S. Department of Energy, July 1993.

8. C. T. Liu, J. A. Horton, and C. A. Carmichael, pp. 377-390 in *Proc. 8th Annual Conf. on Fossil Energy Materials*, N. C. Cole and R. R. Judkins (comp.), U. S. Department of Energy, August 1994..

9. M. Takeyama and C. T. Liu, Mat. Sci. and Eng. A132 (1991) 61.

10. C. T. Liu, P. F. Tortorelli, J. A. Horton, D. S. Easton, J. H. Schneibel, L. Heatherly, C. A Carmichael, M. Howell, and J. L. Wright, pp. 415 - 26 in *Proc. Ninth Annual Conf. Fossil Energy Materials*, N. C. Cole and R. R. Judkins (comp.), U. S. Department of Energy, August 1995.

11. P. F. Tortorelli and J. H. DeVan, pp. 391-400 in *Proc. 8th Annual Conf. on Fossil Energy Materials*, N. C. Cole and R. R. Judkins (comp.), U. S. Department of Energy, August 1994.

12. P. F. Tortorelli and J. H. DeVan, pp. 229-236 in *Proc. Symp. on Oxide Films on Metals and Alloys*, B. R. MacDougall, R. S. Alwitt, and T. A. Ramanarayanan (eds.), Proceedings Vol. 92-22, The Electrochemical Society, 1992.

13. Y-R. He, M. H. Zheng, and R. A. Rapp, pp. 311-324 in *Proc. Ninth Annual Conf. Fossil Energy Materials*, N. C. Cole and R. R. Judkins (comp.), U. S. Department of Energy, August 1995.

14. R. A. Rapp, "Pack Cementation Coatings for Alloys," these proceedings

15. P. F. Tortorelli and J. H. DeVan, pp. 257-70 in Processing, Properties, and Applications of Iron Aluminides, J. H. Schneibel and M. A. Crimp (eds.), The Minerals, Metals, and Materials Society, Warrendale, PA, 1994.

16. P. Kofstad, High Temperature Corrosion, Elsevier, London, 1988.

17. F. Gesmundo and B. Gleeson, to be published in Oxid. Met. 1996.

2.11 DEVELOPMENT OF IRON ALUMINIDES

G. M. Goodwin

Oak Ridge National Laboratory
P.O. Box 2008
Oak Ridge, Tennessee 37831-6096

INTRODUCTION

Alloys based on the intermetallic compound Fe_3Al exhibit many attractive properties, particularly excellent resistance to high temperature oxidation. Their use in commercial applications has been limited, however, by the limited workability of wrought material and the susceptibility of weldments to both hot and cold cracking. Prior efforts [1-5] have systematically evaluated the effect of alloy composition on hot cracking.

By the use of the Sigmajig test [6], we have found that hot cracking can essentially be eliminated by the addition of carbon and the control of maximum levels of niobium, zirconium, and other alloying elements. Cold cracking, however, remains an issue, and recent efforts have been aimed at minimizing its occurrence, concurrent with development of welding filler metals, processes, and procedures aimed at commercial applications.

FILLER METAL DEVELOPMENT

Due to the difficulty in fabricating wrought solid wire of these compositions, the welding development efforts have utilized several alternate forms of filler metal. Early work [1-2] used strip sheared from sheet, which, although useful to investigate compositional effects, could not be considered for commercial applications. Subsequently, aspiration casting, where liquid metal is drawn into a quartz tube producing solid rod, was used as a means for evaluating a number of experimental compositions.[3-5] This technique proved successful, but can only produce rods of limited length (about 12-in. maximum) and diameter (about 1/8-in. minimum), thus restricting its use to the manual gas tungsten arc (GTA) process with relatively high heat input. It was realized from the onset that what was needed was a filler metal of small diameter, (approximately 1/16-in.) available in coil form, which could be used with both the GTA and gas metal arc (GMA) processes, permitting better control of dilution and semi-automatic welding. A novel technique for meeting these needs was found in the form of a composite filler wire, shown in cross-section in Figure 1.

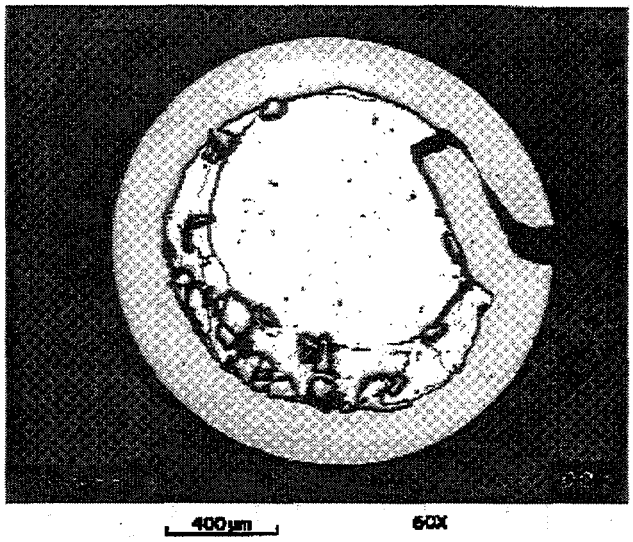

Figure 1. Composite filler wire for producing iron aluminide deposits, consisting of an iron sheath, aluminum core, and other alloying elements in granular form.

The wire consists of an iron sheath of approximately 0.009-in. thickness surrounding a core wire of commercially pure aluminum. Other alloying elements (C, Cr, Mo, Zr, B) are added as granular ferroalloys. After forming and crimping, the composite wire is drawn to eliminate void space and to

arrive at precise final diameter, in this case 0.0625-in. The resulting product is readily produced in coil form and can thus be used with automatic wire feeders for a number of welding processes.

Figure 2 shows a cross-section of a multi-pass weld pad produced using the automatic GMA process on 1-in. thick 2-1/4Cr-1 Mo steel plate.

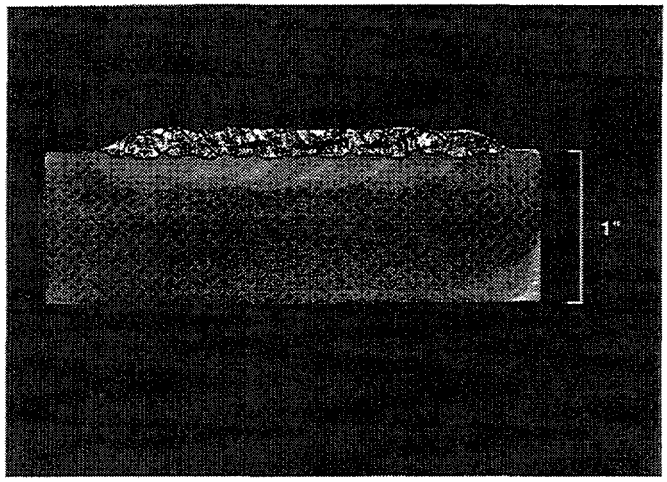

Figure 2. Multipass weld pad produced with composite filler metal using the automatic gas metal arc process on 2 1/4 Cr-1 Mo base plate.

The welding parameters used are summarized in Table 1.

Table I. Welding Parameters for Gas Metal Arc Weld Overlay Using 1/16-in. Diameter Composite Iron Aluminide Wire

Current:	245 Amperes, Reverse Polarity (DCEN)
Voltage:	27 volts
Wire Feed:	190 inches/minute
Travel:	13.1 inches/minute
Shield Gas:	Argon, 45 cubic feet/hour
Bead offset:	3/8-in.
Electrode Stickout:	3/4-in.
Preheat:	350° C
Postweld Heat Treatment:	750° C, 1 hour

The weld deposit had approximately 30% dilution and was free of cracks, voids, and porosity. Usability of the wire was found to be excellent and arc spatter was minimal. It was concluded that this form of wire could readily be used in commercial applications with the automatic GMA or GTA processes.

COMPOSITIONAL EFFECTS

As noted earlier, control of composition of the weld deposit was accomplished to essentially eliminate hot cracking in these alloys.[4] Control of cold cracking, however, has proven to be more elusive, showing a rough correlation with aluminum content[5], and a clear dependence on geometry, weld preheat, and postweld heat treatment conditions. The dependence on aluminum level is known to be complex, based on the observations of cracking in high and very low aluminum level alloys[7]. In order to clarify this relationship, we are preparing wire compositions which will bracket the range of aluminum levels which can be produced using the composite wire technique with dilution levels consistent with commercial practice. The desired chromium level in the alloy is also debatable, depending on the service conditions to be encountered, so heats of the composite wire have been produced with and without chromium. Table II summarizes the alloy compositions currently under study, and notes two additional heats which have been ordered. The latter heats represent the highest and lowest aluminum levels which can be produced with the composite wire approach, based on the thickness of the iron sheath and the diameter of the aluminum core wire.

As is noted in the table, the weld process, substrate, and dilution substantially affect the composition of the overlay clad deposit, particularly the aluminum level. Note that with an aim of 20 weight % Al for an all weld metal (undiluted) deposit, we actually achieved 21.8 weight % using the GTA process; when this same wire was used on dissimilar substrates (2 1/4 Cr-1 Mo steel and 310 stainless steel) with two weld processes, GMA and GTA, the aluminum levels were 12.6 and 15.3 weight % respectively. The higher aluminum loss with the GMA process is undoubtedly due to higher dilution and vaporization in the arc.

HEAT TREATMENT EFFECTS

It was established earlier [4,5] that weld preheat and postweld heat treatment were often effective at avoiding cold cracking during welding or upon subsequent cooling from completion of the weld. Optimization of these heat treatment conditions is important for economic and environmental considerations, as heat treatments are expensive, time consuming, and can cause hardship to the operator.

TABLE II: COMPOSITION OF EXPERIMENTAL HEATS OF IRON ALUMINIDE ALLOYS

HEAT	WEIGHT %	Al	Cr	C	Zr	Mo
Stoody I	Aim, All weld metal	20	7	0.1	0.25	0.25
	Actual, All weld metal	21.8	7.3	0.06	0.40	NA[c]
	Actual, Clad Deposit [a]	12.6	6.0	0.08	0.20	0.44
	Actual, Clad Deposit [b]	15.3	12.7	0.05	0.22	0.04
Stoody II	Aim, All weld metal	20	--	0.1	0.25	0.25
	Actual, All weld metal	21.5	--	0.08	0.25	NA
Stoody III	Aim, All weld metal	12	--	0.1	0.25	0.25
Stoody IV	Aim, All weld metal	26	--	0.1	0.25	0.25

a Single layer automatic gas metal arc on 1-in. thick type 2 1/4 Cr-1Mo steel
b Single layer manual gas tungsten arc on 1/2-in. thick type 310 stainless steel
c NA - Not Analyzed

A series of welds was produced with preheat and postweld heat treatment reduced in 50° C steps starting at 350° C and 750° C respectively. It was found that preheat temperatures as low as 250° C would sometimes yield crack free deposits, but that 350° C was required to completely avoid cracking for a standard test geometry (4x6x1-in. block of 2 1/4 Cr-1 Mo steel). Similarly, reduced postweld heat treatment temperatures would often produce sound deposits which would subsequently crack during liquid penetrant examination. It appears that 350° C and 750° C are minimum temperatures required for the standard geometry with this range of compositions.

ENVIRONMENTAL TESTING

To establish the corrosion resistance of weld overlay clads in a variety of environments, we have prepared specimens of differing geometries and substrates for testing by several organizations.

In house testing at ORNL (Peter Tortorelli) utilizes strips of overlay deposit removed from different substrates, and tested independent of the substrate. This program has evaluated numerous aluminide filler metals. For gas corrosion tests at Babcock & Wilcox (Steven Kung), we clad twenty plate specimens of Type 310 stainless steel with the Stoody I filler metal using the manual GTA process, and for molten salt characterization at Lawrence Livermore National Laboratory (Donald Stevens), we used the same filler metal to overlay rod and plate specimens of Inconel 600. Results from all the tests will help determine the optimized alloy composition.

INDUSTRIAL SERVICE TESTING

In order to demonstrate the performance of the iron aluminide compositions in a commercial environment, we have modified several non-pressure boundary components of a paper mill recovery boiler. These components will be placed in service along with others of conventional materials, and will thus give a side-by-side comparison of performance. Figure 3 shows black liquor nozzles of the splash plate type, used to fire the fuel slurry into the boiler. Each is approximately 6-in. long. Figure 3(a) is a new part made of wrought type 316 stainless steel, and Figure 3(b) shows a similar part which has been removed from service and weld repaired using the Stoody I filler metal.

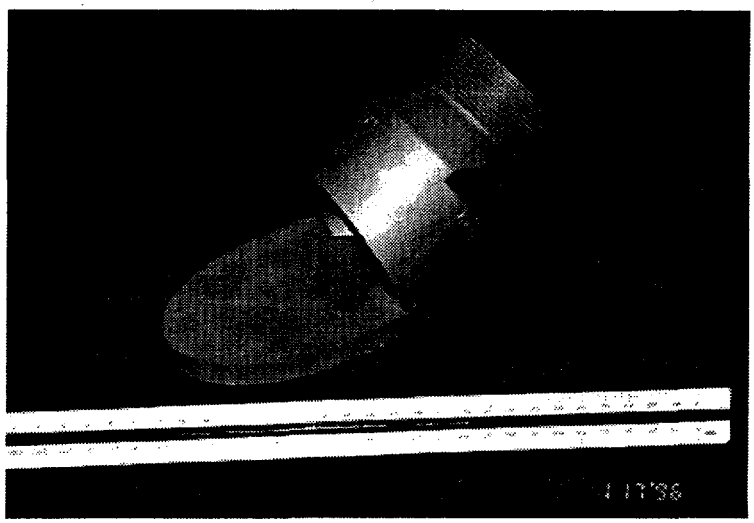

Figure 3. Splash plate type black liquor nozzles:
(a) new

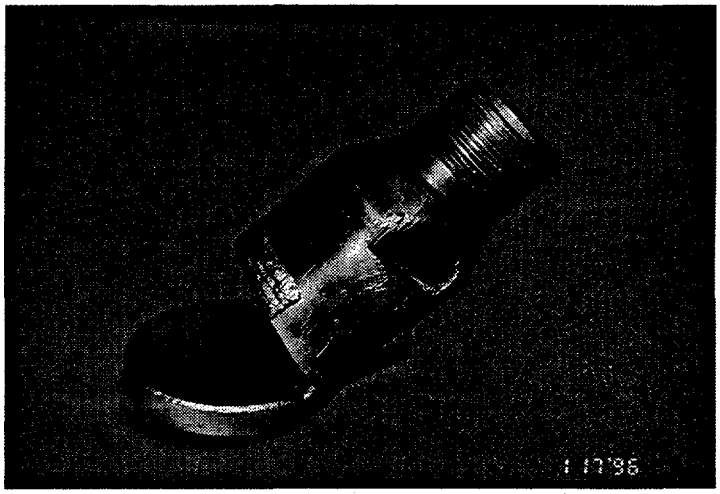

Figure 3. Splash plate type black liquor nozzles:
b) weld repaired after service by overlay cladding of splash plate (circular plate) and top of nozzle barrel. Each is approximately 6-in. long.

The splash plate (circular plate) has two layers of weld overlay which has subsequently been surface ground, and the leading edge of the nozzle barrel has a patch of overlay in a region where erosion commonly occurs.

Figure 4 shows a swirl cone type black liquor nozzle, after service, (a), and after weld overlay repair, (b). Major erosion/corrosion areas which have been clad are the outlet orifice (top), and the leading edge of the swirl cone [(b), left].

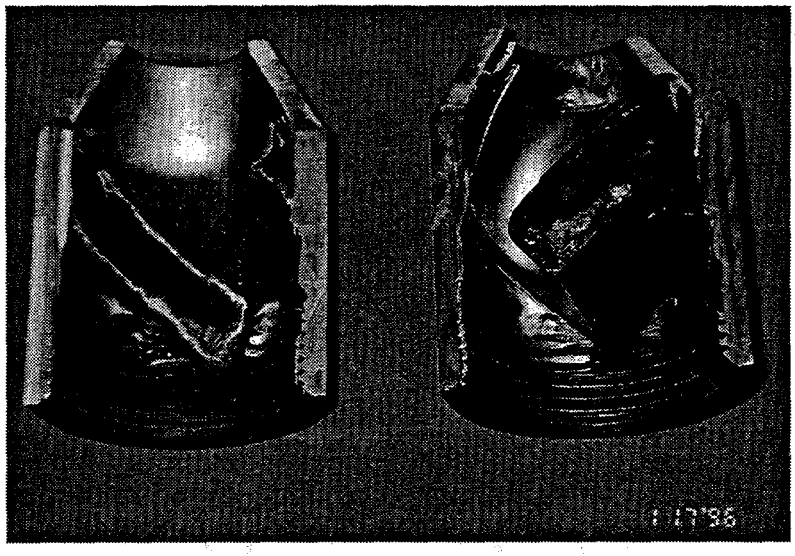

Figure 4. Swirl cone type black liquor nozzles:
(a) After service

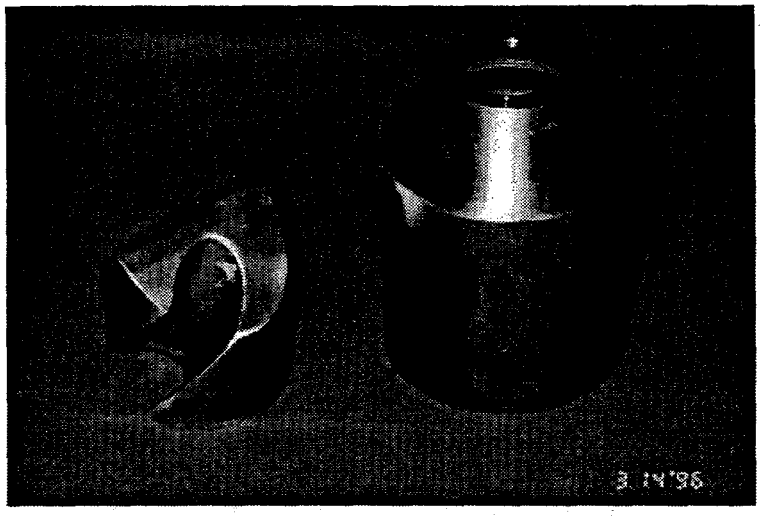

Figure 4. Swirl cone type black liquor nozzles:
(b) Weld overlay repaired at outlet orifice (right, top) and swirl cone leading edge (left, top). Approximately 4-in. long.

Figure 5 shows four sections of a liquor gun port shroud fabricated from 1/2-in. thick type 410 stainless steel plate. These plates are welded into the gun port openings in a hexagonal array (two long plates on the sides, short plates on tops and bottoms) to protect the water wall tubes, and often experience severe erosion/corrosion. The pads of aluminide overlay will give a direct comparison of their performance with that of the standard type 410 plate.

Industrial service testing is seen as an excellent way to rate these new alloys versus conventional alloys, and to guide our development toward additional commercial applications.

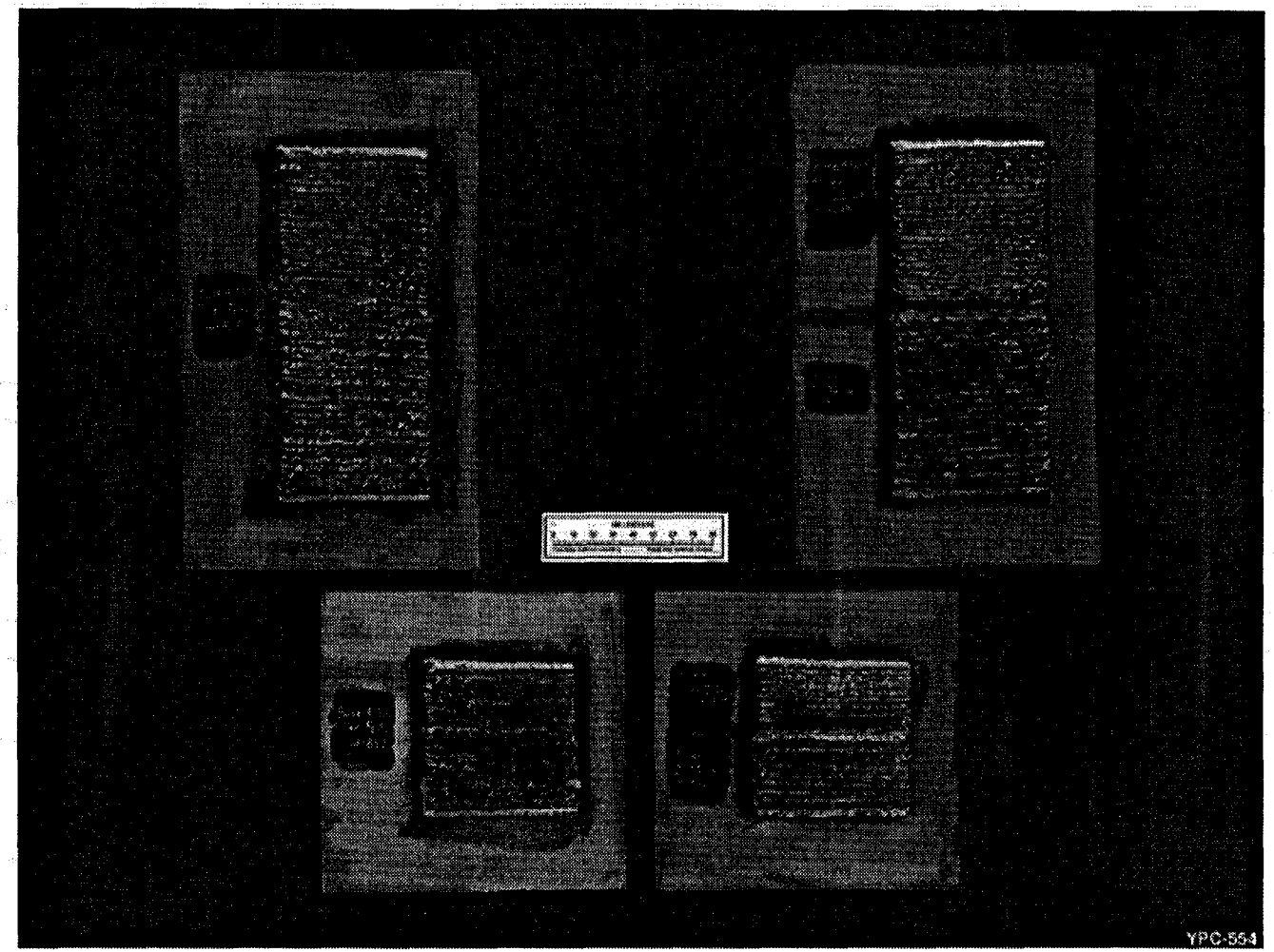

Figure 5. Liquor gun port shroud assembly. Weld overlay pads on 1/2-in. thick stainless steel plate will show comparative erosion/corrosion performance.

SUMMARY

Considerable progress has been made in the development of iron aluminide alloys for weld overlay cladding applications. Filler metals were produced in coil form using a composite approach with an iron sheath and aluminum core wire, permitting the use of automated gas metal arc and gas tungsten arc welding. Compositional modifications were made to essentially eliminate hot cracking, and efforts continue to reduce or eliminate cold cracking by optimizing composition and welding parameters, especially preheat and postweld heat treatment.

Clad specimens were prepared for testing in-house and elsewhere to confirm corrosion performance, and overlay welded components were placed in service in commercial boilers for a side-by-side comparison with currently used materials.

REFERENCES

1. T. Zacharia and S.A. David, *"Weldability of Iron Aluminides"*, proceedings of the Fifth Annual Conference on Fossil Energy Materials, ORNL/FMP-91/1, Oak Ridge National Laboratory, September 1991.

2. T. Zacharia, P.J. Maziasz, S.A. David, and C.G. McKamey, *"Weldability of Fe_3Al Based Iron Aluminide Alloys"*, proceedings of the Sixth Annual Conference on Fossil Energy Materials, ORNL/FMP-92/1, Oak Ridge National Laboratory, July 1992.

3. G.M. Goodwin, C.G. McKamey, P.J. Maziasz, and V.K. Sikka, *"Weldability of Iron Aluminides"*, proceedings of the Seventh Annual Conference on Fossil Energy Materials, ORNL/FMP-93/1, Oak Ridge National Laboratory, July 1993.

4. G.M. Goodwin, P.J. Maziasz, C.G. McKamey, J.H. Devan, and V.K. Sikka, *"Weldability of Iron Aluminides"*, proceedings of the Eighth Annual Conference on Fossil Energy Materials, ORNL/FMP-94/1, Oak Ridge National Laboratory, August 1994.

5. G.M. Goodwin, *"Weld Overlay Cladding With Iron Aluminides"*, proceedings of the Ninth Annual Conference on Fossil Energy Materials, ORNL/FMP-95/1, Oak Ridge National Laboratory, August 1995.

6. G.M. Goodwin, *"Development of a New Hot Cracking Test - The Sigmajig,* Weld J. 66(2) 335-S - 305-S (1987)

7. V.K. Sikka, G.M. Goodwin, D.J. Alexander, and C.R. Howell, *"Welding and Mechanical Properties of Cast FAPY (Fe-16 at % Al-Based) Alloy Slabs"*, ORNL/TM-12944, Oak Ridge National Laboratory, May 1995.

2.12 HIGH-STRENGTH IRON ALUMINIDE ALLOYS

C. G. McKamey and P. J. Maziasz

INTRODUCTION

Past studies have shown that binary Fe_3Al possesses low creep-rupture strength compared to many other alloys, with creep-rupture lives of less than 5 h being reported for tests conducted at 593°C and 207 MPa.[1,2] The combination of poor creep resistance and low room-temperature tensile ductility due to a susceptibility to environmentally-induced dynamic hydrogen embrittlement[3-5] has limited use of these alloys for structural applications despite their excellent corrosion properties.[6] With regard to the ductility problem, alloy development efforts have produced significant improvements, with ductilities of 10-20% and tensile yield strengths as high as 500 MPa being reported.[7,8] Likewise, initial improvements in creep resistance have been realized through small additions of Mo, Nb, and Zr.[1,9-13]

In recent years, further creep strengthening has been produced by using heat treatments to control the microstructure.[14,15] As shown in Fig. 1, for an Fe-28Al-5Cr (at.%) alloy containing additions of Mo, Nb, Zr, C, and B (designated alloy FA-180), heat treating at 1150°C for 1 h has been found to produce creep lives of over 2000 h for tests conducted at 593°C and 207 MPa. Especially interesting is the sharp dependence of creep strength on heat treating temperature, which is illustrated by the data in Fig. 1. In our earlier studies, transmission electron microscropy revealed the presence of fine precipitates which appeared to pin dislocations.[14] This, together with an activation energy for creep of approximately 150 kcal/mole (a value which is about twice that obtained earlier[1] for the binary alloy heat treated at 750°C) and high creep exponents of 7-12 (ref. 15), indicated that the observed strengthening was being produced by a precipitation mechanism. The general conclusion was that the 1150°C heat treatment resulted in the dissolution of coarse particles left over from the melting and casting

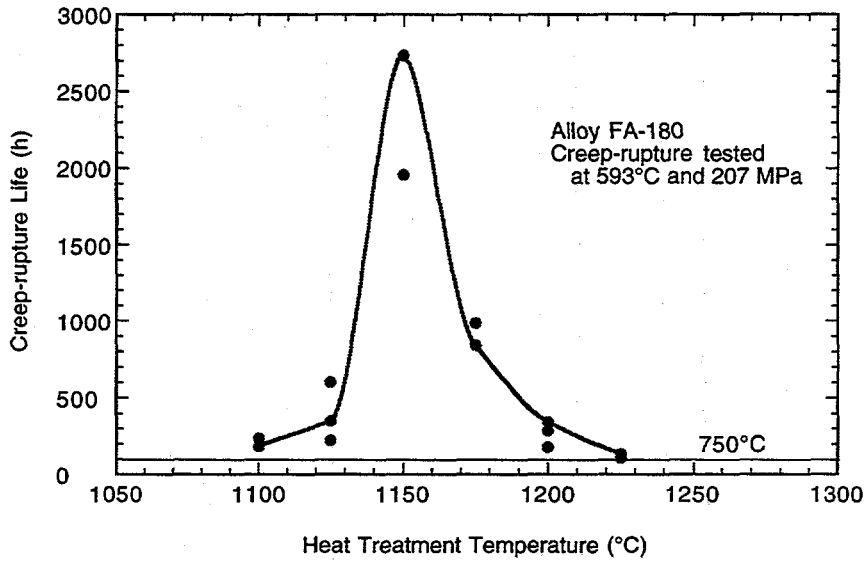

Figure 1. Creep-rupture life as a function of heat treatment temperature (for 1 h) for tests conducted on alloy FA-180 at 593°C and 207 MPa.

process, and then reprecipitation of finer Zr-based precipitates during cooling or the early stages of creep produced the strengthening.

The current research effort is centered on reaching a better understanding of the relationship between microstructure and strengthening mechanism(s) for this alloy and heat treatment. This report summarizes those efforts.

DISCUSSION OF CURRENT ACTIVITIES

The alloy composition used in this study was Fe-28Al-5Cr (at.%) with 0.5% Nb, 0.8% Mo, 0.025% Zr, 0.05% C, and 0.005% B (Oak Ridge National Laboratory designation FA-180). It was prepared by arc-melting and drop-casting into a chilled copper mold. Fabrication to 0.8-mm-thick sheet was accomplished by hot-rolling, beginning at 1000°C and finishing at 600-650°C. After a stress relief heat treatment of 1 h at 700°C, flat tensile specimens (0.8 x 3.18 x 12.7 mm) were mechanically punched from the rolled sheet. Before creep-rupture testing, specimens were further annealed in air for 1 h at 1150°C and then were either air cooled to room temperature or were quenched in oil or water.

Creep-rupture tests were performed in air at temperatures between 593 and 750°C under stresses of 138 to 276 MPa (20-40 ksi). In order to obtain creep exponents and activation energies, minimum creep rates (MCR) were measured as the slope of the linear portion of the test curve and the data were plotted to a power-law equation. The results for quenched specimens were compared to earlier published data on air-cooled specimens.[15]

Optical metallography and scanning electron microscopy (SEM) were used to study the microstructures and fracture modes. Analytical electron microscopy (AEM) using either a Philips CM30 (300 kV) or a CM12 [120 kV, with ultra-thin-window x-ray energy dispersive spectrometry (XEDS) detector] electron microscope was performed on samples cut from the gage portion of selected test specimens.

Creep-rupture tests were conducted on specimens cooled by different methods from the 1150°C heat treatment temperature and the data are presented in Table I. The creep-rupture lives of the rapidly cooled specimens are compared in Fig. 2 with the life of a specimen that had been cooled in air from the 1150°C heat treatment temperature and then tested at 593°C. The more rapidly cooled specimens (oil or water quenched) exhibited the best resistance to creep. Even though the air-cooled specimen had exhibited a very good rupture life of approximately 1959 h when tested at 593°C and 207 MPa, a specimen that had been quenched in oil showed no signs of rupturing (no increase in the very low, steady-state creep rate) after 6480 h, at which time the test was stopped. Likewise, the water quenched specimen that was tested at 650°C under

Table I. Creep-rupture Data for Alloy FA-180 as a Function of the Method Used for Cooling from the 1150°C Heat Treatment

Method of Cooling	Creep-rupture Test Conditions	Life (h)	Eongation (%)	MCR (/s)
air	593°C, 207 MPa	1959	10	8.3×10^{-7}
oil quench	593°C, 207 MPa	>6480[a]	5	2.8×10^{-8}
air	650°C, 241 MPa	2.7	42	2.2×10^{-3}
water quench	650°C, 241 MPa	1637	9	2.2×10^{-7}

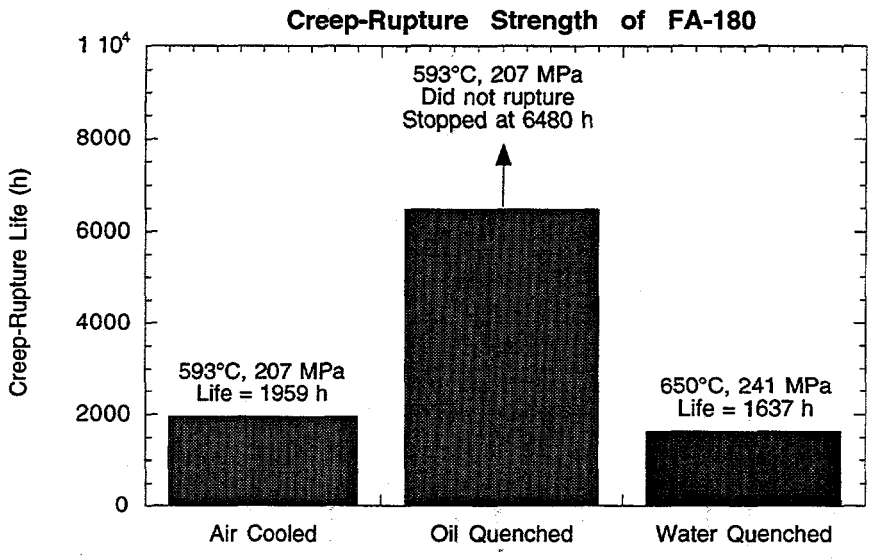

Figure 2. Creep-rupture life of air-cooled versus quenched specimens of alloy FA-180.

a stress of 241 MPa ruptured after 1637 h, while another specimen that had been cooled more slowly in air and tested at the same conditions lasted less than 3 h. The strengthening mechanism, therefore, appears to be different for quenched versus air cooled specimens, although the quenching medium itsefl does not appear to be the cause of that efect.

Creep tests were conducted as a function of temperature and stress in order to determine if the activation energies for creep (Q) and the creep exponents (n) were the same in both the air-cooled and oil-quenched conditions. The results are shown in Figs. 3 and 4. At a stress of 207 MPa (30 ksi), the activation energy for creep in the oil-quenched specimens was determined to be 76.6 kcal/mole, compared to a Q of 141.1 kcal/mole for air-cooled specimens. (The value of Q reported here for the air cooled specimens is slightly different from that reported earlier[15] because it was derived from more data points.) This significant difference in activation energy suggests that a d ifferent rate-controlling mechanism is active in the oil-quenched specimens. A plot of minimum creep rate versus stress (Fig. 4) shows a distinct break at approximately 200 MPa, with the creep exponent increasing at higher stresses. This behavior is also indicative of a change in the rate-

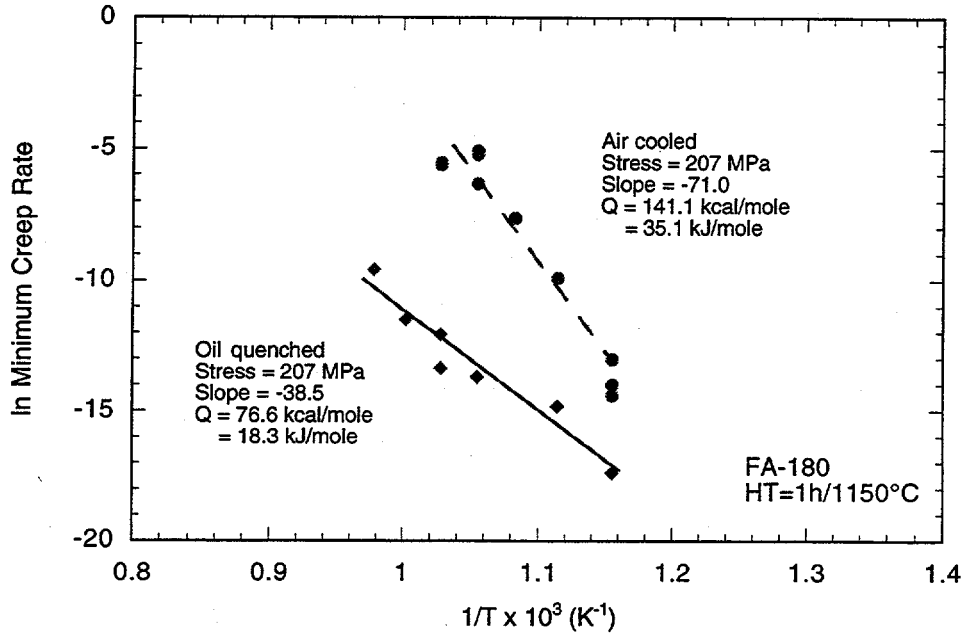

Figure 3. Minimum creep rate versus temperature data for air cooled versus oil quenched specimens of alloy FA-180 heat treated at 1150°C. All tests were conducted at a stress of 207 MPa (30 ksi).

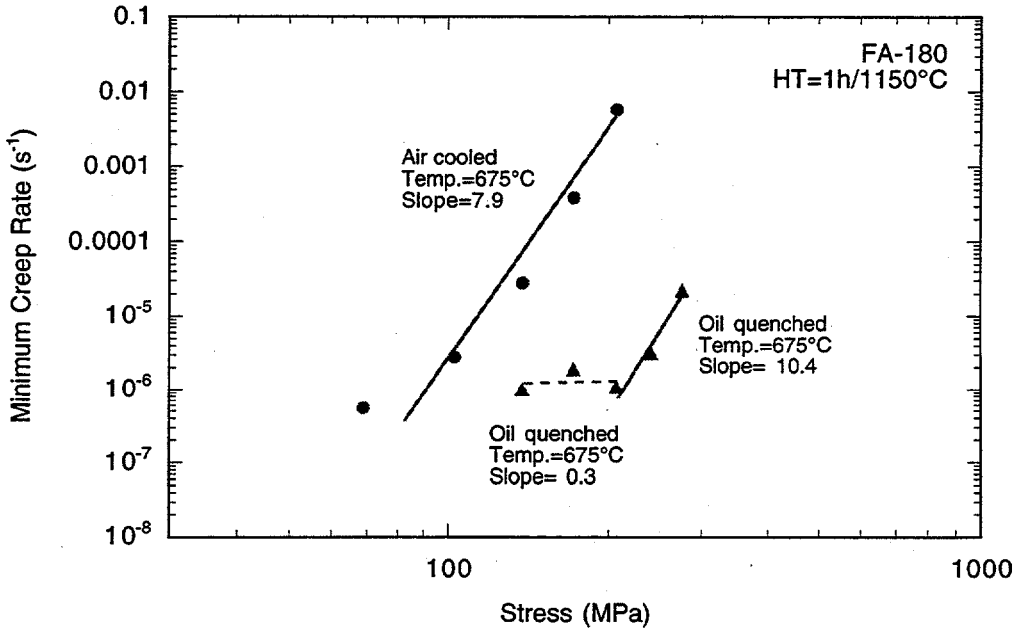

Figure 4. Minimum creep rate versus stress data for air cooled versus oil quenched specimens of alloy FA-180 heat treated at 1150°C. All tests were conducted at 675°C.

controlling creep mechanism with stress and is common in the data for many precipitate-hardened alloys.[16,17] The creep exponent of 10.4 shown in Fig. 4 for the oil-quenched specimens and the creep exponent for the air cooled specimens, which was earlier calculated to be 7.9 (ref. 15), are both indicative of alloys which have been hardened by precipitates or some other dislocation-pinning mechanism.[18,19]

Transmission electron microscopy was used to study the microstructure of the oil-quenched specimen that had been tested for 6480 h at 593°C. The micrograph in Fig. 5 shows that the creep-tested specimen contained networks of two-fold dislocations and many dislocation loops. At a higher magnification (Fig. 6), a few fine precipitates were also visible. Closer examination of the loops (Fig. 7) indicated that they were square or rectangular in shape and were restricted to the orthogonal habit planes (either <110> of <100>). Additionally, the dislocation segments in the loops appeared to be single rather than 2-fold and the four segments of each loop were of the same Burgers vector. For comparison, Fig. 8 shows the microstructure of a specimen in the as-heat-treated-and-oil-quenched (untested) condition. The dominant features are the B2 ordered domains and many black dots visible by black-white strain contrast imaging. In this case, by rotating the specimen through several diffracting conditions, most of the black dots visible in the microstructure in Fig. 8 were identified as dislocation loops, not precipitates. It therefore appears that fine dislocation loops were created in the microstructure as a result of the rapid quench from the 1150°C annealing temperature. Since it is known that vacancies are created in the Fe-Al system by quenching from high temperatures, especially for the B2 structure,[20,21] it is reasonable to assume that these dislocation loops observed in the specimens used in this test are vacancy loops. Vacancy loop nature would also be consistent with their growth during further heat treatment or creep testing. During creep-rupture testing at the temperatures used in this study, the loops provided strengthening by pinning dislocations and grew in size in the process (as indicated by the larger loop size in the as-tested specimen, Fig. 5).

Figure 5. TEM micrograph of FA-180 oil-quenched from a heat treatment at 1150°C and creep tested at 593°C for 6480 h.

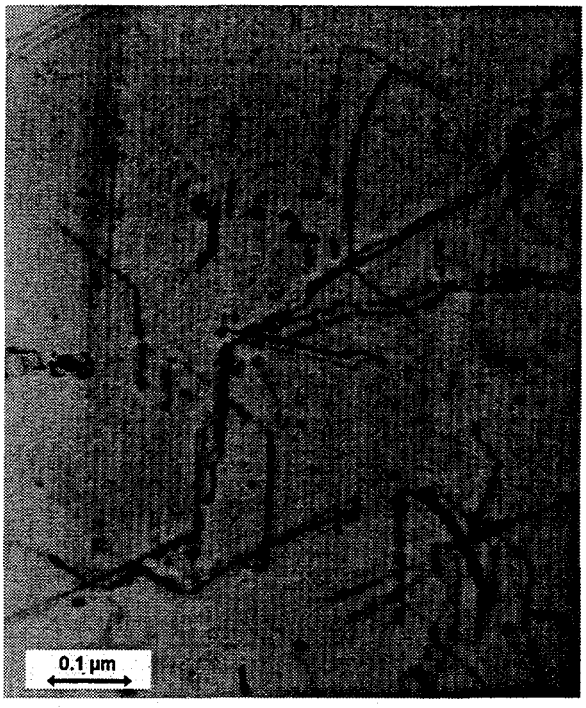

Figure 6. Higher magnification of Fig. 5 showing presence of fine precipitates.

Figure 7. Higher magnification TEM micrograph of dislocation loops visible in Fig. 5.

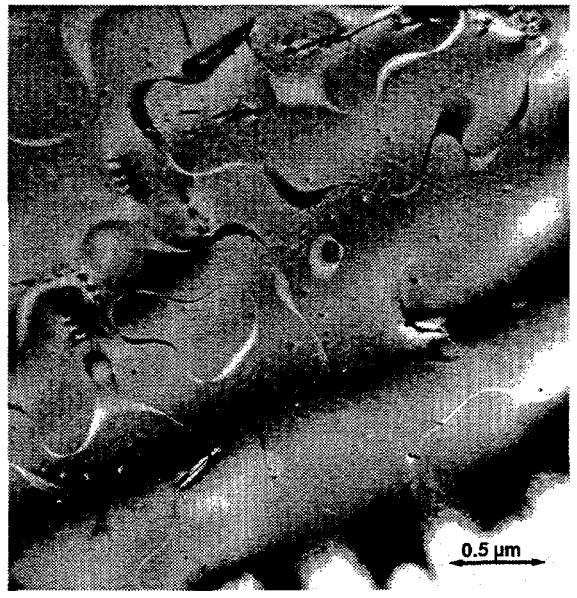

Figure 8. TEM micrograph of alloy FA-180 showing B2 domains and fine dislocation loops (black dots) produced by oil-quenching from a heat treatment at 1150°C.

SUMMARY AND CONCLUSIONS

In summary, earlier studies showed that the creep-rupture strength of Fe_3Al-based alloy FA-180 (Fe-28Al-5Cr-0.5Nb-0.8Mo-0.025Zr-0.05C-0.005B, at.%) was improved significantly by heat treating for 1 h at 1150°C. This strengthening was attributed to the dissolution at 1150°C of coarse particles left over from the melting and casting process and reprecipitation during cooling or during testing at 593°C of fine Zr-based matrix and grain boundary precipitates. In this study, creep-rupture tests were conducted on specimens of FA-180 that had been cooled quickly (oil or water quenched) from the 1150°C heat treatment. The results were compared to the previous data on specimens that were cooled more slowly in air. The more rapidly cooled specimens exhibited the best resistance to creep. This additional strengthening was attributed to the formation of dislocation loops as a result of the rapid quench. These loops pinned dislocations and grew slowly during testing at temperatures of 593-700°C, resulting in a stabilized deformation microstructure.

ACKNOWLEDGEMENTS

Part of this research was sponsored by the U.S. Department of Energy, Assistant Secretary for Energy Efficiency and Renewable Energy, Office for Industrial Technologies, Advanced Industrial Materials Program, under contract DE-AC05-96OR22464 with Lockheed Martin Energy Research Corp.

REFERENCES

1. C. G. McKamey, P. J. Maziasz, and J. W. Jones, *J. Mater. Res.*, **7(8)** (1992), 2089-2106.
2. C. G. McKamey, J. H. DeVan, P. F. Tortorelli, and V. K. Sikka, *J. Mater. Res.*, **6(8)** (1991), pp. 1779-1805.
3. C. T. Liu, C. G. McKamey, and E. H. Lee, *Scripta Metall. Mater.*, **24(2)** (1990), 385-90.
4. C. T. Liu and C. G. McKamey, *High Temperature Aluminides and Intermetallics*, ed. S. H. Whang, C. T. Liu, D. P. Pope, and J. 0. Stiegler, (TMS, Warrendale, PA, 1990), pp. 133-151.
5. C. G. McKamey and C. T. Liu, *Proceedings of ADVMAT/91, First International Symposium on Environmental Effects on Advanced Materials*, edited by R. D. Kane, (Houston, TX: NACE, 1992), paper no. 17-1.

6. P. F. Tortorelli and J. H. DeVan, *Mat. Sci. & Eng.*, **A153** (1992), 573-77.
7. V. K. Sikka, *SAMPE Quart.*, **22(4)** (1991), 2-10.
8. V. K. Sikka, S. Viswanathan, and C. G. McKamey, *Structural Intermetallics*, eds. R. Darolia, J. J. Lewandowski, C. T. Liu, P. L. Martin, D. B. Miracle, and M. V. Nathal, (Warrendale, PA: The Metallurgical Society, 1993), 483-91.
9. P. J. Maziasz and C. G. McKamey, *Mater. Sci. & Eng.*, **A152** (1992), 322-34.
10. D. M. Dimiduk, M. G. Mendiratta, D. Banerjee, and H. A. Lipsitt, *Acta Metall.*, **36** (1988), 2947-58.
11. P. J. Maziasz, C. G. McKamey, and C. R. Hubbard, *Alloy Phase Stability and Design*, eds. G. M. Stocks, D. P. Pope, and A. F. Giamei (MRS, Pittsburgh, PA, 1990), pp. 349-55.
12. C. G. McKamey, P. J. Maziasz, G. M. Goodwin, and T. Zacharia, *Mat. Sci. & Eng.*, **A174** (1994), 59-70.
13. D. G. Morris, M. Nazmy, and C. Noseda, *Scripta Metall. Mater.* **31**, 173 (1994).
14. C. G. McKamey and P. J. Maziasz, in *Processing, Properties, and Applications of Iron Aluminides*, edited by J. H. Schneibel and M. A. Crimp (TMS, Warrendale, PA, 1994), pp. 147-58.
15. C. G. McKamey, Y. Marrero-Santos, and P. J. Maziasz, in *High Temperature Ordered Intermetallic Alloys VI*, edited by J. A. Horton, I. Baker, S. Hanada, R. D. Noebe, and D. S. Schwartz (MRS, Pittsburgh, 1995), pp. 249-254.
16. O. D. Sherby and P. M. Burke, *Prog. Mater. Sci.* **13**, 325 (1968).
17. R. Lagneborg and B. Bergman, *Met. Sci. J.* **10**, 20 (1976).
18. K. Sadananda, H. Jones, C. R. Feng, and A. K. Vasudevan, in *High Temperature Ordered Intermetallic Alloys IV*, edited by L. A. Johnson, D. P. Pope, and J. O. Stiegler (MRS, Pittsburgh, 1991), pp. 1019-25.
19. I. Jung, M. Rudy, and G. Sauthoff, *High Temperature Ordered Intermetallic Alloys II*, edited by N. S. Stoloff, C. C. Koch, C. T. Liu, and O. Izumi (MRS, Pittsburgh, 1987), pp. 263-74.
20. P. Nagpal and I. Baker, *Metall. Trans.* **21A**, 2281 (1990).
21. A. Ball and R. E. Smallman, *Acta Metall.* **16**, 233 (1968).

2.13 LOW-ALUMINUM-CONTENT IRON-ALUMINUM ALLOYS
2.14 COMMERCIAL-SCALE MELTING AND PROCESSING OF FAPY ALLOY

V. K. Sikka and C. R. Howell

and

F. Hall and J. Valykeo*

INTRODUCTION

The FAPY is a Fe-16 at. % Al alloy of nominal composition given in Table 1. The aluminum content of the alloy is such that it remains single phase (α) without the formation of an ordered phase (DO_3). The alloy has good oxidation resistance at temperatures up to 1000°C and has shown significantly superior performance as heating elements as compared to the commonly used nickel-based alloy, Nichrome. Although wire for the heating elements has been fabricated from small (15-lb) laboratory heats, for its commercial applications, the wire needs to be producible from large (1200 to 1500-lb) air-melted heats. The purpose of this study was to produce commercial size heats and investigate their mechanical properties and microstructure in the as-cast, hot-worked, and cold-worked conditions. The results of this study are expected to provide: (1) insight into processing steps for large heats into wire under commercial conditions, and (2) the mechanical properties data on commercial size heats in various product forms.

ALLOY PREPARATION AND PROCESSING

A total of three commercial size heats were used in this study. Two heats of 1200 lb each were melted at Hoskins Manufacturing Company (Hamburg, Michigan) and cast into standard 8-in. tapered ingots. The third heat was air-induction melted at United Defense (Anniston, Alabama). This heat was primarily cast into various sand molds but was also cast into two ingot molds provided by Hoskins. One ingot each from the heats melted at Hoskins and United Defense were received at the Oak Ridge National Laboratory (ORNL) for processing, property, and microstructural evaluation. The chemical analysis of each heat is included in Table 1.

A 5-in.-long section of each ingot was cut from the ingot bottom. The macrostructure of the cut sections of each ingot is shown in Fig. 1. The ingots cast at Hoskins were sound but showed a slightly different microstructure. The ingots cast at United Defense showed a crack in the cross section.

A 2-in.-thick slice was cut form the middle section of each of the 5-in.-long ingot sections. The remaining part of the ingot section was used for machining specimens in the as-cast condition. The 2-in.-thick slice was hot forged 50% at 1150°C. The 1-in.-thick forged plate was hot rolled at 1000°C to

---

*Hoskins Manufacturing Company, Hamburg, Michigan.

Table 1. Comparison of chemical analysis of two FAPY alloy heats made at Hoskins Manufacturing Company and one heat made at United Defense with the target composition

Element	Target	Weight percent		
		Hoskins Manufacturing Company		United Defense Heat 899-40299
		Heat 899-21689	Heat 899-21690	
Al	8.46	8.69	8.45	9.19
Cr	5.50	5.46	5.49	5.31
Zr	0.20	0.20	0.21	0.21
C	0.03	0.054	0.044	0.022
Mo	2.00	2.06	2.10	2.03
Y	0.10	0.13[a]	0.16[a]	0.04[a]
Mn	--	0.34	0.34	0.19
S	--	0.006	0.007	0.011
Cb	--	0.012	0.01	<0.01
B	--	<0.001	<0.001	*b*
N_2	--	0.003	0.002	0.003
O_2	--	0.003	0.003	0.002
Fe	*c*	*c*	*c*	*c*

[a]Estimated.
[b]Not analyzed.
[c]Balance.

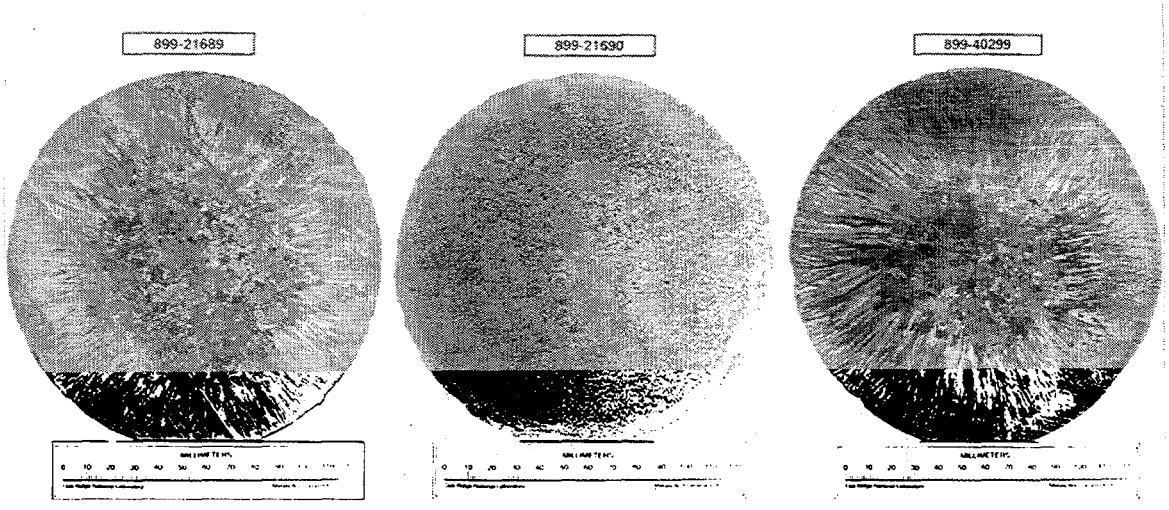

Figure 1. Macrostructure of sections cut from three ingots of FAPY alloy.

0.5-in.-thick plate. This plate was used for machining longitudinal specimens for properties in the hot-rolled condition. A part of the 0.5-in.-thick plate was hot rolled at 1000°C to 0.10-in.-thick sheet. This sheet was rolled to 0.05 in. thickness at 600°C, subsequently annealed for 1 h at 800°C, and cold rolled to 0.030 in. thickness. The cold-rolled sheet was used to punch specimens for testing in the wrought condition.

A square bar of 2- by 2-in. cross section hot rolled from an ingot at Hoskins was also included for testing.

Test bars machined from ingots, hot-rolled plate, hot-rolled bar, and punched from the sheet were all given a 1-h anneal at 800°C in air followed by air cooling prior to testing. In only one case, the sheet specimens were tested in the as-rolled condition, which contained 40% cold work from the rolling process.

TENSILE TESTING AND PROPERTIES

Tensile tests were carried out in air at temperatures varying from room temperature to 800°C. The strain rate for bar specimens was $2.66 \times 10^{-3} s^{-1}$ and $3.33 \times 10^{-3} s^{-1}$ for sheet specimens. Heat numbers of the two ingots tested from Hoskins heats were 899-21689 and 899-21690, respectively. The 0.2% yield strength, ultimate tensile strength, total elongation, and reduction of area for each heat are plotted as a function of test temperature in Figs. 2 and 3. The following observations are made from these figures:

1. The 0.2% yield strength of the as-cast ingot is the lowest from room temperature to 600°C and the highest for the sheet with the hot-rolled plate falling between the two. The cast/forged (bar rolled) bar from Hoskins showed essentially the same yield strength as the sheet. The yield strength of the as-rolled sheet is significantly higher than the annealed sheet up to 400°C. At 600°C, the difference in yield strength between the cold-worked and annealed conditions is significantly reduced.
2. The ultimate tensile strength showed the clear distinction between the cast, hot-rolled, and cold-rolled sheet. At room temperature, ultimate tensile strength of the cast ingot was the lowest followed by the hot-rolled material and sheet. The cast/forged (bar-rolled) bar was lower in ultimate strength than the sheet. The as-rolled sheet showed substantially higher strength than the annealed sheet. Except for the cast ingot, data for other products were well behaved for the entire test temperature range. The cast ingot data showed an unusual trend with temperature in the range from room temperature to < 200°C, where the cast ingot was tested in the brittle range (see the ductility data in Fig. 2(*c-d*).
3. The total elongation plots show that the cast ingot has the least ductility at room temperature, which remains very low up to 150°C. It only increases to a reasonable level of 10% at 200°C. For the hot-rolled plate at ORNL, ductility was very low at room temperature but increased to 10% at 100°C, and matched the sheet ductility at 200°C. The cast/forged (bar rolled) bar processed at Hoskins showed low ductility at room temperature, but it reached 20% at 100°C, which is nearly double the value for the plate hot rolled at ORNL. The annealed sheet showed approximately 20% value at room

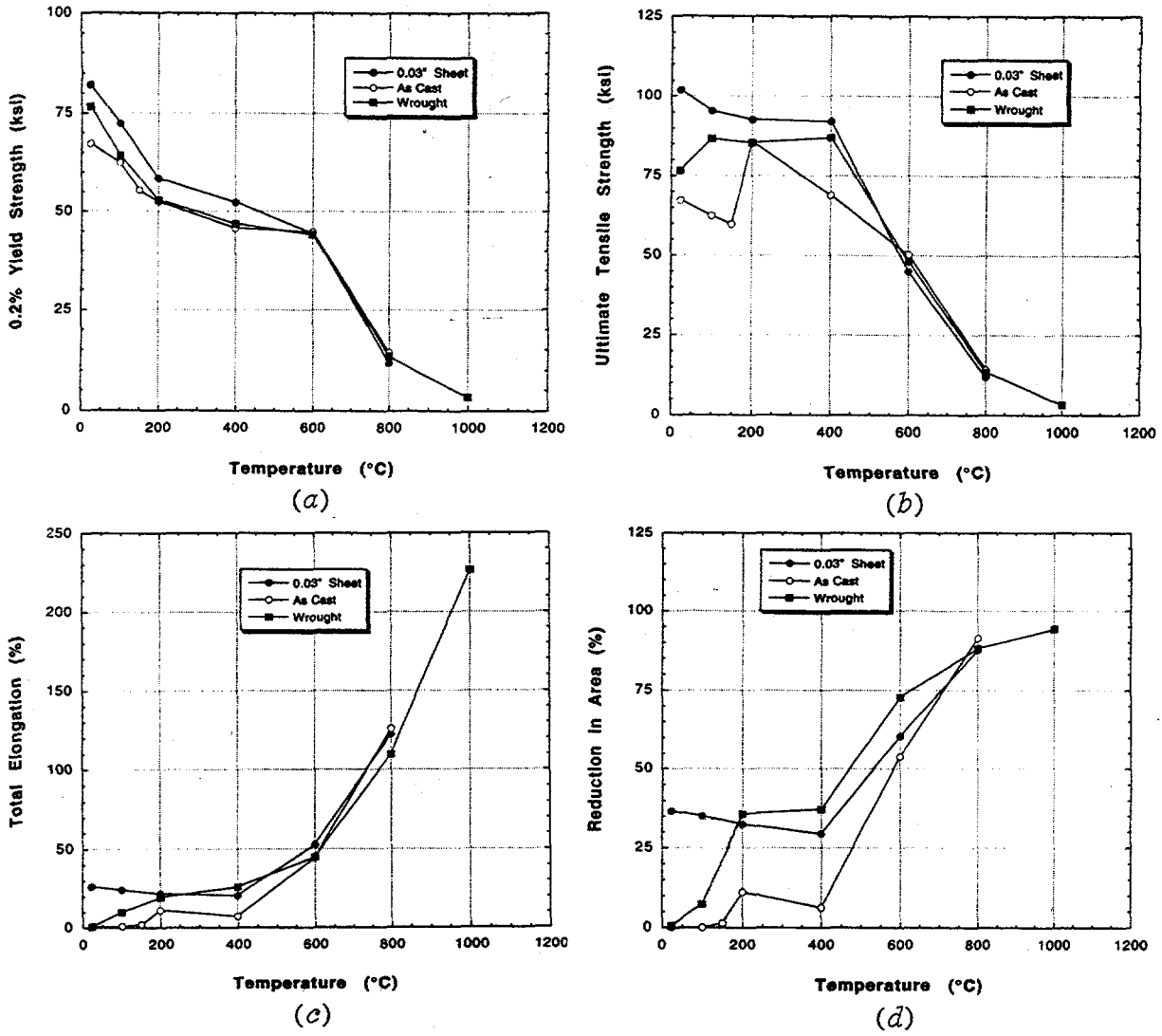

Figure 2. Plots of tensile properties as a function of test temperature for FAPY heat 899-21690: (*a*) 0.2% yield strength, (*b*) ultimate tensile strength, (*c*) total elongation, and (*d*) reduction of area.

temperature, with no trends of brittle- (ductility of 51%) to-ductile (ductility of ≥ 10%) transition. The as-rolled sheet with 40% cold work showed values of 2% up to 600°C, where most of the cold work appears to have recovered. It should be noted that the reduction in ductility of the as-rolled sheet is a consequence of cold work (ductility exhaustion) and is different than the brittle-to-ductile trend observed for the cast and hot-worked conditions. At 800°C, the FAPY alloy is very ductile in cast, hot-worked, and cold-rolled sheet. At 1000°C, the sheet approached the ductility values in the superplastic range (≥ 200%).

4. The reduction of area plots in Figs. 2 and 3(*d*) show trends very similar to those described above for total elongation with the exception that the brittle-to-ductile trends are clearer in these plots.

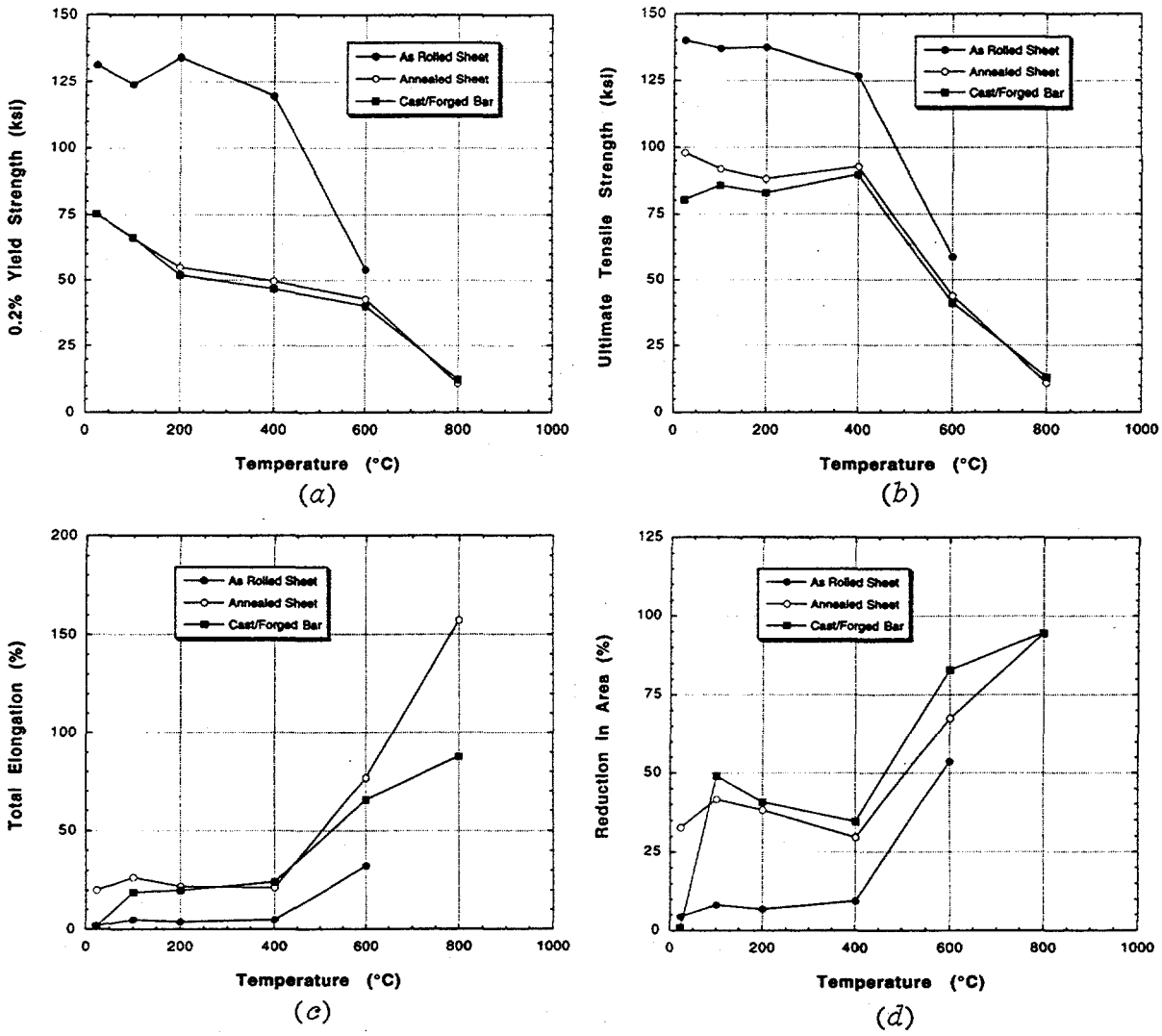

Figure 3. Plots of tensile properties as a function of test temperature for FAPY heat 899-21689: (*a*) 0.2% yield strength, (*b*) ultimate tensile strength, (*c*) total elongation, and (*d*) reduction of area.

MICROSTRUCTURE

Optical microstructures of as-cast, cast and hot-rolled, and cold-rolled sheet are compared for heat 899-21690 of FAPY in Figs. 4 and 5. The microstructures in Fig. 5 are at low magnification, and those in Fig. 5 are at high magnification. These photomicrographs show that processing improves the grain size. The grain size of the cast ingot of 305 μm improved to 254 μm by hot forging and hot rolling to 0.5-in.-thick plate. However, the hot rolling to 0.10 in. thickness followed by cold rolling 40% to 0.030 in. thickness reduced the grain size to 13 μm (23 times finer than that of the cast ingot). The as-cast microstructure in the photomicrographs also showed decoration of grain boundaries with precipitates and some particles in the matrix, and that hot forging and hot rolling removed most of the precipitates from the grain boundaries, with some precipitates still present in the matrix.

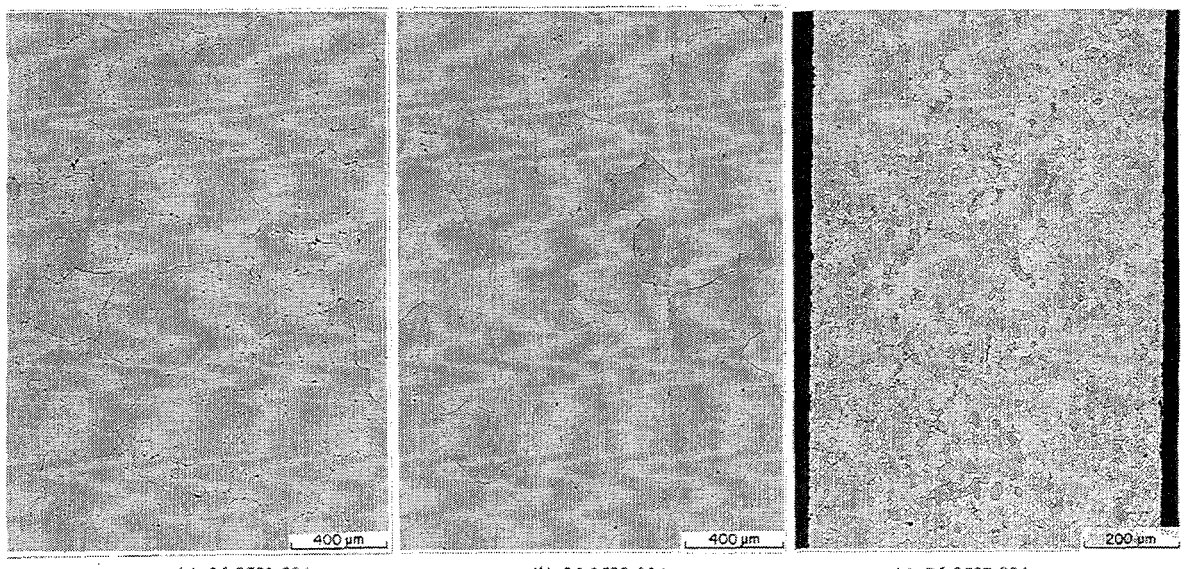

(*a*) 96-0509-004 (*b*) 96-0508-004 (*c*) 96-0507-004

Figure 4. Comparison of low-magnification optical micrographs of: (*a*) as-cast, (*b*) cast and hot-worked, and (*c*) cold-rolled FAPY samples of heat 899-21690. The grain size in three conditions are 305, 254, and 13 µm, respectively.

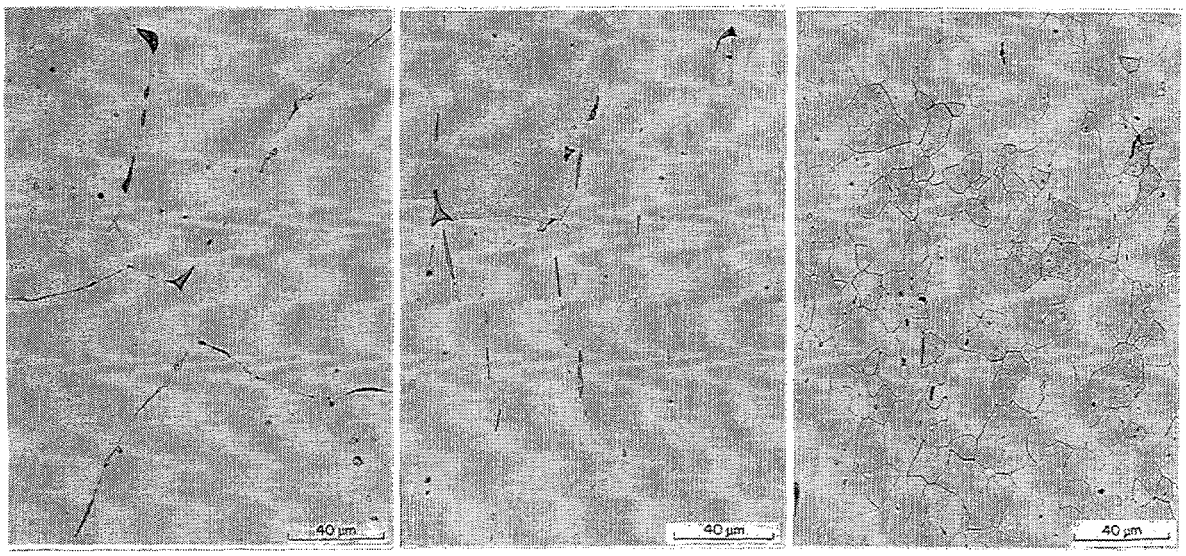

(*a*) 96-0509-006 (*b*) 96-0508-006 (*c*) 96-0507-006

Figure 5. Comparison of high-magnification optical micrographs of: (*a*) as-cast, (*b*) cast and hot-worked, and (*c*) cold-rolled FAPY samples of heat 899-21690.

Scanning electron microscope (SEM) analysis was carried out to determine the composition of precipitates. The backscattered electron images for the cast, hot-worked, and cold-rolled sheet are compared in Fig. 6. Two types of inclusions {bright [higher atomic number (Z)] and gray in color [intermediate atomic number (Z)]} were observed. A detailed compositional analysis at ten locations in the matrix and the particles are shown in Table 2. Based on this analysis, the bright particles are primarily ZrC with a very small amount of Fe and Y. The darker particles are highly enriched with Y and contain substantial amounts of Fe, Al, Cr, and C. The atomic percentages of various elements suggest that the Y containing particles may be $(FeCrC)_3(AlY)$. The backscattered electron images in Fig. 6 show that the ZrC- and Y-containing particle size becomes smaller with hot and cold processing, but their total amount by area remains nearly the same.

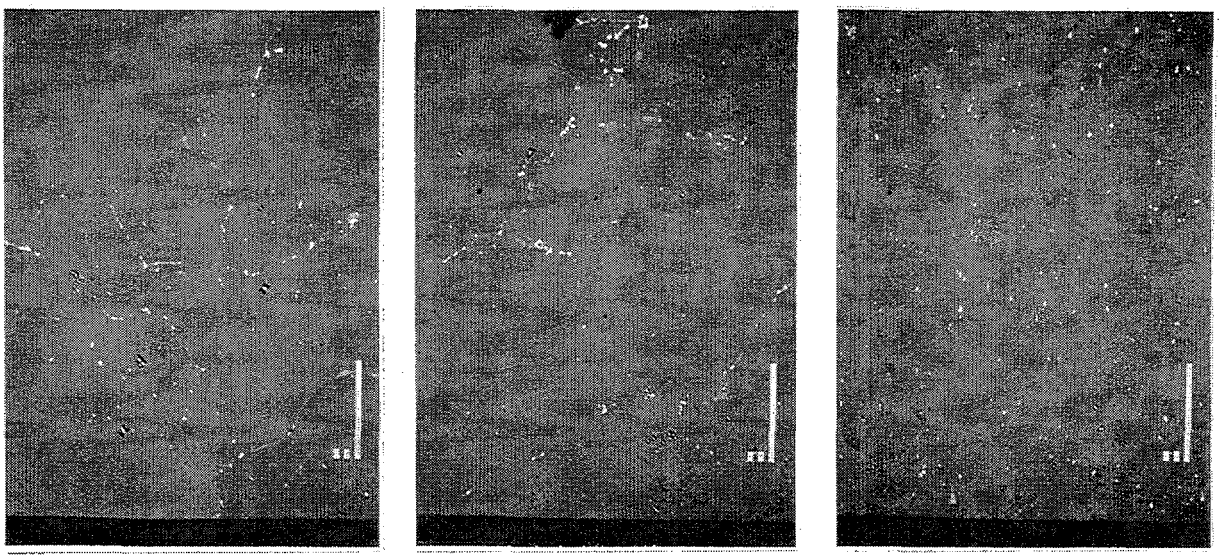

(*a*) 96-0509 (*b*) 96-0508 (*c*) 96-0507

Figure 6. Backscattered electron images of FAPY alloy in: (*a*) as-cast, (*b*) cast and hot-worked, and (*c*) cold-rolled condition.

The fracture surface analysis by SEM (Figs. 7 through 9) of specimens tested at room temperature yielded the following observations:

1. As cast: a mixed mode fracture consisting of intergranular separation with some cleavage occurring at the grain faces.
2. Cast and hot worked: a mixed mode fracture consisting of intergranular separation with possibly more cleavage than the as-cast specimen.
3. Cold-rolled sheet: a mixed mode fracture consisting of brittle regions (cleavage) on either end and a ductile region in the mid section.

Table 2. Chemical analysis of matrix and precipitates in the as-cast sample of FAPY heat 899-21689[a]

Fe	Al	Cr	Mo	Zr	Y	C	Total
			Matrix				
75.8[b]	15.0	5.5	1.1	0.0	0.0	2.6	
84.6[c]	8.1	5.7	2.0	0.0	0.0	0.6	101.1
0.5[d]	0.1	0.1	0.1	--	--	0.2	
			High Z Precipitates				
3.8	0.3	0.4	0.4	42.5	0.4	52.1	
4.6	0.2	0.4	0.8	83.6	0.9	13.5	104.1
2.7	0.2	0.2	0.2	3.6	0.7	0.2	
			Intermediate Z Precipitates				
59.4	16.5	3.7	0.8	0.1	9.0	10.5	
67.9	9.1	4.0	1.5	0.2	16.3	2.6	101.6
0.4	0.1	0.2	0.1	0.1	0.2	0.1	

[a]The same precipitates were observed in the hot- and cold-worked specimens.
[b]Mean composition in normalized atomic percent.
[c]Mean composition in weight percent.
[d]SD = one standard deviation based on ten analyses and expressed in weight percent.

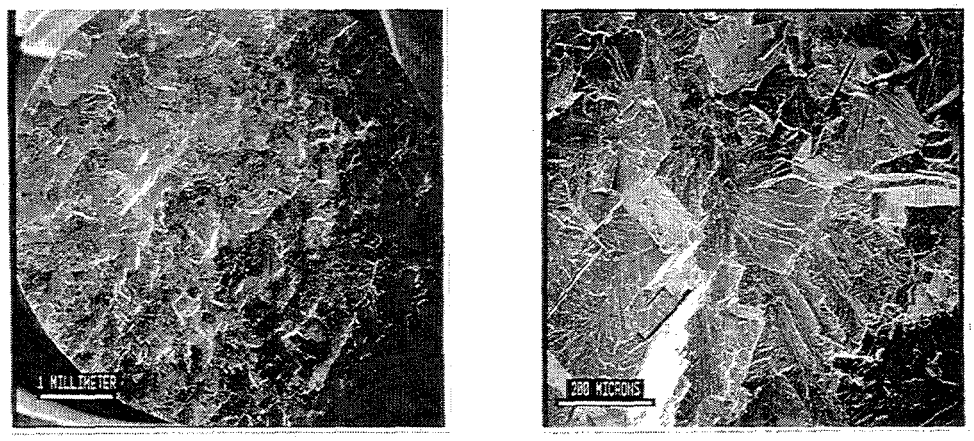

(*a*) 527 (*b*) 526

Figure 7. Fracture surface of FAPY heat specimen 899-21690 in as-cast and hot-worked conditions tested at room temperature: (*a*) low and (*b*) high magnifications.

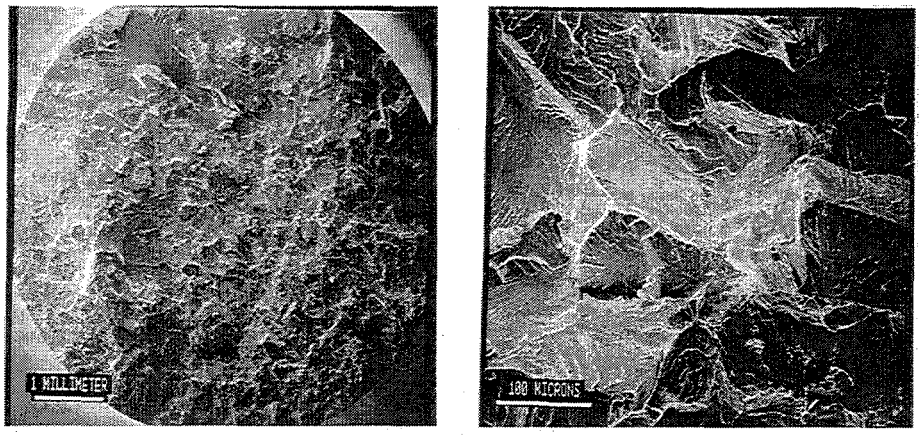

(*a*) 522 (*b*) 520

Figure 8. Fracture surface of FAPY heat specimen 899-21690 in as-cast and hot-worked conditions tested at room temperature: (*a*) low and (*b*) high magnifications.

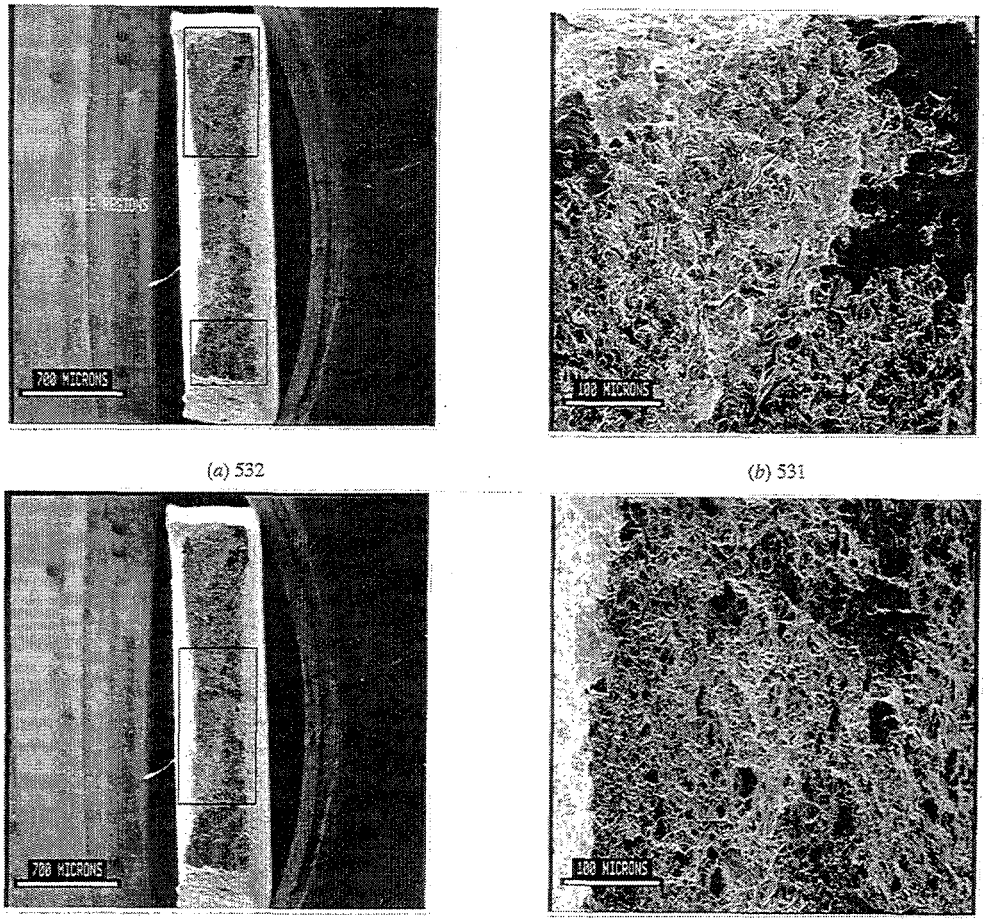

(*a*) 532 (*b*) 531

(*c*) 534 (*d*) 537

Figure 9. Fracture surface of FAPY heat specimen 899-21690 in as-cold-worked condition tested at room temperature: (*a*) and (*b*) end location, and (*c*) and (*d*) mid-section location.

The energy-dispersive X-ray spectra of the fracture surfaces showed little difference in composition of the three specimens.

SUMMARY AND CONCLUSIONS

Two commercial size heats of the FAPY alloy were melted at Hoskins and one at United Defense. One ingot from each of the heats was received at ORNL for processing, properties, and microstructural characterization. A 5-in.-long section was cut from each of the ingots. A 2-in.-thick slab section was cut from each of the 5-in.-long ingot sections for processing response. The remaining ingot section was used to machine specimens in the as-cast condition. The slab was forged and rolled to obtain plate in the cast and hot-worked conditions. Part of the hot-rolled plate was cold rolled into 0.030-in.-thick sheet to obtain the fine-grained wrought microstructure. Tensile tests were conducted from room temperature to 800°C on material in three different conditions. Tests were also conducted on a cast and hot-rolled bar processed at Hoskins. All of the materials were tested after annealing at 800°C for 1 h. One sheet was also tested in 40% cold-worked condition. The as-cast, cast and hot-worked, and cold-rolled material was characterized by optical and SEM. The following conclusions are possible from this work:

1. The fine-grained sheet showed 20% elongation at room temperature. For cast and hot-worked conditions, the 20% elongation reached at 100°C. For the cast condition, it reached a value of only 10% at 200°C.
2. While the cast and cast and hot-worked condition showed transition from brittle-to-ductile transition in tensile ductility, the cold-worked material only showed a reduction in ductility.
3. The cast grain size of 305 μm was refined to only 254 μm by hot working. However, the cold working refined the microstructure to 13 μm.
4. All three conditions showed the presence of ZrC and FeCrAlY precipitates. Both precipitates were primarily at the grain boundaries in the as-cast condition. Processing by hot and cold working moved the precipitates from the grain boundaries and refined their size. However, the total area fraction of the precipitates remained the same in all three conditions.
5. Based on the ductility data, the fine-grained material can be cold worked while the hot-worked material can be worked by warming up the work piece at ≥ 100°C.

ACKNOWLEDGMENTS

The authors thank D. C. Harper and K. S. Blakely for cutting and processing the ingots, H. F. Longmire for optical metallography, L. R. Walker for SEM work, C. A. Blue and D. J. Alexander for paper review, K. Spence for editing, and M. L. Atchley for preparing the manuscript.

Research sponsored by the U.S. Department of Energy, Office of Fossil Energy, Advanced Research and Technology Development Materials Program, [DOE/FE AA 15 10 10 0, Work Breakdown Structure Element ORNL-2(H)], under contract DE-AC05-96OR22464 with Lockheed Martin Energy Research Corp.

2.15 DEVELOPMENT OF IMPROVED AND CORROSION-RESISTANT SURFACES FOR FOSSIL POWER SYSTEM COMPONENTS

V. K. Sikka, M. L. Santella, and G. M. Goodwin

INTRODUCTION

The purpose of this task is to develop the corrosion-resistant surfaces on a variety of fossil power system components. The Fe-Al alloys ranging in aluminum from 16 to 36 at. % are of interest. The surfaces of Fe-Al alloys can be produced by weld overlay. However, because of their limited room-temperature ductility, the production of weld wire for these compositions is not commercially feasible. The alloying element dilution during weld overlay also makes depositing exact surface composition rather difficult.

DISCUSSION OF CURRENT ACTIVITIES

An innovative method for depositing aluminum of the desired concentration on steels and nickel-based alloys has been under development for the last six months. The proof of concept for the newly developed process has already been demonstrated. Other details are currently being worked out. As details are developed, the process will be used to deposit coatings of various aluminum levels on tubes of different compositions and other components. More details of this new process will be described when patent issues are cleared.

2.16 HIGH-TEMPERATURE CORROSION BEHAVIOR OF COATINGS AND ODS ALLOYS BASED ON Fe_3Al

P. F. Tortorelli, B. A. Pint, and I. G. Wright

INTRODUCTION

Iron aluminides containing greater than about 20-25 at.% Al have oxidation/sulfidation resistance at temperatures well above those at which these alloys have adequate mechanical strength.[1] In addition to alloying modifications for improved creep resistance of wrought material, this strength limitation is being addressed by development of oxide-dispersion-strengthened (ODS) iron aluminides[2] and by evaluation of Fe_3Al alloy compositions as coatings or claddings on higher-strength, less corrosion-resistant materials.[3,4] As part of these efforts, the high-temperature corrosion behavior of iron-aluminide weld overlays and ODS alloys is being characterized and compared to previous results for ingot-processed material.

OXIDATION-SULFIDATION OF IRON-ALUMINIDE WELD OVERLAYS AT 800°C

This section contains corrosion data on deposits produced by the GTA process and initial observations of the oxidation/sulfidation behavior of a weld overlay synthesized by gas metal arc (GMA) welding. The development efforts associated with the GTA and GMA processes used to produce the weld overlays are described elsewhere.[3,5]

Rectangular specimens, approximately 18-25 mm x 12 mm, were cut from the weld overlay pads. As in previous oxidation-sulfidation studies,[6,7] coupons were then prepared by grinding away the substrate material so that only weld metal (approximately 1-2 mm thick) remained. Corrosion behavior was characterized by use of a continuous-recording microbalance to measure the weight of these specimens during exposure at 800°C to a flowing (~2 cm^3/s) mixed gas consisting of 5.4% H_2S-79.4% H_2-1.6% H_2O-13.6% Ar (by volume). The oxygen partial pressure, as determined by a solid-state oxygen cell, was 10^{-22} atm, and the sulfur pressure was calculated to be 10^{-6} atm. These types of exposures have been used to characterize the sulfidation resistance of iron aluminides and several other alloys.[6-9] In most cases, a specimen was held in the mixed-gas microbalance system at 800°C for a fixed amount of time, cooled to room temperature, and then removed from the system for subsequent examination. However, two specimens underwent thermal cycling, in which they experienced more than one hold period at the exposure temperature with intermediate cooling, in the same gas, to below 100°C.

The use of welding to produce iron-aluminide coatings results in a loss of selected elements by vaporization and significant mixing of the filler metal and substrate alloys (dilution) during deposition. The final concentrations of the various elements in the weld deposit will depend on the particular filler metal/substrate combination and, therefore, the actual concentrations of the critical elements were determined using samples taken from the same welded plate as used to make the respective corrosion coupons (Table 1). Because there is essentially no aluminum in the substrates, the concentration of this element in the overlay will be significantly less than that of the weld rod/wire used to produce it. The extent of this dilution in aluminum depends on vaporization losses during welding and the relative amount of substrate material melted and thus is affected by parameters such as current, voltage, polarity, travel speed, etc. Similar dilution/enrichment considerations apply to the other elements. The composition of the weld overlays shown in Table I are consistent with the general dilution/enrichment factors found previously.[3,5-7]

Figure 1 shows the isothermal gravimetric results for corrosion specimens cut from the weld deposits listed in Table 1 and exposed to the H_2S-H_2-H_2O-Ar environment for 70-120 h at 800°C. While all the specimens showed relatively low-to-moderate weight gains, there were distinct differences in their gravimetric behavior. These differences were also apparent visually. The surfaces of the specimen which exhibited the greatest sulfidation rate (H1) were almost completely covered with a dark corrosion product, while those of the H2 coupon showed a thin gray scale. The specimen cut from the S1 weld deposit exhibited a weight gain intermediate between H1 and H2 and developed a gray scale over most of its surface area with only some dark corrosion products along one edge. Some spallation of the scales formed on the H1 and S1 specimens occurred during cooling from the exposure temperature. Despite the differences in gravimetric behavior among the various weld overlays, each deposit composition showed substantially better isothermal oxidation/sulfidation resistance than that of conventional Fe-Cr-Ni and Fe-Cr-Al alloys.[8]

Table 1. Weld Deposit Compositions

Weld Deposit	Process	Sub-strate	Concentration (at.%)[a]							
			Al	Cr	Nb	Si	Ni	Mo	Zr	C
H1	GTA	304L	30.4	9.0	0.1	0.3	2.5	0.1	0.2	0.08
H2	GTA	Cr-Mo	37.3	6.2	<0.01	0.1	0.2	0.3	0.1	0.1
S1	GMA	Cr-Mo	21.3	6.0	<0.01	0.1	0.1	0.4	0.2	0.1

[a] Determined by spark source mass spectrometry. Balance is Fe.

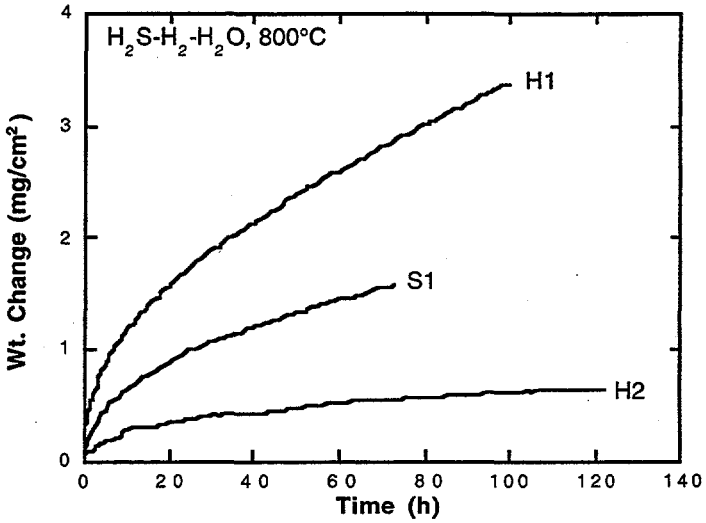

Fig. 1. Weight change versus time for specimens cut from iron-aluminide weld overlays and isothermally exposed to H_2S-H_2-H_2O-Ar at 800°C. The compositions of the weld overlays are shown in Table I.

Two more specimens of the S1 weld deposit were individually exposed in the microbalance system and held isothermally at 800°C in the mixed gas for about 72-74 h, after which they were allowed to cool to below 100°C. As shown in Fig. 2, the measured weight gains of S1-2 and S1-3 over this time period matched those measured for the first S1 coupon (S1-1). After its temperature fell to about 35°C, S1-2 was reheated to 800°C for several more hours, then cooled and removed from the system. In the case of S1-3, the coupon was cycled to below 100°C and back to the exposure temperature twice. For both of these specimens, significant increases in the rate of weight gain relative to the previous isothermal exposure periods were observed. Spallation occurred during the cooling cycles, but the data in Fig. 2 represent cumulative weight gains during the isothermal exposures and do not reflect any of this mass loss. At the end of the cyclic exposures, the specimen surfaces were covered with loosely adherent flakes of a dark corrosion product. Scanning electron microscopy (SEM) revealed a variety of product morphologies (Fig. 3); the platelets and needles resembled what has previously been identified as chromium and iron sulfides.[8,9] Subsequently, the loose scale was removed from the surfaces of the specimens. In both

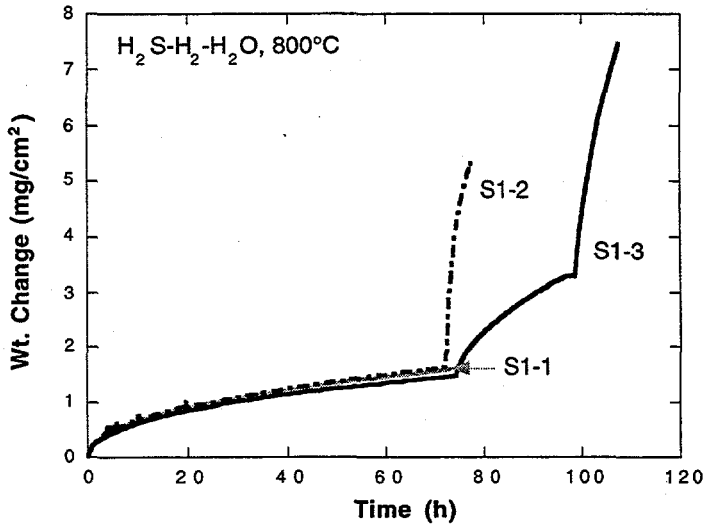

Fig. 2. Cumulative weight gain versus time for three individual specimens cut from weld-overlay S1 and then exposed to H_2S-H_2-H_2O-Ar at 800°C. The breaks in the curves represent reheating to exposure temperature after cooling to below 100°C. S1-1 was not re-exposed.

cases, it was combined with the material which had spalled during cooling or came off during handling to produce a powder that was analyzed by x-ray diffraction (XRD) and energy dispersive x-ray fluorescence (EDX). The corrosion products from S1-3 were a mixture of aluminum, iron, and chromium sulfides with a small amount (<1%) of oxide. Based on the most likely forms of these sulfides as determined by XRD, it appeared that the dominant ones were those incorporating aluminum (Al_2S_3) or iron (Fe_7S_8), with each composing about 45 - 48% of the total analyzed sample. For S1-2, Al_2O_3 was present in the scale in a greater concentration in addition to iron, chromium, and chromium-iron sulfides. Little Al_2S_3 was detected. (It was not possible to determine the relative abundance of the various sulfides formed on S1-2 by EDX.)

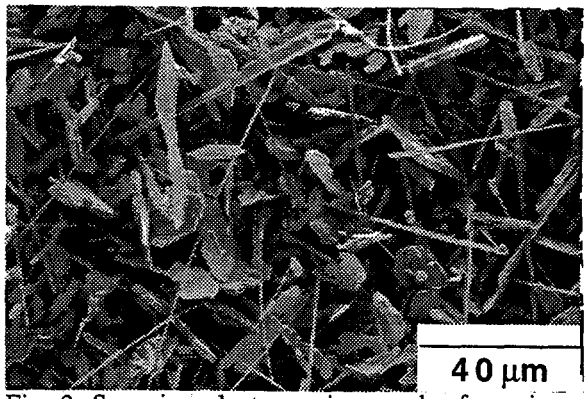

Fig. 3. Scanning electron micrograph of specimen S1-3 after three isothermal exposure periods in H_2S-H_2-H_2O-Ar at 800°C.

The excellent high-temperature corrosion resistance of bulk iron aluminides can be related to the rapid establishment and stability of a protective alumina scale and the absence or inhibited growth of iron and aluminum sulfides.[8] The inclusion of chromium in iron aluminides at levels greater than 2 - 3 at.% promotes more rapid reaction and increases weight gain due to the formation of chromium and iron sulfides.[8,9] On the other hand, little difference in isothermal gravimetric behavior has been observed for variations in Al concentration (22-28% Al).[9] The isothermal weight gain behavior of the S1 specimen exactly matched that of Fe_3Al-5% Cr. Furthermore, the gravimetric data for the S1 composition were reproducible; three separate specimens cut from this weld deposit exhibited nearly identical weight changes over the equivalent isothermal time period (compare the first 72 h of exposure of S1-1, -2, and-3 in Fig. 2). However, these data are at variance with previous results from weld overlays:[6] a coupon with the S1 composition (21% Al-6% Cr) would have been expected to have greater weight gains than those measured in the present study. Variations in minor alloying additions between the present and previous 21-23% Al weld overlays cannot explain the difference in gravimetric behavior; such elements were found to have minimal influence on overall oxidation/sulfidation resistance.[8] More likely, the discrepancy in results is probably due to higher than normal weight gains previously reported for weld overlays with lower aluminum levels[6] because of inadequate mixing during welding and/or rough initial surfaces that allowed localized regions to retain a composition like that of the substrate steel. In this sense, the GMA process, which involves a substantially higher energy input into the weld, may promote more

complete mixing of the deposit and therefore result in more reproducible and better corrosion resistance at high temperatures.

As shown in Fig. 1, the S1 specimen (21.3% Al, 6% Cr) showed somewhat better isothermal oxidation/sulfidation behavior than the alloy containing 30% Al and 9% Cr (H1). This can again be explained on the basis of what is known from studies of the corrosion of bulk iron aluminides in this mixed gas. These studies[8,9] have shown that, under isothermal conditions, variations in chromium concentration have a greater effect on the corrosion behavior of Fe-(20-30%) Al alloys than changes in the aluminum concentration. Therefore, the higher weight gains for H1 (9% Cr) vis-à-vis S1 (6% Cr) are not unexpected. The H1 specimen showed a higher density of the black corrosion products associated with chromium (and iron) sulfides consistent with its higher chromium concentration.

The low rate of corrosion for the 37% Al composition (H2) agrees very well with previous results from weld overlays of similar composition.[6] Compared to gravimetric data for bulk Fe-28% Al-2% Cr and Fe-40% Al-6% Cr,[8] H2 showed a higher initial weight gain, but only a slightly greater longer-term corrosion rate. However, the high aluminum concentration of this deposit led to substantial cracking of the coating. While chemically resistant to this environment, the flaws in this weld overlay would have allowed the corrosive species access to the more susceptible substrate.

As described above, previous results from surface analysis of products formed on bulk iron aluminides and weld overlays revealed that Al_2O_3 and, under certain conditions, Al_2S_3 are predominant corrosion products when there is a higher aluminum content in the alloy, but faster growing sulfides of iron and chromium can form at lower concentrations of this element (< 18-22% Al).[6,8,9] It is the ability to form aluminum-containing scales at the expense of the iron and chromium sulfides that controls the overall corrosion resistance of this class of alloys.[8] These considerations are important in understanding why the specimens of the S1 weld overlay composition (21% Al, 6% Cr) showed low oxidation/sulfidation rates under isothermal conditions, but suffered substantial degradation when subjected to thermal cycling (Figs. 2 and 3). Results from cyclic exposures of bulk iron aluminides (28% Al, ≤ 2% Cr) in this mixed-gas environment showed that, despite some spallation of the corrosion products, the subsequent corrosion rate of alloys upon re-exposure was about the same as that measured initially.[8,9] For these aluminides, Al_2O_3 was able to reform following cooling and re-exposure, but this does not appear to be the case for the S1 weld overlay, where more iron and chromium sulfides form at the expense of aluminum-containing products after a thermal cycle. The XRD and EDX data and SEM observations (Fig. 3) showed that, while Al_2O_3 appeared to be present initially, a substantial fraction of the corrosion products formed after two and three cycles (S1-2 and S1-3,

respectively) were iron, chromium, and chromium-iron sulfides. The presence of these products are associated with the steep increases in weight gain with time shown in Fig. 2. This difference in thermal cycling behavior can be attributed to the lower initial aluminum concentration of the S1 composition (21%) compared to the typical Fe_3Al alloys (28% Al). As mentioned above, the Al concentration of the S1 overlay is close to the critical concentration necessary for good sulfidation resistance of binary Fe-Al alloys.[9] Therefore, a relatively small decrease in its aluminum level will lead to more rapid corrosion associated with predominant growth of iron and chromium sulfides. Such aluminum depletion can occur by formation of aluminum-containing corrosion products followed by spallation during cooling. Upon further exposure, there is insufficient aluminum remaining in the surface regions to maintain the preferential development of the more slowly growing aluminum-containing products, and a higher rate of weight gain is observed, as in the present case. Indeed, the rates of accelerated weight gain observed after the initial exposures (S1-2 and -3, Fig. 2) are similar to those measured for alloys that form scales preferentially composed of transition-metal sulfides.[8]

The present results indicate that the aluminum concentration of the S1 weld overlay (21.3%) appears to be sufficient to maintain corrosion resistance in an aggressive oxidizing/sulfidizing environment under isothermal conditions, but that a greater amount of aluminum needs to be incorporated into the deposit to assure acceptable corrosion behavior of such coatings under thermal cycling conditions. Higher concentrations would not only delay any onset of accelerated reaction caused by aluminum depletion but would also improve the corrosion behavior of iron aluminide coatings containing substrate elements that are deleterious to sulfidation resistance (such as chromium and nickel).[6] However, as noted previously, weld deposits containing high aluminum concentrations are very sensitive to hydrogen-induced cracking which would allow corrosion of the substrate by ingress of reactive species. Therefore, the development of iron-aluminide coatings must involve an optimization of the composition and welding parameters such that good corrosion and cracking resistance are attained.

OXIDATION AND OXIDATION-SULFIDATION OF ODS Fe_3Al ALLOYS

Powders of gas-atomized FAS (Fe-28% Al-2% Cr) and various submicron oxides were mechanically blended in a flowing Ar atmosphere using a high-speed attritor and stainless steel balls.[2,10] The blended powder was canned, degassed, and extruded at 1100°C. For comparison, a FAS powder extrusion without an oxide addition (FASN), ingot-processed Fe-28% Al-5% Cr-0.1% Zr (FAL), and a commercial ZrO_2-dispersed (0.06% Zr) Fe-20% Cr-10% Al alloy (Kanthal alloy APM) were also tested. Cyclic oxidation experiments were conducted at

1200°C in air and in dry, flowing O_2 using procedures described in ref. 2. Oxide additions were made at a standard 0.2 cation % level in order to determine the relative effectiveness of the various additions.

Initial oxidation evaluation was accomplished by conducting 20 2-h cycles at 1200°C as a way to assess the performance of the different dopants. These weight change data are shown in Fig. 4. As a reference, Kanthal APM shows almost no spallation during this test with a weight change almost identical to that measured isothermally.[11] Oxide additions of Ce, La and Sc accelerated the oxidation rate and led to FeO formation in the case of the CeO_2 addition.[10] This detrimental influence has been observed for a number of oxide additions, such as CeO_2 in FeCrAl,[12] and is attributed to "over-doping". In order to test this explanation, smaller amounts of La_2O_3 (0.05%La) and CeO_2 (0.1%) were added to FAS. This approach reduced the negative effects, but did not eliminate them; during longer-term testing (10 x 100 h cycles, see Fig. 5), these alloys exhibited accelerated and breakaway oxidation.

The short-term cyclic oxidation behavior of FAS was similar regardless of whether the added dopant was an oxide of Y, Nd, Yb, Hf or Zr (Fig. 4). In each case, initial specimen weight gain was followed by monotonic decreases in weight signifying some spallation after each thermal cycle. As such, these results did not sufficiently differentiate the effects of the various dopants and longer-term cyclic exposures were required to examine the influence of different oxide additions on oxidation behavior. Data from these exposures showed that Y_2O_3-dispersed FAS performed better than any of the other iron-aluminide alloys (Fig. 5), including the ingot-processed alloy containing Zr (FAL), which has improved scale adhesion relative to other wrought iron aluminides.[13] Because there were only small differences in the parabolic rate constants of the various alloys,[14] the lower rate of weight gain of Y_2O_3-dispersed FAS reflected a reduced degree of scale spallation rather than an effect on scale growth kinetics. (More extensive cyclic oxidation data for Y_2O_3-dispersed FAS can be found in ref. 2.) The Hf, Nd, Yb and Zr

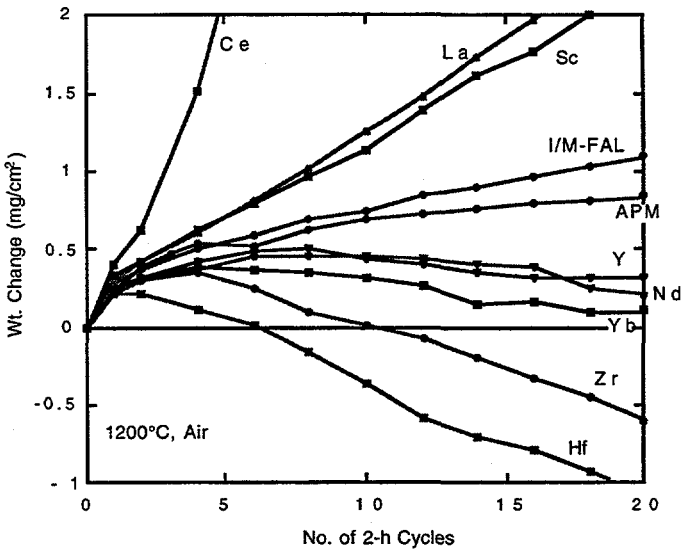

Fig. 4. Specimen weight change versus number of 2-h oxidation cycles for Fe - 28% Al - 2% Cr (FAS) with various cation oxide dispersions (0.2 at.%) in air at 1200°C.

additions did produce some beneficial effect compared to an Al_2O_3 dispersion (which is always present in the as-fabricated ODS FAS alloys); in long-term cyclic exposures, breakaway oxidation was observed for FAS doped only with Al_2O_3.[14]

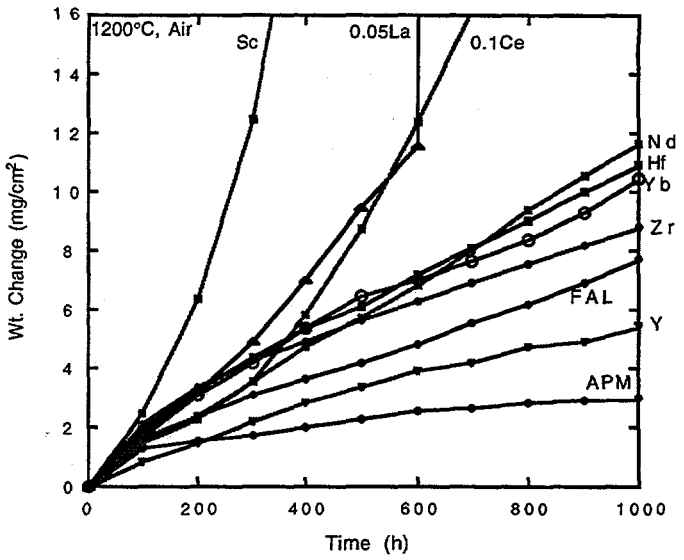

Fig. 5. Total weight change (specimen plus spalled scale) versus time for specimens cyclically oxidized in air at 1200°C (100-h cycles). Except where shown, all cation concentrations were 0.2%.

Although Y_2O_3 has a positive influence on the spallation resistance of FAS, the present results indicate that this dopant is not as effective in iron aluminides as when it is added to FeCrAl and β-NiAl.[14] Likewise, ZrO_2 in FAS did not replicate the effect of this dopant in APM (Fig. 5). There are several possible reasons for the variations in a dopant's effectiveness, including alloy substrate strength and its effect on scale buckling and void formation.[14] Additionally, while 0.2% Y appeared to be an optimum doping level,[14] this may not be true for the other additions. For example, assuming that the Kanthal APM alloy has an optimized ZrO_2 content of 0.06 at.% Zr, the 0.2% Zr addition used in this study may not have produced the best effect that could be achieved with Zr-doping. Lower (0.05%) dopant levels of Zr and Hf are currently being investigated.

As noted in the previous section, Fe_3Al alloys produced by conventional ingot metallurgy (I/M) procedures, and FAS in particular, have excellent sulfidation resistance in H_2S-containing environments.[8,9] Therefore, it is of interest to learn whether ODS iron aluminides show similar corrosion behavior. Preliminary data in this regard were obtained by exposing FASN and FAS-Y_2O_3 (0.2 cation %) to H_2S-79.4% H_2-1.6% H_2O-13.6% Ar using similar experiments as described above for the weld overlay specimens. The results are shown in Fig. 6, which also contains data for FAS, a Fe-28% Al-5% Cr-1% Nb-0.5% C iron aluminide, and a FeCrAl-type Fe- 18% Cr - 12% Al alloy produced by ingot processing (FAS-I/M, FA129-I/M, and Fe-18Cr-12Al-I/M, respectively). Note that the isothermal weight gains of the powder metallurgy-processed alloys were somewhat greater than the I/M FAS, but less than the Fe_3Al-5Cr alloy (FA129-I/M). Much of the difference in the weight gains was established in the early stages of exposure to the oxidizing/sulfidizing environment; at extended times the rates of weight gain

are quite similar for the ingot- and powder-processed FAS alloys. The reason for the more rapid initial weight gains of the P/M alloys is not yet known, but it doesn't seem to be related to increases in the chromium levels during the milling process; the chromium concentrations in FASN and FAS-Y_2O_3 after extrusion were just 2.0 and 2.4%, respectively.

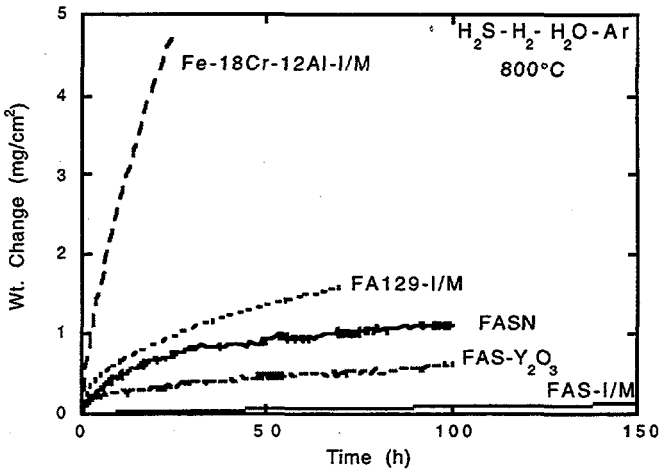

Fig. 6. Weight change versus time for specimens isothermally exposed to H_2S-H_2-H_2O-Ar at 800°C.

Rather, the fine grain size of these as-extruded alloys (about 1 μm) may allow a more rapid diffusion of chromium to the reaction front[15] and result in higher weight gains due to formation of chromium sulfides. As noted above, the presence of chromium in Fe_3Al in excess of about 2% leads to higher corrosion rates in this mixed-gas environment. Nevertheless, these preliminary results for ODS Fe_3Al alloys indicate good overall sulfidation resistance. The weight gains for these materials are significantly less than for a FeCrAl-type alloy (Fig. 6) and are dramatically better than those measured for a stainless steel.[8]

SUMMARY AND CONCLUSIONS

The high-temperature strength limitations of Fe_3Al alloys are being addressed by evaluation of these compositions as coatings or claddings on higher-strength, less corrosion-resistant materials and by development of oxide-dispersion-strengthened (ODS) iron aluminides with oxidation and sulfidation resistance that match or exceed that of ingot-produced versions of these materials. Iron-aluminide coatings were prepared by gas tungsten arc and gas metal arc weld-overlay techniques. All the weld overlays showed good oxidation/sulfidation behavior under isothermal conditions, including a gas metal arc-produced deposit with only 21 at.% Al. A rapid degradation in corrosion resistance was observed under thermal cycling conditions when the initially grown scales spalled and the rate of reaction was then not controlled by the formation of slowly growing aluminum oxides. Higher starting aluminum concentrations (>~25 at.%) are needed to assure adequate oxidation/sulfidation lifetimes of the weld overlays. A variety of stable oxides was added to a base Fe-28 at.% Al-2 % Cr alloy to assess the effect of these dopants on the oxidation behavior at 1200 and 1300°C in air and O_2. A Y_2O_3 dispersion

improved the scale adhesion relative to a Zr alloy addition, but wasn't as effective as it is in other alumina-forming alloys. Preliminary exposures of ODS Fe-28 at.% Al-2% Cr in the H_2S-H_2-H_2O-Ar gas at 800°C showed that the oxidation/sulfidation resistance of these alloys was good.

ACKNOWLEDGMENTS

The authors thank M. Howell for experimental support and J. R. DiStefano, G. M. Goodwin, and C. G. McKamey for their reviews of the manuscript. This research was sponsored by the Fossil Energy Advanced Research and Technology Development (AR&TD) Materials Program, U S. Department of Energy, under contract DE-AC05-96OR22464 with Lockheed Martin Energy Research Corporation. B. A. Pint is supported by the U. S. Department of Energy Distinguished Postdoctoral Research Program administered by the Oak Ridge Institute for Science and Education.

REFERENCES

1. C. G. McKamey, J. H. DeVan, P. F. Tortorelli, and V. K. Sikka, J. Mater. Res. 6 (1991) 1779-1805.

2. I. G. Wright, B. A. Pint, E. K. Ohriner, and P. F. Tortorelli, "ODS Iron Aluminides," these proceedings.

3. G. M. Goodwin, P. J. Maziasz, C. G. McKamey, J. H. DeVan, and V. K. Sikka, pp. 205-10 in *Proc. Eighth Annual Conf. Fossil Energy Materials*, N. C. Cole and R. R. Judkins (comp.), CONF-9405143, U. S. Department of Energy, August 1994.

4. K. Natesan, pp. 591-99 in Heat-Resistant Materials II, K. Natesan, P. Ganesan, and G. Lai (eds.), ASM International, August 1995.

5. G. M. Goodwin, "Weld Overlay Cladding with Iron Aluminides," these proceedings.

6. P. F. Tortorelli, J. H. DeVan, G. M. Goodwin, and M. Howell, pp. 203-12 in Elevated Temperature Coatings: Science and Technology I, N. B. Dahotre, J. M. Hampikian, and J. J. Stiglich (eds.), The Minerals, Metals, and Materials Society, Warrendale, PA, 1995.

7. P. F. Tortorelli, G. M. Goodwin, M. Howell, and J. H. DeVan, pp. 585-90 in Heat-Resistant Materials II, K. Natesan, P. Ganesan, and G. Lai (eds.), ASM International, August 1995.

8. J. H. DeVan, pp. 107-115 in Oxidation of High-Temperature Intermetallics, T. Grobstein and J. Doychak (eds.), The Minerals, Metals, and Materials Society, 1989.

9. J. H. DeVan and P. F. Tortorelli, Mater. at High Temp. 11 (1993) 30-35.

10. B. A. Pint, K. B. Alexander, and P. F. Tortorelli, pp. 1315-20 in High-Temperature Ordered Intermetallic Alloys VI, J. A. Horton, I. Baker, S. Hanada, R. D. Noebe, and D. S. Schwartz (eds.), The Materials Research Society, Pittsburgh, PA, 1995.

11. B. A. Pint, A. J. Garratt-Reed, and L. W. Hobbs, Mater. High. Temp. 13 (1995) 3.

12. B. A. Pint, "Study of the Reactive Element Effect in ODS Iron-Base Alumina-Formers," submitted for publication in Mater. Sci. Forum, March 1996.

13. P. F. Tortorelli and J. H. DeVan, pp. 257-70 in Processing, Properties, and Applications of Iron Aluminides, J. H. Schneibel and M. A. Crimp (eds.), The Minerals, Metals, and Materials Society, Warrendale, PA, 1994.

14. B. A. Pint, P. F. Tortorelli, and I. G. Wright, "The Oxidation Behavior of ODS Iron Aluminides," submitted for publication in Werst. Korros., March 1996.

15. G. J. Yurek, D. Eisen, and A. J. Garratt-Reed, Metall. Trans. A 13A (1982) 473-85.

2.17 CORROSION PROTECTION OF ULTRAHIGH TEMPERATURE INTERMETALLIC ALLOYS

P. F. Tortorelli

The results of this project are combined with those of 2.10, "Development of Cr-Nb Alloys," and reported in that section.

2.18 ODS IRON ALUMINIDES

I. G. Wright, B. A. Pint, P. F. Tortorelli, and E. K. Ohriner

INTRODUCTION

Interest in advanced cycles that involve indirectly-fired gas turbines, in which coal- or gas-fired high-temperature heat exchangers are used to heat a working fluid in a closed system, has led to investigation of materials for heat exchangers capable of operation at temperatures of the order of 1200 to 1300°C. The candidate materials are ceramics and, possibly, oxide dispersion-strengthened (ODS) alloys. An ODS FeCrAl alloy was found to meet the strength requirements for such an application, in which the working fluid at 0.9 MPa was to be heated from 800 to 1100°C over a tube length of 4 m [1].

The oxidation life of ODS FeCrAl alloys is determined by their ability to form or reform a protective alumina scale, and can be related to the time for the aluminum content of the alloy to be depleted to some minimum level [2]. As a result, the service life is a function of the available aluminum content of the alloys and the minimum aluminum level at which breakaway oxidation occurs, hence there is a limit on the minimum cross section which can be safely employed at temperatures above 1200°C. Because of their significantly higher aluminum content (≥28 atom %/≥16 wt. percent compared to ≈9 atom %/5 wt. percent), alloys based on Fe_3Al afford a potentially larger reservoir of aluminum to sustain oxidation resistance at higher temperatures and, therefore, offer a possible improvement over the currently-available ODS FeCrAl alloys, providing they can be strengthened in a similar manner.

The main thrusts of this program are to develop the alloy processing parameters that are required to achieve the typical ODS alloy structure that confers creep strength at extreme temperatures,and to optimize the alloy oxidation behavior to provide increased service life compared to ODS-FeCrAl alloys intended for the same applications. Development of the desired alloy microstructure involves control of the size and distribution of the oxide dispersoid, as well as the desired alloy grain size and shape. The ability to control the recrystallization of ODS alloys is very dependent on the homogeneity of the initial alloy powder, in terms of the size and distribution of the dispersed oxide particles, and on the level of strain and temperature applied in the recrystallization step.

DISCUSSION OF CURRENT ACTIVITIES

Development of Mechanical Alloying Parameters for ODS-Fe_3Al

A two-liter size horizontal attritor mill (Zoz GmbH, Kreustal, Germany) was installed at ORNL in order to perform mechanical alloying of iron aluminide powder while maintaining oxygen contents comparable to those in commercial mechanically alloyed materials. The grinding media consisted of a high-carbon alloy steel ball of 5 mm diam. The rotational speed of the mill was maintained at 900 rpm, and the milling atmosphere was a static vacuum. The mill was operated by placing the media and powder in the mill, evacuating with a mechanical pump to a pressure of about 5×10^{-2} torr over several hours, and sealing the mill by use of a vacuum valve.

The starting powder was (in weight percent): Fe-15.9Al-2.2Cr-0.02B (FAS), which was screened to -100 /+400 mesh. An addition of 0.47% Y_2O_3 powder was made to each run. Two sources of Y_2O_3 were used: one was a powder of nominal size of 5 μm. The second source of Y_2O_3 was a colloidal suspension of Y_2O_3 in water, with a reported particle size of 0.1 μm. This material was dried and heated at 500 ° C for 1 hr to produce a powder which had a typical particle size of 0.5 to 1 μm. After conditioning the mill and grinding media by running the mill with FAS powder for 4 hr, an initial milling run was made using the 5 μm size Y_2O_3 addition. The mill contained 2 kg of media and 200 g of powder. Samples were taken of the powder after total milling times of 1, 2, 4, 8, and 16 hr. The milling was stopped at 32 hr. Samples were taken through a sampling tube which allowed the milling chamber to remain under vacuum until the end of the total 32 hr run time. The samples were analyzed for oxygen and nitrogen content, and the powder characterized by scanning electron microscopy (SEM). Samples were also polished metallographically and viewed by SEM.

Three additional mill runs were made, each for 24 hr, using colloidal Y_2O_3 with 2 kg of grinding media. The powder weights were 200, 300, and 400 g, corresponding to 10, 15 and 20% of media weight. Two runs were also made using 3 kg of media and powder weights of 450 and 600 g, corresponding to 15 and 20% of media weight. About 60 g of powder was typically found compacted against the corner of the chamber wall, and this material was segregated from the loose powder recovered from the mill. The weight gains during milling were measured, and the increase in powder weight was attributed to wear of the steel grinding media.

The powders were placed in mild steel cans (5 cm OD and about 3 cm ID), evacuated and sealed. Prior to extrusion, the cans were preheated to 1100°C for 1 hr; an extrusion ratio of 10:1 was used. An additional extrusion of the 600 g lot of milled powder was made at an extrusion ratio of 16:1. The extruded material from the 200 g powder lot (10:1 extrusion ratio) and the materials from

the 600 g powder lot (10:1 and 16:1 ratios) were examined by optical metallography and chemically analyzed for oxygen, nitrogen and carbon. Metallographic analysis was performed on as-extruded material and also on samples heated at 1275°C for 8 hr in an evacuated quartz tube. Transmission electron microscopy (TEM) was performed on the alloy extruded at the 16:1 ratio.

The average particle size of the initial milled powder samples was found to increase up to 4 hr of milling, then decrease to 16 hr , after which it remained constant. Also, the particle size of the milled powder and its appearance in SEM showed no obvious changes after 24 hr milling at mill loadings of 2 or 3 kg of media and 200 to 600 g of powder. The polished powder samples when viewed by SEM contained a distribution of light-colored streaks, which were shown by energy dispersive X-ray analysis to be essentially pure iron. These regions apparently were associated with wear particles from the steel balls which become distributed in the milled powder. The oxygen content of the milled powder as a function of milling time is shown in Fig. 1. The calculated starting oxygen content consists of 1,000 ppm from the addition of 0.47% of Y_2O_3 and 60 ppm in the FAS powder. The increase in oxygen content up to 1,700 ppm after 32 hr was attributed to leakage of air into the mill. The attritor mill when running empty had a leak up rate of about 0.03 torr/min, as compared to a leak-up rate of about 0.005 torr/min when idle. The increase in oxygen content with time was consistent with the measured leak-up rate. An effort was made to determine the source of the increased leak rate while the mill was operating. Helium leak detection was not successful in measuring any transport of helium into the mill.

A weight gain after was measured as a result of the milling process, apparently due to wear of the media; its dependence on the milling parameters (after 24 hr of milling) is shown in Fig. 2. The trend was to a significant decrease in weight gain at higher ratios of powder:media weight. The weight gains ranged from 3% at a10% ratio to about 1% at a 20% ratio. The effect of changing the media

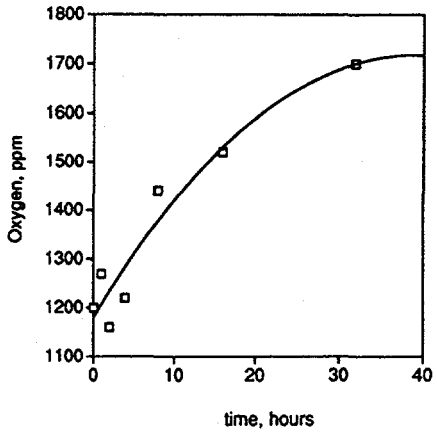

Fig. 1. Oxygen pickup during vacuum attritor milling

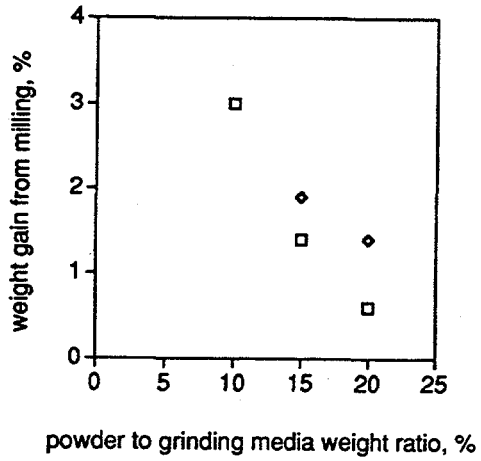

Fig. 2 Effect of milling parameters on weight gain from media wear

weight from 2 to 3kg appeared to have a minimal effect on the relative weight gain in milling.

The microstructures of the extrusions examined to date are shown in the optical micrographs in Figs. 3 (a) and (b) . All the materials showed oxide stringers elongated in the extrusion direction. The extrusion produced from material milled with 200 g of powder and 2 kg of media had a uniform microstucture, whereas the extrusions produced with higher mill loading exhibited regions of large grains, which were attributed to inadequate mixing of Y_2O_3 particles during the milling. TEM of the material milled with a powder load of 600g and extruded at a ratio of 16:1 indicated a bimodal distribution of oxide particles with the larger particles in the range of 0.2 to 1 μm. The smaller particles were mostly in the range of 0.01 to 0.03 μm. Preliminary analysis showed that all of the particles were complex oxides containing both yttrium and aluminum. The matrix was the ordered B2 phase.

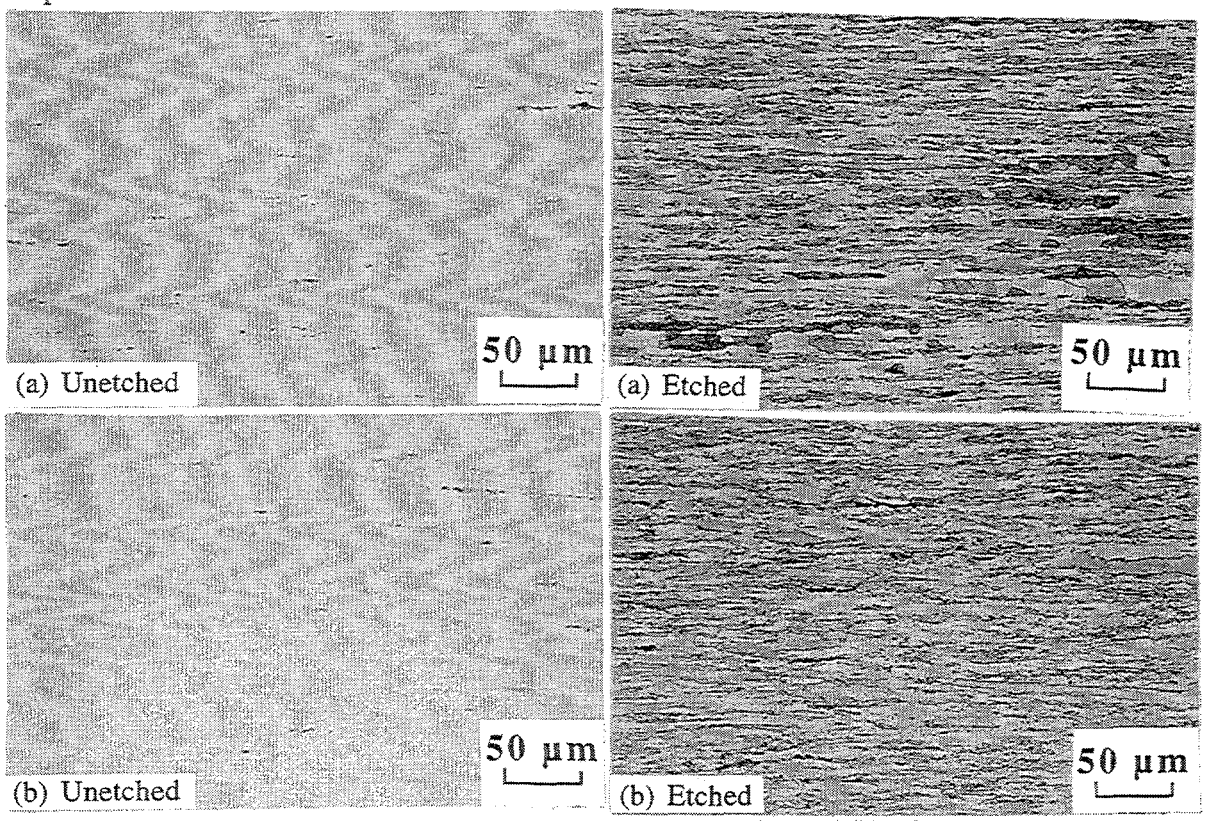

Fig. 3. Microstructures of extruded alloy powders (a) 10:1 and (b) 16 :1

Chemical analysis results of three extruded bars are shown in Table 1. The oxygen contents, in the range of 1,620 to 1,760 ppm and the nitrogen contents, in the range of 100 to 180 ppm, are consistent with those obtained in an earlier 32 hr milling run; the oxygen contents are significantly lower than those obtained in a smaller attritor mill used in this program (of the order of 1% by weight) and are very similar to those reported for commercial mechanically-alloyed materials. The

Table 1. Chemical Analysis of Extruded Bars

Sample Powder		Extrusion Ratio	Concentration, ppm			
Lot No.	Size, g		Oxygen	Nitrogen	Carbon	Sulfur
220	200	10:1	1,620	160	740	20
360B	600	10:1	1,640	180	370	20
360A	600	16:1	1,760	100	400	20

carbon contents for the 600 g powder lot of 370 and 400 ppm are within, but on the high end of the range of carbon contents measured in previous work, and found in commercial ODS materials. The 740 ppm carbon value for the 200 g lot is considered high for this type of material. The carbon content of the steel balls is about 1%; the observed wear of the media would result in a calculated increase in carbon content in the milled powder of 100 to 300 ppm. These values are somewhat lower than the measured carbon contents shown in Table 1, but are within a factor of 2 of the measured values; there may be another source of comparable magnitude.

The microstucture following heating at 1275°C in vacuum was characterized by large quantities of porosity in all three materials. This is shown in Fig. 4 for the as-polished sections. It is not clear if this issue is unique to the material produced for this study. Porosity that apparently results from interdiffusion has been seen in long-term oxidation experiments with similar alloys. Since the mild steel can which jacketed each extrusion was left attached to the samples which were heat treated, it is possible that interdiffusion between the steel and the sample is a cause of porosity. The porosity

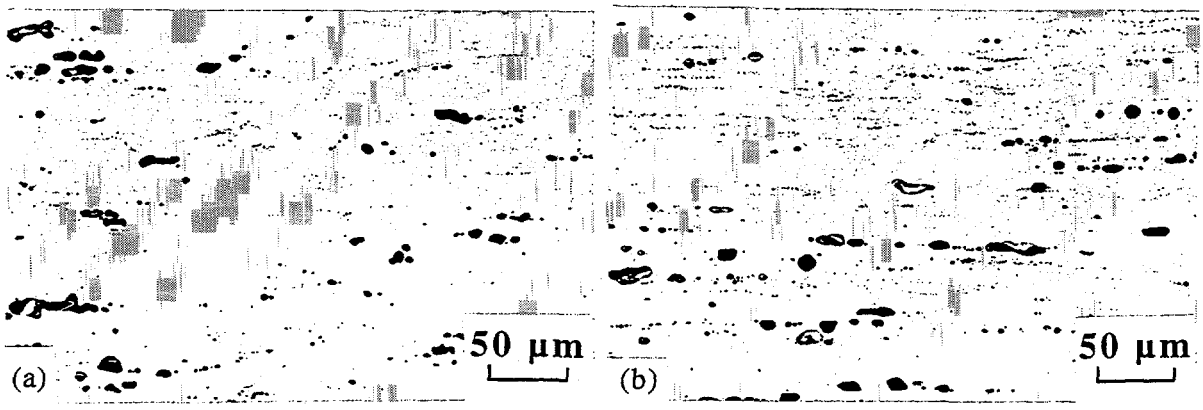

Fig. 4. Porosity in extruded alloys (600 g mill load) after recrystallization heat treatment (a) extruded at 10:1 and (b) extruded at 16:1

levels appeared to be higher in regions near the edges of the specimens near the boundary with the can material. Porosity in some ODS materials has been attributed to entrapped argon for those powders milled in an argon atmosphere, but this is not likely here since the powder was milled in vacuum. However, the atomization of the FAS powder was performed with argon, and some gas could have be entrapped in hollow atomized powder particles. Another possible explanation is that carbon in the alloy reacted at the elevated temperature with oxygen present as alumina, or in some other form, to produce gaseous CO which built up sufficient internal pressure to form voids. Preliminary thermodynamic calculations show that this can be a possibility.

The material from the 600 g milling lot showed localized regions of visible grains among large regions with no visible grain boundaries. The material from the 200 g milling lot could not be etched to show any grain boundaries, which may indicate that very large grains had been achieved by this treatment, although additional characterization is needed to confirm this.

High-Temperature Oxidation Behavior of ODS-Fe_3Al Alloys

The alloys studied were two commercially-available oxide dispersion-containing FeCrAl-based alloys—Kanthal APM and INCO MA956—and an ODS-Fe_3Al alloy (FAS3Y) made in an earlier phase of the program at ORNL. The compositions of the alloys are shown in Table 2. Kanthal APM is not optimized for high-temperature creep strength, but forms a protective alumina scale that exhibits excellent resistance to spallation [3]; this alloy, therefore, was considered a standard of high-temperature oxidation resistance. INCO MA956 represents the class of ODS alloys available as high-strength, high-temperature tubing. The Kanthal APM was obtained in the form of 1 mm-thick strips [3], whereas the MA956 was a nominally 3 mm-thick plate. The ODS-Fe_3Al alloy was an as-extruded rod, nominally 1.6 mm (0.625 in) diameter.

Table 2. Compositions of Alloys (weight percent)

Constituent	FAS3Y	Kanthal APM	INCO MA956*
Dispersoid	Y_2O_3-Al_2O_3	ZrO_2-Al_2O_3	Y_2O_3-Al_2O_3
Cr	2.25	20.42	19.22
Al	16.3	5.54	4.32
Y	0.37	<0.01	0.5
Zr		0.10	
Ti	0.07	0.03	0.36
Si	0.10	0.23	
Mn	0.15	0.08	
C	0.03	0.03	0.01
O	0.0533**	0.0526	0.20
S	0.0061	0.001	0.011

*Analysis for sample of rod stock
**Before mechanical alloying

Specimens of dimensions 1.5 x 1.0 x 0.2 cm, or 1.25 diameter discs of thickness 1-2 mm from the ODS-Fe_3Al, were polished to a 0.3 μm alumina surface finish, and ultrasonocally cleaned in acetone and methanol before exposure. Each specimen was placed in individual lidded, cylindrical alumina crucibles, which were then exposed in air for 500 hr intervals to 5,000 hr at 1000°C, and at 1100, 1200 and 1300°C at 100 hr intervals up to 1,500 hr. The alumina crucibles were baked at 1400°C for 8 hr prior to use. Separate weighing of the specimens and crucibles allowed the total weight gain and the extent of scale spallation to be measured. The specimens and the crucibles (containing any spalled oxide) were weighed after cooling to room temperature on a Mettler model AE 240 balance.

The trends in specimen weight change are shown in Fig. 5. The ODS-FeCrAls exhibited net weight gains at all four temperatures, whereas the ODS-Fe_3Al showed a net weight loss, following an initial gain, at 1100°C and higher. The overall oxidation rates (rate of oxygen uptake), from the sum of the specimen weight change and the spalled scale, as well as the weight of spalled scale showed that, at 1000°C, the oxidation rate of the ODS-Fe_3Al alloy was essentially the same as that of APM, with slightly more spallation from the ODS-Fe_3Al. With increasing temperature, the overall rate of

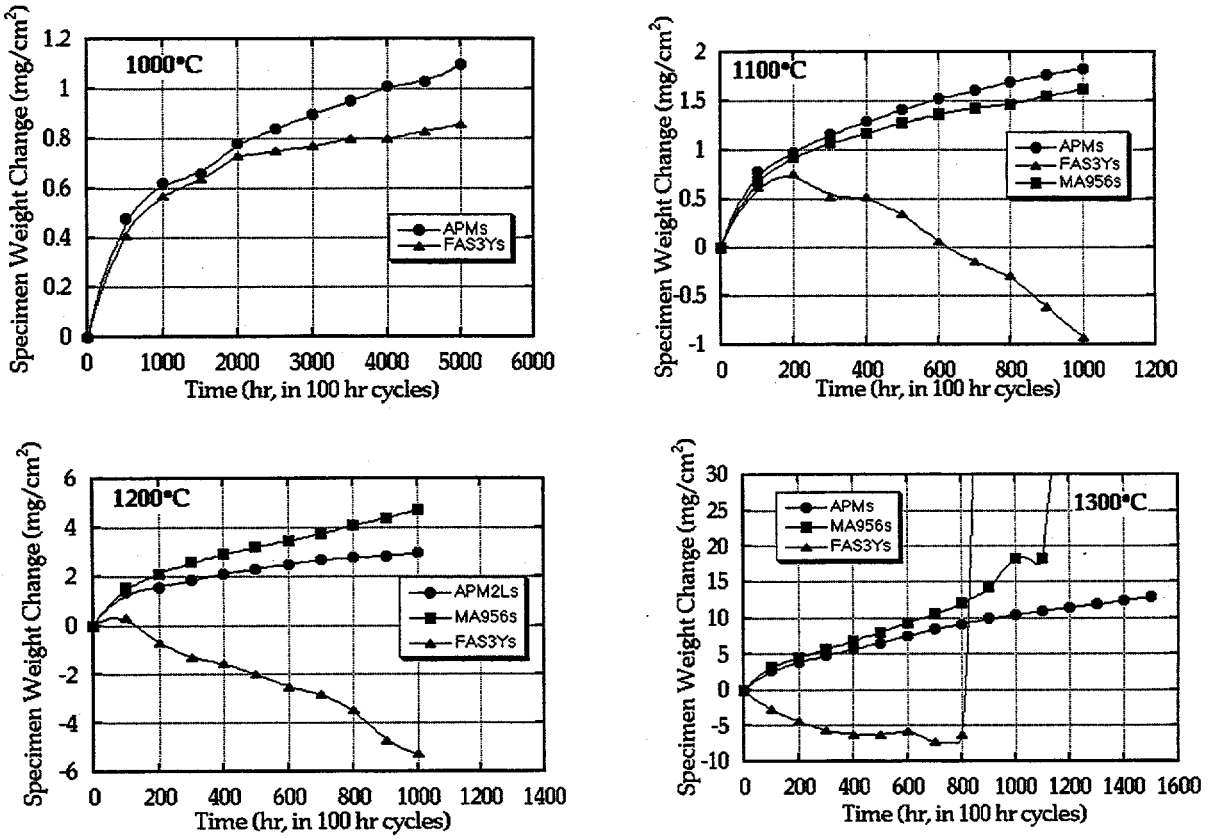

Fig. 5. Specimen weight change data after exposure to thermal cycling conditions

oxygen uptake of the ODS-Fe_3Al increased faster than that for APM as a result of the increasing rate of scale spallation. The oxidation behavior of MA956 was intermediate between these two alloys. Log-log plots of these data were made to determine the values of the parameters k and n in the oxidation rate equation, expressed as:

$$\Delta m = k \,.\, t^n \tag{1}$$

where Δm is the weight change due to oxygen uptake, t is time, and k and n are constants. The values of the oxidation rate exponents, n, are listed in Fig. 6. The excellent oxidation behavior of APM was reflected in values of n that were consistently less than expected for parabolic scale growth ($n = 0.5$). The n values for the other two alloys, which suffered increasing degrees of scale spallation with increasing temperature, increased from slower to faster than parabolic as the extent of scale spallation increased.

For ODS-FeCrAl alloys, the lifetime under high-temperature oxidation conditions may be limited by the ability of the alloy to maintain or reform its protective alumina scale [2]. Hence, a major point of comparison between ODS-Fe_3All and competing ODS-FeCrAl alloys is the oxidation-governed lifetime for a given thickness of alloy. Using the same considerations as Quadakkers, and Bongartz [2,4], the kinetic data reported above were used to construct 'oxidation life diagrams' for the three alloys. As long as the oxidation of the alloy involves the formation (and reformation following scale spallation) of an alumina scale, the effective life of the alloy can be calculated from a knowledge of the rate of consumption of aluminum (proportional to Dm, mg/cm^2), and the total amount of aluminum available. Measurements on specimens oxidized to the point of breakaway oxidation, where an alumina scale no longer forms have shown the aluminum concentration profile in the alloy remains essentially flat [4,5], so that the aluminum reservoir available for use in protective scale formation can be calculated from:

- the initial aluminum content of the alloy (C_o, weight percent),
- the aluminum level at which a protective alumina scale can not longer be formed (C_b), and
- the thickness of the section being oxidized (d, cm).

Hence:

$$k \,.\, t^n \,.\, M = (C_o - C_b)/100 \,.\, d/2 \,.\, r \tag{2}$$

where M is the aluminum corresponding to the oxygen uptake, given by (mole Al/mole oxygen in Al_2O_3), r is the density (mg/cm^3) of the alloy, the units of k are mg/cm^2.hr, and t is in hours. Rearranging, the time at which a protective alumina scale can no longer be formed, or the time to breakaway oxidation (t_b) becomes:

$$t_b = [4.44 \times 10^{-3} \,.\, (C_o - C_b) \,.\, r \,.\, d/k]^{1/n} \tag{3}$$

Values of C_b have been determined to be of the order of 1.15 wt. percent for APM [4] (the same

value was assumed here for MA956), and 1.8 to 2.4 wt. percent for Fe_3Al [5]. The resulting diagrams relating lifetime (t_b) to wall thickness (d) are shown in Fig 6. Figure 7 summarizes the effect of temperature on the oxidation-governed lifetime of the three alloys for a section thickness of 2.5 mm

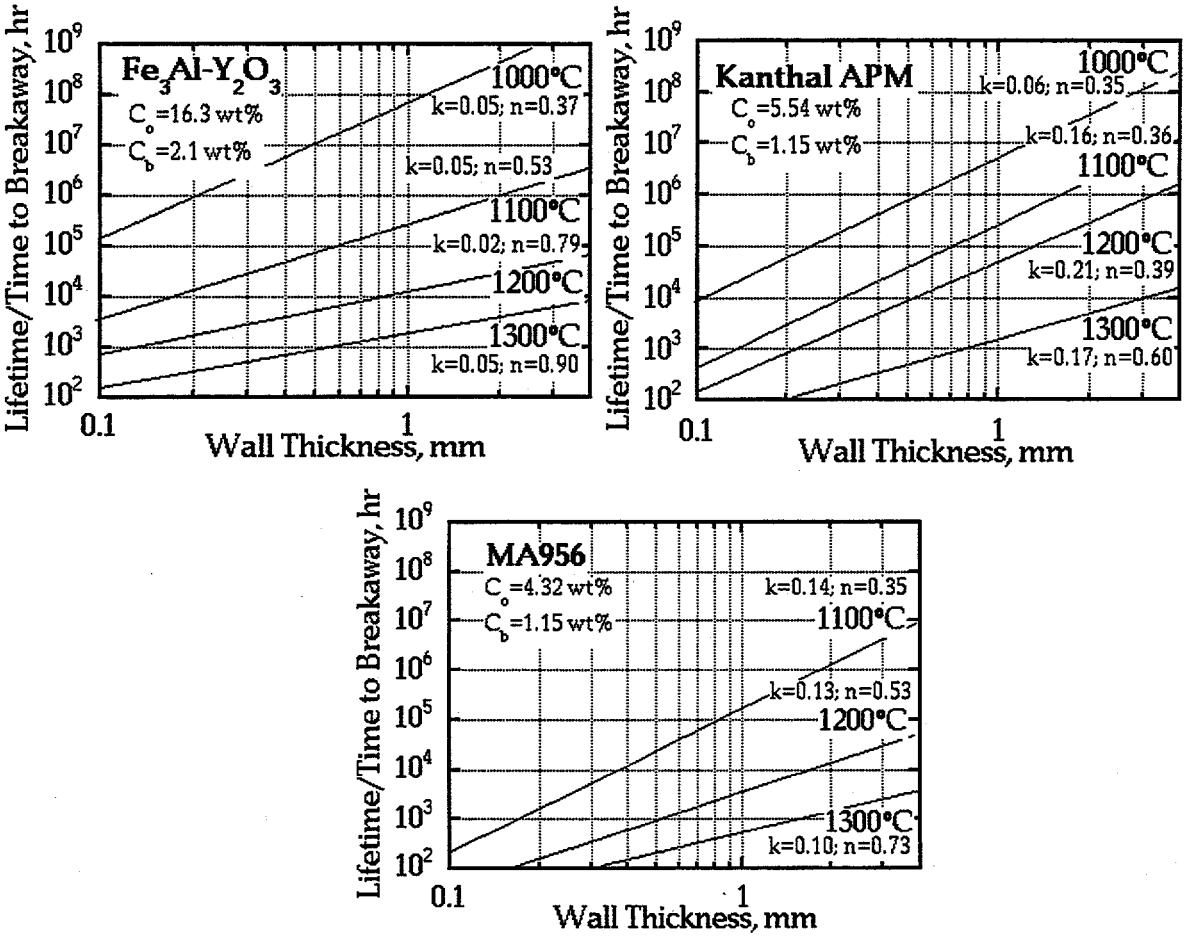

Fig. 6. Calculated oxidation-governed lifetimes as a function of wall thickness

(0.1 in.). Overall, at 1000°C when the extent of scale loss from FAS3Y by spallation is small, its larger usable aluminum reservoir (16.3 vs 4.65 wt. percent) results in a longer life than for APM. As the proportion of the aluminum reservoir consumed to replace scale lost by spallation increases with increasing temperature, the advantage of the large initial reservoir of FAS3Y compared to APM is lost. The effect of increasing scale spallation on the oxidation-governed life of APM becomes apparent only above 1200°C. In contrast, the moderate scale spallation of MA956 results in calculated lifetimes similar to those of FAS3Y. These oxidation exposures are continuing to determine if scale spallation eventually plays a role in limiting the oxidation lifetime of APM, and to generate data that can be used to test and refine the approach outlined here.

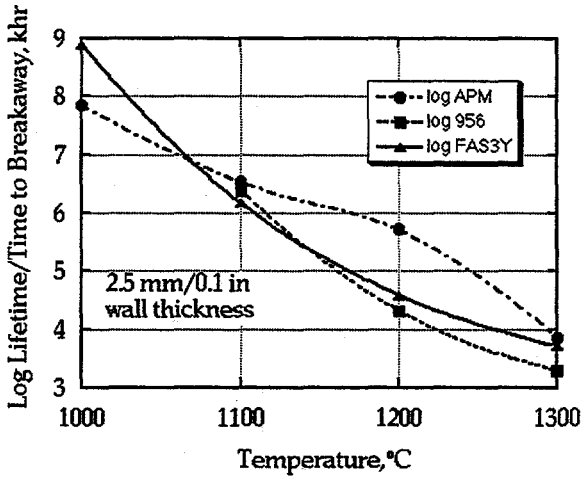

Fig. 7. Comparison of calculated lifetimes for a 2.5 mm thick alloy section

SUMMARY AND CONCLUSIONS

Milling in a static vacuum produced low levels of oxygen contamination in the alloy, similar to those found in commercial-scale ball-milled powder. There remains a possibility of achieving even lower levels of oxygen pick-up, below the range of 500 to 700 ppm now obtained, by better understanding of sealing issues associated with the mill.

Wear of the steel grinding media gives rise to several issues associated with the milled powder:

- an increase in the average iron content of the powder, which can readily be compensated by adjusting the initial powder composition to compensate for increase in iron content during milling,
- inhomogeneity as evidenced by local iron-rich regions in the milled powder associated with wear particles detached from the grinding media toward the end of the milling run, and
- an increase in carbon content in the milled powder. There use of ceramic media is a possibility, but experience of its use in milling of ductile metal powder has not been good.

The heat treatment of the extruded materials at 1275°C for 8 hr resulted in very large grains in fully-milled alloy, and etching was unable to reveal any grain boundaries. The Y_2O_3 powder currently available appears to be too coarse to achieve a uniform distribution of very fine particles. An experimental batch of Y_2O_3 having a nominal 30 nm particle size has been ordered from a commercial vendor.

Currently the most important issue is the porosity seen in all materials following heat treatment at 1275°C. Possible sources appear to be:

- Kirkendall voids from interdiffusion with the mild steel can,
- entrapped argon from the atomization process of the original powder, or
- reaction of carbon impurity with oxygen present as alumina, or in some other form, to produce

gaseous CO which builds up sufficient internal pressure to form voids. Preliminary thermodynamic calculations show that this can be a possibility.

The overall rate of oxidation of an ODS-Fe_3Al at 1000°C in air under thermal cycling conditions was found to be similar to that of the ODS-FeCrAl alloys Kanthal APM and INCO MA956 whereas, from 1100 to 1300°C its oxidation rate was faster than those alloys due to a greater tendency to scale spallation. Nevertheless, the larger reservoir of aluminum in the ODS-Fe_3Al resulted in a longer calculated oxidation-governed lifetime for the ODS-Fe_3Al at 1000°C, for a given alloy thickness. At 1100 and 1300°C, all three alloys exhibited essentially the same calculated lifetimes but, in the intervening temperature range, APM clearly gave the longest lifetimes, with FAS3Y slightly better than MA956. Exposures are continuing to generate oxidation kinetics for a larger fraction of the alloy lifetimes, to allow the calculations to fully reflect the actual oxidation behavior. Work is in progress with the aim of decreasing the tendency for scale spallation by the ODS-Fe_3Al alloy, which could result in an obvious lifetime advantage, commensurate with its larger aluminum reservoir, compared to the ODS-FeCrAl alloys.

REFERENCES

1. Starr F., White A. R., Kazimierzak B., *in* Materials for Advanced Power Engineering 1994, D. Coutsouradis, et al., Eds., (Kluwer Academic Publishers, 1994) pp. 1393-1412

2. Quadakkers W. J., Bongartz K., Schubert F., Schuster H., *in* Materials for Advanced Power Engineering 1994, D. Coutsouradis, et al., Eds., (Kluwer Academic Publishers,1994) pp. 1533-1542

3. Pint B. A., Garratt-Reed A. J., Hobbs L. W., Materials at High Temperatures, **1** (1995) 3

4. Quadakkers W. J., and Bongartz K., Werkstoffe u. Korrosion, **45** (1994) 232

5. DeVan J. H., Tortorelli P. F., Bennett M. J., Proc. Eighth Annual Conference on Fossil Energy Materials, Oak Ridge, TN, (CONF-9405143; ORNL/FMP-94/1, 1994) pp. 309-320

6. Alexander K. B., Pint B. A., Oak Ridge National Laboratory, unpublished work.

7. Pint B. A., Alexander K. B., Tortorelli P. F., "The Effect of Various Oxide Dispersions on the Oxidation Resistance of Fe_3Al," *in* Proc. Symp. on High Temperature Ordered Intermetallics VI, J. Horton, S. Hanada, I. Baker, R. D. Noebe and D. Schwartz, Eds., (MRS , Pittsburgh, PA, 1995) v.364, p.1315-20

8. Stasik M. C., Pettit F. S., Meier G. H., Ashary A., Smialek J. L., Scripta Met. et Mat., **31** (1994) 1645

9. Pint, B. A., "Study of the Reactive Element Effect in ODS Iron-Base Alummina Formers," to be presented at the 4th Intl. Symposium on High-Temperature Corrosion, Les Embiez, France, June 1996.

2.19 DEVELOPMENT OF IRON-ALUMINIDE HOT-GAS FILTERS

P. F. Tortorelli, I. G. Wright, and R. R. Judkins

INTRODUCTION

Removal of particles from hot synthesis gas produced by coal gasification is vital to the success of these systems. In Integrated [Coal] Gasification Combined Cycle systems, the synthesis gas is the fuel for gas turbines. To avoid damage to turbine components, it is necessary that particles be removed from the fuel gas prior to combustion and introduction into the turbine. Reliability and durability of the hot-gas filtering devices used to remove the particles is, of course, of special importance. Hot-gas filter materials include both ceramics and metals. Numerous considerations must be made in selecting materials for these filters. Constituents in the hot gases may potentially degrade the properties and performance of the filters to the point that they are ineffective in removing the particles. Very significant efforts have been made by DOE and others to develop effective hot-particle filters and, although improvements have been made, alternative materials and structures are still needed.

One of the critical considerations for metal filters is their ability to withstand the rigors of the coal gasification environment which is highly carburizing and may be highly sulfidizing depending on the coal used and the extent of sulfur removal. A family of iron-aluminide alloys has the potential for excellent resistance to these modes of attack.[1,2] ORNL, Pall Corporation, and Ametek Specialty Metals Division have collaborated on the development of porous metal filters made of sintered iron-aluminide alloys. The successful development of these filters appears to offer several significant advantages over other metal filters. The iron-aluminide alloys, as indicated above, have outstanding high-temperature sulfidation resistance. In addition they have excellent oxidation resistance and should be highly resistant to carburization. Other alloys, particularly stainless steel alloy types 316 and 310, have not performed well in highly sulfidizing and carburizing environments. In demonstration tests at the Westinghouse gasification pilot plant (Waltz Mill site), types 316 and 310 stainless steel sintered metal filters were severely embrittled by carburization/sulfidation and sulfidation, respectively.

The purpose of this project is to provide technical support to the Pall Corporation in its development of porous sintered iron-aluminide filters for hot-particle removal from product streams in coal gasification systems. The ORNL role is to provide specialized expertise in the areas of corrosion analysis, microstructural characterization, alloy selection, and processing

based on extensive experience with iron aluminides and materials performance in fossil energy systems. ORNL's contribution via this project should aid the timely completion of Pall's development and demonstration efforts.

DISCUSSION OF CURRENT ACTIVITIES

Results of thermochemical calculations and prior experience with iron aluminides was used to prepare input on test conditions and alloy selection for the prototypic filter tests to be conducted by Pall Corporation. One aspect of this work involved thermochemical calculations (based on SOLGASMIX) of the equilibrium gas compositions of representative air- and oxygen-blown synthesis gases at both actual gasifier pressures and that of the filter tests (1 atm). (These calculations were similar to ones previously done to examine carbon formation in gasifiers.[3]) These results were used to determine the most appropriate test conditions. ORNL also provided recommendations of specific alloy compositions and the need for preoxidation treatments for consideration by Pall in development of their test plan. Microstructural analyses of specimens of filter components made from stainless steel, alloy X, and iron aluminide and exposed at the Dakota Gas facility are in progress.

REFERENCES

1. C. G. McKamey, J. H. DeVan, P. F. Tortorelli, and V. K. Sikka, J. Mater. Res. 6 (1991) 1779-1805.

2. P. F. Tortorelli and J. H. DeVan, pp. 257-70 in Processing, Properties, and Applications of Iron Aluminides, J. H. Schneibel and M. A. Crimp (eds.), The Minerals, Metals, and Materials Society, Warrendale, PA, 1994.

3. P. F. Tortorelli, R. R. Judkins, J. H. DeVan, and I. G. Wright, "Carbon Formation and Metal Dusting in Hot-Gas Cleanup Systems of Coal Gasifiers," pp. 292 - 301 in *Proc. Advanced Coal-Fired Power Systems '95 Review Mtg.*, Vol. 1, H. M. McDaniel, D. J. Mallet, and V. K. Venkataraman (eds.), DOE/METC-95/1018, U. S. Department of Energy, June 1995.

2.20 Mo-Si ALLOY DEVELOPMENT

C. T. Liu, L. Heatherly, and J. L. Wright

Oak Ridge National Laboratory
Metals and Ceramics Division
P. O. Box 2008
Oak Ridge, TN 37831-6115

ABSTRACT

The objective of this task is to develop new-generation corrosion-resistant Mo-Si intermetallic alloys as hot components in advanced fossil energy conversion and combustion systems. The initial effort is devoted to Mo_5-Si_3-base (MSB) alloys containing boron additions. Three MSB alloys based on Mo-10.5Si-1.1B (wt %), weighing 1500 g were prepared by hot pressing of elemental and alloy powders at temperatures to 1600°C in vacuum. Microporosities and glassy-phase (probably silicate phases) formations are identified as the major concerns for preparation of MSB alloys by powder metallurgy. Suggestions are made to alleviate the problems of material processing.

INTRODUCTION

The objective of this task is to develop new-generation corrosion-resistant Mo-Si alloys for use as hot components in advanced fossil energy conversion and combustion systems. The successful development of Mo-Si alloys is expected to improve the thermal efficiency and performance of fossil energy conversion systems through an increased operating temperature, and to increase the service life of hot components exposed to corrosive environments at high temperatures (to as high as 1600°C). The initial effort will be devoted to Mo_5-Si_3-base alloys containing boron additions.

It is known that $MoSi_2$ containing 66.7 at. % Si is very resistant to oxidation at high temperatures, but it is brittle with poor fracture resistance at ambient temperatures.[1-5] Mo_5Si_3 containing a lower level of Si (37.5 at. %), on the other hand, is expected to have better fracture resistance; however, its poor oxidation resistance was a major concern for structural use.[6-10]

The recent work by Mufit Akinc and others indicates that the oxidation resistance of Mo_5Si_3 can be dramatically improved by alloying with several percent of boron and carbon additions.[11-14] Boron-modified Mo_5Si_3 alloys showed excellent oxidation resistance in air at temperatures to 1300°C. In addition, these silicide alloys exhibited fracture resistance better than $MoSi_2$. Mo_5Si_3 has a melting point to as high as 2180°C, which is higher than that of $MoSi_2$ by 160°C. The combination of excellent oxidation resistance with the high melting point, makes boron-modified Mo_5Si_3-base alloys attractive for structural use at temperatures to 1600°C.

At present, the mechanical properties of the Mo-Si alloys have not been well characterized. The mechanical properties at ambient and elevated temperatures are closely related to microstructural features and material processing. Developmental work is thus required to prepare sound materials with controlled microstructures. The phase relationship of the ternary system Mo-Si-B has not been completely determined, and additional work is needed to identify phases existing in the multi-component alloy system. All this information is critical for evaluation of the Mo_5Si_3-based alloys as new structural materials for high-temperature applications.

RESULTS

In order to assess the potential of B-modified Mo_5-Si_3 alloys, the initial effort of this task is devoted to the fabrication of reasonably large heats for evaluation of their mechanical and metallurgical properties. Based on the creep studies at Ames Laboratory, Mufit Akinc[11,12,15] suggested the alloy composition Mo-10.5Si-1.1B (wt %) for further alloy development. According to the Mo-Si-B ternary system,[16,17] this alloy contains three phases: Mo_3Si, T1(Mo_5Si_3), and T2[$Mo_5(Si,B)_3$].

Table 1 shows the compositions of the alloys used in the current study. All the alloys are based on the base composition of Mo-10.4Si-1.1B, in which different levels of C and Zr are added for control of oxygen and oxides in the alloys. The alloy MSB-1 was prepared using $MoSi_2$ alloy powder diluted with Mo and B powders (see Table 2). Carbon at a level of 0.13 wt % was added to reduce the oxygen content in the alloy. The powders with a total weight of 1500 g were thoroughly mixed and cold pressed into a green compact in an inert gas chamber. The green compact with a density of 3.1 g/cc was then hot

pressed inside a graphite die at temperatures to 1600°C in a vacuum furnace. Figure 1 shows the profiles of temperature, load and thickness reduction the alloy compact experienced. The compact was essentially held at 1600°C for about 80 min at a stress of ~7 ksi. The hot-pressed ingot showed no indication of macroscopic cracks (Fig. 2), with a final density of 7.9 g/cc.

Table 1. Composition of MSB Alloys Prepared by Powder Metallurgy (PM)

Alloy Number	Composition (Wt %)
MSB-1	Mo-10.5Si-1.1B-0.13C
MSB-2	Mo-10.4Si-1.1B-0.6C-0.2Zr
MSB-3	Mo-10.4Si-1.1B-1.0C

Table 2. Processing of MSB Alloys

Alloy Number	Charge Material	Processing[a]	Density (g/cc)
MSB-1	$MoSi_2$,Mo,B, and C powders	CP+Hp/1600°C/80 min/7 Ksi	7.9
MSB-2	Mo,Si,B,Zr, and C powders	CP+HP/1600°C/80 min/7 Ksi	8.3
MSB-3	Mo,Si,B, and C powders	CP+HP+1600°C/80 min/7Ksi	8.3

[a]CP = cold pressing
HP = hot pressing

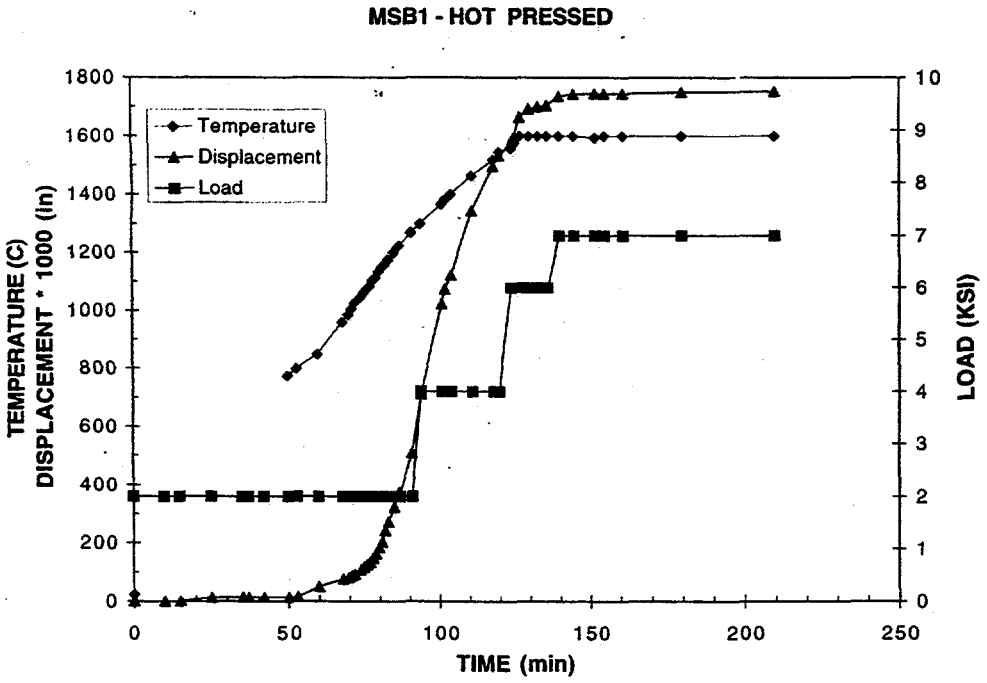

Fig. 1. Temperature, applied load, and thickness reduction of the alloy MSB-1 during hot pressing at temperatures to 1600°C.

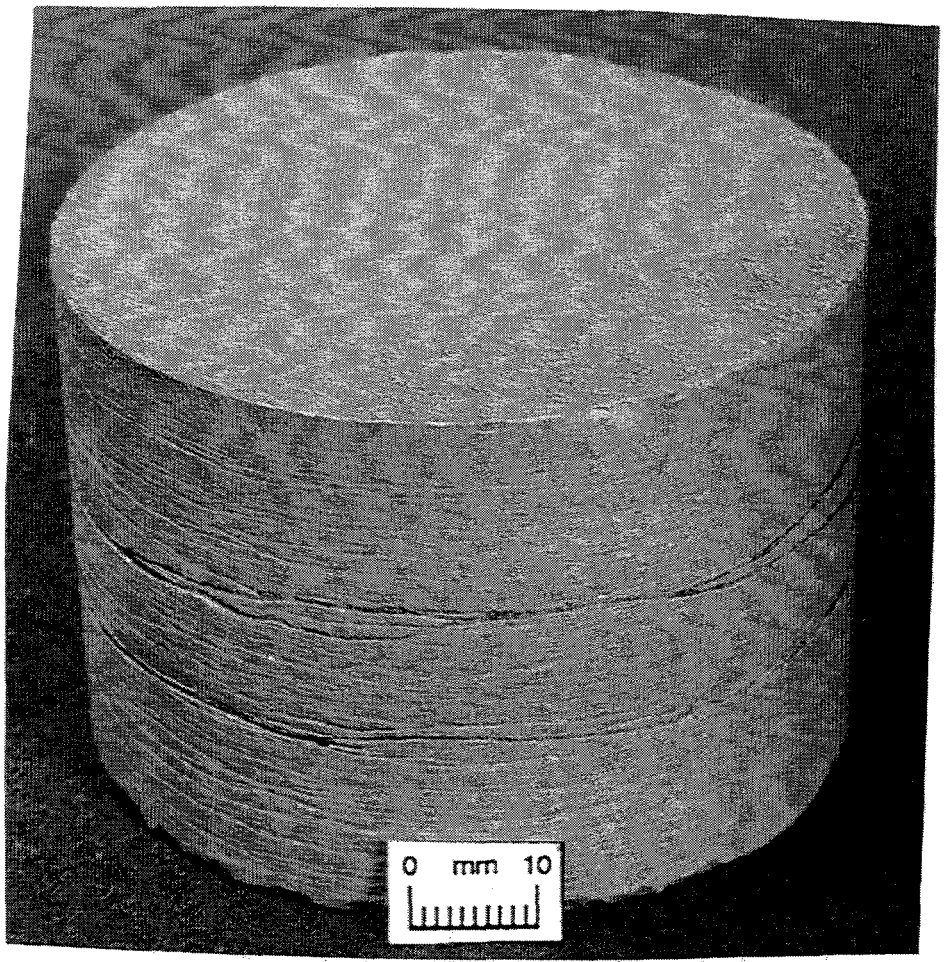

Fig. 2. Alloy MSB-1 prepared by hot pressing at 1600°C.

Figure 3 shows the microstructure of MSB-1 in the hot-pressed and heat treatment conditions. In the hot-pressed condition, the alloy contains fine porosities and oxide particles (appearing as black dots in Fig. 3) in the alloy matrix. In order to control the microstructure, the alloy was annealed for 1 d at 1200 to 1700°C in vacuum. As shown in Fig. 3b, annealing at temperatures to 1700°C caused only a small increase in porosity size. Figure 4 shows the second-phase particles revealed by etching. Button-type specimens were machined from the alloy compact and annealed for 1 d at 1200°C. Tensile tests at room temperature indicated that the alloy fractures prior to macroscopic yielding, with a fracture strength of 186 MPa. Examination of the fracture surface reveals the formation of glass phases, possibly silicate phases, at grain boundaries (Fig. 5). This observation suggests that adding 0.13 wt % C is insufficient to suppress the formation of glassy phases based on silicates.

The PM alloy MSB-2 was prepared in the same way as MSB-1, except that 0.2% Zr and more carbon (0.6%) were added to the alloy. Carbon was added to reduce the oxygen content, and zirconium was added to scavenge residual oxygen and form stable Zr oxides in the alloy. Figure 6 shows the microstructural features of MSB-2. Black dots in Fig. 6 are microcavities which distribute nonuniformly in the matrix. Some large second-phase particles (Fig. 6b) are observed, which contain a high level of Zr, probably ZrO_2, as evidence from energy dispersive x-ray spectroscopic analyses. It is important to point out that microcracks are formed essentially around these large particles. We believe that these microcracks were formed due to thermal stresses generated from different thermal expansion coefficients between the alloy matrix and Zr oxides. Tensile tests showed a low fracture strength of 110 MPa for this alloy tested at room temperature. These results suggest that Zr embrittles the alloy through the formation of large Zr oxide particles.

In order to solve the problems identified in the alloys MSB-1 and MSB-2, we prepared the alloy MSB-3 with the composition of Mo-10.4Si-1.1B-1.0C. In this alloy, carbon at a level of 1 at. % was added to remove oxygen, and Zr was not added in order to avoid the formation of large Zr oxide particles. The PM alloy MSB-3 was successfully prepared by hot pressing with a final density of 8.3 g/cc. Figure 7 shows the microstructure of the alloy in the hot pressing condition. No large oxide particles or microcracks are revealed in this material; however, clustered microporosities (as black dots) are still detected in the alloy matrix.

(a)

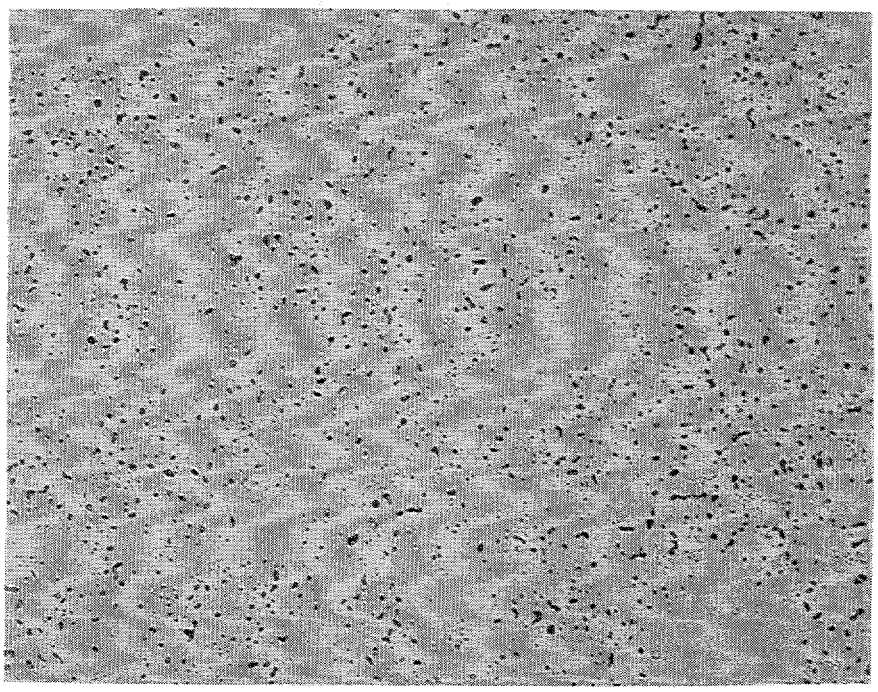

(b)

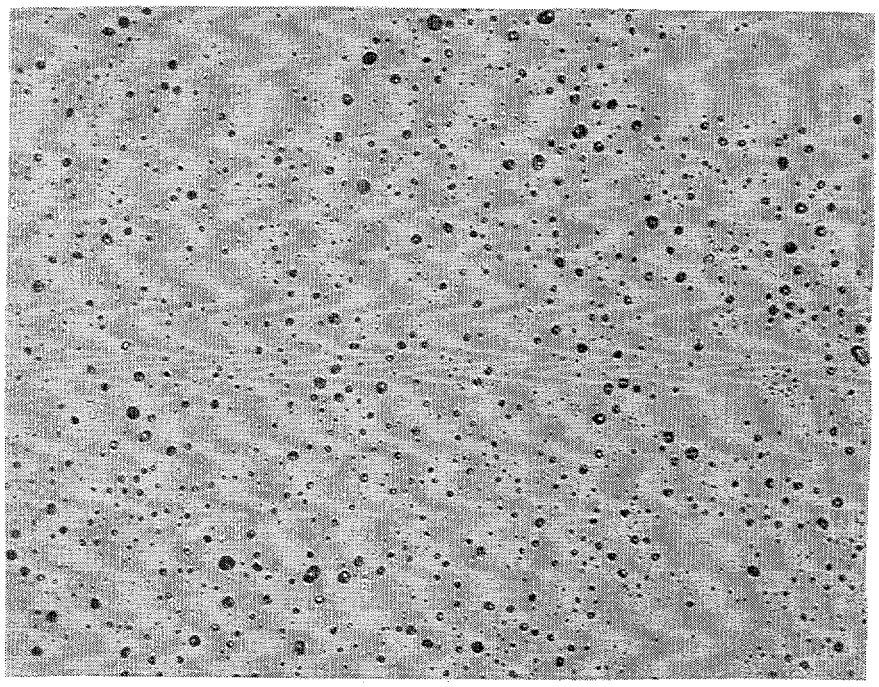

Fig. 3. Optical micrographs of MSB-1 produced by hot pressing of powders (a) as-pressed condition, (b) annealed 1 d/1600°C; 500X.

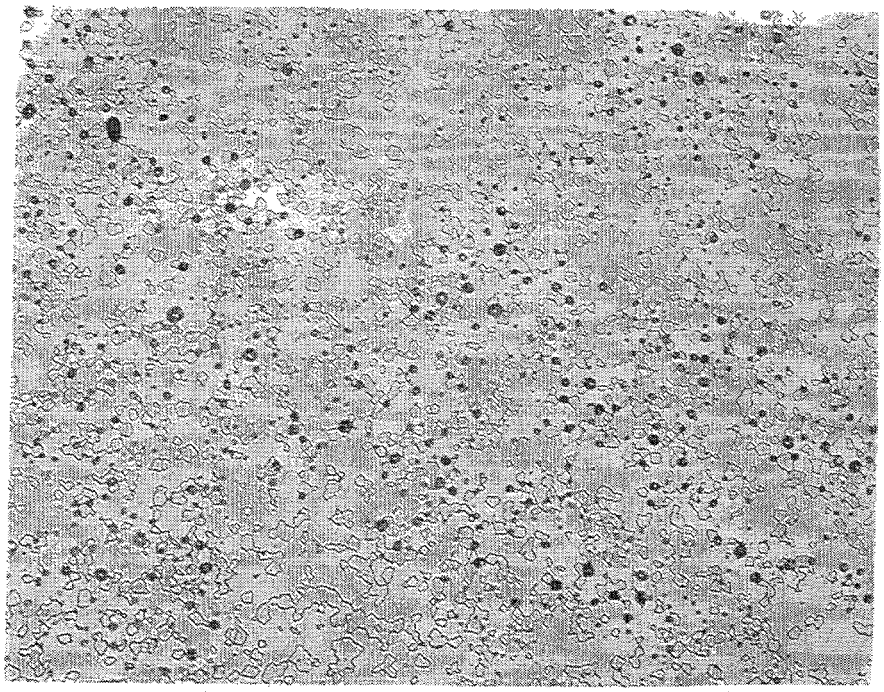

Fig. 4. Optical micrographs of MSB-1 produced by hot pressing and annealing for 1 d at 1600°C; 500X.

Fig. 5. Fractograph of MSB-1 fractured by tensile testing at room temperature. The white lines are glassy phases formed around grain-boundary regions, 100X.

(a)

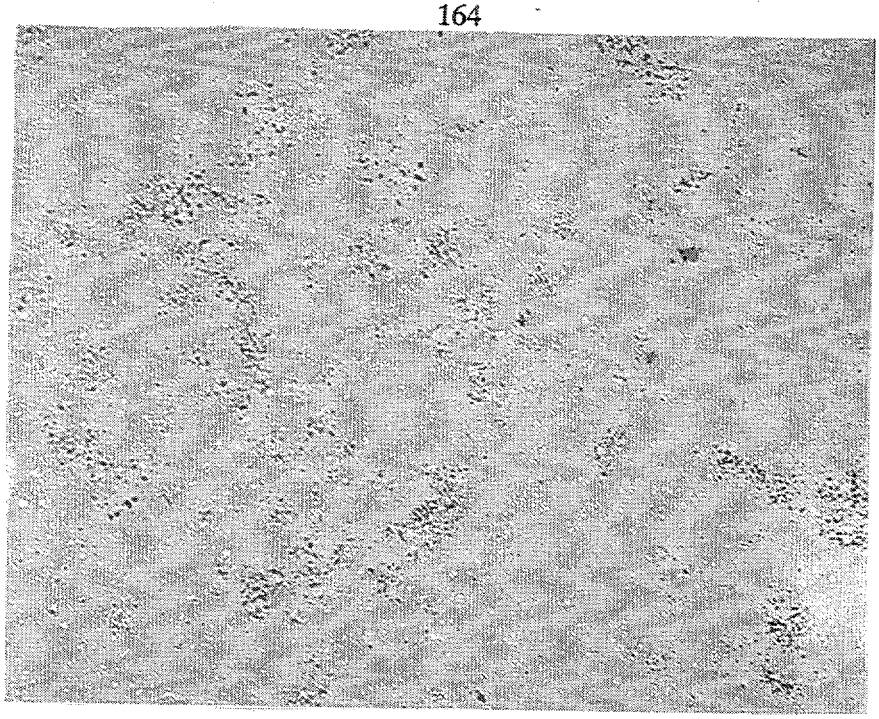

(b)

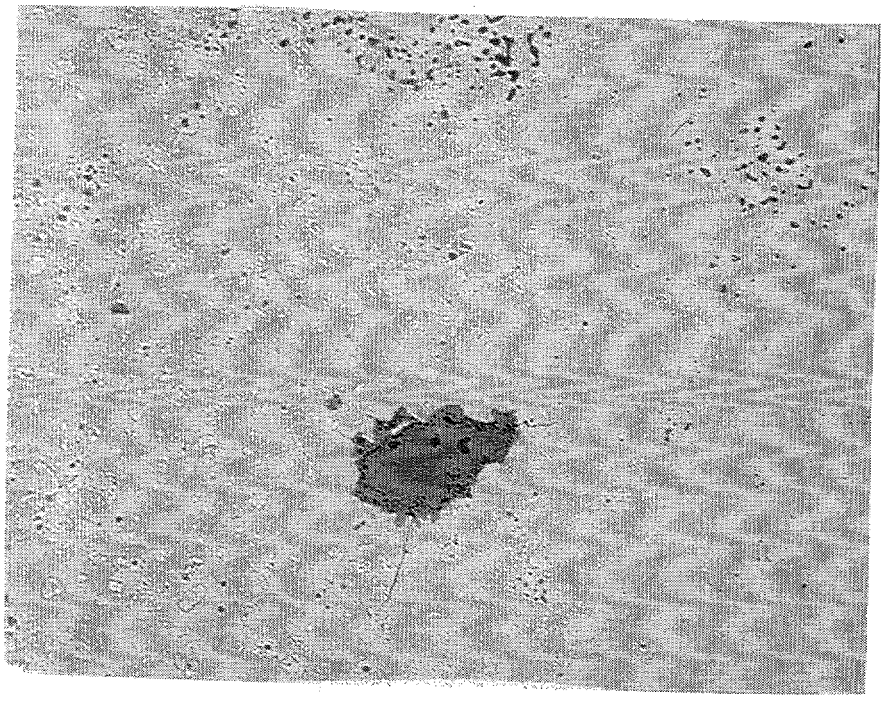

Fig. 6. Optical micrographs of MSB-2 produced by hot pressing at 1600°C; (a) 200X, and (b) 500X.

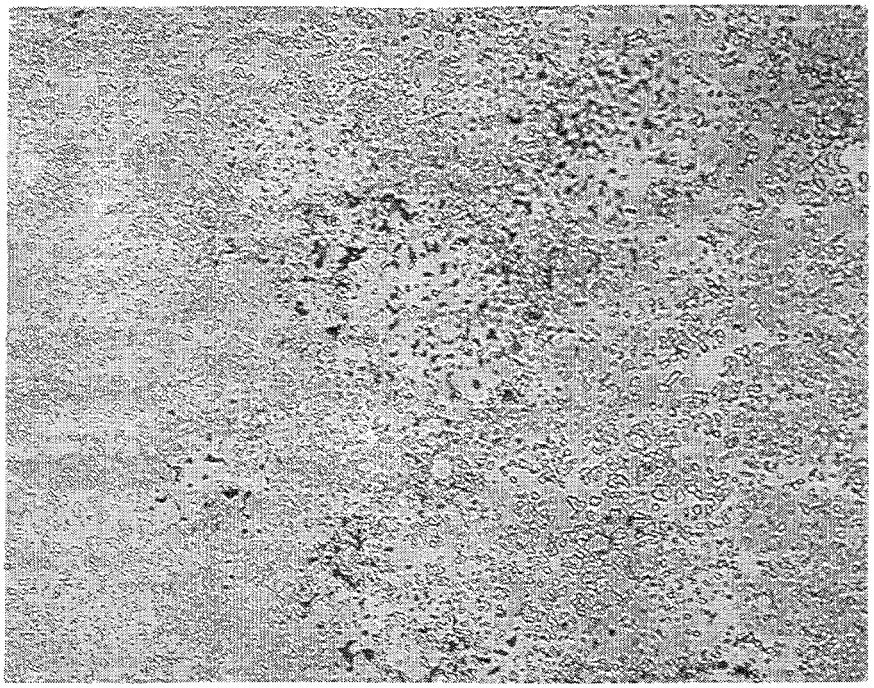

Fig. 7. Optical micrograph of MSB-3 produced by hot pressing at 1600°C.

FUTURE WORK

The key problems for the MSB alloys prepared by PM are microporosities and glassy phases. We plan to reduce microporosities by isothermally hot forging at high temperatures. The glassy phases based on silicates could be eliminated if a proper amount of carbon is added to remove the oxygen content in the alloy powders used in the current study. The MSB alloys contain three phases: Mo_3Si, Mo_5Si_3, $Mo_5(Si,B)_3$, and the morphology of the phases will be further controlled by thermomechanical treatment. We also plan to prepare the alloys by melting and casting, followed by hot extrusion. The hot extrusion will be used to reduce cast defects and to refine the microstructure of these multiphase alloys.

The mechanical properties of the MSB alloys with an optimum microstructure will be characterized by tensile testing as functions of test temperature and environment at ORNL. The fracture surfaces will be carefully analyzed in order to identify the cause of low-temperature brittleness. The alloys

with good tensile properties will be forwarded to Ames Laboratory for further characterization of their mechanical (e.g. creep properties) and metallurgical properties.

ACKNOWLEDGMENT

Thanks are due to Gwen Sims and Sharon Knee' for preparation of the manuscript.

REFERENCES

1. B. F. Glip, P. D. Desai, and C. Y. Ho, *Bibliography on Silicides*, MIAC Report 3, Metals Information and Analysis Center, West Lafayette, IN (1993).

2. J. Schlichting, *High Temperatures-High Pressures*, **10**, 241 (1978).

3. J. J. Petrovic, *MRS Bulletin*, **XVIII**, 35 (1993).

4. A. K. Vasudevan and J. J. Petrovic, *Matls. Sc. & Eng. A*, **A155**, 1 (1992).

5. P. J. Meschter and D. S. Schwarts, *JOM* **41**, 52 (1989).

6. D. L. Anton and D. M. Shah, p. 733 in *Mat. Res. Soc. Symp. Proc.* **213** (1991).

7. D. P. Mason and D. C. Van Aken, p. 1129 in *Mat. Res. Soc. Symp. Proc.* **288** (1993).

8. K. Sadananda and C. R. Feng, p. 157 in *Mat. Res. Soc. Symp. Proc.* **322**.

9. R. Barlett, J. W. McCamont, and P. R. Gage, *J. Am. Ceram. Soc.* **48**, 551 (1965).

10. J. B. Berkowitz-Mattuck and R. R. Dils, **112**, 583 (1965).

11. A. J. Thom, M. K. Meyer, M. Akinc, and Y. Kim, p. 413, *Processing and Fabrication of Advanced Materials for High Temperautre Applications—III*, eds. T. S. Srivatsan and V. A. Ravi, TMS, Warrendale, PA (1993).

12. M. K. Meyer, M. J. Kramer, and Mufit Akinc, *J. Intermetallics*, Vol. **4**, (1996) in print.

13. B. Aronsson, T. Lundstrom, and S. Rundqvsit, *Borides, Silicides and Phosphides: A Critical Review of their Preparation, Properties and Crystal Chemistry*, London: Methuen & Co., Ltd. (1965).

14. R. A. Cutler, p. 787, *Ceramics and Glasses-Engineered Materials Handbook*, Vol. **4**, ed. S. J. Schneider, Jr., ASM International, Materials Park, USA (1991).

15. Mufit Akinc, Private Communications, May 1995, Ames Laboratory, Ames, Iowa, 50011.

16. H. Nowotny, E. Dimakopoulu, and H. Kudielka, *Monatsh. Chem.* **88**, 180 (1957).

17. H. Nowotny, E. Parthe, R. Kieffer, and F. Benesovsky, *Monatsh. Chem.* **85**, 255 (1954).

2.21 THE MECHANICAL RELIABILITY OF ALUMINA SCALES AND COATINGS

K. B. Alexander, K. Prüßner, and P. F. Tortorelli

INTRODUCTION

In many high-temperature fossil energy systems, corrosion and deleterious reactions with gases and condensable products in the operating environment often compromise materials performance. The presence of a stable surface oxide (either as thermally-grown scales or deposited coatings) can effectively protect the materials from these reactions if the oxides are slow-growing, dense and adherent to the substrate. The protection these brittle oxide films provide has long been a critical issue, particularly for applications involving severe high-temperature thermal cycles or very aggressive (for example, sulfidizing) environments. The various factors which control the scale/coating integrity and adherence are not well understood. The present multilaboratory collaborative work is intended to define the relationships between substrate characteristics (composition, microstructure, and mechanical behavior) and the structure and protective properties of deposited oxide coatings and/or thermally grown scales. Through such studies, the ultimate goal is to assure environmental protection through effective processing and materials selection leading to the development of corrosion-resistant, high-temperature materials for improved energy and environmental control systems.

The Oak Ridge National Laboratory (ORNL) work described in this paper is being conducted in collaboration with work sponsored by the Department of Energy's Office of Fossil Energy at Argonne National Laboratory (ANL) and Lawrence Berkeley National Laboratory (LBNL) as well as in concert with on-going interactions that are part of the Office of Basic Energy Sciences' Center of Excellence for the Synthesis and Processing of Advanced Materials. The Center of Excellence on Mechanically Reliable Surface Oxides and Coatings includes participants from ORNL, ANL, LBNL, Idaho National Engineering Laboratory (INEL) and Lawrence Livermore National Laboratory (LLNL). Each of these laboratories has appropriate expertise in areas of materials characterization, modeling, and coating/deposition techniques relevant to studies of oxide scales and coatings.

The initial work is focusing on several model systems, all of which form stable, slow-growing alumina scales at elevated temperatures. Systems were chosen which were relevant to ongoing technological interests as well as to represent a range of both "soft" and "stiff" substrates in order to explore the role of the substrate on the mechanical reliability of the oxide

scale. This paper will discuss work on the initial system chosen: alumina scales on iron-aluminum alloys with and without zirconium.

EXPERIMENTAL PROCEDURES

Three iron aluminide alloys have been studied to date. Their compositions and common designations are listed in Table 1.

Table 1. Compositions of iron-aluminum alloys used in this study.

Alloy Designation	Concentration[a] (at. %) Al	Cr	Zr	Nb	Other
FA186	28	5			
FA129	28	5	-	0.5	0.2 C
FAL	28	5	0.1	-	0.05 B

[a] Balance is Fe.

Ingots of these alloys were prepared by arc melting and casting. These were then rolled to a final thickness of between 0.8 and 1.3 mm. Rectangular specimens (typically 12 x 10 mm) were prepared from these sheets. Details of the magnetically-filtered cathodic-arc plasma-synthesis process used to deposit alumina coatings on FA186 and FAL alloys are described elsewhere.[1]

Gravimetric measurements under thermal cycling conditions were used to establish overall corrosion behavior at 1000°C. These cyclic oxidation experiments were conducted in static air by exposing coupons in individual pre-annealed alumina crucibles to a series of 24-h exposures. Scanning electron microscopy (SEM) was performed on oxidized coupons as well as on polished cross-sections through the scale.

A Nanoindenter™ was used to evaluate the mechanical properties of the oxide scales. Hardness and modulus measurements were obtained using a pyramidal Berkovitch indenter. Cracks were generated within the scale for cracking threshold measurements using a cube-corner indenter.[2] For these experiments, a series of indents at different loads were generated across a polished cross-section of a scale. The cracks were subsequently imaged in an SEM.

Room temperature four-point bend testing of oxidized coupons was performed *in situ* in a scanning electron microscope. The geometry of the bending rig is such that the tensile surface of the specimen is continuously observed during loading. The load is continuously monitored

and both still and video images of the tensile surface during loading and unloading can be acquired.

RESULTS AND DISCUSSION

The oxidation rate was significantly reduced for the iron-aluminide alloy containing zirconium (FAL) as shown by the thermal-cycling weight gain data in Fig. 1. Distinctive differences were also observed in the morphology of the oxide scales formed on the two alloys. As described previously,[3] the FAL alloy exhibited flat, uniform oxide surfaces with no evidence of spallation during thermal cycling, whereas a significant amount of spallation was observed after thermal cycling of the FA129 alloy, Fig. 2. Cross-sections through the scale on the FAL alloy showed that the scale was completely adherent but exhibited some porosity, Fig. 3. Zirconium-rich particles were also observed at the metal/oxide interface after oxidation of FAL alloys (Fig. 3).

The beneficial effect of zirconium on the oxidation resistance of Fe_3Al alloys is now well-documented over a temperature range of 900-1300°C. [3-5] However, its role in improving oxidation behavior is not well-defined. The present results show that zirconium-rich particles form at the oxide-metal interface and there is also some evidence that zirconium ions accumulate in the alumina scale.[6] This is consistent with the dynamic segregation behavior observed for reactive-element additions in many alumina-forming systems.[7] Other work has shown that the presence of Zr in the Fe-28Al-5Cr system suppresses segregation of sulfur to the metal-oxide interface. [8]

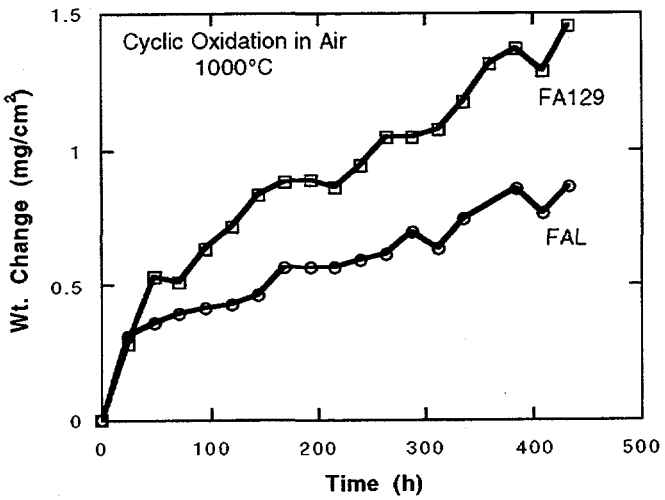

Fig. 1 Total weight gain (specimen + spall) as a function of time for FAL and FA129 cyclically oxidized in air at 1000°C. Each point is a single thermal cycle.

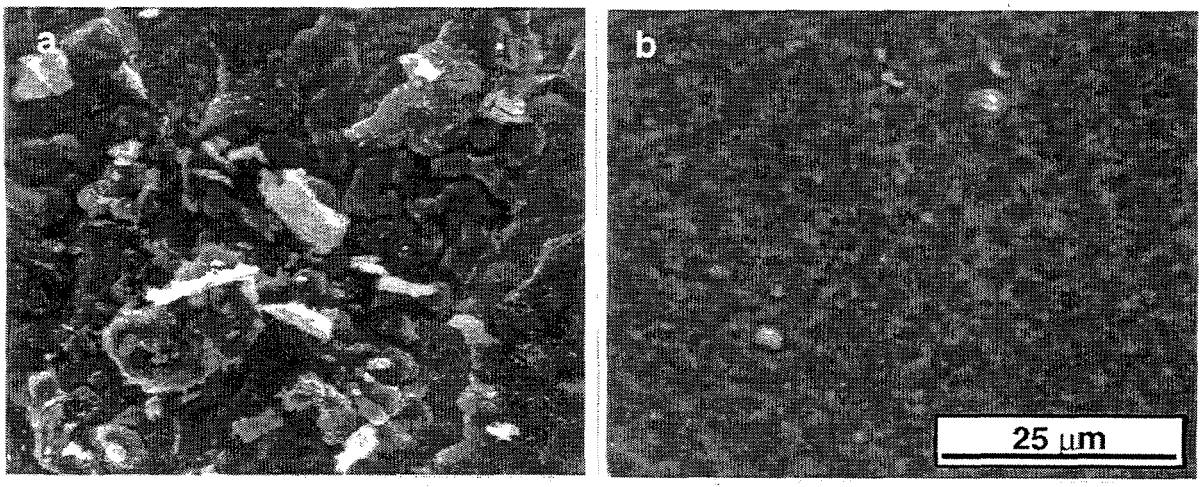

Fig. 2. SEM micrographs of iron-aluminide alloys that were oxidized for 48 h (2 - 24 h cycles) in air at 1000°C. (a) FA129 and (b) FAL. (From Ref. 3)

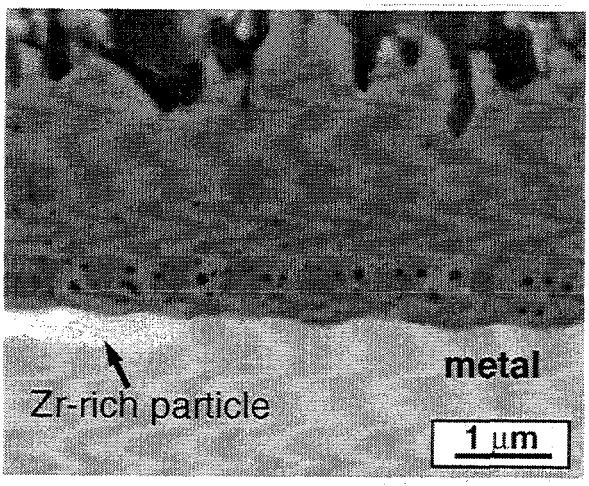

Fig. 3. Back-scattered electron image of oxide scale (2 x 24 h cycles at 1000°) in air) formed on FAL. Porosity within the scale is obvious. Zirconium-rich particles were observed at the metal/oxide interface.

The mechanical reliability of scales depends not only on their intrinsic characteristics such as adherence and defect structure, but also on their response to residual and imposed stresses. For the cracking threshold experiments, performed on an alumina scale grown on FAL, no cracking was detected at 2-μm-wide indents generated with a load of 10mN (1g). Higher loads generated much larger indents and extensive cracking from the corners of the pyramidal indents. The indentation size-indentation load relationship obtained from these experiments is shown in Fig. 4, along with nanoindentation data obtained from single crystal sapphire (indicated as a range).[2]

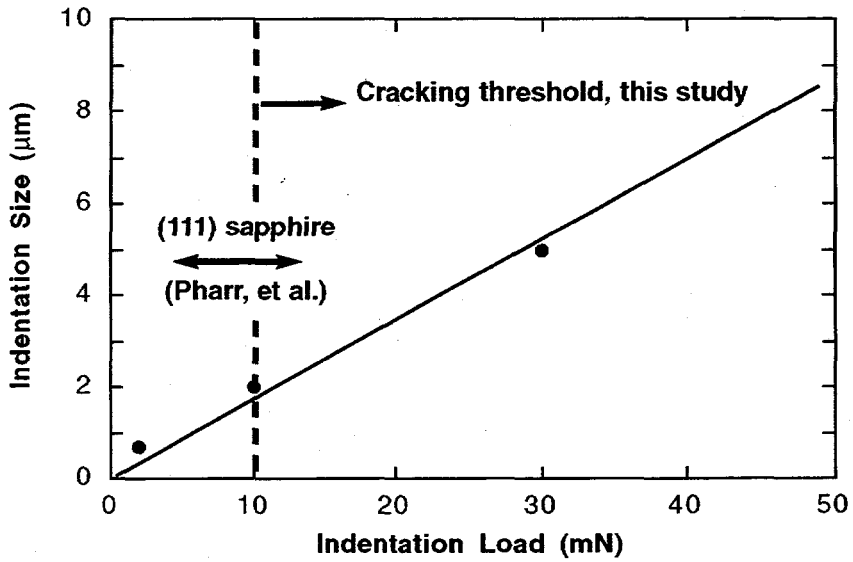

Fig. 4. Indentation size (full width) as a function of indentation load for indents in alumina scale on iron-aluminide. A cube-corner indenter was used for these experiments to attain higher stresses at a given indentation depth and thus induce cracking. Cracks were not observed below the indicated cracking threshold.

Note that the approximate cracking threshold measured for the alumina scale is in agreement with that measured for bulk single crystal α-Al_2O_3. Since cracking was not observed during nanoindentation until the indent was larger than 2 μm, fracture toughness measurements will be problematic since the oxide scale dimensions are typically smaller than the dimensions required to obtain valid indentation crack length measurements. However, the ability to precisely position and create small cracks within the microstructure, especially at or near the metal/oxide interface is encouraging. Such experiments will allow the examination of how crack propagation occurs within the scale and the role of the microstructure on this process.

The four-point-bending experiments also provide information as to how the scale/substrate system responds to imposed stresses. During loading of an FAL coupon with a thin (submicron) oxide scale, sets of parallel, regularly-spaced cracks were observed to spontaneously form on the tensile surface of the specimen after a critical load was reached, Fig. 5. Little growth of the cracks occurred during further loading. Although two sets of nearly orthogonal cracks were observed, the cracking was not perpendicular to the tensile axis. Although the metal substrate was plastically deformed approximately 30° over approximately 1

cm, the oxide scale remained fully intact with no spallation. Since the scale remained adherent, and cracking was so fine and occurred nearly 45° to the tensile axis, it is suspected that the substrate played a larger role in the deformation process than would be observed for thicker scales. Residual stresses in the oxide may also play a role. The crack spacing and critical load behavior was qualitatively similar to previous bend testing of alumina scales.[9]

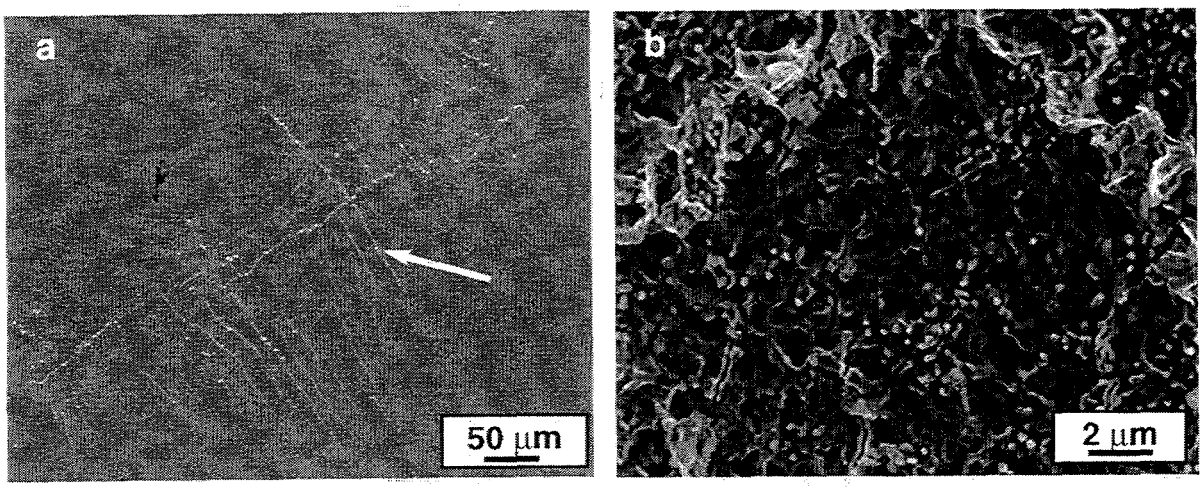

Fig. 5. SEM micrographs of cracking that occurs spontaneously within the scale during four-point-bend loading . The tensile loading direction is horizontal.

The microstructure of the plasma-deposited alumina coatings on FAL was examined in cross-section in the as-deposited condition as well as after exposure for 96 h at 1000°C in air. The surfaces of the deposited films were highly reflective. A comparison between the plasma-deposited alumina film and a thermally-grown scale is shown in Fig. 6. Both the surface and the metal/oxide interface are considerably smoother for the plasma-deposited film. Transmission electron microscopy[10] and X-ray diffraction studies[11] have shown that the as-deposited film is fully amorphous.

After oxidation (96 h at 1000°C in air), the uncoated FAL specimen exhibited an approximately 2-2.5 μm thick oxide scale. The total alumina thickness after oxidation on a specimen which had been coated with a 0.6-μm-thick plasma-deposited coating prior to oxidation was about 1 μm, as shown in Fig. 7. Zirconium-rich particles were observed at the metal/oxide interface in the case of the uncoated FAL, but not for the coated FAL specimen. A comparison between an as-deposited coating and a coated specimen which had been oxidized is shown in Figs. 6b and 6c. Note that the roughness of the metal/oxide interface has increased,

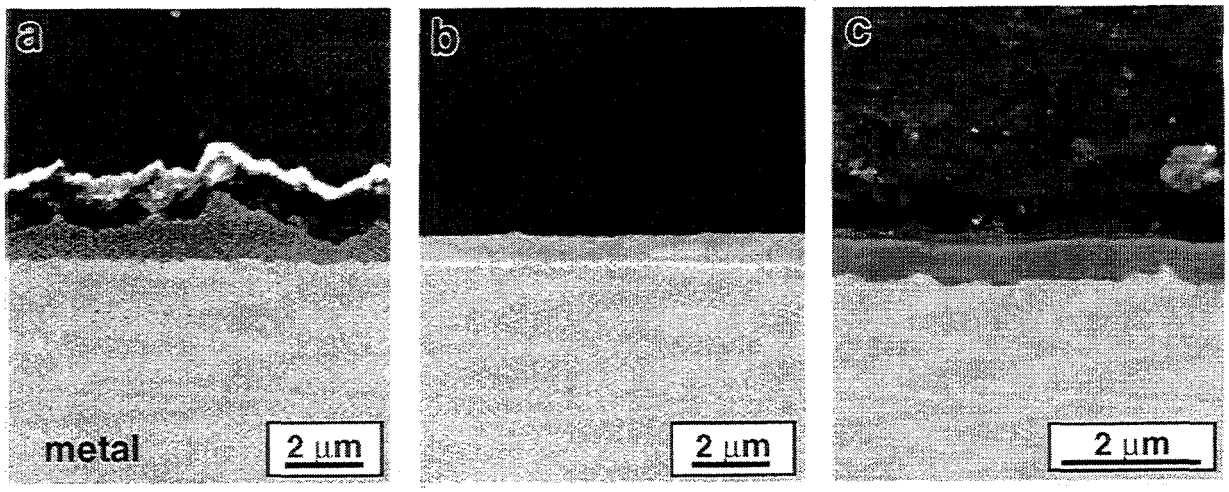

Fig. 6. SEM micrographs of alumina scales on FAL (a) thermally-grown alumina (2 x 24 h cycles at 1000°C), (b) plasma-deposited amorphous alumina, and (c) plasma-deposited film which has subsequently been oxidized for 96 h at 1000°C.

whereas the smoothness of the gas interface has been retained. Auger electron spectroscopy experiments have indicated that the new thermally-grown oxide forms at the metal/oxide interface, beneath the deposited film.[11] Additional experiments on FA186 have confirmed this

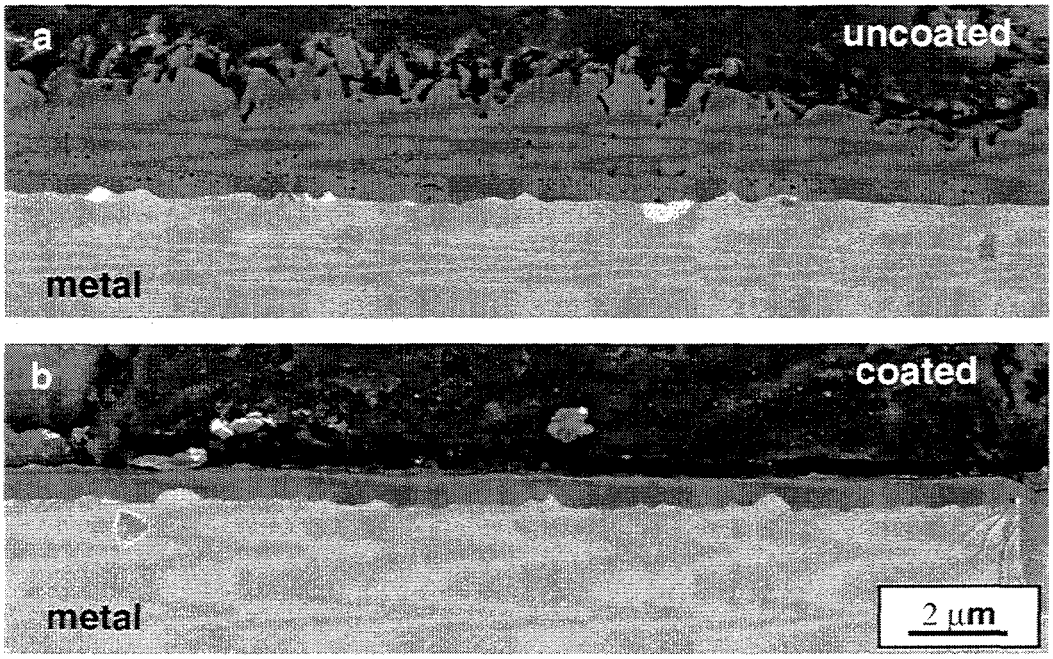

Fig. 7. SEM micrographs showing the effect of an amorphous plasma-deposited coating on the subsequent oxidation behavior of FAL. Cross-sections through oxide scales formed after 96h at 1000°C in air for (a) uncoated FAL and (b) FAL coated with 0.6μm-thick amorphous alumina prior to oxidation.

growth location, since the oxide film (plus thermally-grown oxide) completely spalls from the metal substrate on cooling consistent with a new thermally-grown oxide/metal interface forming during oxidation and subsequently controlling the adherence in these coated systems after oxidation. [11] These observations are all consistent with the growth of new oxides beneath the deposited film being controlled by the transport of oxygen through the film, rather than by the outward diffusion of aluminum. The presence of the amorphous alumina film obviously diminishes the oxidation rate for the coated FAL alloys, most probably by affecting the transport rate of oxygen and/or by suppressing the formation of the rapidly-growing transition oxides that form initially on bare metal surfaces during oxidation. The absence of zirconium-rich particles at the oxide/metal interface probably reflects diminished oxygen transport through the deposited film.

SUMMARY AND CONCLUSIONS

The mechanical reliability of scales and coatings can be assessed by traditional means such as gravimetric experiments and observations of adherence (or spallation) during thermal cycling. Other means to establish and study scale adherence such as measurements of the mechanical properties of scales and their response to stress and/or cracking as a function of processing, composition, and microstructure can also yield important insights into the mechanisms controlling the long-term reliability of protective scales. The adherence of the metal/oxide interface is clearly of the utmost importance as demonstrated by the oxidation experiments on the plasma-deposited coatings. Despite the fact that the oxidation rate was significantly diminished by the presence of the coating, the reliability of the coating was determined by the properties of the thermally-grown oxide/metal interface; which in turn is controlled (in this case) by the substrate composition. This multilaboratory project seeks to further explore and understand the fundamental relationships among properties, structure, and mechanical reliability of surface oxides that provide corrosion protection at high temperatures.

ACKNOWLEDGMENT

The authors thank M. Howell for experimental support. This research was sponsored by the Fossil Energy Advanced Research and Technology Development (AR&TD) Materials Program and the Division of Materials Science, U S. Department of Energy, DE-AC05-96OR22464 with Lockheed Martin Energy Research Corp. Research was performed in part with the SHaRE User Facilities at ORNL.

REFERENCES

1 I. W. Brown and Z. Wang, pp. 239-46 in *Proc. Ninth Annual Conf. Fossil Energy Materials*, N. C. Cole and R. R. Judkins (comp.), CONF-9505204, U. S. Department of Energy, August 1995.

2. D. S. Harding, W. C. Oliver, and G. M. Pharr, Mater. Res. Soc. Symp. Proc. 356 (1995) 663-68.

3. P. F. Tortorelli and K. B. Alexander, pp. 247-56 in *Proc. Ninth Annual Conf. Fossil Energy Materials*, N. C. Cole and R. R. Judkins (comp.), CONF-9505204, U. S. Department of Energy, August 1995.

4.J. H. DeVan, P. F. Tortorelli, and M. J. Bennett, "Environmental Effects on Iron Aluminides," pp. 309 - 20 in *Proc. Eighth Annual Conf. Fossil Energy Materials*, N. C. Cole and R. R. Judkins (comp.), CONF-9405143, U. S. Department of Energy, August 1994.

5. P. F. Tortorelli and J. H. DeVan, pp. 257-70 in Processing, Properties, and Applications of Iron Aluminides, J. H. Schneibel and M. A. Crimp (eds.), The Minerals, Metals, and Materials Society, Warrendale, PA, 1994.

6. J. A. Horton, Oak Ridge National Laboratory, unpublished results.

7. B. A. Pint, Oxid. Met. 45 (1996) 1-37.

8. P. Y. Hou, Lawrence Berkeley National Laboratory, unpublished results.

9. M. M. Nagl, S. R. J. Saunders, and V. Guttmann, Mater. High Temp. 12 (1994) 163-168.

10. K. B. Alexander and K. Prüβner, Oak Ridge National Laboratory, unpublished results.

11. P. Y. Hou, K. B. Alexander, Z. Wang, and I. G. Brown, "The Effect of Plasma Synthesized Alumina Coatings on the Oxidation Behavior of Iron Aluminides", accepted for publication in High Temperature Coatings II, The Minerals, Metals, and Materials Society, Warrendale, PA, 1996.

2.22 HIGH-TEMPERATURE CORROSION RESISTANCE OF CERAMICS AND CERAMIC COATINGS

P. F. Tortorelli

INTRODUCTION

Ceramics and ceramic composites offer the potential to operate fossil energy systems at the higher temperatures necessary for improved energy efficiency and better environmental control. However, because many fossil fuel-derived processes contain sulfur, chlorine, and carbon, as well as oxygen, degradation from high-temperature corrosion and environmental effects arising from reactions of solids with gases and condensible products is a common life-determining factor in operating systems. Ceramic-based products are not immune to such degradation; adequate corrosion resistance must be assured to exploit the technical and economic potential of such materials. This is normally accomplished by using stable, sound oxides that exist in their bulk form, that naturally grow as surface layers upon exposure to an oxidizing environment (such as SiO_2 formed on SiC), or that are deposited as a coating on a more susceptible material. It is therefore important to examine the critical issues with respect to environmental stability of ceramics that have the potential to be corrosion resistant in particular fossil environments. Key aspects include not only chemical compatibility, but the influence of the environment on the mechanical behavior of the ceramic materials. In addition, for coatings, the mechanical reliability of the ceramic is a key issue in that an otherwise corrosion-resistant surface layer must remain sound and adherent in order to provide protection to the underlying substrate.

The purpose of this work is to support the development of advanced ceramics and ceramic composites for applications in fossil environments by examining critical issues related to high-temperature corrosion resistance. More specifically, the overall objective of this task is to examine the chemical compatibility and reliability of potentially corrosion-resistant ceramics being developed as protective overcoats and/or structural materials as parts of other work elements funded by the AR&TD Program.

DISCUSSION OF CURRENT ACTIVITIES

The focus of this task is on the high-temperature corrosion of developmental ceramics that show potential as low moduli, low expansion fiber coatings in composites and/or as protective overcoats of susceptible ceramics. Therefore, the coatings to be investigated, and the order in which they are examined, depends on progress being made in the synthesis efforts, many of which are also being supported by the AR&TD Program. Because of this, execution of this task has been delayed due to the lack of appropriate, adequately characterized coatings. A small fraction of the expected effort has been expended on preparing the experimental exposure facilities for the oxidation and corrosion experiments. It is anticipated that a series of well-characterized mullite coatings on SiC and Si_3N_4 will be received from Boston University by the end of the third quarter of FY 1996. This will be used for the initial isothermal and cyclic oxidation experiments.

2.23 MATERIALS SUPPORT FOR HITAF

K. Breder, R. J. Parten, and H. T. Lin

INTRODUCTION

The purpose of this project is to compare structural ceramic materials proposed for use in the air heater of a coal fired high temperature furnace (HITAF) for power generation. This new generation of coal fired power plants with increased efficiency, fewer emissions and lower costs are currently being developed[1,2] under the Combustion 2000 program funded by Pittsburgh Energy Technology Center (PETC). Large improvements in efficiencies will require a change to combined cycles that employ gas turbines and steam turbines (Brayton Cycle) instead of exclusive reliance on steam turbines. Extremely high temperature working fluid is required to boost the efficiency, and the result is that the power plant sub-systems will be exposed to much more corrosive environments than in the present systems. The uses of ceramic heat exchangers are being investigated for those new power plants because of the potential for producing a clean, hot working fluid for the gas turbine.

Two industrial groups are currently funded under phase 2 of Combustion 2000, one team led by Foster Wheeler Development Corporation, and the other by United Technologies Research Center, and work in this project is intended to address some of the more long term needs for material information for design of these systems. Phase 1 of the present project focused on determining mechanical properties of some candidate materials at elevated temperatures in hot air.[3] Also in Phase 1 some preliminary coal ash corrosion work was performed.[4-6] In Phase 2 the emphasis is on evaluating the behavior of these candidate materials in a corrosive coal slag environment. This is performed by evaluating the corrosive attack of tube sections after exposure to coal ash at several temperatures in a laboratory furnace, as well as evaluation of tubes exposed in a pilot scale combustor. An initial creep evaluation of two of the candidate ceramics have been carried out.

DISCUSSION OF CURRENT ACTIVITIES

Materials

Two of the materials studied in Phase I of this project were used in a set of flexural creep measurements. These were NT230 SiSiC from Saint Gobain Norton Industrial Ceramics and Lanxide DIMOX SiC_p reinforced Al_2O_3 from DuPont Lanxide Composites Inc. Both these ceramics had exhibited some creep during the high temperature dynamic fatigue measurements. NT230 SiSiC is siliconized silicon carbide and contains free silicon metal (8 vol%) and some residual porosity. The SiC_p/Al_2O_3 which is manufactured by the Lanxide Direct Oxidation process (DIMOX) contains 48 vol% SiC_p, 38 vol% Al_2O_3 and 13 vol% Al-alloy, and some residual porosity. The SiSiC ceramic was tested as machined while the Lanxide DIMOX was reoxidized by the manufacturer after machining.

The coal ash exposure experiments have been carried out using ceramic tubes. They are NT230 SiSiC from Saint Gobain Norton and Lanxide DIMOX SiC_p/Al_2O_3 from DuPont Lanxide Composites Inc. as described above, β-SiC from Coors Ceramics Co., and Hexoloy sintered α-SiC from Carborundum Co. The tubes were nominally 50 mm (2") OD and 38 mm (1.5") ID and were cut into 150 mm (6") long sections for exposure. A thorough description of the materials have been given previously.[3]

Experimental Procedure

Flexural creep tests were carried out using the SiC_p reinforced Al_2O_3 and the Siliconized SiC materials. These were shown in the dynamic fatigue experiments in phase 1 to exhibit excessive creep at some of the higher temperatures. The creep tests were conducted at temperatures between 1200°C and 1410°C in air at outer fiber stress levels ranging from 75 to 200 MPa in air. The test bars (3 x 4 x 50 mm) were loaded in a sintered α-SiC four-point flexure fixture with inner and outer spans of 20 and 40 mm, respectively. The desired stresses were applied to the tests specimens through an α-SiC push rod via a dead weight loading system. The displacement of the bend bars was measured by a high-temperature three-probe extensometer whose output was continuously recorded. The outer fiber stress and corresponding deformation strain were calculated based on the procedures described by Hollenberg et al.[7]

The slags for the exposure experiments were gathered from the taps of three cyclone-fired utility boilers. Two types of Illinois #6 bituminous coals were used. One was from coal burned at the Central Illinois Public Service Coffeen Plant [labeled Coffeen] and was produced from a low sulfur producing mine. The low sulfur (in the form of low FeS_2 content) leads to high viscosity of the slag, so therefore 1.5% limestone was added at the power plant to reduce the viscosity. The second Illinois #6 coal was from the Illinois Power Company Baldwin Plant [labeled Baldwin] and was a mixture of Illinois #6 and Illinois #5 coals, resulting in a typical slag with less Ca and more Fe than the batch from the Coffeen plant. The third slag came from coal burned at the Northern States Power Riverside Plant, and was produced from the Rochelle mine, Wyoming [labeled Rochelle]. Approximately 3% petroleum coke was added at the power plant.

Each slag was analyzed at the University of North Dakota Energy and Environmental Research Center (UNDEERC)[8] and was split from the main barrel according to ASTM D 2013 "Standard Method of Preparing Coal Samples for Analysis." The chemical compositions of the three coal ashes are given in Table 1.

Table 1. Chemical composition of the coal ashes.

Oxide, wt%	Coffeen	Baldwin	Rochelle
SiO_2	52.5	53.4	47.0
Al_2O_3	16.3	18.6	18.6
Fe_2O_3	13.5	17.6	5.3
TiO_2	0.7	0.7	1.4
P_2O_5	0.2	0.0	0.6
CaO	13.1	7.1	19.7
MgO	1.2	0.9	5.7
Na_2O	0.8	0.0	0.9
K_2O	1.6	1.7	0.4
SO_3	0.1	0.0	0.4

The test temperatures were 1090°C to produce a condition of sintered ash, 1260°C for a viscous molten ash, and 1430°C for a fluid molten ash. The tube-sections were placed in a box furnace; an initial layer of coal slag was added; and the furnace was brought up to temperature in 2 h. In order to replenish the coal slag 75 ml was added to each tube

length every 48 h through the top of the furnace. Total exposure time was 500 h after which the furnace was slowly cooled to room temperature. After inspection each tube was cut into 14 C-ring specimens for strength testing. The C-rings were placed in a mechanical test system containing a box furnace, re-heated to the exposure temperature and loaded in compression to failure at a fast loading rate (45 N/s). The strength was evaluated using the appropriate formula for C-rings in compression.[9] Three tubes were cut into C-rings and tested in the as-received condition in order to provide base-line strength data at each test temperature. The strength data were analyzed using Weibull statistics[10,11] and fractography was performed.

One tube section each 300 mm long of each material were exposed in a pilot scale combustor in order to tie the laboratory experiments to systems testing. The combustor was a 220 kW (750 000 Btu/h) pilot scale combustor at UNDEERC burning the same type of Illinois #6 coal from the Baldwin plant as described above.[12] The tube was placed in the coal stream in a section at a temperature between 1340°C and 1370°C and the total run was 100 h. One tube of the SiC_p reinforced Al_2O_3 material was placed in the radiant section at the Combustion and Environmental Research Facility (CERF) at (PETC) at a temperature between 1050°C and 1250°C. The CERF is a 150 kW (500 000 Btu/h) pilot scale combustor, and the tube was exposed in the combustor for 1000 h while miscellaneous eastern bituminous coals were burned for other experimental applications.[13] Both these tubes were sectioned into C-rings and strength tested at 1260°C as described above.

Results

Creep Results

The creep rates measured for SiC_p reinforced Al_2O_3 and SiSiC (NT230) are shown in Figs. 1 and 2, respectively. The results show that the creep rates for SiC_p reinforced Al_2O_3 at 1200°C are rather low but a significant increase in the creep rate is seen as the temperature is raised to 1300°C. The creep rates for the SiC_p reinforced Al_2O_3 were compared to the creep measured previously for a SiC whisker reinforced Al_2O_3 and it is seen that the particulate reinforced material compared favorably, in spite of the fact that the latter contained a significant amount of residual metal alloy.[14-16] Tensile creep experiments on this material is currently underway to investigate these properties in further detail.

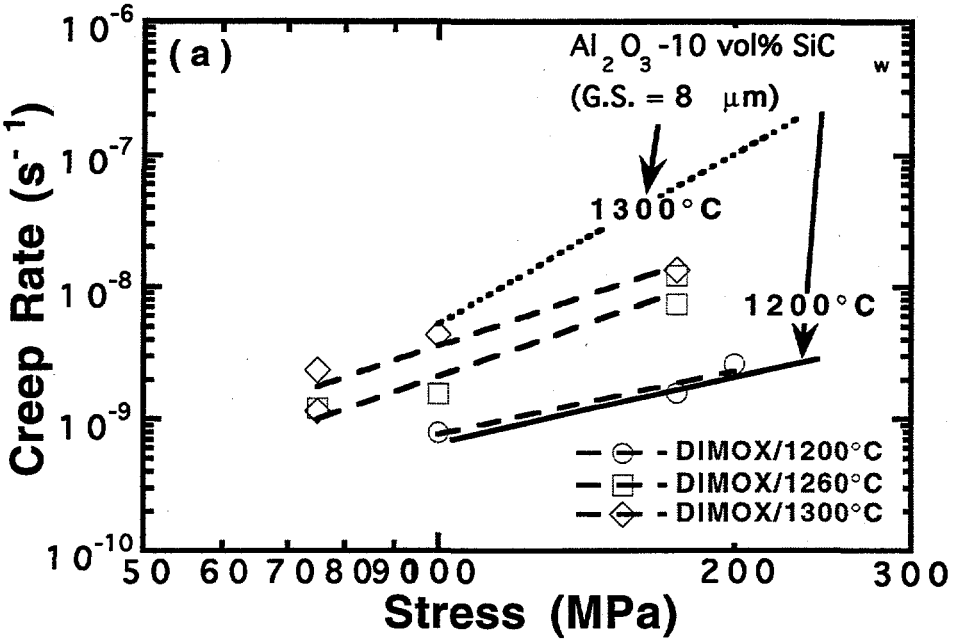

Figure 1. Comparison of measured creep rates for SiC_p reinforced Al_2O_3 (Lanxide Dimox) and SiC whisker reinforced Al_2O_3.

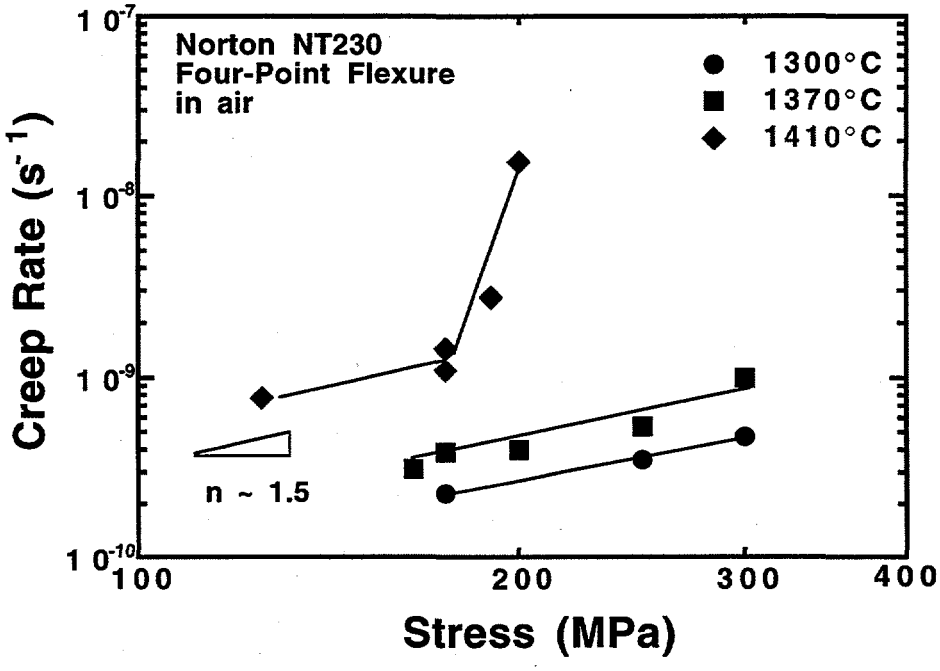

Figure 2. Creep rates for NT230 SiSiC at 1300, 1370 and 1410°C.

The creep rates fro the SiSiC are extremely low at temperatures under 1410°C. At that temperature the residual Si-metal in the material melts, and both a significant increase in creep rats and a transitional behavior at higher applied stresses are observed.

Exposure in the Laboratory Furnace

Following are descriptions of the tubes after 500 h exposure in the laboratory furnace. The visual appearance did not vary much between the materials, but varied between the coal slags and temperatures. Of a test matrix of 9 conditions for each material two are remaining at the present time.

At 1090°C the Baldwin slag was lightly sintered together but did not stick to the surface of the tubes except in certain small spots. The surface of the SiC_p reinforced Al_2O_3 was discolored gray-brown from its original gray color, but did not show any obvious surface damage. The surfaces of the other three ceramics remained essentially unchanged with the exception of a few spots of sintered slag stuck on to them.

At 1090°C the Coffeen slag was also lightly sintered together, and a layer was loosely sintered onto the tube. When the slag was peeled off, there was no obvious surface damage, but some brown discoloration from this darker slag was observed. The viscosity for the two coal slags was similar at 1430°C, but the temperature where the slag starts to solidify was somewhat higher for the Baldwin than the Coffeen slag, and this may explain the difference in appearance at this temperature. Details pertaining to the different viscosities will be included with detailed microprobe work later in the project.

The Rochelle slag was also just loosely sintered on to the tubes after exposure to 1090°C. The slag was yellow-brown in color, but had not caused any discoloration of the tubes.

At 1260°C the Baldwin slag was fused onto the tubes. The slag was brown and had a shiny glazed appearance on the side of the tube, and was black with large bubbles on the top surface where the slag had been applied.

At 1260°C the Coffeen slag was also well fused onto the tubes, but the appearance was less glazed and the color was uniformly matte brown. There were small bubbles in the slag, but fewer large bubbles at the surface.

At 1430°C the Baldwin slag was very well fused onto the slag in a thinner layer than for 1260°C. The color was generally matte brown.

At 1430°C the Coffeen slag was very well fused onto the tube in a thin brown layer. Few bubbles had developed, and it was obvious that the slag had been very fluid at that temperature.

Exposure in Coal Combustors

The tubes which had been exposed in the UNDEERC combustor at a temperature between 1340°C and 1370°C (Baldwin slag), had a highly glazed, even brown slag layer fused onto them. There was some slag build-up on one side, containing areas with large bubbles under the surface. Some material loss was observed on one side of the tubes, this was more pronounced for the SiC_p reinforced Al_2O_3 ceramic than for any of the other specimens. Each of the C-rings that were cut were measured and the dimensions will be compared to the as-received dimensions. The appearance of the slag on these tubes was very similar to the appearance of the slag on the tube from the laboratory furnace, (Baldwin slag at 1260°C) indicating a similar temperature level. However, the wall recession was in some cases more severe, indicating that the combustor environment, in which there is rapidly moving combustion gases passing over the tube, could be more severe than the furnace environment.

The slag on the SiC_p reinforced Al_2O_3 tube exposed at PETC at a temperature between 1050°C and 1250°C, was less sintered, which confirmed that the exposure temperature had been under the temperature for creating molten slag. The slag was discolored, was lightly sintered together, and was well attached to the tube. There did not seem to be a serious wall recession for this tube.

Strength Testing

Figure 3 shows the average strengths for the as received C-rings as well as the average strength measured after exposure at the UNDEERC and PETC pilot scale combustors. C-rings from the tubes exposed in both the pilot scale combustors were strength tested at 1260°C. From the ranges of temperatures given, this was in the high-end for the tube exposed at PETC and in the low end for the tubes exposed at UNDEERC; however, the temperature was chosen as a common denominator, and for ease of comparisons to the as-received data.

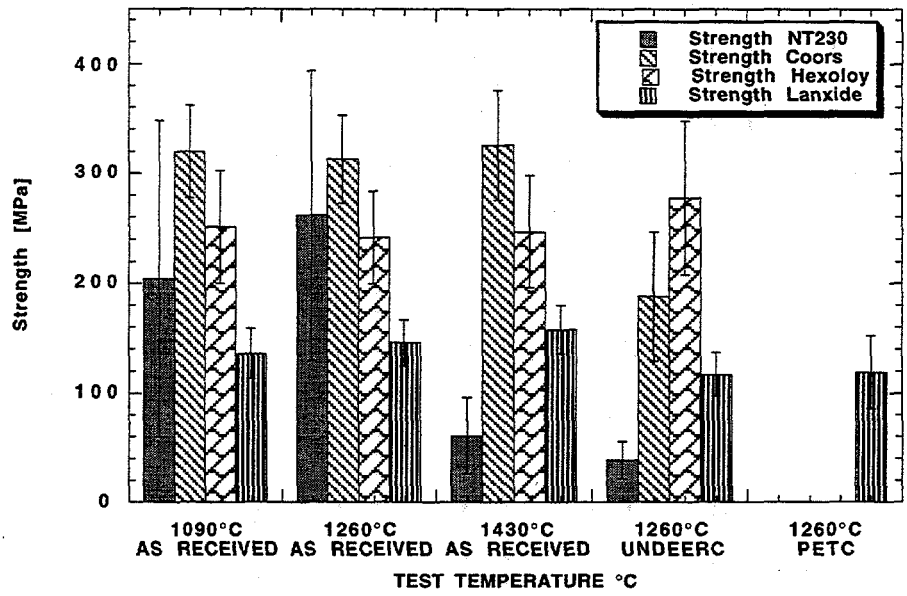

Figure 3. Comparison of strength of C-rings before and after exposure in pilot scale combustor.

Statistical analysis of the strength results for the NT230 SiSiC material showed that there was a significant drop in strength for the specimens tested at 1430°C. This is to be expected as the melting point for Si is 1410°C. The residual strength of the NT230 after the 100 h exposure in the UNDEERC combustor was significantly reduced compared to the as-received strength measured at 1260°C. The exposed specimens showed some reduction in wall thickness, and the preliminary fractography indicated that fracture generally was initiated from corrosion pits generated during the exposure. The overall variability in the strengths measured for this material was large (high standard deviation and low Weibull modulus), similar to what was observed previously in flexure testing of this material.[3]

The strength of the Coors β-SiC material remained the same over the entire temperature range, but a significant reduction in strength was observed after exposure in the UNDEERC combustor. The preliminary fractography for these specimens indicated a predominance of failure from surface pits or pores, probably related to the exposure.

Detailed Scanning Electron Microscopy (SEM) work is needed to determine the extent of these pits.

The strength of the Hexoloy α-SiC was unaffected by the temperature or the exposure at UNDEERC. The exposed specimens failed mostly from pores, but in contrast to the β-SiC the pores in these specimens were mostly in the volume near the surface, and as such unaffected by the exposure. The as-received specimens failed from similar types for pores throughout, consistent with the constant stress level.

The strength of the Lanxide SiC_p reinforced Al_2O_3 ceramic remained unaffected by the elevated temperatures, however, these were all lower than the room temperature strength for this material. After exposure in the two pilot scale combustors there was a slight but significant reduction in strength for this material. However, the strengths of the specimens from the two combustor runs were not significantly different, in spite of the fact that there was an order of magnitude difference in the exposure times for these tubes. This result indicates that the exposure temperature plays a very important role, and that significant differences in life-times may occur for only moderate changes in material exposure temperature. Further, the results indicate that it is important to investigate the influence of the coal chemistries. Also, microprobe studies of the reaction layers will give important additional information on the difference observed for the different slags.

SUMMARY

The measured creep rates for the two materials in this study that were shown to exhibit creep was low at moderate and intermediate temperatures (1090 - 1260°C) but higher creep rates and transitional behavior was observed for higher temperatures.

Four SiC-based ceramics were exposed to three different coal slags in a laboratory furnace. The materials were also exposed in a 100 h pilot scale combustor using one of the same coals. Initial strength testing after exposure indicated large differences between the materials in level of strength degradation and failure mechanisms.

ACKNOWLEDGMENTS

Research sponsored by the U.S. Department of Energy, Office of Fossil Energy, Pittsburgh Energy Technology Center, Advanced Combustion Technology Program, DOE/FE AA 20 10 00 0, under contract DE-AC05-96OR22464 with Lockheed Martin Energy Research Corp.

REFERENCES

1. J. M. Klara, "HIPPS: Beyond State-of-the-art. Part 1," *Power Eng.* **12** 37-39 (1993).

2. J. M. Klara, "HIPPS can Compete with Conventional PC Systems, Part 2," *Power Eng.* **1** 33-36 (1994).

3. K. Breder and V. J. Tennery, "Materials Support for HITAF, Final Report for Phase I," ORNL/TM-12815, Oak Ridge Nat. Laboratory, Oak Ridge, TN, 1995.

4. T. M. Strobel, J. P. Hurley, K. Breder, and J. E. Holowczak, "Coal Slag Corrosion and Strength Degradation of Silicon Carbide/Alumina Composites," *Cer. Eng. Sci. Proc.*, **15** [4] 579-86 (1984).

5. T. M. Strobel, J. P. Hurley, K. Breder, and J. E. Holowczak, "Coal Slag Corrosion and Strength Degradation of Siliconized Silicon Carbide," *Cer. Eng. Sci. Proc.*, **16** [5] 911-18 (1985).

6. K. Breder, V. J. Tennery, T. M. Strobel, J. P. Hurley, and J. E. Holowczak, "Strength Measurements of Monolithic SiC and Al_2O_3/SiC Composites After Exposure to Coal Slag," *J. Am. Cer. Soc.* **78** [10] 2837-40 (1995).

7. G. W. Hollenberg, G. R. Terwilliger, and R. S. Gordon, "Calculation of Stress and Strain in Four-Point Bending creep Tests," *J. Am. Cer. Soc.* **54** [4] 196-99 (1971).

8. J. P. Hurley, "Support Services for Ceramic Fiber-Ceramic Matrix Composites" ORNL/Sub/94-SS112/01, Oak Ridge National Laboratory, Oak Ridge, TN 1995.

9. O. M. Jadaan, D. L. Shelleman, J. C. Conway, Jr. J. J. Mecholsky, Jr., and R. E. Tressler, "Prediction of the Strength of Ceramic Tubular Components: Part1 - Analysis," *Journal of Testing and Evaluation*, **19** [3] 181-91 (1991).

10. W. Weibull, "A Statistical Theory for the Strength of Materials, "Ingeniörsvetenskapsakademien, Handligar, No. 151 (1939).

11. S. Duffy and E. Baker, Manual for Spread Sheet Macro for Estimation of Weibull Parameters Based on the Maximum Likelihood Method, Civil Eng. Dep., Cleveland State University, Cleveland Ohio, 1995.

12. T. M. Strobel, J. P. Hurley and J. R. Gunderson, "Pilot-Scale Testing of Silicon-Based Ceramics," to be published in *Cer. Eng. Sci Proc.* **17** [4-5] 1996.

13. K. Natesan, M. Freeman, and M. Mathur, "Corrosion Performance of Materials for Advanced Combustion Systems," pp. 71-83 in Proceedings of the Ninth Annual Conference on Fossil Energy Materials, N. C. Cole and R. R. Judkins, Eds. U. S. Department of Energy, Oak Ridge, 1995.

14. H. T. Lin and P. F. Becher, "Creep behavior of a SiC-Whisker-Reinforced Alumina," *J. Am. Cer. Soc.* **73** [5] 1398-81 (1990).

15. H. T. Lin and P. F. Becher, "High-Temperature Creep deformation of Alumina-SiC-Whisker Composites," *J. Am. Cer. Soc.* **74** [8] 1886-93 (1991).

16. H. T. Lin and K. Breder, "Creep Deformation in Alumina-SiC Composite Produced Via a Directed Metal Oxidation Process," submitted for publication 1995.

3. ENVIRONMENTAL ANALYSIS SUPPORT

R. L. Miller

Activities in environmental analysis support included assistance to the Morgantown and Pittsburgh Energy Technology Centers (METC and PETC) in reviewing and preparing documents required by the National Environmental Policy Act (NEPA) for projects selected for the Clean Coal Technology (CCT) Program. An important activity was the preparation for METC of a final Environmental Assessment (EA) for the proposed Externally Fired Combined Cycle (EFCC) Project in Warren, Pennsylvania. In addition, a post-project environmental analysis was prepared for PETC to evaluate the Demonstration of Advanced Combustion Techniques for a Tangentially-Fired Boiler in Lynn Haven, Florida.

3.1 ENVIRONMENTAL SUPPORT TO THE CLEAN COAL TECHNOLOGY PROGRAM

R. L. Miller

Work during this period focused on the preparation for DOE's Morgantown Energy Technology Center (METC) of a final Environmental Assessment (EA) for the Externally Fired Combined Cycle (EFCC) Project in Warren, Pennsylvania. Proposed by the Pennsylvania Electric Company (Penelec) and selected by DOE in the fifth solicitation of the CCT Program, the project would be sited at one of the two units at Penelec's Warren Station. The EFCC Project proposes to replace two existing boilers with a new "power island" consisting of a staged coal combustor, slag screen, heat exchanger, an indirectly fired gas turbine, and a heat recovery steam generator. Subsequently, Unit 2 would operate in combined-cycle mode using the new gas turbine and the existing steam turbine simultaneously. The gas turbine would generate 25 megawatts of electricity so that Unit 2 output would increase from the existing 48 megawatts generated by the steam turbine to a total of 73 megawatts. Operation of a conventional flue gas desulfurization dry scrubber as part of the EFCC technology is expected to decrease SO_2 emissions by 90% per kilowatt-hour of electricity generated, and NO_x emissions are anticipated to be 60% less per kilowatt-hour of electricity generated because of the staged combustor. Because the EFCC technology would be more efficient, less carbon dioxide (CO_2) would be emitted to the atmosphere per kilowatt-hour of electricity produced.

Potential resource areas of concern associated with the project include surface water resources, ecological resources, and archaeological resources. In particular, the potential effect of the heated discharge of once-through cooling water from the turbine condensers on aquatic life in the Allegheny River has been evaluated. A mussel survey conducted as part of the EA did not find either of the two endangered mussel species present in the vicinity of Warren Station. As recommended by the U.S. Fish and Wildlife Service, a survey was not conducted for other threatened species such as the Ohio lamprey because these species are more mobile and would be able to avoid any potential areas of adverse impact. Archaeological investigations have identified significant prehistoric, protohistoric, and historic occupations on the Warren Station site. There has been an ongoing investigation at this site, which is fenced and located east of the proposed project site near the eastern boundary of Warren Station. A cultural resources survey

recommended no further investigation of the proposed construction site because it has already been extensively disturbed and graded. However, it is expected that a plan would be developed for dealing with unanticipated finds during construction. Finally, Penelec has committed to installing liners at the active ash disposal area and ash ponds to minimize potential impacts to the groundwater.

Also during this period, a post-project environmental analysis was prepared for PETC to evaluate the Demonstration of Advanced Combustion Techniques for a Tangentially-Fired Boiler. Proposed by Southern Company Services (SCS) and selected by DOE in the second solicitation of the CCT Program, the project demonstrated the reduction of NO_x emissions from a pulverized coal-fired boiler by the use of a combustion control technique called the Low NO_x Concentric Firing System (LNCFS). The LNCFS technology separates the fuel and the air streams by directing the coal and the secondary air tangentially into the furnace at different angles. This technique causes the combustion of the fuel to occur in an oxygen-deficient zone prior to mixing with the secondary air. In addition, the LNCFS minimizes furnace wall slagging by passing air over the furnace wall tubes.

The project was demonstrated at the existing 180 megawatt Plant Lansing Smith Unit 2, owned by SCS's Gulf Power Company in Lynn Haven, Florida. The plant is representative of a large class of tangentially-fired boilers. An important feature of this project was that NO_x reduction levels and boiler performance were demonstrated on an operating utility boiler using long-term data. The long-term data were compared to pre-retrofit baseline data and statistically analyzed to provide data that allowed calculation of achievable emissions limits.

Findings from previous analyses indicated that the only environmental impact associated with this project that warranted evaluation was the decrease in NO_x emissions. No wastewater or solid waste streams were affected. Therefore, this environmental analysis focused on the effect of the demonstrated reduction of NO_x emissions, particularly within the context of meeting regulations. Ozone, a secondary pollutant formed from complex photochemical reactions involving NO_x and volatile organic compounds (e.g., unburned hydrocarbon exhaust from mobile sources), also was examined because of its dependence on NO_x in the atmosphere. The scope of the environmental analysis was expanded to include potential replication of the project at other locations in the future. The analysis accomplished this objective by using a framework that compared results with germane federal and state environmental regulations.

During the demonstration, the LNCFS was found to reduce average long-term NO_x emissions by up to 45% from baseline operations to achieve emission rates as low as 0.34 lb/MMBtu. These emissions are less than the current limit stipulated under Title IV of the Clean Air Act Amendments of 1990, but are not expected to meet future requirements for sources located in ozone transport regions or located in states mandating further controls in their implementation plans. Results of sampling for hazardous air pollutants revealed no appreciable differences in inorganic emissions between baseline conditions and the demonstrated technology. The only substantial difference in performance between baseline and the technology was a change in excess oxygen.

4.0 BIOPROCESSING RESEARCH

E. N. Kaufman

This section describes research and development activities performed for the Fossil Energy Bioprocessing Research Program. This program includes fundamental research for coal applications that investigates advanced reactor design for conversion of coal and coal liquids, the use of enzymes in pure organic media, and development of biological processes for the conversion of coal residuum. In addition, the program includes studies on advanced bioreactor systems for the treatment of gaseous substrates and the conversion to liquid fuels, removal of heteroatoms from heavy oils, renewable hydrogen production, remediation of oil containing soils. The program also includes natural gas and oil technology partnership support.

4.1 FUNDAMENTAL BIOPROCESSING RESEARCH FOR COAL APPLICATIONS

E.N. Kaufman

INTRODUCTION

The purpose of this program is to gain a fundamental understanding and sound scientific technical basis for evaluating the potential roles of innovative bioprocessing concepts for the utilization and conversion of coal. The aim is to explore the numerous ways in which advanced biological processes and techniques can open new opportunities for coal utilization or can replace more conventional techniques by use of milder conditions with less energy consumption or loss.

There are several roles where biotechnology is likely to be important in coal utilization and conversion. These include potential bioprocessing systems such as: conversion of coal to liquids or gases; biocatalytic beneficiation of coal-derived liquids for the removal of heteroatoms or heavy metals, biocatalytic upgrading of coal-derived liquids and conversion to useful chemical feedstocks; biocatalytic removal of SO_x and NO_x from coal combustion off-gas; environmental control technology for the removal or destruction of hazardous materials in process effluents and/or solid residues; and the removal and utilization of CO_2 from combustion off-gas. Effective bioprocesses for such applications will require detailed knowledge of the biological process mechanisms and advanced bioreactor technology that can be optimized for high productivity, as well as supporting upstream and downstream processes that will allow an effective integrated bioprocess.

DISCUSSION OF CURRENT ACTIVITIES

The efforts in FY 1994-5 have been directed toward 3 primary areas of research: (1) study and development of **Advanced Bioreactor Concepts**; (2) use and enhancement of **Biological Catalysts in Organic Media**; and (3) **Bioconversion of Coal Residuum**.

Advanced Bioreactor Concepts

In order to be economically feasible, all of the potential applications of biotechnology to coal processing will require efficient and inexpensive bioreactors and contactors. Biocatalysts and reactor schemes for further processing the coal derived liquid produced must also be addressed. The aim of this task is to develop advanced bioreactor concepts that are compatible with continuous operation and maximum throughput. In previous years we have developed a fluidized bed reactor for solid coal conversion. In FY 95-6 we have developed an electro-spray reactor for the efficient mixing of aqueous and organic phases that may be utilized for the biological processing of coal liquid. Using high

intensity electric fields, and taking advantage of the differing electrical conductivities of the biocatalyst containing aqueous phase and the organic coal liquid, the electro-spray reactor is able to form a fine emulsion (5 μm) with minimal energy utilization. Whereas impeller based mixers impart energy to the entire bulk solution to form an emulsion, the electro-spray reactor focuses energy only upon the liquid liquid interface. Energy requirements are three orders of magnitude lower when using the electro-spray reactor as compared to impeller based systems.

Biological Catalysts in Organic Media

There are several potential coal bioprocessing concepts that could use an organic solvent or produce liquid organic products, for example, the bioconversion of coal to liquids in an organic solvent or the bioprocessing of coal-derived liquids. For such a process, the biocatalyst (microorganism or enzyme) must be compatible with the organic medium. Naturally occurring enzymes may be modified by covalently attaching hydrophobic groups that render the enzyme soluble and active in organic solvents and have the potential to greatly expand applications of enzymatic catalysis. The reduction of elemental sulfur to hydrogen sulfide by a hydrogenase isolated from *Pyrococcus furiosus* has been investigated as a model system for organic biocatalysis. While the native hydrogenase catalyzed the reduction of sulfur to H_2S in aqueous solution, no activity was observed when the aqueous solvent was replaced with anhydrous toluene. Hydrogenase modified with PEG *p*-nitrophenyl carbonate demonstrated its native biocatalytic ability in toluene when the reducing dye benzyl viologen was also present. Neither benzyl viologen nor PEG *p*-nitrophenyl carbonate alone demonstrated reducing capability. PEG modified cellulase and benzyl viologen were also incapable of reducing sulfur to H_2S, indicating that the enzyme itself and not the modification procedure is responsible for the conversion in the nonpolar organic solvent. Sulfide production in toluene was tenfold higher than that produced in an aqueous system with equal enzyme activity (Figure 1); demonstrating the advantages of organic biocatalysis. Applications of bioprocessing in nonaqueous media are expected to provide significant advances in the areas of fossil fuels, renewable feedstocks, organic synthesis, and environmental control technology.

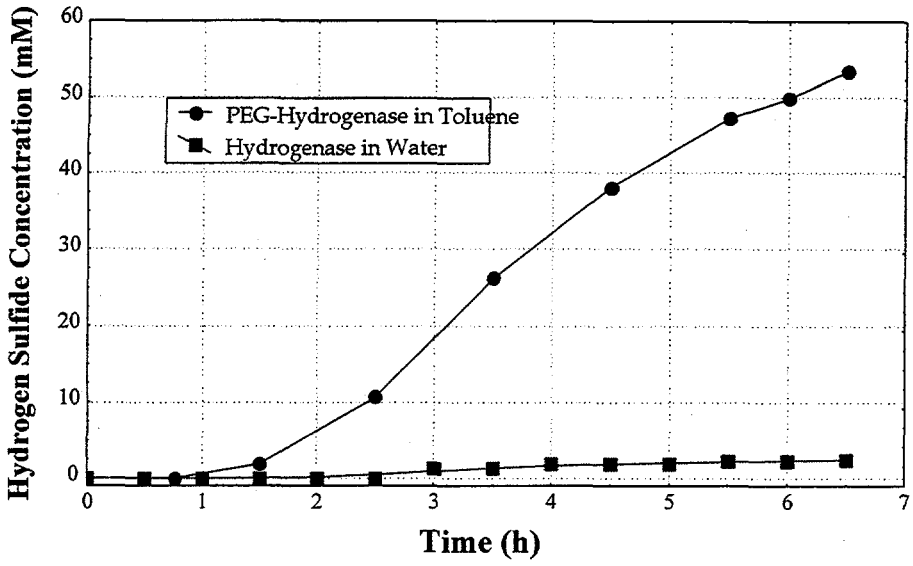

Figure 1. Production of H_2S from sulfur with PEG-hydrogenase (0.63 u/mL, 50 mg benzyl viologen) in 10mL toluene and unmodified hydrogenase (0.63 u/mL) in 10mL of 0.2M borate buffer, at pH 8.4. Production of sulfide ion the organic system is ten-fold higher than the aqueous, demonstrating the potential advantages of organic biocatalysis.

Bioconversion of Coal Residuum

The burning of coal at power plants produces sulfur dioxide which causes acid rain. Disposable sorbents such as limestone are utilized in many of today's flue gas desulfurization (FGD) systems. The absorption of SO_2 onto limestone produces calcium sulfite and carbon dioxide. This country utilizes less than 5% of its FGD gypsum and disposes the remaining 15 - 20 million tons per year, thus requiring a massive landfill volume. In the past year, we have demonstrated a combined chemical and biological process for the recycling of FGD gypsum into calcium carbonate and elemental sulfur. In this process, a mixed culture of sulfate-reducing bacteria (SRB) utilize inexpensive carbon sources such as sewage digest or synthesis gas to reduce FGD gypsum to hydrogen sulfide. The sulfide is then oxidized to elemental sulfur via reaction with ferric sulfate, and accumulating calcium ions are precipitated to calcium carbonate using carbon dioxide. Employing anaerobically digested-municipal sewage sludge (AD-MSS) medium as a carbon source, SRB's in serum bottles demonstrated a FGD gypsum reduction rate of 8 mg L^{-1} $h^{-1}(10^9$ cells$)^{-1}$. A chemostat with continuous addition of both AD-MSS media and gypsum exhibited sulfate reduction rates as high as 1.3 kg FGD gypsum/m^3•d. The increased biocatalyst density afforded by cell immobilization in a columnar reactor allowed a productivity of 152 mg SO_4/L•hr or 6.6 kg FGD gypsum/m^3•d. Both reactors demonstrated 100% conversion of sulfate, with 75 to100% recovery of elemental sulfur and as high as 70% COD utilization. Calcium carbonate was recovered from the reactor effluent upon precipitation using carbon dioxide. It was demonstrated that SRB's may

also use synthesis gas (CO, H_2, and CO_2) in the reduction of gypsum, further decreasing process costs. The formation of two marketable products — elemental sulfur and calcium carbonate — from FGD gypsum sludge, combined with the use of a low-cost carbon source and further improvements in reactor design, promises to offer an attractive alternative to the landfilling of FGD gypsum.

ACKNOWLEDGMENTS

This work was supported by the Advanced Research and Technology Development Program of the Office of Fossil Energy, U.S. Department of Energy under contract DE-AC05-96OR22464 with Lockheed Martin Energy Research Corp.

REFERENCES

E.N. Kaufman, M. H. Little, and P.T. Selvaraj, "A Biological Process for the Reclamation of FGD Gypsum Using Mixed Sulfate-Reducing Bacteria with Inexpensive Carbon Sources." 1996, *Applied Biochemistry and Biotechnology*. (submitted for publication).

E.N. Kaufman, M. H. Little, and P.T. Selvaraj, "Recycling of FGD Gypsum to Calcium Carbonate and Elemental Sulfur Using Mixed Sulfate Reducing Bacteria with Sewage Digest as a Carbon Source." 1996, *Journal of Chemical Technology and Biotechnology*. (in press).

Tsouris, C., H. M. Lizama, M. A. Spurrier, T. L. Takeuchi, and T. C. Scott, "Hydrodynamics of Bioreactors Systems for Liquid-Liquid Contacting," *Appl. Biochem. And Biotech.* (1996) in press.

Tsouris, C., V. M. Shah, M. A. Spurrier, and M. K. Lee, "Experiments on Electrostatic Dispersion of Aqueous Droplets into an Organic Stream," *Chem. Eng. Commun.* (1996). in press.

C.A. Woodward and E.N. Kaufman, "Enzymatic Catalysis in Organic Solvents: Polyethylene Glycol Modified Hydrogenase Retains Sulfhydrogenase Activity in Toluene." 1996, *Biotechnology and Bioengineering*. (in press).

E.N. Kaufman, J. N. Petersen, Y. Wang and M. H. Little. "Experimental and Numerical Characterization of Liquid Fluidized Beds of Coal." 1995, *Chemical Engineering Science* **50**: 3703-3714.

E. N. Kaufman, M. H. Little, C. A. Woodward, and C. D. Scott, "Enzymatic and Hydrodynamic Studies of a Liquid/Solid Fluidized-Bed Reactor for Coal Bioconversion," in D.S. Holmes and R.W. Smith (eds.), *Minerals Bioprocessing II*, The Minerals, Metals and Materials Society, Warrendale, PA,1995, 254-267.

E.N. Kaufman, C.D. Scott, C.A. Woodward, and T.C. Scott, "Use of Modified Enzymes for the Solubilization/Liquefaction of Bituminous Coal in a Fluidized-Bed Reactor," 1995, *Appl. Biochem. and Biotech.* **54:** 233-248.

Y. Wang, J. N. Petersen and E. N. Kaufman. "Modeling the Biological Solubilization of Coal in a Liquid Fluidized Bed Reactor." 1995 *Appl. Biochem. Biotech.* **51:** 437-448.

W.A. Weigand and E.N. Kaufman, "Bioprocessing Research Overview," 1995, *Appl. Biochem. and Biotech.* **51:** 293.

4.2 ADVANCED BIOREACTOR SYSTEMS FOR GASEOUS SUBSTRATES: CONVERSION OF SYNTHESIS GAS TO LIQUID FUELS AND REMOVAL OF SO_X AND NO_X FROM COAL COMBUSTION GASES

P. T. Selvaraj and E. N. Kaufman

INTRODUCTION

The purpose of this research program is the development and demonstration of a new generation of gaseous substrate based bioreactors for the production of liquid fuels from coal synthesis gas and the removal of NO_x and SO_x species from combustion flue gas. This R&D program is a joint effort between the staff of the Bioprocessing Research and Development Center (BRDC) of ORNL and the staff of Bioengineering Resources, Inc.(BRI) under a Cooperative Research and Development Agreement (CRADA). The Federal Coordinating Council for Science, Engineering, and Technology report entitled "Biotechnology for the 21st Century" and the recent Energy Policy Act of 1992 emphasizes research, development, and demonstration of the conversion of coal to gaseous and liquid fuels and the control of sulfur and nitrogen oxides in effluent streams. This R&D program presents an innovative approach to the use of bioprocessing concepts that will have utility in both of these identified areas.

Coal is thermochemically converted to synthesis gas consisting of carbon monoxide, hydrogen, and carbon dioxide. Conventional catalytic upgrading of coal synthesis gas into alcohols or other oxychemicals is subject to several processing problems such as interference of the other constituents in the synthesis gases, strict CO/H_2 ratios required to maintain a particular product distribution and yield, and high processing cost due to the operation at high temperatures and pressures. Recently isolated and identified bacterial strains capable of utilizing CO as a carbon source and converting CO and H_2 into mixed alcohols offer the potential of performing synthesis gas conversion using biocatalysts. Biocatalytic conversion, though slower than the conventional process, has several advantages such as decreased interference of the other constituents in the synthesis gases, not requiring strict CO/H_2 ratios and decreased capital and operating costs as the biocatalytic reactions operate at ambient temperatures and pressures. Several biocatalytic schemes have been proposed for the production of alcohols from synthesis gas. *Clostridium ljundahlii* catalyzes conversion of CO, H_2 and CO_2 into acetate and ethanol. However, the efficient biocatalytic production of liquid fuels from synthesis gas is constrained by low solubility of substrates and high cell density required for timely and complete substrate conversion. Therefore, the commercializable liquid fuel production requires the design of novel gas-phase bioreactors that combine high cell density with high product yield and high rate of substrate flux to the biocatalyst.

Development of such gas phase bioreactors also has application in the removal of SO_x and NO_x constituents from coal combustion flue gases, since this is an analogous process with many of the same types of process restraints and problems. Microorganisms such as

sulfate reducing bacteria and *Pseudomonas denitrificans* have been shown to interact with SO_x and NO_x respectively, however, efficient bioreactor systems for possible use in flue gas processing have not been developed and tested.

DISCUSSION OF CURRENT ACTIVITIES

Research conducted at ORNL during FY 1995-6 has focused upon flue gas conversion whereas BRI has had the lead role in conversion of synthesis gas to liquid fuels. Key impact parameters in flue gas treatment are the minimization of carbon and energy costs for the bioreactor and the optimization of reactor volumetric productivity through increased biomass density. To this end, we have investigated low cost carbon and energy sources as well as novel reactor designs utilizing the immobilization of the biocatalyst.

In laboratory studies of the reduction of SO_x, the principal nutrient for the biocatalyst is lactic acid. This carbon source would be far too expensive to use in a large scale process. We have investigated the use of low cost nutrients in order to improve the economic viability of a biological flue gas treatment process. Anaerobically digested-municipal sewage sludge (AD-MSS) medium has been used as sole carbon and energy source for the a mixed culture of sulfate reducing bacteria (SRB) and heterotrophs in the reduction of SO_x to hydrogen sulfide with subsequent chemical conversion to elemental sulfur. Municipal sewage sludge is readily available at a negative or near zero cost. Through the use of a mixed bacterial population, a more robust biocatalyst is achieved which is less sensitive to upsets in anaerobic conditions and which is better able to utilize a variety of carbon and energy sources. We have optimized the process of converting diffused air flotation sewage solids to AD-MSS media, minimizing the conversion time and use of added chemicals, and maximizing the yield of organic acids which serve as the carbon and energy sources for the biocatalyst. Figure 1 demonstrates the variety and yield of organic acids available in the AD-MSS media. Recently, we have also investigated the use of coal synthesis gas (CO, CO_2, and H_2) as a substrate for the biocatalyst. Initial results have revealed that a mixed culture of SRB are capable of utilizing syngas as the sole carbon and energy source in SO_x reduction, and efforts are underway to optimize syngas utilization and SO_x conversion in this system.

A successful reactor design for flue gas treatment must maximize volumetric productivity (mass of SO_x reduced per reactor volume per unit time) in order to decrease the capital cost of the reactor unit. We have investigated the use of immobilized cell reactors in order to maximize the biocatalyst density in the reactor. Gelatin beads used for cell immobilization proved too chemically fragile and were not able to withstand the high sulfite concentrations within the reactor. Porous polymeric beads proved more robust and have been utilized in reactor operation for more than nine months (see Figure2). We have achieved volumetric productivities in excess of 16 mmole SO_2/L*hr with 100% conversion of the SO_x.

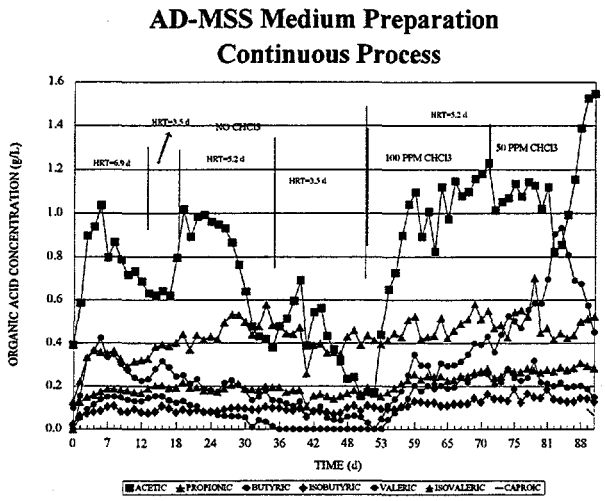

Figure 1. Organic acids present in AD-MSS media. Sewage serves as an inexpensive source of organic acids for use as carbon and energy sources for sulfate reducing bacteria which are cable of converting SO_x in flue gases.

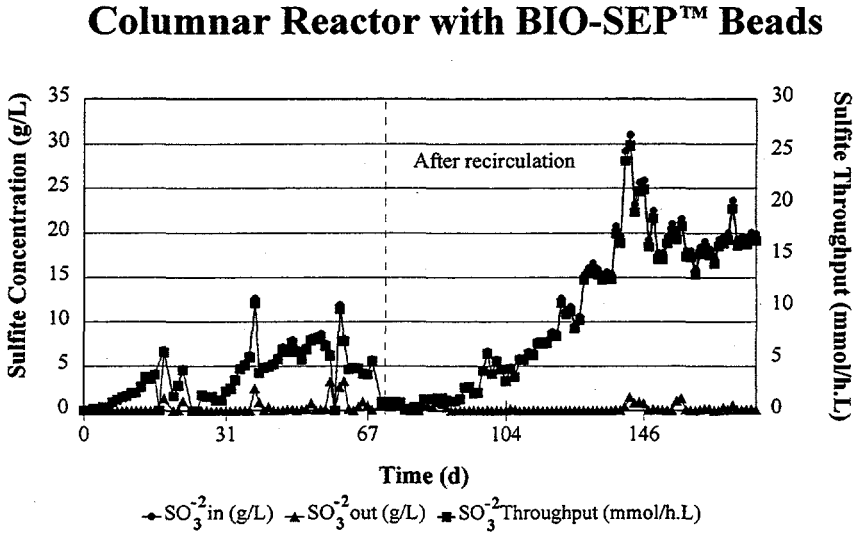

Figure 2 Conversion of SO_x in an immobilized cell bioreactor.

Future research will investigate the use of synthesis gas as a carbon and energy source for flue gas treatment bioreactors. Reactor design will be modified to account for the low solubility of the syngas in aqueous media. Mist, trickle bed and fixed bed reactors will be investigate as will systems for improved mass transport of the synthesis gas. ORNL will also be taking a larger role in the synthesis gas to liquid fuels project, investigating reactor design and solvent systems for improved mass transport.

ACKNOWLEDGMENTS

This work was supported by the Advanced Research and Technology Development Program of the Office of Fossil Energy, U.S. Department of Energy under contract DE-AC05-96OR22464 with Lockheed Martin Energy Research Corp.

REFERENCES

P.T. Selvaraj G. B. Meyer, and E.N. Kaufman, "Microbial Reduction of Sulfur Dioxide in Mixed Cultures of Sulfate Reducing Bacteria." 1996, *Applied Biochemistry and Biotechnology*. (in press).

4.3 REMOVAL OF HETEROATOMS AND METALS FROM HEAVY OILS BY BIOCONVERSION PROCESSES

E. N. Kaufman

INTRODUCTION

Biocatalysts, either appropriate microorganisms or isolated enzymes, will be used in an aqueous phase in contact with the heavy oil phase to extract heteroatoms such as sulfur from the oil phase by bioconversion processes. Somewhat similar work on coal processing will be adapted and extended for this application. Bacteria such as *Desulfovibrio desulfuricans* will be studied for the reductive removal of organically-bound sulfur and bacteria such as *Rhodococcus rhodochrum* will be investigated for the oxidative removal of sulfur. Isolated bacteria from either oil field co-produced sour water or from soil contaminated by oil spills will also be tested. At a later time, bacteria that interact with organic nitrogen may also be studied. This type of interaction will be carried out in advanced bioreactor systems where organic and aqueous phases are contacted. One new concept of emulsion-phase contacting, which will be investigated, disperses the aqueous phase in the organic phase and is then recoalesced for removal of the contaminants and recycled back to the reactor.

This program is a cooperative research and development program with the following companies: Baker Performance Chemicals, Chevron, Energy BioSystems, Exxon, Texaco, and UNOCAL. After verification of the bioprocessing concepts on a laboratory-scale, the end-product will be a demonstration of the technology at an industrial site. This should result in rapid transfer of the technology to industry.

DISCUSSION OF CURRENT ACTIVITIES

Biological removal of organic sulfur from crude oil offers an attractive alternative to conventional thermochemical treatment due to the mild operating conditions afforded by the biocatalyst. In order for biodesulfurization to realize commercial success, reactors must be designed which allow for sufficient liquid / liquid and gas / liquid mass transfer while simultaneously reducing operating costs. To this end, we have investigated the use of electro-spray reactors (see Figure 1) for the desulfurization of the model compound dibenzothiophene (DBT) as well as actual crude oil. The electro-spray reactor creates an emulsion of aqueous biocatalyst in the organic phase by concentrating forces at the liquid /liquid interface rather than imparting energy to the bulk solution as is done in impeller mixed reactors. Characterization of emulsion quality and determination of rates of DBT oxidation to 2-hydroxybiphenyl (2-HBP) were performed for both batch stirred reactors and in electro-spray reactors. Crude oil has also been run in the EPC and samples are currently being analyzed by Texaco in order to determine the degree of desulfurization.

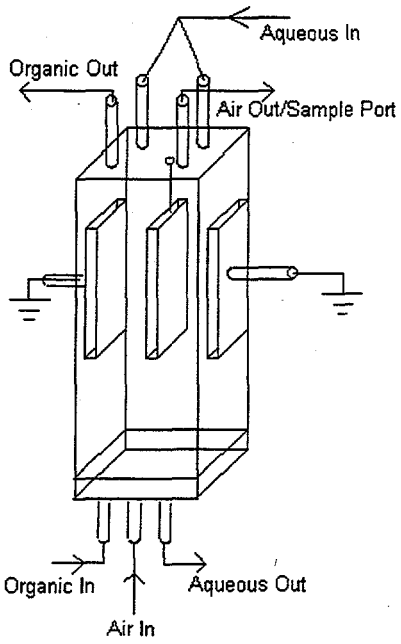

Figure 1 Schematic of the emulsion phase contractor. Electric fields are used to create a fine emulsion of water in oil in order to given the biocatalyst sufficient access to the sulfur compounds in crude oil.

ACKNOWLEDGMENTS

This work was supported by the Office of Oil & Gas Processing, U.S. Department of Energy under contract DE-AC05-96OR22464 with Lockheed Martin Energy Research Corp.

REFERENCES

E.N. Kaufman, J.B. Harkins, M. Rodriguez, S.E. Murphy, P.T. Selvaraj and C. Tsouris, "Development of an Electro-Spray Bioreactor for Crude Oil Processing." 1996, *Fuel Processing Technology.* (submitted for publication).

H.M. Lizama and E.N. Kaufman, "Biotreatment of H_2S in the Petroleum Industry," in D.S. Holmes and R.W. Smith (eds.), *Minerals Bioprocessing II*, The Minerals, Metals and Materials Society, Warrendale, PA, 1995, 241-253.

Tsouris, C., H. M. Lizama, M. A. Spurrier, T. L. Takeuchi, and T. C. Scott, "Hydrodynamics of Bioreactors Systems for Liquid-Liquid Contacting," *Appl. Biochem. And Biotech.* (1996) in press.

Tsouris, C., V. M. Shah, M. A. Spurrier, and M. K. Lee, "Experiments on Electrostatic Dispersion of Aqueous Droplets into an Organic Stream," *Chem. Eng. Commun.* (1996). in press.

H.M. Lizama, L.A. Wilkins, and T.C. Scott, "Dibenzothiophene Sulfur Can Serve as the Sole Electron Acceptor During Growth by Sulfate-Reducing Bacteria," (1995) *Biotechnology Letters,* **17**: 113-116

4.4 RENEWABLE HYDROGEN PRODUCTION FOR FOSSIL FUEL PROCESSING

E. Greenbaum, J. W. Lee, C. V. Tevault, and S. L. Blankinship

INTRODUCTION

In the current and prevailing concept of photosynthesis, the Z-scheme, first proposed by Hill and Bendall (*1*), PSII can split water, but is not thought to be able to perform one of PSI's assigned functions—the reduction of ferredoxin/$NADP^+$ essential for CO_2 assimilation. The Z-scheme therefore requires both PSII and PSI working in sequence for complete photosynthesis using water as the source of electrons and CO_2 as the terminal electron acceptor. Despite disagreement from several investigators (*2–9*), the Z-scheme has become the textbook model of photosynthesis (*10–14*). Recently, we have demonstrated that sustained photoassimilation of CO_2 and evolution of H_2 and O_2 in minimal medium can be achieved by the PSII light reaction without involvement of PSI in a PSI-deficient mutant of *Chlamydomonas* grown photoheterotrophically using an organic nutrient (acetate) (*15*). In this paper, we report a more exciting discovery that PSI-deficient mutants of *Chlamydomonas* were capable of growing photoautotrophically with CO_2 as the sole source of carbon. Since the Z-scheme requires both PSI and PSII working together in series for complete photosynthesis, it predicts that PSI-deficient mutants of green algae will not grow photoautotrophically. The discovery of photoautotrophic growth of PSI-deficient green algae without any organic nutrients, therefore, provides clear and solid evidence for the existence of a new type of photosynthesis—"PSII photosynthesis" that is an alternative to the Z-scheme. Our discovery may also provide an explanation for many "anomalous" quantum requirements that have been reported over the last 50 years, but failed to be explained by the Z-scheme.

DISCOVERY OF PHOTOAUTOTROPHIC GROWTH

Photoautotrophic growth of several PSI-deficient mutants of *Chlamydomonas* such as F8 (CC-1047) and B4 was first observed when acetate-grown aliquots were inoculated into 75 ml of minimal medium (*16*) in sterilized Erlenmeyer flasks and incubated under continuous actinic illumination [photosynthetically active radiation (PAR), 20 $\mu E \cdot m^{-2} \cdot s^{-1}$] provided by

daylight fluorescent lamps. The minimal medium contained only water and mineral elements plus a small amount of residual acetate. The flasks that contained the liquid culture were capped with phenolic screw caps that allowed air (CO_2) exchange (Fig. 1). Constant shaking of the culture flasks with a gyratory shaker at a speed of 140 rpm facilitated air exchange for CO_2 supply. Under these conditions, the algal cultures grew for months. The initial population immediately after inoculation was about 5.0×10^4 cells/ml for all cultures. Based on population growth monitored by counting algal cell density in the media using a microscopic hemacytometer, the algal cell doubling time at their logarithmic growth phase was 10, 10, and 6.7 days for F8, B4, and wild-type 137c, respectively, at the relatively low light intensity of 20 $\mu E \cdot m^{-2} \cdot s^{-1}$. The logarithmic phase lasted about 40–60 days, followed by a nearly linear growth phase. After about 100 days of incubation, the cell populations rose to more than 50 times the initial population. Growth was also visually apparent. The initial algal population was so low that the liquid culture looked essentially colorless. As incubation continued, the cultures grew progressively greener for months. Figure 1 is an illustration of the culture after 100 days of continuous illumination at 20 $\mu E \cdot m^{-2} \cdot s^{-1}$.

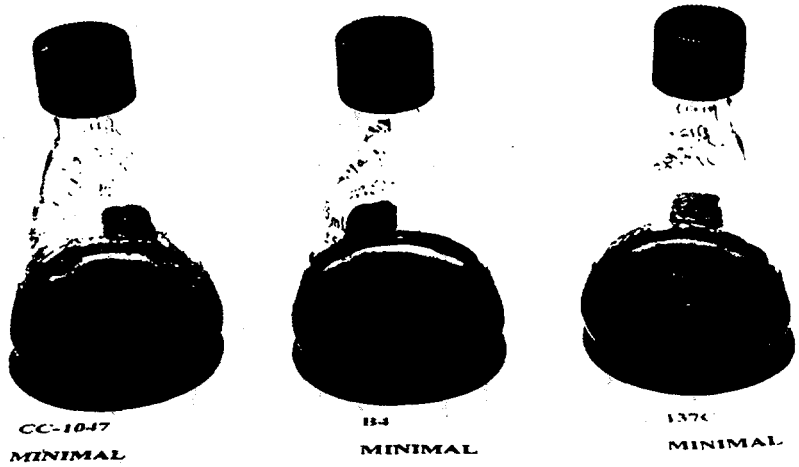

Figure 1. Photoautotrophic growth of PSI-deficient green algae F8 (CC-1047) and B4 using atmospheric CO_2 as the sole source of carbon in a minimal medium. The initial algal population following inoculation was 5×10^4 cells/ml, a concentration sufficiently low such that each liquid culture initially was essentially colorless. Incubation under continuous illumination (PAR, 20 $\mu E \cdot m^{-2} \cdot s^{-1}$) for a few months resulted in progressively greener cultures. The picture shows dark green cultures after 100 days of incubation. F8 and B4 cultures finally grew almost as green as the wild-type 137c. This was direct visual evidence that the PSI-deficient mutants can grow photoautotrophically.

Using the above photoautotrophically grown cultures as inocula, photoautotrophic growth was further demonstrated at moderate actinic intensity (PAR, 200 $\mu E \cdot m^{-2} \cdot s^{-1}$), where the growth was much faster. In these further experiments, photoautotrophic growth was studied using vertical glass growth tubes that were specially designed for algal growth and simultaneous measurement of CO_2 photoassimilation and O_2 and H_2 evolution, using an in-line CO_2 analyzer (LI-6252, Li-Cor Instruments, Inc.) with a flow-detection system described previously (*17*). Day and night cycles were mimicked by 12 hr of darkness and 12 hr of illumination (200 $\mu E \cdot m^{-2} \cdot s^{1}$) provided by daylight fluorescent lamps that were controlled by an electronic timer. The liquid culture in each tube (38 cm long and 3 cm in diameter) was continuously bubbled with 700 ppm CO_2 in helium or air at a rate of 50 ml/min to supply CO_2 and to agitate the algal suspension. Algal growth was measured by cell population and chlorophyll (chl) content. As illustrated in Fig. 2A and 2B, both the chl content and cell population rose quickly with time. With the supply of 700 ppm CO_2 in air and 200 $\mu E \cdot m^{-2} \cdot s^{-1}$ illumination, the cell doubling time was 1.0, 1.1, and 0.60 days for F8, B4, and 137c, respectively, which lasted for 2-3 days.

The data (Fig. 2A and 2B) also demonstrated that the mutants were able to grow not only in air but also in anaerobiosis when CO_2 was supplied in the helium atmosphere. The pattern of photoautotrophic growth for CO_2 in helium was similar to that for CO_2 in air. This is important since it indicated that neither an aerobic process such as mitochondrial respiration or chlororespiration (*18*, *19*) nor anaerobic hydrogenase activity (*20*) is a requirement for cell growth. Although the absence of atmospheric O_2 slowed the growth of the wild type by about 7%, it did not significantly affect the growth rate for F8 and B4, which was supported solely by PSII photosynthesis.

VERIFICATION FOR SOURCES OF CARBON, ELECTRONS AND ENERGY

The evidence that the carbon and electrons for cell growth are acquired from CO_2 fixation and water splitting was obtained by simultaneously measuring CO_2, O_2, and H_2 in the carrier gas effluent after bubbling through the growth tubes described above. The data clearly

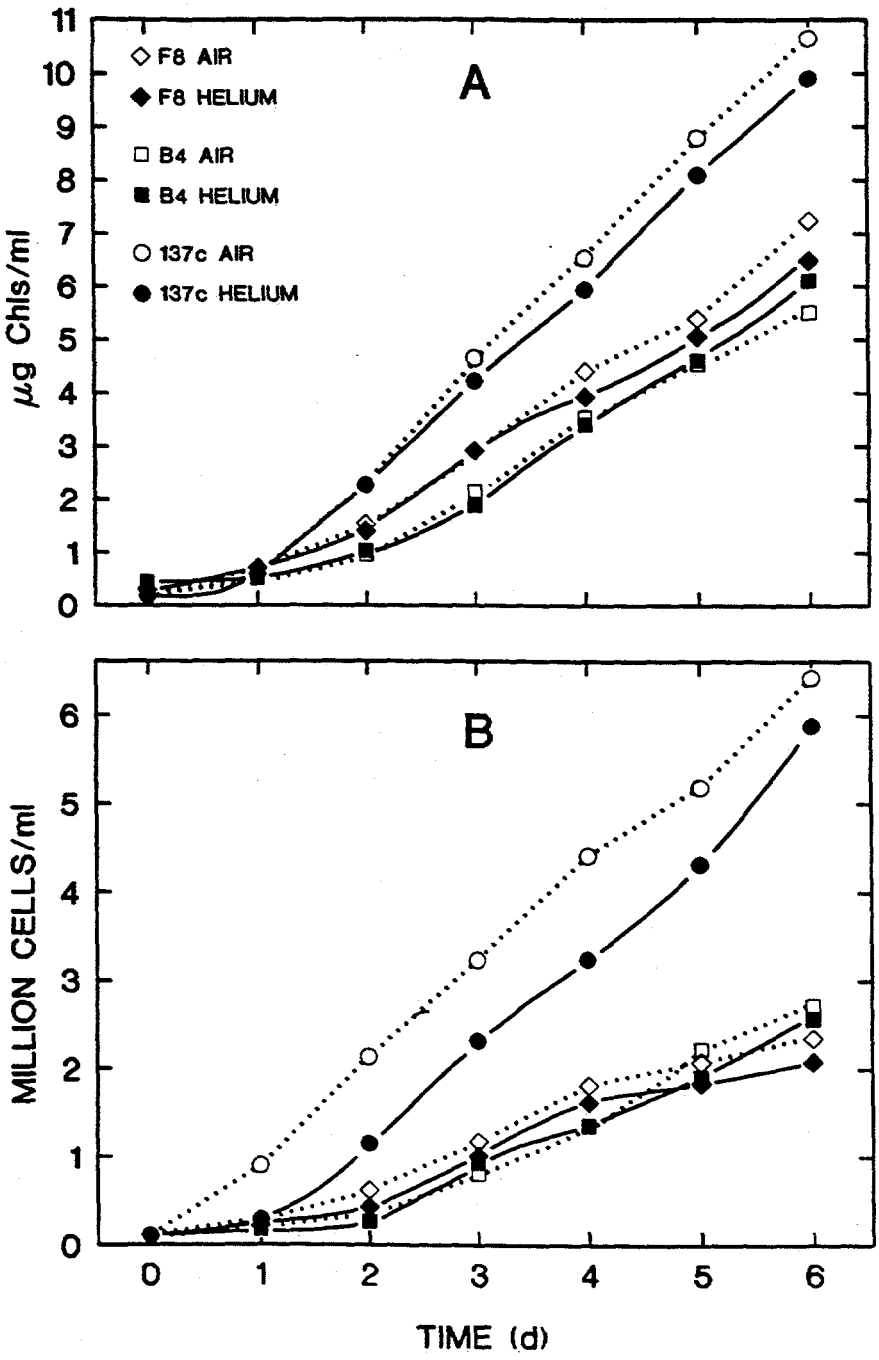

Figure 2. Photoautotrophic growth curves of PSI-deficient mutants F8 (diamonds), B4 (squares), and wild-type 137c (circles) using 700 ppm CO_2 in either air (open symbols) or helium (filled symbols) with cycles of 12 hr of darkness and 12 hr of light (PAR, 200 $\mu E \cdot m^{-2} \cdot s^{-1}$). The population growth was measured by both chl content (**A**) and cell density (**B**) of the cultures in the minimal medium.

demonstrated that both CO_2 uptake and O_2 evolution were light dependent (Fig. 3). Photoassimilation of CO_2 by the PSI-deficient mutants was stable in both aerobic (Fig. 3A) and anaerobic conditions (Fig. 3B). At steady-state photosynthesis, about 40% of the CO_2 supplied by the carrier gas was taken up by the algae, corresponding to a maximal photosynthesis rate of about 100 μmol $CO_2 \cdot hr^{-1} \cdot$ mg chl^{-1}. Under aerobic conditions, as expected, hydrogenase activity (H_2 production) was completely inactivated (Fig. 3A). However, the pattern and rates of CO_2 photoassimilation under aerobic conditions were rather similar to those under anaerobic conditions (Fig. 3B). These results indicated that neither hydrogenase activity nor any respiratory process (such as mitochondrial respiration or chlororespiration) is required by PSII photosynthesis. Even under anaerobic conditions where hydrogenase is activated, photoevolution of H_2 occurred only upon the initial onset of actinic illumination when the Calvin cycle for CO_2 reduction had not been fully activated. At steady state, H_2 evolution approached zero and reduction of CO_2 by the Calvin cycle became the exclusive sink for the reductant generated by photosynthetic water splitting. This hydrogen pattern is similar to that in wild-type *Chlamydomonas* reported previously and can be explained by light activation and dark inactivation of the Calvin cycle (*21*).

The simultaneous measurements of CO_2 uptake and O_2 evolution (Fig. 3B) also revealed that the photosynthetic quotient (CO_2 uptake/O_2 evolved) can be less than unity. After the first light cycle, the quotient (CO_2/O_2) during steady-state photosynthesis was as low as 0.90 in both the PSI-deficient algae and the wild type. The observed photosynthetic quotient is expected if CO_2 is reduced not only to the level of sugars, which would correspond to a quotient of unity, but also to the level of lipids and proteins, both of which are necessary for cell growth and correspond to photosynthetic quotients of <1 (*22*). The measured photosynthesis therefore is consistent with the observed cell growth.

Another aspect of the discovery is that PSII photosynthesis drives not only cell division but also cell development and mobility. The physical activity and morphological development of these algal cells were examined using both light microscopy and scanning electron microscopy. At the early stage of culture, within 30 days of illumination at 20 μE$\cdot$ $m^{-2} \cdot s^{-1}$ (or within the first 2 days in the case of 200 μE$\cdot$ $m^{-2} \cdot s^{-1}$), the PSI-deficient algae were mostly static green cells lacking flagella. Their cell size (volume) was, however, about 3-4

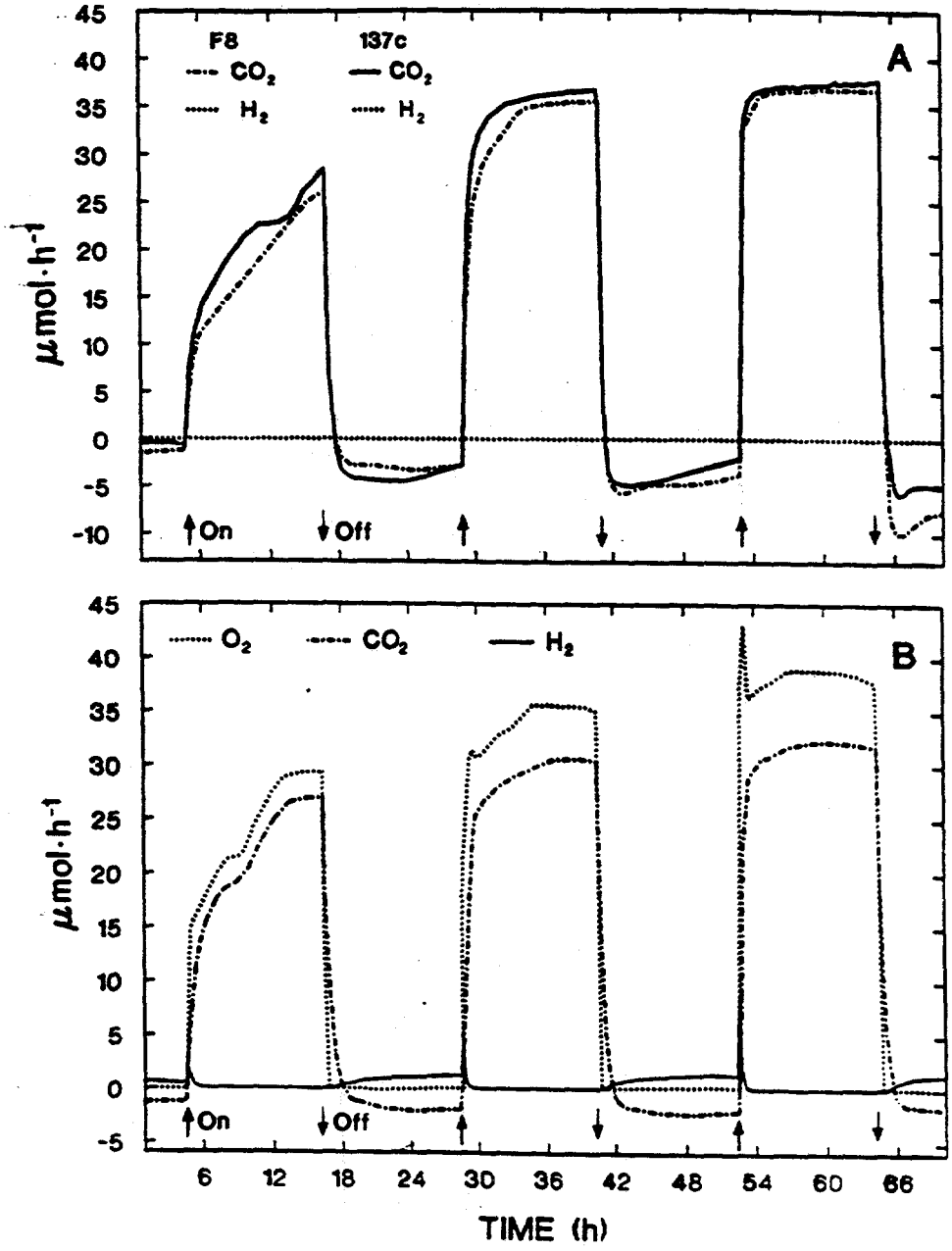

Figure 3. Photoassimilation of CO_2 and zero-rate production of H_2 by F8 and 137c with 700 ppm CO_2 in air (**A**); photoassimilation of CO_2 and evolution of O_2 and H_2 by F8 with 700 ppm CO_2 in helium (**B**). In each case, the initial algal population in the minimal medium (140 ml) was such that the chl concentration was about 0.4 μg/ml. The actinic illumination (PAR, 200 μE· m^{-2}· s^{-1}) was provided by daylight fluorescent lamps. The upward and downward arrows mark the on- and off-phases, respectively, of the actinic illumination.

time larger than the wild-type cells. After about 60 days of incubation under 20 $\mu E \cdot m^{-2} \cdot s^{-1}$ (or after 3 days with 200 $\mu E \cdot m^{-2} \cdot s^{-1}$), many of the mutant cells developed flagella and were able to swim actively in the liquid medium as observed under light microscopy. Similar cell development and mobility were observed also in the growth experiments that were conducted under anaerobic conditions. These results again demonstrated that cell growth and development can be achieved by PSII photosynthesis without the involvement of respiratory processes.

EXAMINATION OF PSI DEFICIENCY

Mutant F8 was obtained from mutagenesis by UV treatment and characterized as a stringent mutant that completely lacks CPI (the core of PSI) and two low-molecular-weight (20- and 21-kilodalton) polypeptides (*23*). Mutant B4 was obtained following metronidazole enrichment (*24*). Before and after our growth experiments, PSI content of these mutant algae was examined and complete absence of PSI was confirmed. Figure 4 presents a typical set of measurements for PSI reaction center (P700) photochemical activity by absorbance spectroscopy in thylakoid membranes that were isolated from these photoautotrophically grown algal cells. No P700 activity was detected in either F8 or B4, while the P700 signal was easily seen in the wild type. Based on signal-to-noise ratio, the chl:P700 ratio was larger than 30,000:1 in F8 and B4, whereas it was 943 (± 40):1 in 137c. Clearly, these PSI-deficient mutants grow photoautotrophically without PSI. PSII alone is sufficient to drive photosynthetic electron transport from water to the terminal acceptor CO_2 in living cells. As previously discussed (*15*), per-photon energy captured by PSII photochemistry at 680 nm (1.8 eV) is energetically sufficient to drive water splitting and the reduction of CO_2, with a maximum energy efficiency of about 68%. Therefore, although our findings are surprising because they contradict the long-held belief that PSI is essential for oxygenic photosynthesis and for photoautotrophic growth with water as electron donor, they still obey the laws of thermodynamics.

The role of PSI in photosynthesis could therefore be rather accessory, but apparently beneficial for natural survival. As shown in Fig. 2, the presence of PSI enhanced the rate of photoautotrophic growth by about 30–40% in 137c, compared with the PSI-deficient mutants (F8 and B4). Furthermore, as previously discussed *(15)*, the presence of PSI also confers

resistance to photoinhibition. As demonstrated by a photoautotrophic growth experiment under high light intensity (PAR, 2000 $\mu E \cdot m^{-2} \cdot s^{-1}$, equivalent to full sunlight intensity in summer) with air, the mutants grew from an initial population of 6.5×10^4 cells/ml to a final culture density about 8.5×10^5 cells/ml in 12 day-and-night cycles and 46.6% of the cells became colorless (photobleached), while the wild type reached a culture density of 1.72×10^6 cells/ml with only 7.8% of the cells photodamaged. These results indicate that PSI-deficient mutants can grow photoautotrophically even under high light intensity with air, although they have less rsistance to photoinhibition than the wild-type.

UNIVERSALITY OF THE DISCOVERY

As mentioned earlier, F8 and B4 were generated from different sources, yet they have a common ability to grow photoautotrophically. In addition to F8 and B4, similar photoautotrophic growth was observed in initial experiments using several other nuclear PSI-deficient mutants such as ac9 (CC-521), ac80 (CC-544), and F23 (CC-1062) and a chloroplast PSI-deficient mutant, 10-3C (CC-2046), that were provided by the Duke University *Chlamydomonas* Genetic Center. Therefore, this common growth ability suggests that the observed PSII photosynthesis is most likely universal, rather than a chance observation unique to a particular mutant.

Over the last 50 years, there has been a heated debate over whether the quantum requirement for photosynthesis is less than or greater than 8 photons (hν) per molecule of O_2 evolved. By analyzing measurements that have been made since 1950, Pirt (1986) and Osborne and Geider (1987) have concluded that the minimal quantum requirement is 5 to 6 $h\nu/O_2$ in wild-type green algae (*25*, *26*). Such values, if correct, cannot be explained by the Z-scheme since it predicts a quantum requirement of at least 8 $h\nu/O_2$. These previously-reported quantum requirements may, however, be consistent with the PSII photosynthesis we demonstrated in many PSI-deficient mutants of green algae such as F8, B4, ac9, and 10-3C. The minimal quantum requirement for PSII photosynthesis should be 4 $h\nu/O_2$, since PSII photosynthesis uses a single light reaction (PSII) instead of two (PSI and PSII). Pathway studies with chemical inhibitors indicated that in PSII photosynthesis, electron flow from PSII to ferredoxin/$NADP^+$ reduction is through the plastoquinone pool and cytochrome b/f

complex (*27*). With consideration of both practical energy loss such as a loss of about 15% excitations in PSII antenna and involvement of PSI activity such as PSI cyclic photophosphorylation, a quantum requirement (4 $h\nu/O_2$) for PSII photosynthesis can explain the reported values of 5 to 6 $h\nu/O_2$ in wild-type green algae (*25*, *26*). The previously reported quantum requirement (5 to 6 $h\nu/O_2$) therefore indicates that the PSII photosynthesis that we demonstrated in the mutant algae may occur even in the wild type under the right conditions.

Finally, the latest measurements for many C_3 higher plants by Osborne (1994) also showed a quantum requirement of < 8 $h\nu/O_2$, such as 7.67 ± 0.10 $h\nu/O_2$ for *Atriplex littoralis* and 7.69 ± 0.16 $h\nu/O_2$ for *Vicia faba* (*28*). This finding, again, cannot be explained by the Z-scheme. Based on high energy consumption in the multiple-cell tissue, Myers (1980) and Bell (1985) have estimated that the minimal quantum requirement for Z-scheme photosynthesis would be at least about 10 $h\nu/O_2$ in C_3 higher plants (*22*, *29*). Since PSII photosynthesis can have twice the energy efficiency of the Z-scheme, the observed quantum requirement in these higher plants can, in principle, be explained by the occurrence of PSII photosynthesis. Therefore, PSII photosynthesis may occur not only in green algae but also in higher plants, and the Z-scheme may not be the only mode of oxygenic photosynthesis. The obligatory series concept embedded in the Z-scheme of photosynthetic electron transport must now be reevaluated. We can now also conceive of significantly higher photosynthetic productivity for food, biomass, and H_2 production by application of the discovery.

REFERENCES AND NOTES

1. R. Hill and F. Bendall, *Nature* **186**, 136 (1960).
2. D. I. Arnon, H. Y. Tsujimoto, B. D. McSwain, *Nature* **207**, 1367 (1965).
3. H. J. Rurainski, J. Randles, G. E. Hoch, *Biochim. Biophys. Acta* **205**, 254 (1970).
4. H. J. Rurainski, J. Randles, G. E. Hoch, *FEBS Lett.* **13**, 98 (February 1971).
5. W. Arnold and J. R. Azzi, *Proc. Natl. Acad. Sci. USA* **61**, 29 (1968).
6. S. J. Pirt, Y. K. Lee, A. Richmond, M. W. Pirt, *J. Chem. Tech. Biotechnol.* **30**, 25 (1980).

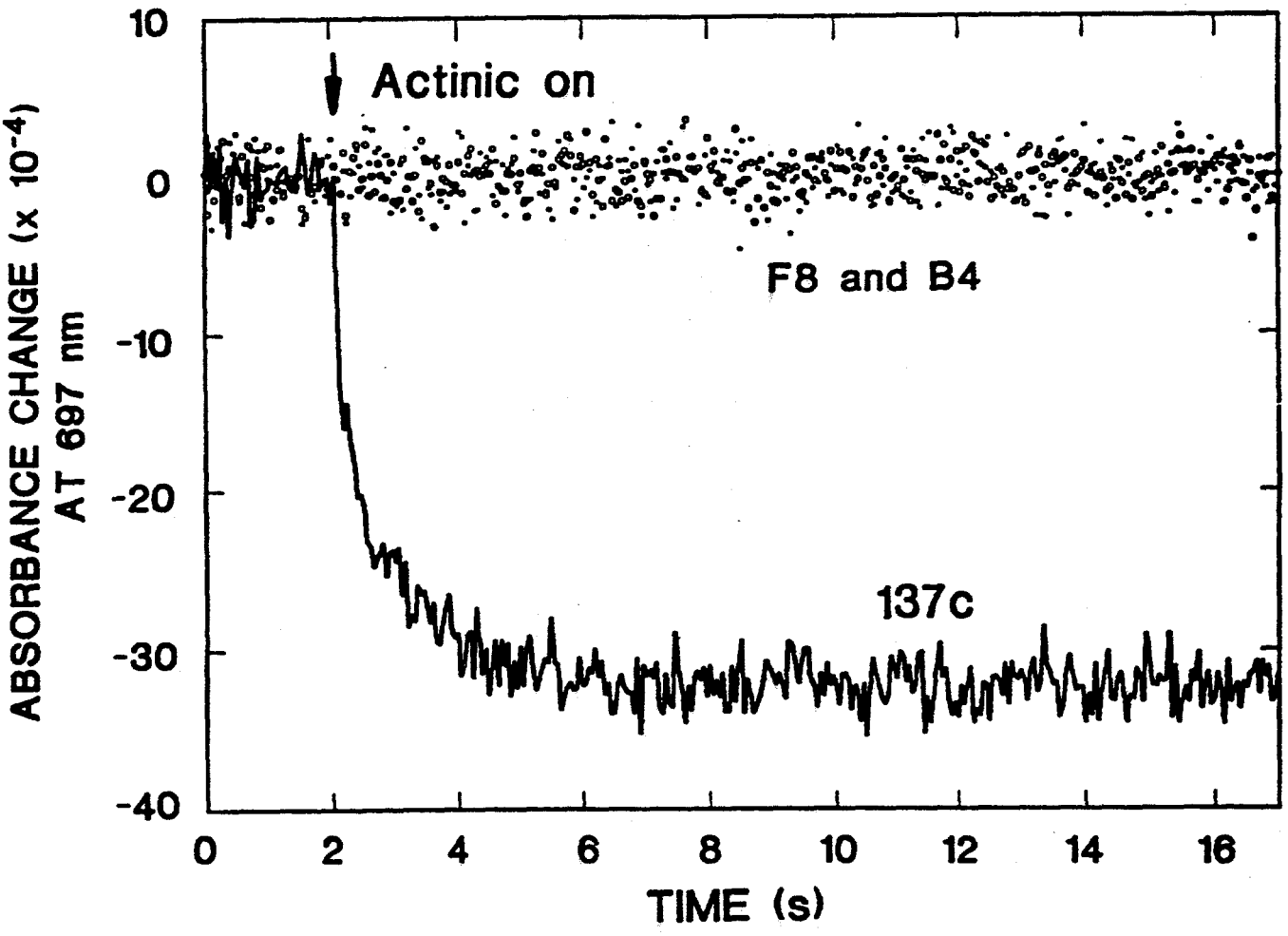

Figure 4. A typical set of reversible P700 photooxidation data obtained from thylakoids that were isolated from photoautotrophically grown cells of F8 (dots), B4 (circles), and 137c (line). The thylakoids were treated with cyanide (CN^-) to inhibit plastocyanin, which otherwise may interfere with P700 measurement by donating its electrons to the PSI reaction centers. The chl concentration was 47 μM for all samples (thylakoids). Before the measurements, the samples were dark adapted in the presence of ascorbate so that the PSI reaction centers were all kept in their reduced state (P700). The photoconversion of P700 to $P700^+$ was measured as the absorbance change at 697 nm. The downward arrow marks the onset of actinic illumination.

7. B. A. Osborne and R. J. Geider, *Plant Cell Environ.* **10**, 141 (1987).

8. B. A. Osborne and R. J. Geider, *Photosyn. Res.* **16**, 291 (1988).

9. D. I. Arnon and J. Barber, *Proc. Natl. Acad. Sci. USA* **87**, 5930 (1990).

10. L. Stryer, *Biochemistry* (W. H. Freeman and Company, New York, ed. 4, 1995), pp. 658–664.

11. F. B. Salisbury and C. W. Ross, *Plant Physiology* (Wadsworth Publishing Company, Belmont, CA, ed. 3, 1985), pp. 191–194.

12. T. W. Goodwin and E. I. Mercer, *Introduction to Plant Biochemistry* (Pergamon Press, Oxford, UK, ed. 2, 1986), pp. 117–124.

13. B. Alberts *et al.*, *Molecular Biology of the Cell* (Garland Publishing, Inc., New York, 1983), pp. 517–519.

14. J. Darnell, H. Lodish, D. Baltimore, *Molecular Cell Biology* (Scientific American Books, Inc., New York, 1986), pp. 901–903.

15. E. Greenbaum, J. W. Lee, C. V. Tevault, S. L. Blankinship, L. J. Mets, *Nature*, **376**, 438 (1995).

16. The composition of the minimal medium was essentially the same as that of N. Sueoka, *Proc. Natl. Acad. Sci. USA*, **46**, 83 (1960), except that the concentration of NH_4Cl, $CaCl_2$, and $MgSO_4$ in our minimal medium was 7.5, 0.35, and 0.41 mM, respectively.

17. J. W. Lee, S. L. Blankinship, E. Greenbaum, *Appl. Biochem. Biotechnol.* **51/52**, 379 (1995).

18. Y. W. Kow, D. L. Erbes, M. Gibbs, *Plant Physiol.* **69**, 442 (1982).

19. P. Bennoum, *Biochim. Biophys. Acta* **1186**, 59 (1994).

20. E. S. Bamberger, D. King, D. L. Erbes, M. Gibbs, *Plant Physiol.* **69**, 1268 (1982).

21. Briefly, when algae have been dark adapted and the fermentative hydrogen production pathway is turned on, the Calvin cycle is inactivated. Consequently, upon illumination all reducing equivalents are shunted through the ferredoxin/hydrogenase pathway. As the Calvin cycle is activated by the light, it subsequently becomes the exclusive sink for reducing equivalents [D. Graves, C. Tevault, E. Greenbaum, *Photochem. Photobiol.* **50**, 571 (1989)]. The monotonic decrease in the rate of hydrogen evolution, complemented by the parallel rise in CO_2 assimilation, reflects the real-time activation of the CO2 reduction pathway (Fig. 3B). When illumination was off, fermentative hydrogen production appeared again.

22. L. N. Bell, *Energetics of the Photosynthesizing Plant Cell* (Harwood Academic Publishers, London, 1985), chaps. 6, 7, and 9.

23. J. Girard, N. H. Chua, P. Bennoun, G. Schmidt, M. Delosme, *Curr. Genet.* **2**, 215 (1980).

24. C. Roitgrund and L. J. Mets, *Curr. Genet.* **17**, 147 (1990).

25. S. J. Pirt, *New Phytol.* **102**, 3 (1986).

26. B. A. Osborne and R. J. Geider, *New Phytol.* **106**, 631 (1987).

27. J. W. Lee and E. Greenbaum, in preparation (1996).

28. B. A. Osborne, *Plant Cell Environ.* **17**, 143 (1994)

29. J. Myers, *Primary Productivity in the Sea*, W. Ruhland, Ed. (Springer-Verlag, Berlin, 1980), pp. 1–16.

4.5 BIOLOGICAL QUALITY OF SOILS CONTAINING HYDROCARBONS AND EFFICACY OF ECOLOGICAL RISK REDUCTION BY BIOREMEDIATION ALTERNATIVES

A. J. Stewart, G. E. Napolitano and B.E. Sample

INTRODUCTION

This project provides technical support to the Petroleum Environmental Research Forum (PERF; a consortium of petroleum companies) on environmentally acceptable endpoints that may be used to help assess the ecological risk of petroleum hydrocarbon residuals in soils. The project, was designed in consultation with PERF representatives and focuses on the relationship between "chemically available" and "biologically available" measurements of petroleum hydrocarbon compounds in soils, a discrepancy of considerable interest to the petroleum industry. Presently, clean-up standards for soils contaminated with total petroleum hydrocarbon (TPH) constituents are based on concentrations of TPH, as measured in solvent extracts of soil samples. Interestingly, TPH includes a complex mixture of compounds which differ from one another in molecular weight and toxicity. Based on various studies with insecticides, herbicides and metals, some compounds apparently can slowly permeate into soil particles. If this situation occurs, the particle-embedded compounds may be extractable by use of organic solvents, and yet be unavailable biologically. This hypothesis serves as the central focus for our study. If this hypothesis is correct, then soil clean-up standards based on solvent-extractable TPH data may be more stringent than necessary to achieve a desired level of environmental risk. The economic significance of this possibility is considerable, because clean-up costs to achieve a low-risk status would, in most cases, be lower than those needed to achieve a standard based on present limits, which are based on measurements of "extractable" TPH.

As originally proposed, our project had four tasks. These included (1) development of a ecological risk-assessment framework that could be used to guide cost-effective clean-up strategies for TPH-contaminated soils; (2) testing of various TPH-contaminated soils, to provide estimates of the relationship between extractable TPH and soil toxicity; (3) development of chemical analysis methods for (a) rapid and quantitative assessment of TPH constituents in soils, and (b) analysis of microbial communities in petroleum-contaminated soils; and (4) summarizing information about bioremediation alternatives for TPH in soils, thus allowing more effective use of this alternative in certain clean-up situations.

A reduction in the anticipated level of funding for the project, plus a delay in obtaining the authorized funding, required us to reschedule several activities in Task 1 and to substantially reduce or delay activities planned for Task 4. Thus, this report summarizes progress to date in Task 1, Task 2 and Task 3, with emphasis on the latter two.

Task 1. Development of ecological risk assessment methods and tools

Preliminary work began on subtask (a), Framework for assessing ecological risks of petroleum hydrocarbons in soil. Progress included contacting numerous individuals involved in related work, and sketching of a conceptual model for risks from petroleum hydrocarbons in soil.

Task 2. Testing of TPH-contaminated soils for toxicity to earthworms

Task 2 involves conducting tests to assess the biological quality of various soil samples, some of which contain elevated concentrations of TPH. These tests use earthworms (*Eisenia foetida*) as "biodetectors" (Gibbs et al. 1995). In each test, replicate 100-gram portions of the soil are placed in

separate containers, and a pair of earthworms (pre-weighed) and a standard amount of fermented alfalfa (used by earthworms as food) is added to each container. Twenty-one days after a test has been started, the worms in each replicate of each sample are harvested and re-weighed. When the worms have been harvested, the soil in each replicate is also inspected carefully for earthworm cocoons (reproductive propagules); the number of cocoons per replicate is recorded. These data permit quantification of a soil's biological quality, in terms of earthworm survival, growth (change in weight), and reproduction.

The TPH-contaminated soil samples that are being shipped to ORNL for testing were collected from various petroleum-industry sites where prior releases of petroleum hydrocarbons occurred, such as refineries, shipping depots, production operations, etc. Each "TPH-contaminated" soil sample sent for testing also came with a corresponding "reference" soil, obtained from near the contaminated site. The reference-soil samples were presumed to be good controls, in that they either lack measurable levels of TPH, or contain TPH at concentrations much lower than those in soil from their contaminated-site counterpart. To unveil relationships between THP concentration and earthworm responses, we prepared various concentrations of each THP-contaminated soil by diluting it with appropriate amounts of "reference site" soil prior to testing with earthworms.

Ultimately, fourteen or more THP-contaminated soils (and their corresponding reference soils) will be analyzed rigorously with these methods. To date, we have completed screening-level tests with two TPH-contaminated soils (coded M and I), principally to verify efficacy of the dilution procedure and the earthworm testing method. The responses of the earthworms to these four soils (M and I, reference and highest-tested dilution) are summarized in Table 1.

Table 1. Survival, growth and reproduction of *Eisenia foetida* in reference and TPH-contaminated soil samples from two locations (coded M and I).

Soil Code and Type	TPH (mg/Kg)[a]	Survival (%)	Growth (mg/pair)[b]	Reproduction (cocoons/replicate)[c]
M - reference	140	100	123.5 ± 9.8	2.8
M- contaminated	10,000	100	82.8 ± 6.6	1.0
I - reference	30	100	50.9 ±16.1	0
I - contaminated	105	100	84.2 ± 7.4	0

[a]Computed as the sum of aliphatic and aromatic compounds, determined by Iatroscan, for non-diluted soil.
[b]Mean ± standard error per replicate, for 10 replicates.
[c]Mean number of cocoons per replicate, for 10 replicates.

The information in Table 1 shows that even moderately high concentrations of TPH constituents may not always be toxic to earthworms. In one dilution of soil from site M, where the TPH concentration was as high as 1,950 ppm, earthworms survived, grew and reproduced. The data in Table 1 also shows that constituents other than TPH may affect earthworm growth and reproduction. TPH concentrations in the reference and contaminated soil samples from site I were equal to or less than 105 ppm, but earthworm growth and reproduction in these soils was low compared to earthworms tested in the reference soil from site M, where the concentration of TPH was 140 ppm.

In general, toxicity testing can be used to meet one of two main objectives. When only full-strength (i.e., non-diluted) portions of environmental media are tested, it is possible to determine whether or not the sample ***is*** toxic. Testing strategies that depend upon the use of this "no dilution" approach for assessing the biological quality of water in receiving streams are well developed (cf. Stewart et al. 1990, Stewart et al. 1996). Alternatively, various concentrations of a sample can be tested, by use of a dilution series. With this strategy, it is possible to determine ***how toxic*** the sample is. The dilution-series strategy for toxicity testing is widely used to provide estimates of the toxicity of waste waters or pure chemicals. The difference between these two testing strategies is fundamental, and strongly influences the way in which the toxicity data can best be analyzed statistically (Stewart 1996). In the present project, PERF participants expressed a desire for use the latter approach, which could permit direct and quantitative comparison of a soil's toxicity to a soil's TPH content. Unfortunately, while the dilution-series strategy works well for aqueous media, its application to solid-phase heterogeneous media, such as soil, is problematic. One key difficulty is that of achieving a uniform mix of the contaminated soil and its diluent, particularly when the contaminated sample is highly contaminated. Earthworms, for example, may simply be able to detect and avoid small "patches" of contaminated soil, and thus have essentially zero exposure, unless the contaminated material is dispersed enough to be "unavoidable". Another important consideration is that factors such as soil organic matter content, pH, or particle-size distribution can affect the ability of earthworms to grow and reproduce, and that soils are spatially heterogeneous with respect to these factors, at small spatial scales. For this reason, "reference" soils and "contaminated" soils may affect earthworms differently, even if all contaminants in the "contaminated" soil were to be somehow removed.

In the screening-level assessments of soils from the M and I sites reported here, we prepared dilutions of each contaminated soil by adding various amounts of that site's corresponding reference soil. Each mixture was then tested with earthworms as described previously. The relationship between earthworm growth and concentration of TPH in the mixtures was then graphed, and the graph for each site was inspected visually for evidence of a dose-dependent response (Fig. 1a,b). A weak negative correlation was evident for earthworm growth and THP concentration in soil from site M (Fig. 1b), but no conspicuous dose-response pattern was obvious for soil from site I (Fig. 1a). This result suggests that more definitive test outcomes could be obtained by testing soils using a broader range of TPH concentrations (e.g., up to 5,000 ppm, perhaps with 1,000-ppm increments).

Growth responses of the earthworms in dilutions of contaminated soil from site I also suggested either that reference soil from this site inhibited worm growth (relative to soil from site M), or that the presence of low concentrations of TPH (greater than 200 ppm, but less than 1,870 ppm) increased the growth of the worms. Since earthworm reproduction in soils from I was zero in all mixtures of contaminated and reference soil, the former hypothesis is more plausible. This response could be due either to the presence of one or more unsuspected contaminants in the reference soil at this site, or to biologically significant differences in physical or physicochemical characteristics between the contaminated and reference soils from I.

An abstract of this portion of the study has been prepared and was recently submitted to the Society for Environmental Toxicology and Chemistry (SETAC); it will be presented, in poster or oral from, to members of this society at the SETAC meetings this autumn.

Task 3. Chemical analysis of petroleum-contaminated soils by thin-layer chromatography

Assessment of TPH residuals at petroleum-contaminated sites can be problematic, because TPH includes a complex suite of contaminants that have a wide range of environmental characteristics. Conventional analytical techniques, such as gas-chromatography/mass spectrometry or flame ionization

detection can provide the level of resolution needed for detailed characterization and target compound quantification (Douglas et al. 1992). However, these techniques are not suitable for estimating the full extent of hydrocarbon contamination in some instances, particularly in cases where TPH constituents are dominated by non-volatile components (e.g., naphthenic acids and asphaltenes). As a consequence, many studies and clean-up procedures rely on the "oil and grease" content of contaminated soils as a measure of petroleum contamination. This method involves a gravimetric determination of residual oil or total extracted materials, which has merit due to its extreme simplicity and low cost. However, these measurements provides no information on contaminant composition.

Thin-layer chromatography with flame ionization detection (TLC-FID, Iatroscan analyzer) offers a rapid, accurate method for the analysis of non-volatile organic materials, and still provides information about hydrocarbon class composition. This instrument is used widely in biological research (Napolitano 1994), but is underutilized in various areas of environmental chemistry (Karlsen and Larter 1991). If the instrument is properly calibrated and the operational parameters are standardized, TLC-FID permits a rapid and accurate quantification of total petroleum hydrocarbons (TPH), and offers the possibility of separation and quantification of the major components of TPH.

Petroleum hydrocarbons from contaminated soils were extracted overnight with a mixture of chloroform and methanol (1:1, v/v). The analysis method consisted of spotting a small volume of sample (typically 1-2 μL) on ten silica-coated quartz rods (Chromarods SIII). Three chromatographic developments in solvent systems of increasing polarities (hexane, toluene, and dichloromethane : methanol) were used for constituent separation. Figure 2 shows the high correlations obtained (r= 0.99) between TLC-FID response and gravimetric determinations, both for various hydrocarbon standards and for TPH from contaminated soils. These methods allowed complete separation of aliphatic hydrocarbons, aromatic hydrocarbons, resins and asphaltenes, starting from mixtures of the materials. Figure 3a shows the separation of the major hydrocarbon classes that can be achieved by Iatroscan methods, for an extensively-contaminated soil sample from Mexico.

Estimates of the petroleum content in soils containing low to moderate amounts of TPH by non-selective methods (e.g., oil and grease, or IR absorption analysis) are also vulnerable to interference caused by the presence of naturally occurring hydrophobic compounds (i.e., biogenic lipids). The TLC-FID method being developed for use in the present project allows the quantification of aromatic and aliphatic hydrocarbons without interference from soil biogenic lipids. A reliable and accurate measurement of aromatic hydrocarbons is of environmental concern, because this petroleum fraction commonly contains highly toxic constituents. As shown in Figure 3, the Iatroscan method allows clear separation of aliphatic and aromatic hydrocarbons from a contaminated soil, despite the presence of a natural "background" mixture of phospholipids, triacylglycerols and sterols.

Analysis by TLC-FID following extraction is also very rapid (we can process about ten samples per hour), which makes this technique especially suitable for synoptic studies or for the screening of a large number of samples, before deciding upon more detailed and costly methods of analysis.

The analysis method described above was developed to support of the present project, and is a significant accomplishment. An abstract outlining this aspect of the study was recently submitted to SETAC; it will be presented, in poster or oral presentation, at the SETAC meetings this autumn.

Task 4. Information about bioremediation alternatives for TPH in soils

No progress was made on this task this year; due to budgetary constraints.

Miscellaneous progress

We have attended several PERF meetings, hosted in Berkeley, California; Toronto, Canada; and Houston, Texas, to share technical progress with PERF representatives in the Environmentally Acceptable Endpoints projects area. We are also developing additional points of contact with petroleum industry representatives, relating directly to issues of soil contamination, processing of TPH-contaminated wastes, and soil clean-up. Two such areas include phytoremediation (a technology for cleaning up soils, based on the use of plants and their root--associated microbes), and use of constructed wetlands to treat petroleum-contaminated wastewaters. Both of these areas are of interest to the petroleum industry at large, for possible application to industry-wide pollution problems, and to research staff at ORNL.

References

Douglas, G. S., K. J. McCarthy, J. A. Dahlen and W. G. Steinhaur. 1992. The use of hydrocarbon analyses for environmental easement and remediation. *J. Soil Contam.* **1**:197-216.

Karlsen, D. A. and S. R. Larter. 1991. Analysis of petroleum fractions by TLC-FID: applications to petroleum reservoir descriptions. *Org. Geochem.* **5**: 03-617.

Napolitano, G. E. 1994. The relationship of lipids with light and chlorophyll measurements in freshwater algae and periphyton. *J. Phycol.* **30**:943-950.

Stewart, A. J., L.A. Kszos, B.C. Harvey, L.F. Wicker, G.J. Haynes, and R.D. Bailey. 1990. Ambient toxicity dynamics: assessments using *Ceriodaphnia* and fathead minnow larvae in short-term tests. *Environ. Toxicol. Chem.* **9**:367-379.

Stewart, A. J., W. R. Hill, K. D. Ham, S. W. Christensen and J. J. Beauchamp. 1996. Chlorine dynamics and toxicity in receiving streams. *Ecol. Appl.* **6**: (in press).

Stewart, A. J. 1996. Ambient bioassays for assessing water-quality conditions in receiving streams. *Ecotoxicology* **5**: (in press).

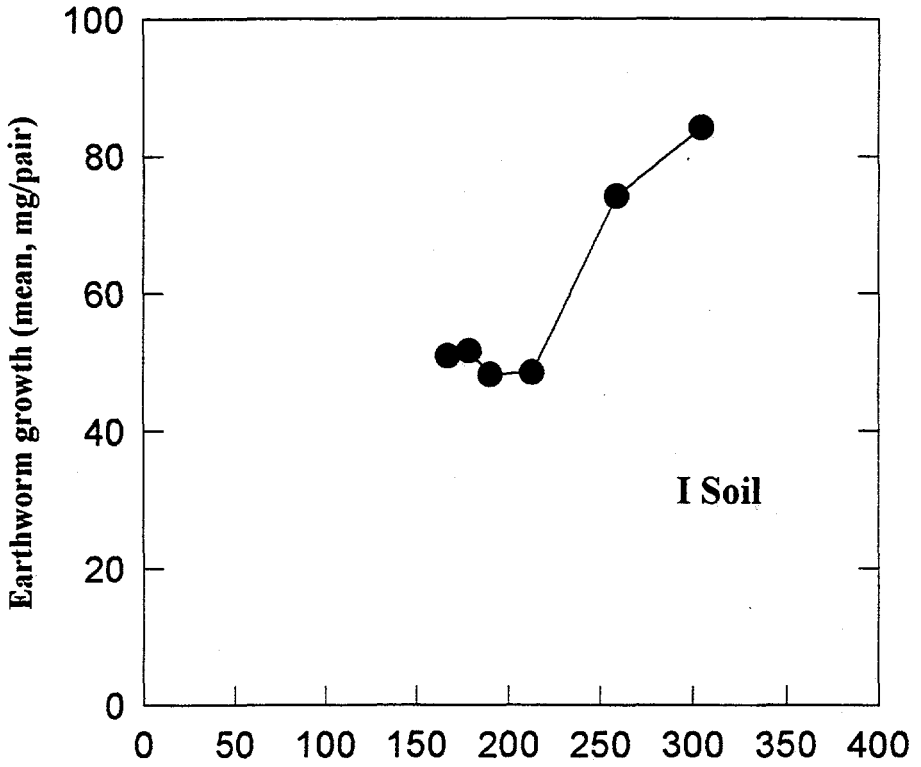

Figure 1a. "TPH" concentration (mg/kg; aliphatics + aromatics)

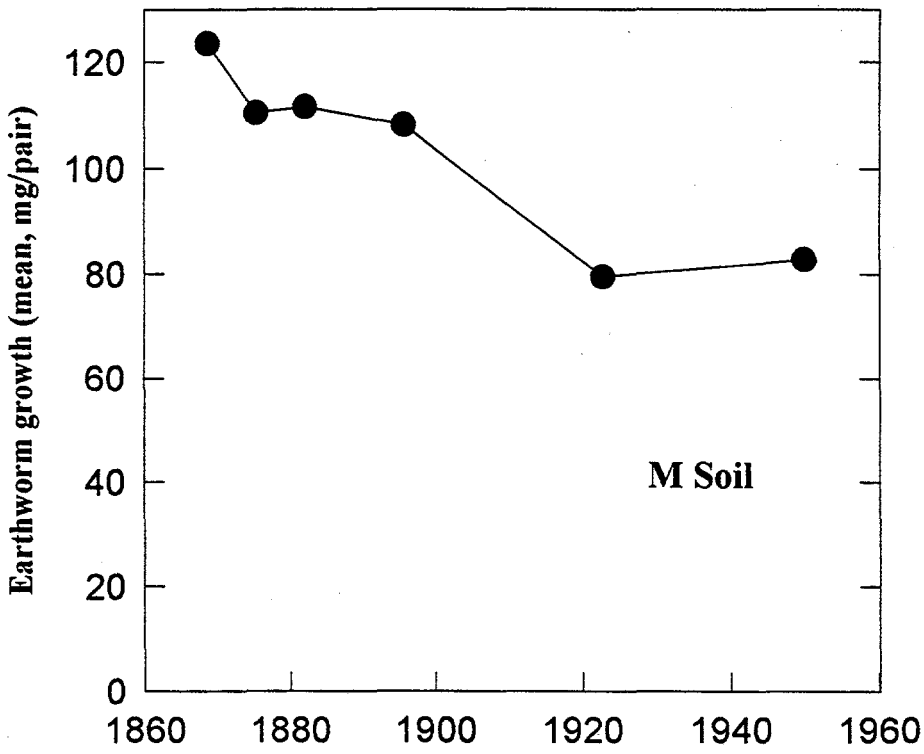

Figure 1b. "TPH" concentration (mg/kg; aliphatics + aromatics)

Figure 1. Earthworm growth (mean, milligrams dry weight per pair) in various dilutions of soil from two sites (I, upper panel; M, lower panel) containing measureable levels of total petroleum hydrocarbons.

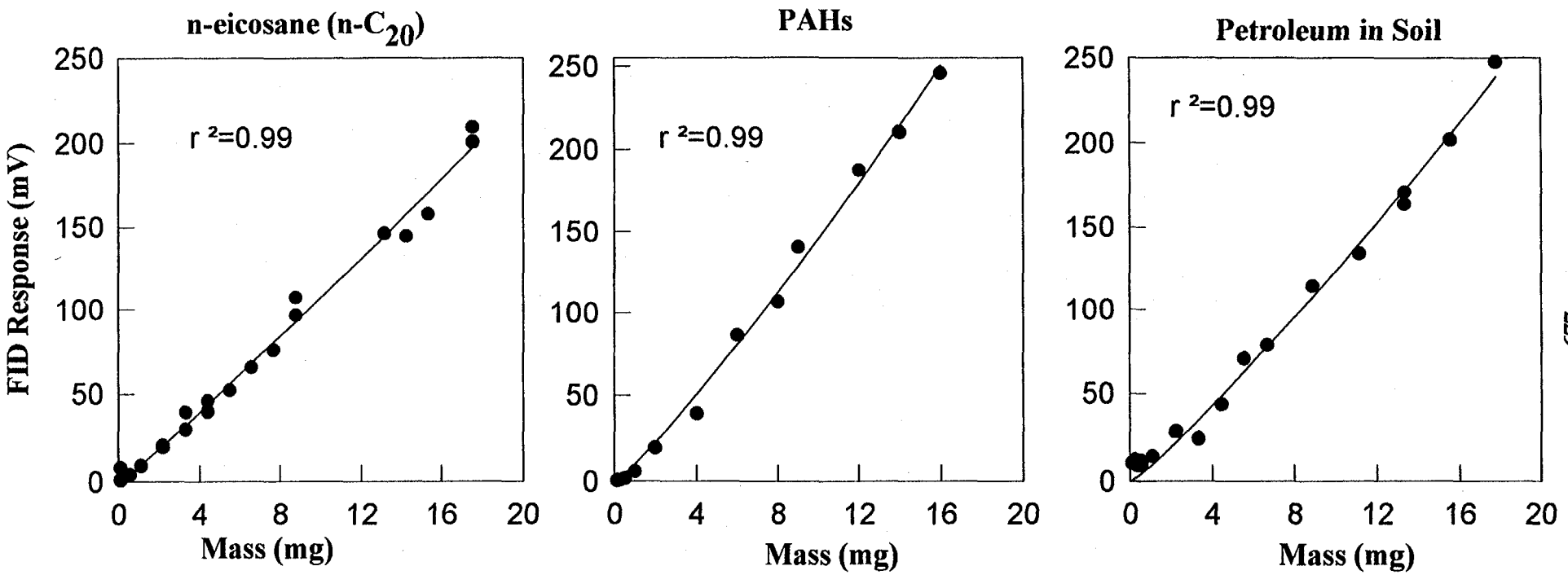

Figure 2. Calibrations of the TLC-FID systems with an aliphatic hydrocarbons (n-eicosane), a commercial mixture of polycyclic aromatic hydrocarbons (PAHs), and TPH in a contaminated soil.

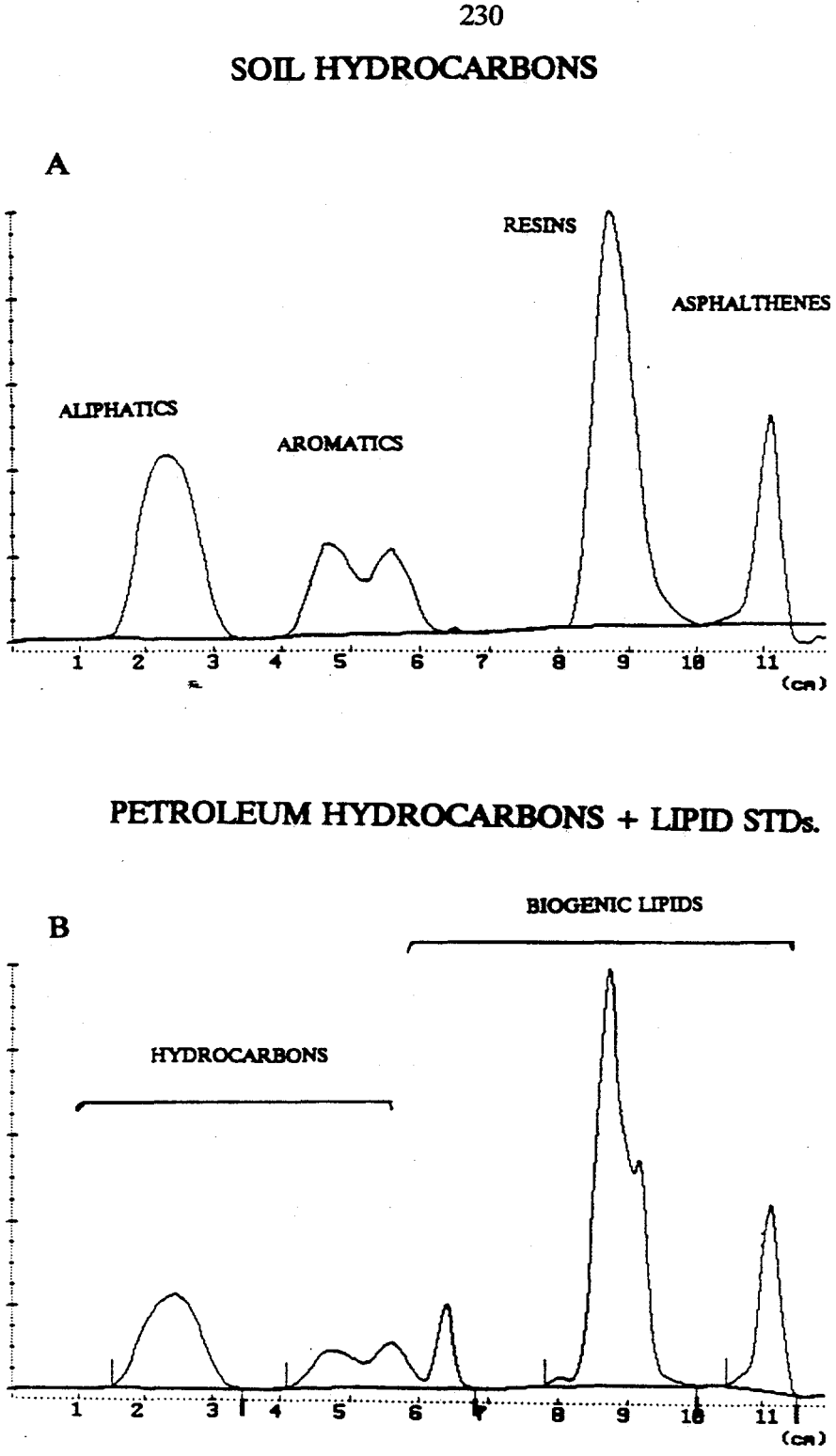

Figure 3. A. Typical separation of hydrocarbon classes in a petroleum contaminated soil. B. Separation of non-polar hydrocarbons (aliphatic and aromatic) from biogenic lipids. Solvent systems were: hexane (30 min.), toluene (15 min.), and dichloromethane:methanol (95:5, 5 min.).

4.6 NATURAL GAS AND OIL TECHNOLOGY PARTNERSHIP SUPPORT

T. W. Schmidt

INTRODUCTION

The Natural Gas and Oil Technology Partnership expedites development and transfer of advanced technologies through technical interactions and collaborations between the national laboratories and the petroleum industry - majors, independents, service companies, and universities.

The Partnership combines the expertise, equipment, facilities, and technologies of the Department of Energy's national laboratories with those of the U.S. petroleum industry. The laboratories utilize unique capabilities developed through energy and defense R&D including electronics, instrumentation, materials, computer hardware and software, engineering, systems analysis, physics, and expert systems. Industry contributes specialized knowledge and resources and prioritizes Partnership activities.

The areas of technology are:

Borehole Seismic Technology addresses cutting-edge geophysical methods for improved reservoir characterization with a focus on improved borehole hardware. The Partnership catalyzed formation of a 25-company Borehole Seismic Forum which has become the industry focal point for this technology.

Oil Recovery Technology addresses a broad range of technologies aimed at improving production from existing fields and with specific emphasis on assisting independent producers. The industry interface is an Industry Review Panel consisting of more than 20 individuals representing independents, majors, and the service companies.

Drilling and Completion Technology aims at better access to the reservoir through improved drilling and completion technologies. Currently, the laboratories participate in several joint industry projects fostered by two industry organizations: the Drilling Engineering Association (DEA) and the Completion engineering Association (CEA).

DISCUSSIONS OF CURRENT ACTIVITIES

During 1996 T. W. Schmidt participated in the development of the recommendations for funding of the Borehole Seismic Program for 1996 on behalf of Oak Ridge National Laboratory. This involved the evaluation of four existing projects and one new project. The laboratory also participated in selecting a more rational process for reviewing projects. T. W. Schmidt also contributed in the preparation of one of three new proposals submitted to Natural Gas and Oil Technology Partnership for consideration for 1996 funding under the Oil Recovery Technology Program. Other activities include program planning with the Partnership and project monitoring.

5. COAL COMBUSTION RESEARCH

C. S. Daw

This section describes research and development related to coal combustion being performed for the Fossil Energy Program under the direction of the Morgantown Energy Technology Center. The key activity involves the application of chaos theory for the diagnosis and control of fossil energy processes.

5.1 ANALYSIS OF FBC DETERMINISTIC CHAOS

C.S. DAW

DISCUSSION OF CURRENT ACTIVITIES

Background

It has recently been discovered that the performance of a number of fossil energy conversion devices such as fluidized beds, pulsed combustors, steady combustors, and internal combustion engines are affected by deterministic chaos. It is now recognized that understanding and controlling the chaotic elements of these devices can lead to significantly improved energy efficiency and reduced emissions. Application of these techniques to key fossil energy processes are expected to provide important competitive advantages for U.S. industry.

Status Summary

Analysis of fluidized bed, pulsed combustion, and bubble column measurements has continued during this reporting period. Because no new Fossil Energy Program funds have been received, we have continued activities in conjunction with other programs. An important new development has been the recognition that the exhibited chaotic behavior is a type of spatio-temporal dynamics that can be modeled as simple low-dimensional nonlinearities that are perturbed by high-dimensional substructure. This recognition may lead to a whole new approach for control.

Fluidized Beds and Bubble Columns

A paper demonstrating spatio-temporal yet globally low-dimensional behavior in rising bubble chains has been accepted for publication in a special issue of Chemical Engineering Journal [1]. Simple open-loop control between various types of periodic and chaotic bubbling has been demonstrated using periodic perturbations to the air flow. Experiments to demonstrate

closed loop control are now underway.

Moderate levels of activity continue in developing new fluidized bed diagnostics. Two papers have been published in collaboration with Babcock and Wilcox on analysis of pressurized fluidized bed signals [2,3]. Three other papers on slugging characterization and control were published [4-6].

Pulsed Combustion

An experimental thermal pulse combustor has been constructed and is now being tested at the University of Tennessee. Of the same basic design as the combustor modeled in two previous papers [7,8], the combustor is intended to provide a test bed for demonstrating chaos control. Initial efforts have been directed at characterizing the basic dynamic patterns and identifying appropriate control parameters. Initial control tests are expected to utilize perturbations to inlet fuel flow as the primary control parameter.

REFERENCES

1. K. Nguyen, C.S. Daw, P. Chakka, M. Cheng, D.D. Bruns, C.E.A. Finney, and M.B. Kennel, "Spatio-temporal dynamics in a train of rising bubbles" accepted for publication in Chemical Engineering Journal.

2. T.A. Fuller, T.J. Flynn, and C.S. Daw, "Dynamic Comparison of Pressure Measurements From the AEP Tidd PFBC and MIT's Quarter-Scale Cold Model," Proceedings of the 13th International Conference on Fluidized Bed Combustion, Orlando, pp693-702, May 7-10, 1995.

3. T.A. Fuller, T.J. Flynn, and C.S. Daw, "Dynamic Boiler Measurements: A Practical Approach," accepted for publication in Chemical Engineering Journal.

4. M. Vasudevan, C.E.A. Finney, K. Nguyen, N.A. van Goor, D.D. Bruns, and C.S. Daw, "Stabilization and Destabilization of Slugging Behavior in a Laboratory Fluidized Bed," Proceedings of the 13th International Conference on Fluidized Bed Combustion, Orlando, pp1001-1014, May 7-10, 1995.

5. C.S. Daw, C.E.A. Finney, M. Vasudevan, N.A. van Goor, D.D. Bruns, E.J. Kostelich, C. Grebogi, E. Ott, and J.A. Yorke, "Self-organization and chaos in a fluidized bed," Physical Review Letters, vol. 75, no. 12, pp 2308-2311, 18 Sept., 1995.

6. C.S. Daw, C.E.A. Finney, and M. Vasudevan, "Measuring and Controlling Chaotic Dynamics in a Slugging Fluidized Bed," 3rd Experimental Chaos Conference, Heriot-Watt University, Edinburgh, August 21-23, 1995.

7. C.S. Daw, J.F. Thomas, M.A. Rhode, R.W. Rollins, and A.J. Markworth, "Controlling Cycle-by-Cycle Variation in a Pulse Combustor," Proceedings of the 1995 Joint Technical

Meeting of the Central and Western States Sections of the Combustion Institute and the American Flame Research Committee, San Antonio, April 23-26, 1995.

8. M.A. Rhode, R.W. Rollins, A.J. Markworth, K.D. Edwards, K. Nguyen, C.S. Daw, and J.F. Thomas, "Controlling Chaos in a Model of Thermal Pulse Combustion," Journal of Applied Physics, vol. 78, no. 4, 15 August, 1995.

6. FOSSIL FUELS SUPPLIES MODELING AND RESEARCH

P. N. Leiby

The fossil fuel supplies modeling and research effort focuses on models for U.S. Strategic Petroleum Reserve (SPR) planning and management. Topics covered included new SPR oil valuation models, updating models for SPR risk analysis, and fill-draw planning. Another task in this program area is the development of advanced computational tools for three-dimensional seismic analysis.

6.1. STRATEGIC PETROLEUM RESERVE PLANNING AND MODELING

P. N. Leiby

INTRODUCTION

The Strategic Petroleum Reserve (SPR) is a government-owned stockpile of crude oil intended to serve as a buffer against possible oil market disruptions. The overall purpose of this project is to develop and apply improved models and tools for SPR management. Current project efforts emphasize developing new modeling tools to explicitly and flexibly portray oil market uncertainty and SPR planning risk.

DISCUSSION OF CURRENT ACTIVITIES

Oak Ridge National Laboratory (ORNL) conducts model development and planning analyses for Strategic Petroleum Reserve (SPR) drawdown, distribution and other management activities, in support of the Office of Management Operations, Petroleum Reserves. The roles and objectives are:

1. to utilize, maintain, modify, and report on SPR analysis models;
2. to support development of SPR oil valuation and bid analysis tools;
3. to evaluate potential applications of DIS-Risk model approach to related energy policy issues;
4. to study role and value of risk information in SPR planning;
5. to evaluate SPR planning alternatives and roles of SPR;
6. to provide analytical support for the SPR office.

Activities This Year

- Tested a statistical method for valuing SPR crude oils, based on their attributes. A report was submitted, "Imputing Prices of Non-Marketed Crude Oil Blends

with a Statistical Attribute Pricing Model," July 12, 1995. The "attribute pricing method" may supplement existing crude valuation methods in the SAVE model. Its merits are that it is founded in a well-established theory of consumer and producer choice behavior, it is based on historically observed pricing relationships, and it reproduces historical pricing patterns for marketed crudes reasonably closely. It has the potential value of including the effect of more crude oil attributes than sulfur and gravity, but no such attributes were available in the data available for this test. While the data included a broad distillation fraction (everything below the 650 degree cut, or all light and middle distillate fractions), this broad measure was too closely correlated with API gravity to provide useful new information.

- Completed planned revisions to the DIS-Risk model and delivered the model to DOE sponsors. This included updating the DIS-Risk model to use the latest DOE oil market assumptions, consistent with the AEO/IEO95. This is part of the normal model maintenance tasks required. NEMS modules were used to produce the needed reference data. The model has been tested with these changes. Advantages of the new DIS-Risk model are an improved windows interface, faster run time, and more useful reports.

- The SPR dynamic programming size/drawdown model (ORNLTEIS) was modified and re-compiled to take full advantage of the latest personal computer hardware and software technology.

ORNL also provided some general analytical support to the SPR Office, including:

- Reviewing the Deployment Planning Guide spreadsheet with consideration for: what it seeks to do; which of its data or relationships may need revision or updating; what new functionality might be added to it with modest effort.

- Commenting on methodologies for summarizing multiple estimates of SPR crude value from the SAVE model.

- Reviewing the latest version of the DOE SAVE model.

- Reviewing DOE analyses of SPR leasing approaches.

6.2 ADVANCED COMPUTATIONAL TOOLS FOR 3-D SEISMIC ANALYSIS

J. Barhen[†], C.W. Glover[†], H.K. Liu[‡], V.A. Protopopescu[†], D.B. Reister[†], N.B. Toomarian[*], and C.T. White[+]

[†] Center for Engineering Systems Advanced Research
Oak Ridge National Laboratory

[‡] Department of Electrical Engineering
University of Southern Alabama

[*] Jet Propulsion Laboratory
California Institute of Technology

[+] Department of Mathematics
University of Tennessee

INTRODUCTION

1 Purpose

The global objective of this effort is to develop advanced computational tools for 3-D seismic analysis, and test the products using a model dataset developed under the joint aegis of the United States' Society of Exploration Geophysicists (SEG) and the European Association of Exploration Geophysicists (EAEG). The goal is to enhance the value to the oil industry of the SEG/EAEG modeling project, carried out with US Department of Energy (DOE) funding in FY '93-95.

The primary objective of the ORNL Center for Engineering Systems Advanced Research (CESAR) is to spearhead the computational innovations techniques that would enable a revolutionary advance in 3-D seismic analysis. The CESAR effort is carried out in collaboration with world-class domain experts from leading universities, and in close coordination with other national laboratories and oil industry partners.

2 Background

The development of a 3-D structural and stratigraphical model of hydrocarbon reservoirs is crucial for the future ability of the exploration industry to economically discover and produce oil and gas. It requires extensive use of 3-D seismic data. These computational tasks are extremely expensive and new ideas and methods are necessary to render them timely, efficient, and cost-effective. An important step for the advancement of the state-of-the-art in 3-D seismic technology has been the collaborative 3-D Seismic Modeling Project undertaken by the SEG, the EAEG, and DOE under GONII. This international collaboration has designed realistic subsurface models for two challenging and relevant exploration plays: a sub-salt reservoir and an overthrust structure. Two extensive 3-D seismic surveys have been carried out over these geological models, using thousands of supercomputer CPU hours and generating terabytes of data.

It is important to note that, in order to perform the GONII survey computations, the national laboratories (LANL, LLNL, and ORNL) had to rely on a code developed by the Institut Français du Petrole. Notwithstanding this codes' limitations (explicit scheme, low source frequency, cumbersome treatment of absorbing boundary conditions), it was judged by industry superior to computational tools available at the time nationally. Thus, large amounts of funding were expended by DOE to develop a parallel version of the French

code and produce synthetic seismograms using it.

The present effort is carried out in the framework of the Advanced Computing Technology Initiative (ACTI). It leverages long-term basic research activities pursued at CESAR under DOE/BES/ERP funding. ORNL's aim is to develop leading edge US capabilities in this application area of vital importance to the national economy by leapfrogging state-of-the-art seismic computation methods currently dominated by European (French) technology. The new algorithms will be implemented on a wide range of scalable parallel computers, from a network of workstations to massively parallel systems. The availability of computer algorithms and software applications for exploiting the computational power and data-handling capabilities of parallel computers is essential to the routine adoption of 3-D seismic technology among oil companies. Demonstrating the effectiveness of the developed methods on the synthetic datasets produced by the 3-D Modeling Project will accelerate the adoption of the processing advances by the seismic industry. Additionally, the open publication of new methods tested on these models will assure their relevance as benchmarks, and an open discussion of the results obtained will assure a wide benefit to all companies.

3 Approach and ORNL Tasks

The project was originally undertaken as a set of collaborative efforts between three national laboratories (LANL, LLNL, and ORNL), five universities (Caltech, Stanford, Colorado School of Mines, Houston, and Rice), and industry. Other partners joined subsequently. SEG acts as the coordinator of the industry efforts and fourteen U.S. companies are participating. Below is a list of the ongoing ORNL tasks and the main collaborators for each task. Topics being pursued at Los Alamos and Livermore include elastic modeling of the SEG/EAEG structures for comparison with the acoustic results, physical model development, dataset imaging approximate methods, evaluation of new cost-effective 3-D prestack imaging methods, and seismic imaging and inversion via multilevel distributed parallel processing. Individual tasks are linked in that they all make use of the SEG / EAEG models and have as their common goal the testing and evaluation of state-of-the-art and new methods for evaluating the subsurface structures for oil and gas prospects.

Task 1. Time-Parallel Algorithms (ORNL, Caltech, Chevron, Unocal). Recently ORNL and Caltech / JPL have jointly developed and successfully demonstrated the concept of time-parallelism for modeling. The formalism enables the use of fully implicit methods which, due to their unconditional stability, dramatically reduce the number of time steps, and provide a massive degree of coarse-grain temporal parallelism with minimal communication and synchronization requirements. Such algorithms have proven to be highly suitable for implementation on massively parallel MIMD architectures such as the Cray T3D and the Intel Paragon. We proposed to apply our methodology to the solution of the acoustic wave equation, with specific implementation targeted at the code developed by the Institut Français du Petrole, which had been chosen for use in the SEG/EAEG modeling effort. Our results will be validated, in coordination with SEG/EAEG, IFP, and the oil industry, against more conventional simulations performed at other national laboratories (LANL, LLNL) on the same benchmark models.

Task 2. Neural Networks (ORNL, JPL, Unocal, Chevron, Shell, Marathon). Neural networks are adaptive nonlinear dynamical systems that can carry out useful information processing by means of their state response to initial or continuous input. We proposed to apply neural network approaches to several specific areas: classification of seismic signatures, nonlinear parameter estimation, data dimensionality reduction, lithology estimation, velocity model estimation, and event tracking. The primary benefit of such paradigms is that they are distribution independent, and that they have been shown to produce more accurate classification results than conventional statistical techniques. Furthermore, our fast "adjoint operator" learning algorithms for processing static and time-dependent information patterns are particularly relevant to large-scale SEG applications such as distributed parameter estimation and history matching. Finally, neural networks can be efficiently used to reduce the dimensionality of seismic data by providing a nonlinear version of principal component analysis, a technique well established in the realm of linear models.

Task 3. Global Optimization (ORNL, CWP/CSM, CogniSeis, Texaco, Shell, Unocal). The quality of the solution of many inverse problems, particularly those involving distributed parameters, depends to a great extent on the availability of good optimization paradigms. We proposed to apply a new fast global optimization technique developed by ORNL to the residual statics problem, in connection with the SEG models.

Task 4. Holographic Visualization of Seismic Data (ORNL, University of Southern Alabama, Lumin Inc., Texaco, Chevron, Standard Int'l). From the beginnings of seismic exploration, it has been the geophysicist's dream to dynamically visualize in three dimensions subsurface geology structures from seismic datasets. Seismic data can be sensed from natural ground motion or echoes generated by man-made acoustic sources. The amplitude and phase detected by an array of geophones are typically stored in digital form, and can be used as input to the pixels of a spatial light modulator (SLM). The objective of this task was to apply novel optoelectronic computing techniques to store, reconstruct, and display the 3-D subsurface structures. The optical display method is based on the projection to a 3-D medium, using laser light, of the seismic data represented in the SLM. The resolution and quality of the displayed results depend on the number of sensors in the field and the total number of pixels in the SLM. Nonlinear signal processing methods including neural networks are being used for the pre-processing and reduction of the data for more effective and efficient display applications. The new technology will initially be applied to the 3-D geologic models under development by the SEG and the oil industry.

4 Milestones

The main results of the ORNL contribution to the overall project are the development of leading-edge computational capabilities, enabling U.S. oil companies to successfully address some of the most complex issues in exploratory seismic analysis. Codes developed by investigators working on this project will be made available. General results of the project are being presented at public meetings. Participation of companies in each subtask ensures that knowledge of all work and codes is available to industry as they are developed.

The milestones listed below reflect a task starting date of April 10, 1995.

- 03/96 - Implementation and tests of new absorbing boundary conditions for acoustic wave equation.
- 07/96 - Application of global optimization to seismic residual statics.
- 09/96 - Application of neural networks to seismic parameter estimation.
- 10/96 - Proof of concept demonstration of seismic holography.
- 12/96 - Implementation of unconditionally stable virtually explicit method for massively parallel solution of acoustic wave equation.

These milestones assumed full and timely funding of the tasks.

DISCUSSION OF CURRENT ACTIVITIES

5 Unconditionally Stable Algorithms for Massively Parallel Solution of the Acoustic Wave Equation (V.A. Protopopescu, C.T. White, and J. Barhen)

5.1 Background

Propagation of acoustic, elastic, or electromagnetic waves in the atmosphere, oceans, or terrestrial crust is often cast in the form of semi-infinite or infinite problems. Typical examples are found in underwater acoustics, seismic wave propagation, and electromagnetic wave generation by cosmic objects or antennas. However, for computational purposes these infinite problems must be made finite. Several approaches have been investigated to deal with this aspect. One possibility is to map the infinite domain into a finite one. Another approach is to use smaller computational domains by substituting the true equations with simpler

ones in the exterior domain. In this way one can use the form of the solution of the simplified equations to construct boundary conditions for the true equations in the inner domain.

The most widely used approach has been to introduce artificial computational boundaries without changing the governing differential equations. On the artificial boundaries one should impose boundary conditions that ensure that the incident waves are fully transmitted and the reflection is, ideally, zero. These artificial boundary conditions imposed on the solution of the wave equation in a (semi) infinite domain are called absorbing boundary conditions (ABCs). ABCs have been widely used in the numerical modeling of wave propagation (see for instance, [1-15] and references therein). Theoretically, pseudo-differential operators can be constructed on the artificial boundaries to ensure perfect transmission (i.e., no reflection) of the outgoing waves. Unfortunately, except in the simplest one-dimensional case, these boundary conditions are non-local in both space and time and are not practical for numerical calculations. Moreover, some of the (local) approximations of these boundary conditions lead to ill-posed problems for the wave equation [1,3,7]. Even when the local approximations lead to well-posed problems, the perfectly absorbing property of the boundary is limited to certain angles of incidence (usually normal incidence) [1,7,9-12].

To enhance the (imperfect) absorptive quality of the artificial boundaries, additional damping and filtering mechanisms have been devised [4,5,14–16]. However, although they reduce reflection, sometimes to very low levels, dampers, sponges, and filters introduce an extra computational burden and may inherently prevent the implementation of more efficient computational methods, e.g., parallelization.

Finally, even in the absence of filters/sponges and assuming that local stable approximations of ABCs have been constructed, the continuous boundary conditions have to be again approximated by discrete ABCs which are then coupled to a standard interior discretization of the partial differential equations. Therefore, it seems more natural to look directly for discrete versions of ABCs.

5.2 Objective

The aim of our effort is to develop a set of discrete ABCs for the acoustic wave equation that would eliminate or circumvent most of the difficulties mentioned above.

In particular, we have focused on the following objectives:

- Construct discrete ABCs from "first principles" as applied to the discretized wave equation.
- The discrete ABCs should be local in both space and time. Their calculation would involve a stencil compatible to the stencil used in solving the interior equation.
- The resulting efficient elimination (or severe reduction) of reflection, would make unnecessary the use of sponges, filters, and other artificial devices.
- The simplicity of the ABCs and their consistency with the interior equation would eventually make it possible to fully parallelize the numerical code for solving the acoustic or elastic wave equations.
- The performance of the new ABCs will be measured with respect to the French C3D code [5], which uses paraxial PDEs in combination with a sponge at the absorbing boundaries.

5.3 Approach

In constructing the discrete ABCs, we assume that the (parallelipipedic) domain is discretized in the form:

$$(0,1,\ldots,N+1)\times(0,1,\ldots,N+1)$$

or

$$(0,1,\ldots,N+1)\times(0,1,\ldots,N+1)\times(0,1,\ldots,N+1)$$

for the 2-D or 3-D case, respectively. The boundaries, in the form of surfaces, edges, or corners have at least one coordinate equal to either 0 or $N+1$.

The new ABCs generalize, to the multidimensional case, the idea of the characteristics that works exactly in the 1-D problem. The following conditions were derived:

2-D Boundary Conditions. The relationship implemented at the $I = 0$ *Face* is:

$$\begin{aligned} u^{n+1}(0,j) &= \alpha[u^n(1,j) + \frac{1}{2}(u^n(0,j+1) + u^n(0,j-1))] \\ &\quad + (1-2\alpha)u^n(0,j) \qquad\qquad 0 < j < N+1 \end{aligned} .$$

Similar expressions hold for the other faces. At the *Corner* $I = 0$, $J = 0$ we impose:

$$u^{n+1}(0,0) = \alpha\,(u^n(1,0) + u^n(0,1)) + (1-2\alpha)u^n(0,0) \ .$$

Here, and in the next expressions, α is a parameter that depends on the speed of sound in the medium and the discretization steps. 3-D Boundary Conditions We list here, as example, the absorbing boundary conditions for one face, edge, and corner. Similar expressions are derived for the other corresponding boundaries. Face: $I = 0$

$$\begin{aligned} u^{n+1}(0,j,k) &= \alpha[u^n(1,j,k) + \frac{1}{2}(u^n(1,j+1,k) + u^n(0,j-1,k) \\ &\quad + u^n(0,j,k+1) + u^n(0,j,k-1))] \\ &\quad + (1-3\alpha)u^n(0,j,k) \qquad\qquad 0 < j,\ k < N+1 \end{aligned}$$

Face: $I = N+1$

$$\begin{aligned} u^{n+1}(N+1,k) &= \alpha[u^n(N,j,k) + \frac{1}{2}(u^n(N+1,j+1,k) + u^n(N+1,j-1,k) \\ &\quad + u^n(N+1,j,k+1) + u^n(N+1,h,k-1))] \\ &\quad + (1-3\alpha)u^n(N+1,j,k) \qquad\qquad 0 < j,\ k < N+1 \end{aligned}$$

Edge $I = 0,\ J = 0$

$$\begin{aligned} u^{n+1}(0,0,k) &= \alpha[u^n(1,0,k) + u^n(0,1,k) \\ &\quad + \frac{1}{2}(u^n(0,0,k+1) + u^n(0,0,k-1)] \\ &\quad + (1-3\alpha)u^n(0,0,k) \end{aligned}$$

Corner $I = 0,\ J = 0,\ K = 0$

$$\begin{aligned} u^{n+1}(0,0,0) &= \alpha[(1,0,0) + u^n(0,1,0) + u^n(0,0,1)] \\ &\quad + (1-3\alpha)u^n(0,0,0) \end{aligned}$$

The new ABCs are local in both time and space and are compatible with the discretized equation used for the interior of the domain. As seen in Figures 1 and 2, their performance is comparable to that achieved with the French C3D code, which uses the considerably more complex paraxial PDEs. The reflection is minimal, considering that the amplitude of the signal at the source is 10^5. In both approaches sponges have been used, which may hamper the ability to exactly diagonalize (and thus fully parallelize) the numerical system.

We are currently investigating the trade off between the somewhat greater reflection allowed by the discrete ABCs vs. the increase in speed due to parallelization, and also proceeding with the unconditionally stable parallelization of the acoustic wave equation using the novel absorbing boundary conditions.

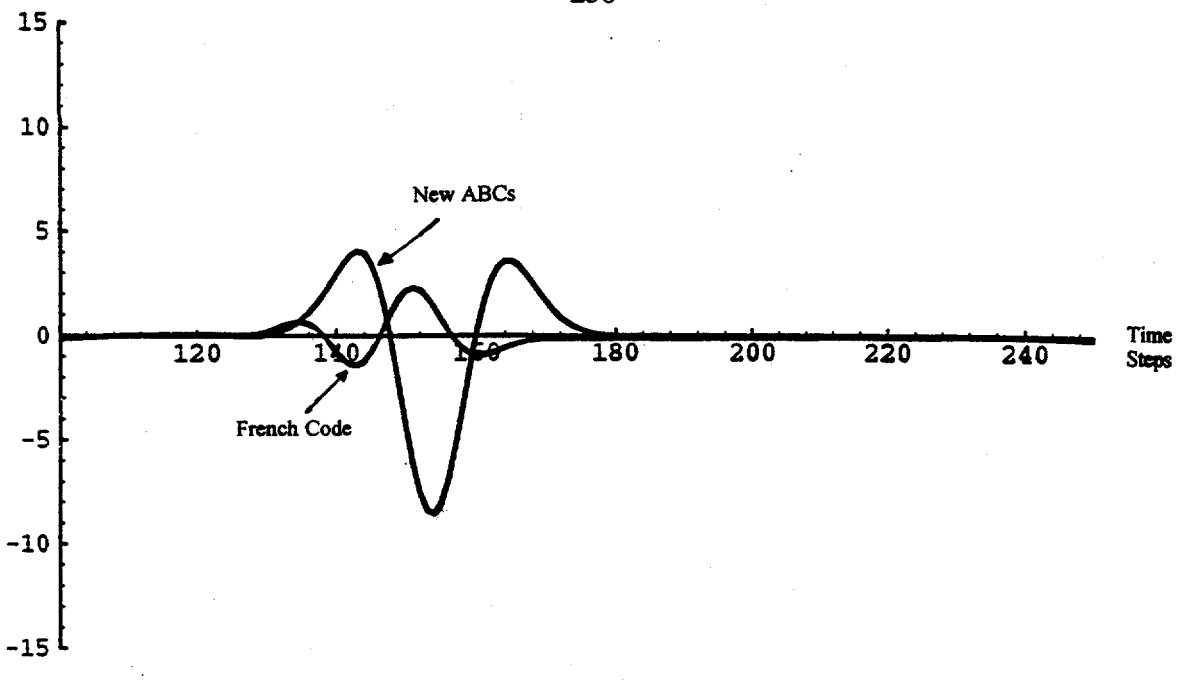

Figure 1
Amplitudes of the reflected waves at the receiver location as a function of time; 0° angle
Source Strength is 10^5

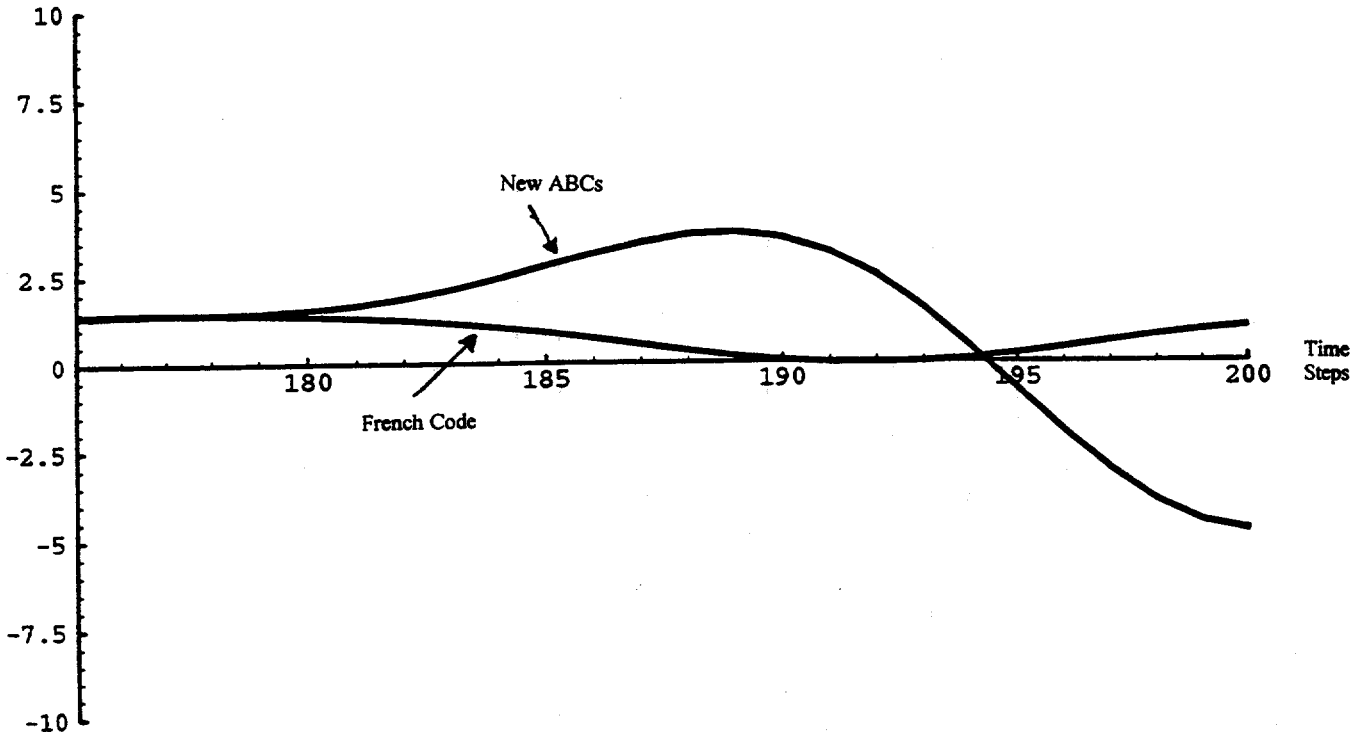

Figure 2
Amplitudes of the reflected waves at the receiver location as a function of time; 41° angle
Source Strength is 10^5

References

1. B. Engquist and A. Majda, Absorbing Boundary Conditions for the Numerical Simulations of Waves, Math. Comp, **31**, 629 (1977).
2. M. Israeli and S.A. Orszag, Approximation of Radiation Boundary Conditions, J. Comp. Phys., **41**, 115 (1981).
3. A. Bamberger, P. Joly, and Y.E. Roberts, Second Order Absorbing Boundary Conditions for the Wave Equations: A Solution for the Corner Problem, SIAM J. Numer. Anal., **27**, 323 (1990).
4. J. Sochacki, R. Kubíchek, J. George, W.R. Fletcher, and S. Smithson, Absorbing Boundary Conditions and Surface Waves, Geophysics, **52**, 60 (1987).
5. L. Anné, J. Brac, and H. Tran, Propagation 3D d'Ondes Acoustiques, Institut Français du Pétrole, April 1993.
6. J. Nordström, Accurate Solutions of the Navier-Stokes Equations Despite Unknown Outflow Boundary Data, J. Comp. Phys., **120**, 184 (1995).
7. B. Engquist and A. Majda, Radiation Boundary Conditions for Acoustic and Elastic Wave Calculations, Comm. Pure and Appl. Math, **32**, 313 (1979).
8. Chengbin Peng and M. Nafi Toksöz, An Optimal Absorbing Boundary Condition for Finite Difference Modeling of Acoustic and Elastic Wave Propagation, J. Acoust. Soc. Am., **95**, 733 (1994).
9. R.L. Higdon, Absorbing Boundary Conditions for Difference Approximations to the Multi-dimensional Wave Equation, Math. Comp., **47**, 437 (1986).
10. R.L. Higdon, Numerical Absorbing Boundary Conditions for the Wave Equation, Math. Comp. **49**, 65 (1987).
11. R.L. Higdon, Radiation Boundary Conditions for Elastic Wave Propagation, SIAM J. Numer. Anal., **27**, 831 (1990).
12. L.T. Long and J.S. Liow, A Transparent Boundary for Finite Difference Wave Equation, Geophysics, **55**, 201 (1990).
13. Xiaobing Feng, Absorbing Boundary Conditions for Electromagnetic Wave Propagation, Math. Comp., to appear.
14. C. Cerjan, D. Kosloff, R. Kosloff, and M. Reshef, A Nonreflecting Boundary Condition for Discrete Boundary Condition for Discrete Acoustic and Elastic Wave Equations, Geophysics, **50**, 705 (1985).
15. D.R. Burns and R.A. Stephen, Three-Dimensional Numerical Modeling of Geoacoustical Scattering from Seafloor Topography, J. Acoust. Soc. Am., **88**, 2338 (1990).
16. J.P. Berenger, A Perfectly Matched Layer for the Absorption of Electromagnetic Waves, J. Comp. Phys., **114**, 185 (1994).

6 Application of Global Optimization to Residual Statics (D.B. Reister and J. Barhen)

6.1 Background

Seismic energy is transmitted from a source, reflected from a structure, and detected at a receiver. The transit times are often perturbed by geological irregularities near the surface. Residual statics corrections are small adjustments to the travel times at both the source and receiver. Calculation of residual statics corrections is one of the most challenging optimization problems in the oil and gas industry from an economic viewpoint. The corrections must be applied to all data that is recorded on land, and many datasets that are recorded underwater. Every major oil company and seismic consulting firm has a group of experts on this problem. ORNL has a state of the art computer code for global optimization, Terminal Repeller Unconstrained Subenergy Tunneling (TRUST). With ACTI support, ORNL has been applying TRUST to the residual statics problem using data and code supplied by both Professor John Scales from the Colorado School of Mines and John DuBose of CogniSeis Development, a major seismic consulting firm. Preliminary results of ORNL's methodology are so encouraging, that CogniSeis has expressed strong interest in licensing TRUST.

6.2 The Residual Statics Optimization Problem

Seismic energy is detected by receivers that are regularly spaced along a line. The source of seismic energy is moved to each of the receiver locations to produce a shot. Time series data is collected from the detectors for each shot and the source of seismic energy is moved to the next receiver location for the next shot. The time series data is stored as Fourier coefficients. Common midpoint (CMP) stacking is used to increase the signal-to-noise ratio. The midpoint is a point on the line that is equidistant from the source and receiver. If both the source and the receiver are moved toward the CMP, the next shot will have the same midpoint. The "fold" of the data is the number of datasets with the same CMP. Between 1960 and 1980, improvements in data acquisition systems allowed typical values for the fold to increase from one to twelve. Today, thirty is a typical value.

Variations in elevation and in near surface geology create time delays in the recorded data. To reduce the variations in the data, residual statics corrections are performed. The statics corrections are done in a surface consistent manner; that is, the correction time shifts depend only on the shot and receiver locations and not on the ray path from shot to receiver. As shown in Figure 3, the shot correction is the time from the shot to the Datum plane, while the receiver correction is the time from the Datum plane to the receiver. The remainder of this section will describe the mathematical details of calculating the residual statics corrections.

The time T_{IJ} for seismic energy to travel from source I to receiver J via midpoint K is:

$$T_{IJ} = S_I + R_J + G_K + M_K Y_{IJ} \tag{1}$$

where S_I is the source correction, R_J is the receiver correction, G_K and M_K are the midpoint corrections, and Y_{IJ} is the surface distance from the source to the receiver. The measured data are the travel time and the distance, while the unknowns are: S_I, R_J, G_K, and M_K. We will assume that the traveltime data has been adjusted to remove the midpoint corrections.

Data is provided by trace $[t = 1, NT]$. For each trace, the data consists of the Fourier components of the time series data $[f = f_{low}, f_{high}]$. The data $[D(f,t)]$ are complex numbers. Each trace consists of data from a source $[I(t)]$ to a receiver $[J(t)]$ via a midpoint $[K(t)]$. For each midpoint K, the data are stacked:

$$H(K,f) = \sum_t \exp[2\pi f(S_I + R_J)] D(f,t) \; . \tag{2}$$

The statics corrections $(S_I + R_J)$ are determined to maximize the total energy E in the stacked data:

$$E = \sum_K \sum_f |H(K,f)|^2 \; . \tag{3}$$

6.3 Optimization Algorithms

TRUST solves the following optimization problem: given an objective function $f(\boldsymbol{x})$, where $\boldsymbol{x}$ is an N dimensional vector that is constrained to lie in a domain (U), find the global minimum $(\boldsymbol{x}^{\boldsymbol{G}})$; that is, find a point $\boldsymbol{x}^{\boldsymbol{G}}$ in U such that $f(\boldsymbol{x}^{\boldsymbol{G}}) \leq f(\boldsymbol{x})$ for all $\boldsymbol{x}$ in U. Since the goal in the residual statics problem is to maximize the total energy (E), the objective function for TRUST is: $f(\boldsymbol{x}) = -E$. The TRUST methodology combines the concepts of subenergy tunneling and non-Lipschitzian "terminal" repellers. The evolution of a deterministic nonlinear dynamical system incorporating these concepts provides the computational mechanism for reaching the global minimum.

From an operational perspective, a series of cycles is executed. At the start of each cycle, TRUST moves from a local minimum, reached during the previous cycle $(\boldsymbol{x}^*)$ along a direction $\boldsymbol{p}$. For the first cycle, $\boldsymbol{x}^*$ is the initial point $(\boldsymbol{x}^I)$. Define the function $g(\boldsymbol{x})$ by: $g(\boldsymbol{x}) = f(\boldsymbol{x}) - f(\boldsymbol{x}^*)$. Initially, $\boldsymbol{x} = \boldsymbol{x}^* + \delta\boldsymbol{p}$, and the algorithm tunnels in the $\boldsymbol{p}$ direction until either $g(\boldsymbol{x})$ is negative or $\boldsymbol{x}$ escapes from U. If $g(\boldsymbol{x})$ is negative,

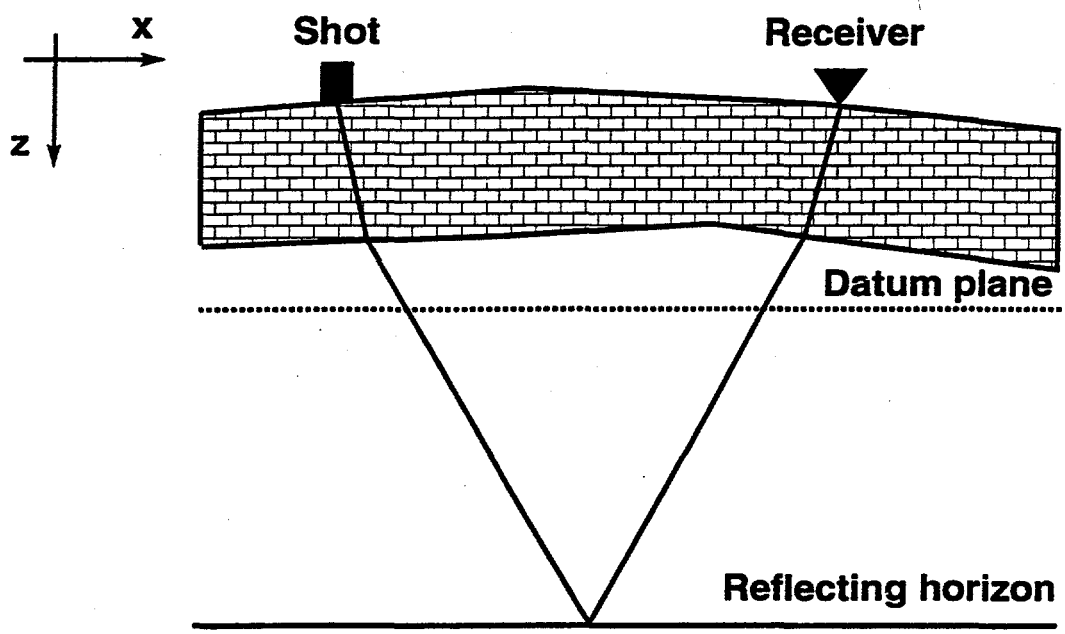

Figure 3
Definition of the residual statics corrections

TRUST finds the local minimum and the next cycle begins. When x escapes from U, the last found local minimum is the global minimum.

A rigorous proof has shown that TRUST will find the global minimum for the one dimensional case (where x is a scalar). In the multidimensional case, only global descent can be proven. In practice, however, TRUST has been very successful in solving the standard SIAM benchmark problems (the highest dimension for these benchmark problems was ten). On the other hand, if we embed an N dimensional problem into one dimension, we can also prove [1] that TRUST will find the global minimum. However, the function evaluations become prohibitively expensive for large values of N.

6.4 Results

John DuBose has provided ORNL with both a FORTRAN code to evaluate the objective function and three synthetic datasets. The datasets are somewhat smaller than the typical datasets that are collected during seismic surveys by the oil industry. The first two datasets have 24 shots and 50 receivers (thus, the dimension of x is 74). The number of CMPs is 51 and the average fold is 12. The number of traces is 653 and the number of frequency bands is 25. The first dataset has no noise and no static corrections. Thus, the minimum value of the objective function occurs at the point $x = 0$. The second data has both noise and static corrections.

The third dataset is larger and was designed to be extremely difficult to solve. It has 77 shots and 77 receivers (thus, the dimension of x is 154). The number of CMP is 133 and the average fold is 11. The number of traces is 1462 and the number of frequencies is 49. The value of the objective function at the point $x = 0$ is 263, while the maximum value is 1303.

The maximum value for the residual statics corrections for all test cases is 50. Ideally, we would like to start TRUST at the point where all components of the x vector are equal to 50 and execute the algorithm (tunnel and find local minima) until all components of the x vector escape the domain. Then the last minimum value should be the global minimum. However, since most of the residual statics corrections are expected to be small, the local minimum that can be found from the point $x = 0$ should be close to the value of the global minimum.

We determined that the statics problems were ill-conditioned. For instance, there are several directions for which the objective function is constant. For example, adding a constant to either all of the shot statics or to all of the receiver statics does not change the value of the total energy. Finding the local (and global!) minima of an ill-conditioned problem is difficult. To improve the conditioning for the first two datasets, we set one of the static corrections equal to zero for both the shot and receiver statics. Hence, we reduced the dimension from 74 to 72. To make the problem well conditioned for the third dataset, we have performed a coordinate transformation:

$$x = Ay \tag{4}$$

where the transformation matrix (A) is not square and the y vector has a lower dimension than the x vector.

Remarkably, TRUST successfully found the optimum solution for the first dataset, both with and without conditioning. For the second dataset, DuBose found an optimal solution with four large static corrections for the receivers. TRUST found an optimal solution without any large static corrections that had a value of the objective function that was very close DuBose's optimum value.

The third dataset was designed to have an optimum value that was significantly lower than the value that would be found by steepest descent starting at the origin. We are currently studying the data set. At this stage, TRUST has not yet located the global minimum. The best estimate achieved for $-E$ is -1205 (the global minimum being -1303). Efforts will focus on enhancing the algorithm that determines in which direction to tunnel after reaching a local minimum.

References

1. J. Barhen and V. Protopopescu, "Generalized TRUST Algorithms for Global Optimization", in *State of the Art in Global Optimization*, C.A. Floudas and P.M. Pardalos eds., Kluwer Academic Press, 163-180 (1996).

7 Neural Network Application to Seismic Parameter Estimation (C.W. Glover, N.B. Toomarian, and J. Barhen)

7.1 Objective

The objective of the research reported here is to determine whether artificial neural network (ANN) computing techniques can provide an accurate estimation of petrophysical parameters that describe reservoir properties. Specifically, ORNL and JPL are to apply their advanced ANN algorithmic techniques to obtain functional relationships between perturbations of subsurface rock properties (e.g., sand layer thickness, effective porosity, ratio of clay to sand, and saturation) to seismic response information (e.g., depth, s- and p-wave velocities, amplitude-versus-offset (AVO) slope and intercept). A seismic data set is generated by a numerical simulation of a field seismic experiment. This dataset will represent a known lithology and will be used to judge the ANN's estimation accuracy. Once ANN techniques are developed for this problem and their accuracy determined, they will be applied to real seismic data.

7.2 Background

The oil industry acquires and must process large volumes of various types of geoscience data to locate prospective places for oil and gas reservoirs. This data is extensively manipulated before it is analyzed and interpreted. Every data manipulation step is important and processing time can be extensive. It is imperative that the efficiency of the data manipulation and data reduction be improved. This is where ANNs may help the oil industry.

The characterization and prediction of reservoir properties is one major area where ANNs may offer improvement. The oil industry uses seismic data to characterize large volumes of the Earth's upper crust. However, this data provides only gross structure information on the size and orientation of the various underlying strata. On the other hand, well log data provide a detailed characterization of the strata but only in a very localized region, and it is far more expensive to obtain than the seismic data. To find a reservoir and characterize it, one must associate the detailed well log data with the seismic data. This will allow one to accurately extrapolate detailed information over a large volume. The strength of ANN technique lies in its ability to capture and approximate nonlinear mappings between two datasets; in this case the relationship between well log and seismic data. Thus, the use of ANN techniques may improve the efficiency and accuracy in the manipulation of geoscience data.

The research reported here investigated the accuracy of ANN computing techniques in estimating petrophysical parameters that describe reservoir properties based on seismic response information.

7.3 Approach

Our approach focuses on quantitative measures to determine the accuracy of ANNs in obtaining functional relationships between reservoir properties and seismic response data. An Unocal simulation program provided precise and unambiguous data for this study. The ANN's structure is determined using the JPL/ORNL adjoint operator method. The seismic response data which is used as input to the ANN is transformed so that different features do not dominate and bias the ANN's results. The k-fold-cross-validation method is used to estimate the accuracy and its confidence interval for all ANNs used in this study. The number of free parameters (size) in the ANN are determined by confidence interval measures. These techniques are discussed in more detail below.

7.3.1 Seismic Data

An Unocal simulation program provided the data used in this study. This program used as input reservoir properties and generated seismic response information based on a model. The simulation program generated approximately 22,000 records with values for the following 21 attributes:

Reservoir Parameters

SWE	-	Sand Water Saturation
EFFPOR	-	Sand Effective Porosity
THICKNESS	-	Sand Thickness
RATIO	-	Clay/Sand Ratio within Sands

Seismic Attributes

DEPTH/TIME	-	Depth (ft.)/Two-way Seismic Travel Time
GREF-0	-	Normalized, Rectified Near Offset Amplitude (AVO)
SLOPE-0	-	AVO Least Squares Slope of *GREF-0*
GREF-1	-	Intercept of Fit to Normalized, Rectified Amplitude Fit
SLOPE-1	-	Fluid Factor Attribute
GREF-2	-	(Ro-Rwet) of Unnormalized Intercept
SLOPE-2	-	(G-Gwet) of Unnormalized Signed Amplitude Fit
GREF-3	-	Ro Intercept of Unnormalized Signed Amplitude Fit
SLOPE-3	-	G or Slope of Unnormalized Signed Amplitude Fit
SLOPE-4	-	(Ro + G)/2 of *GREF-3* and *SLOPE-3*
SLOPE-5	-	Another Combination of the Above
SLOPE-6	-	Ro*G
SLOPE-7	-	(Ro + G)/2 of Normalized, Rectified Amplitude Fit
VINT	-	p-wave Velocity of Sands
SVINT	-	s-wave Velocity of Sands
RHOB	-	Density of Sands
INDEX	-	Control Index for Perturbations (not considered)

The data consisted of a 152 stacked seismic traces each of which had as low as four and as high as 338 sample points per trace. The ANNs are to predict the four reservoir parameters from some or all the 18 seismic attributes.

7.3.2 ANN Approach to Parameter Prediction

At the outset it was decided to use a separate ANN to predict each of the four reservoir parameters rather than one ANN to predict all four. This approach offers several advantages. First, it allows us treat the prediction of a given parameter as a separate problem, independent from the others. Thus, we can tailor our approach specifically for a given parameter. For example, in the analysis of the reservoir parameters we noticed that *EFFPOR* and *RATIO* variables take on a continuous range of values. This suggest that the ANNs should be used as nonlinear regression algorithms. On the other hand, the *SWE* and *THICKNESS* variables take on discrete values, where each value can be treated as a class. Thus, the ANN will be used as a classification algorithm. Second, using a different ANN for each parameter allows us to determine and use only those input variables that significantly affect the parameter prediction. Finally, separate ANNs can always be combined in a hierarchical manner to predict other reservoir parameters.

7.3.3 Adjoint Operator Method for ANN Architecture

The unique ORNL/JPL adjoint operator method is used to determine the appropriate ANN architecture for this application. This method is implemented in a computer code that allows the user to determine the most appropriate ANN architecture for the problem at hand. This method views an ANN as a set of coupled nonlinear differential equations:

$$\dot{u}_n + u_n = f_n\left(\sum_n W_{nm} T_{nm} U_m + I_n\right) \tag{5}$$

where u_n represents the output of the n-th neuron. In Eq. (5), $\dot{u}$ is the derivative of u_n with respect to time (or iteration). T_{nm} is the strength of the synaptic coupling from the m-th to the n-th neuron. The sigmoidal functions $\mathcal{L}_\backslash$ modulate the neural responses; typically, $f_n(x) = tanh(x)$. W_{nm} is the connectivity matrix consisting of binary numbers that indicate whether neuron n receives input from neuron m. When W_{nm} is 1 then neuron n is connected to neuron m. The W_{nm} matrix is an input to the code; hence, the analyst can decide as to which neurons should be connected. This approach allows one easily to select, test, and compare different neural architectures by changing the values of this matrix. I_n is an external input to a neuron (not from another neuron). Its use in conjunction with the **Teacher Forcing** paradigm is explained below. Without the teacher forcing I_n, applies only to the input neurons. The goal in this code is to minimize the difference between the desired and actual output from the network for each training sample, i.e., the learning error function is:

$$E = \frac{1}{2KN} \sum_k \sum_{n \in \text{output}} (d_n - u_n)^2 \ , \tag{6}$$

where d_n is the desired out for n-th neuron, and the summation is performed over the output neurons only, for all K samples. We use a gradient based iterative approach for updating the values of the matrix T. Without going into the mathematical details (see, e.g., [1-3]), we arrive at:

$$T_{nm}^{t+1} = T_{nm}^{t} - \Delta\eta \frac{\partial E}{\partial T_{nm}} \ . \tag{7}$$

Here, the superscript t indicates the iteration number, Δ is a constant step size, and η is the learning rate. In the current code we have the option of keeping this learning rate constant or changing its value adaptively based upon the gradient. In the latter case, if the gradient has a high value, the learning rate is going to be small and vice versa. This is analogous to walking down a hill. If the hill is very steep, one takes small steps. On the other hand, if the slope is moderate, one can run by taking big steps. Specifically, we evaluate η to be the following:

$$\eta = \left(\frac{\partial E}{\partial T}\right)^{-1/3} \ . \tag{8}$$

The RHS of Eq (8) often occurs in dynamical systems referred to as a **Terminal Attractor** dynamics, where the "terminal" (non-Lipschitzian) properties arise from the exponent parameter selected, e.g., as $-1/3$. In order to calculate (E/T), in principle one needs to calculate (u/T). The latter can be calculated by differentiating the neural dynamics Eq. (5). This will lead to a system of coupled linear equations, also known as forward sensitivity equations, the right hand side of which depend on T_{nm}. These equations have to be solved as many times as they are parameters in the system, i.e., N^2 where in N is number of neurons. An alternative approach exists, based upon the concept of **Adjoint Operators**, that calculates the value of (E/T) directly, without calculating explicitly the value of (u/T) [1,3]. This approach reduces the computational cost, and hence, the training time in a fully connected network by $O(N^2)$.

An additional feature of the code is the option to use a **Teacher Forcing** [1,2] term. Our past experience with fully connected networks indicates that the teacher forcing term reduces the training time dramatically. The neural activation dynamics specified by Eq. (5) does not include any explicit information regarding the desired network output. This amounts to asking a person to go to a destination goal without telling them where the destination is. The only direction that this person would get is at the end of each trail, when a destination is reached. At this stage it will be informed as to how far and in which direction it is from the desired goal. To better account for such an effect, the external input term, I_n, in Eq. (5) has to be modified, to include explicit information regarding the desired network output. Specifically,

$$I_n = \begin{cases} a_n & ; \quad n \in \text{input set} \\ 0 & ; \quad n \in \text{hidden set} \\ \lambda(d_n - u_n)^2 & ; \quad n \in \text{output set} \end{cases} . \tag{9}$$

Here a_n is the NN input, and λ is a positive parameter, value of which can be modulated in different ways. In the present code we can select one of two available models:

$$\lambda(t) = \lambda_0 \left[1 - e^{-E(t)}\right] \qquad (a)$$

$$\lambda(t) = 1 - \frac{t}{n_t} \qquad (b) \tag{10}$$

Above, t denotes the iteration number, E is the total error, and n_t is total number of learning iterations allowed.

Our initial effort focused on integrating the different modules into one coherent program. Once completed, several preliminary test cases were executed. The tests were conducted on similar data (input and output set) with different architectures constructed using the connectivity matrix. Based upon the training time needed for different architectures, we concluded that a feedforward architecture with one or two hidden layers is best suited for the application at hand. Furthermore, it became clear that one network will not be able to predict all desired attributes. This can be easily understood. For example, in order to predict effective porosity, we need to use a network in a mapping mode, while predicting rock saturation level or thickness of a layer is a classification problem. Hence, we decided to apply a modular approach, i.e., use different network with different architectures for each of the attributes.

7.3.4 Input Data Preparation

Much of the success with any regression or classification algorithm comes from the analysis and preparation of the input data. Rather than blindly using all 18 seismic attributes for inputs to the ANN, we carried out an analysis of these attributes to determine those that carry a significant amount of information to be useful for our problem. This reduces the input space's dimension. Next, we scaled all attributes to the same range of values so that no one parameter dominates the ANN training phase. These steps, discussed below, are crucial in achieving the best performance from the ANN.

7.3.5 Scaling

Scaling ANN input data equalizes the importance of all input variables and speeds learning. Raw data can differ by several orders of magnitude. For example, one input attribute may have values on the order of 0.00001 while another is around 100,000. The larger number will quickly saturate ANN processing elements (nodes). Saturated nodes produce constant output values corresponding to the maximum of their dynamic range. The ANN weight update rule is proportional to the derivative of the node's activation function at the current output value. For a saturated node the derivative is almost zero and its weight stops learning. The data should be scaled to match the node's dynamic range to alleviate this problem.

We used a linear mapping to map each input variable's range to the node's dynamic range. The input variables' range were determined from the full data set. A linear activation function was used for the input nodes whose dynamic range was chosen to be [0, 1] or [-1, 1], depending on the particular ANN. Thus all data was mapped to the appropriate interval.

7.3.6 Dimensionality Reduction

In theory we can use all 18 seismic attributes as input to the ANN and it should perform satisfactorily. The problem with such an approach, in practice, is that the training time is significantly increased without much performance improvement. The ANN spends time learning meaningless correlations amongst a large number

of input variables due to idiosyncrasies in individual training cases. Reducing the number of input variables allows the ANN to focus on only significant correlations. The problem is to find those variables involved in the "significant correlations". There is no magic prescription for this and we rely on a combination of heuristics and statistical measures to determine the "significant variables".

The experience of our Unocal collaborators was the first heuristic used to reduce the dimensionality of the input space. They suggested that we focus our attention on the following seismic attributes in the prediction of reservoir parameters: *DEPTH/TIME*, *GREF-0*, *SLOPE-0*, *GREF-3*, *SLOPE-3*, *SLOPE-4*, *VINT*, *SVINT*, and *RHOB*. We performed an extensive statistical and graphical analysis of this attribute set to determine whether it could be reduced further.

A principle component analysis (PCA) was performed to determine whether any of the remaining nine variables are highly correlated and can be combined. The sample covariance matrix, $\Sigma = [c_{ij}]$, is an $N \times N$ matrix whose elements are given by

$$c_{ij} = \frac{1}{N-1} \sum_{k=1}^{L} (x_{ik} - m_i)(x_{jk} - m_j)$$

where x_{ik} is the kth sample out of L total samples of the ith variable, for the $N = 9$ variables mentioned above. The elements c_{ij} can be expressed in terms of the correlation coefficient ρ_{ij} and variances σ_i as

$$c_{ij} = \rho_{ij}\sigma_i\sigma_j$$

A value of $\rho_{ij} \approx 1 (\approx 0)$ indicates a large correlation (no correlation) between variables x_i and x_j. This analysis revealed correlations among the *GREF* variables ($\rho_{ij} \approx 0.75$), among the *SLOPE-0*, *SLOPE-3* variables ($\rho_{ij} \approx 0.65$), and among the *VINT*, *SVINT*, and *RHOB* variables ($\rho_{ij} \approx 0.75 - 0.85$). These variable combinations are candidates for merger to reduce the problem dimensionality.

These correlations were verified by examining graphs of these variable combinations as a function of some of the reservoir parameters. The graphs revealed that as a reservoir parameter changed, say *EFFPOR*, the *VINT*, *SVINT* differed essentially by additive constants. It was also noticed that the *SLOPE-4* variable showed essentially no discernable trend as a function of the reservoir parameters. Thus it was dropped from consideration, because it may act as noise and cause the ANN to learn erroneous information.

In the results reported below, various combinations of input variables were used. In each case, the smallest set of input variables was tried first to see if it provided a satisfactory prediction of a given reservoir parameter, if not, then the set was enlarged to include more input parameters.

7.3.7 Data Transformation

The ANN estimation of the *THICKNESS* parameter was treated as a pattern classification problem because it took on only six discrete values. Each value was treated as a class. To reduce the dimensionality of the ANN's input space, we decided to seek a nonsingular transform [4] that preserves the class separation, while it transforms the original input space $\boldsymbol{X}$ into a lower dimensional space $\boldsymbol{Y}$.

We consider a criterion function J, that rewards maximal separation among the classes. There are many criteria functions that may be chosen; the one we use is given by

$$J = tr(S_w^{-1} S_b)$$

where the *within-class scatter* S_w of samples around their expected class mean vectors M_i are expressed by

$$S_w = \sum_{i=1}^{L} P_i E\left\{(\boldsymbol{X} - M_i)(\boldsymbol{X} - M_i)^T | \omega_i\right\} = \sum_{i=1}^{L} P_i \Sigma_i \ .$$

The *between-class scatter* S_b is expressed by

$$S_b = \sum_{i=1}^{L} P_i(M_i - M_0)(M_i - M_0)^T$$

and the expected vector of the mixture distribution is

$$M_0 = E\{\boldsymbol{X}\} = \sum_{i=1}^{L} P_i M_i \ .$$

We are looking for a transform A from an n-dimensional space $\boldsymbol{X}$ to an m-dimensional space $\boldsymbol{Y}$ $(m < n)$;

$$\boldsymbol{Y} = A^T \boldsymbol{X}$$

The optimization of the criteria function is given by the following three steps:

Express J in terms of the m-dimensional $\boldsymbol{Y}$-space,

$$J(m) = tr(S_{wY}^{-1} S_{bY}) = tr\left\{(A^T S_{wX} A)^{-1}(A^T S_{bX} A)\right\}$$

take the derivative with respect to A and set it to zero,

$$\frac{\partial J(m)}{\partial A} = -2S_{wX} A S_{wY}^{-1} S_{bY} S_{wY}^{-1} + 2S_{bX} A S_{wY}^{-1} = 0$$

and solve for the optimum nonsingular transform A,

$$(S_{wX}^{-1} S_{bX})A = A(S_{wY}^{-1} S_{bY}) \ .$$

We want to diagonalize the above equation to find those eigenvalues and their associated eignevectors that contribute the most to the separation of the classes. Diagonalizing this equation is equivalent to simultaneously diagonalizing the two matrices S_w and S_b. To see this we choose a transform A such that

$$A^T S_{wX} A = I \ \text{ and } \ A^T S_{bX} A = K \tag{11}$$

is satisfied. In general K is not diagonal. The first equation above is satisfied if A is chosen to be

$$A = \Lambda_A^{-1/2} \Phi_A$$

where Λ_A and Φ_A are the eigenvalue and eigenvector matrices for S_{wX} . Next, we seek to diagonalize K by solving for its eigenvalue and eigenvector matrices, Λ_K and Φ_K,

$$\Phi_K^T K \Phi_K = \Lambda_K \ \text{ and } \ \Phi_K^T I \Phi_K = I \ .$$

Substituting Eq. (11) in for K above yields

$$A^T S_{bX} A \Phi_K = A^T S_{wX} A \Lambda_K \Phi_K$$

or

$$S_{xW}^{-1} S_{bX} \left[\Lambda_A^{-1/2} \Phi_A\right] \Phi_K = \left[\Lambda_A^{-1/2} \Phi_A\right] \Lambda_K \Phi_K \ .$$

This transform projects the input space $\boldsymbol{X}$ onto the m eigenvectors of $S_{wX}^{-1} S_{bX}$ that optimize J. This projection is closely related to Fisher's Linear Discriminant. The linear discriminant boundaries are perpendicular to the line connecting $\boldsymbol{M}_i$ and $\boldsymbol{M}_j$ for $i \neq j$ in this m-dimensional space.

We will transform all the input vectors for the *THICKNESS* problem according the transformation

$$[\Lambda_A^{-1/2} \Phi_A] \Phi_K \ .$$

7.3.8 ANN Accuracy Measures

We want to estimate the ANN performance on all future samples presented to it after training. This is clearly impossible unless the underlying probability distribution that the training samples were drawn from is exactly equal to the probability distribution from which the future examples will be drawn. The final application's probability distribution must be "similar" to the training probability distribution for a measure of accuracy to have any meaning. This statement is true for any regression and/or pattern recognition method.

Even if this caveat is true and the probability distributions are equal, we can only provide an estimate P of a statistic p and bound our estimate with a confidence interval because we used a finite training set and P is then a random variable. One method to estimate the confidence interval is to use the Moiré-Laplace Theorem and the assumptions it éntails. It states that the probability that P is within $z\,\sigma_p$ of p with a confidence δ is given by

$$Pr\left[-z < \frac{P-p}{\sigma_p} < z\right] \approx \delta \ ,$$

where σ_p is the variance of P. Only in the limit as we train on all possible samples does the confidence approach one. Even for this highly restricted problem of equivalent underlying probability distributions, we are forced to estimate confidence bounds on a statistic that measures the generalization of the ANN. Thus, any estimate of a statistic describing the accuracy of an ANN is a random number and by itself is meaningless unless it is accompanied by a corresponding confidence interval.

The proportion of successful predictions an ANN produces, p, is the statistic we would like to estimate from a finite sample set as our measure of the ANN's accuracy. The proportion of successful predictions P the ANN produces on a test set D_{tst} after its vector matrix T of weight parameters has been fixed to T^* by training is given by

$$P = \frac{1}{n} \sum_{<x_i, y_i> \in D_{tst}}^{n} \varphi\left[f(D_{trn}, T^*, \boldsymbol{x}_i \in X), \boldsymbol{y}\right]$$

where φ is an indicator function that produces a value of one when a sample $\boldsymbol{x}_i$ is drawn from a test set D_{tst} and the ANN yields the correct output vector $\boldsymbol{y}_i$, and otherwise its zero. Simply put, this is the accuracy of the ANN on the test set D_{tst}.

7.3.9 Holdout Method

The holdout method is a technique to validate a statistic p from a finite sample set. The holdout method consists of ℓ samples drawn from a set D with a given probability distribution to obtain a sample set D_ℓ. The sample set D_ℓ is divided into a training set D_{trn} and a test set D_{tst}. The bootstrap and k-fold-cross-validation techniques are the two main variations of the holdout method.

The bootstrap method randomly draws members of the training and test sets by sampling from D_ℓ with replacement. The ANN is trained from D_{trn} and a tested on D_{tst}. This process is repeated to build an estimate of P and it variance σ_P^2. The confidence interval is determined from σ_P^2 accordingly.

The k-fold-cross-validation technique partitions the data in k mutual exclusive partitions. The first k - 1 partitions is used for D_{trn} and the kth for D_{tst} where the accuracy is computed. Next, partitions $1, 2, \ldots, k-2, k$ are used for D_{trn} and the $k-1$ partition is used for D_{tst}; then partitions $1, 2, \ldots, k-3, k-1, k = D_{trn}$ and the $k-2$ partition is used for D_{tst}; and so until k accuracy measures have been obtained along with their variance.

Kohavi [5] compared the bias and variance tradeoff between the bootstrap and k-fold-cross-validation techniques for finite sample sizes and found that bootstrap method has a smaller variance than k-fold-cross-validation, but the bias is much larger. For this reason, Kohavi concluded that k-fold-cross-validation may provide a better operational estimate of a classifier's accuracy than bootstrap. In addition, he showed that $k = 10$ partitions is sufficient for the estimated accuracy with a 95% confidence interval to enclose the expected accuracy. For this reason, we employed the k-fold-cross-validation technique with a $k = 10$ partitions to estimate our ANNs accuracy and confidence intervals.

7.4 Results

Each section below presents the results of our ANN estimation for a different seismic parameter.

7.4.1 Estimating *THICKNESS*

The *THICKNESS* parameter was the hardest reservoir parameter to estimate because it took on only six values (5, 10, 25, 50, 100, 200 ft) for a very wide range of input parameter values. We treated each of the six values as members of six different classes and used the ANN to predict the *THICKNESS* class given its input values. The adjoint analysis indicated that a fully connected, feedforward, multilayered ANN is an appropriate architecture for this pattern classification problem.

The ANN input space initially consisted of *GREF-0*, *SLOPE-0*, *GREF-3*, *SLOPE-3*, *VINT*, *SVINT*, and *RHOB* seismic parameters. A transformation to an eigenspace (as discussed in Section 3.4) reduced the number of inputs to five eigenvectors. The entire dataset was projected into this space and linearly scaled to the [0, 1] interval.

The ANN's output consisted of six nodes, one for each class. The *THICKNESS* classes were represented by the following vectors:

(1, 0, 0, 0, 0, 0)	=	5 ft,
(0, 1, 0, 0, 0, 0)	=	10 ft,
(0, 0, 1, 0, 0, 0)	=	25 ft,
(0, 0, 0, 1, 0, 0)	=	50 ft,
(0, 0, 0, 0, 1, 0)	=	100 ft,
(0, 0, 0, 0, 0, 1)	=	200 ft.

All hidden layer nodes used the *tanh* activation function with a response range of [-1, 1], while the output nodes used a sigmoid activation function with a range of [0, 1].

The entire transformed and scaled data was randomly partitioned into ten subsets. These partitions were combined according to the k-fold-cross-validation procedure into ten training and testing pairs, such that

Training Set #1	=	Partitions 1, 2, ..., 9	and	Test Set #1 = Partition 10;
Training Set #2	=	Partitions 1, 2, ..., 8, 10	and	Test Set #2 = Partition 9;
	.			
	.			
	.			
Training Set #10	=	Partitions 2, 3, ..., 9	and	Test Set #10 = Partition 1;

These sets were used to obtain all accuracy estimates and their associated confidence intervals.

The number of hidden layers and the number of nodes per hidden layer in the ANN's architecture was determined experimentally. Initially, a single hidden layer was used with 10 nodes. All weights were initialized with values between ± 0.1 and Training Set #1 was shuffled for presentation to the ANN. The ANN's error on Test Set #1 was monitored along with the training set's error as a function of the number of epochs (1 epoch = 1 full presentation of the training set's examples). As the number of epochs increases both the training set error and test error decrease, up to a point where the training set error continues to decrease and the test set error starts to increase. Just prior to this point we extract the error on Test Set #1 and use this value in our accuracy estimate. This process is repeated for the remaining Sets. The ten accuracy estimates are then averaged, variances extracted, and their 95% confidence intervals are computing according to the formulas outlined in Section 7.3.8. This process is repeated for each ANN of a given size.

Figure 4 displays the mean accuracy and confidence intervals for ANNs with one and two hidden layers and with a differing number of nodes in the hidden layers. The input space used to generate these points was not transformed to the eigenspace, but was the seven seismic parameters discussed above. The lower curve represents the mean accuracy for an ANNs with 10, 20, 30, and 40 nodes in a single hidden layer. The upper curve represents the mean accuracy for an ANNs with 10 (5x5), 20 (15x5), 25(15x10), 30 (20x10), and 40 (25x15) nodes in a two hidden layers.

The two layer ANN architecture provides a higher accuracy than a single hidden layer ANN.

Figure 5 displays the mean accuracy and confidence intervals for ANNs with two hidden layers and where the input data were transformed into the eigenspace.

These results show that the transformed data consistently yields a higher accuracy than the untransformed data and that the ANN size is smaller. In the course of this investigation, we also found that the number of iterations needed to reach convergence is reduced by about a factor of 2/3.

Our results indicate that a two hidden layer ANN with 15 nodes in the first hidden layer and 10 nodes in the second will be approximately 94% $\pm$ 1% accurate on any future examples drawn from the probability distribution that was used to generate the training/test data. Thus, one can expect roughly similar accuracy for any *THICKNESS* estimates generated from the numerical simulation model used in this study.

7.4.2 Estimating *POROSITY*

In order to estimate effective porosity from seismic data, we have employed a feed forward three layer network in mapping mode. The input layer consist of four neurons with following four attributes as input:

- Depth,
- 0-Offset,
- AVO-Slope, and
- P-Velocity.

The hidden layer had 10 neurons, and output layer had only one neuron. To train and test the network, we choose about 2200 first data points. Out of this data set we choose randomly 200 data points for training the network. The network was tested on all 2200 dataset.

Figure 6 shows the desired values vs. predicted values of porosity by the network.

7.4.3 Water Saturation Estimation - *SWE*

For each trace the value of the water saturation is constant, hence, the problem of estimating the water saturation becomes a classification problem. Since the input attributes vary dramatically over time, to classify the saturation level based upon raw attributes becomes a hard, if not impossible, one. This led us to extract some features that more represent each trace rather changing values within a trace. To this end, we integrated all the attributes over time for each trace. The advantages of this feature are rather remarkable. In this way, the amount of data to be manipulated is reduced dramatically (from over 22000 to about 150),

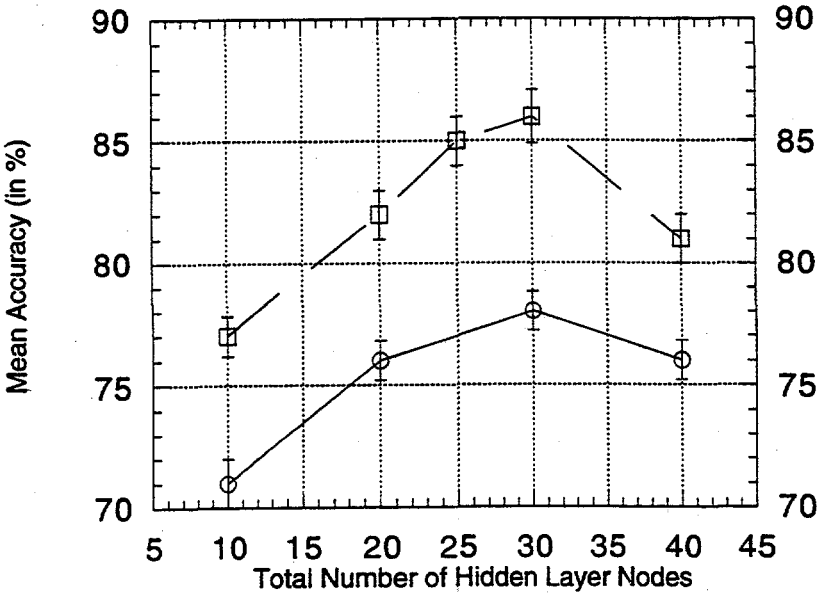

Figure 4
Mean accuracy and confidence intervals for ANNs with one and two hidden layers and with a differing number of nodes in the hidden layers

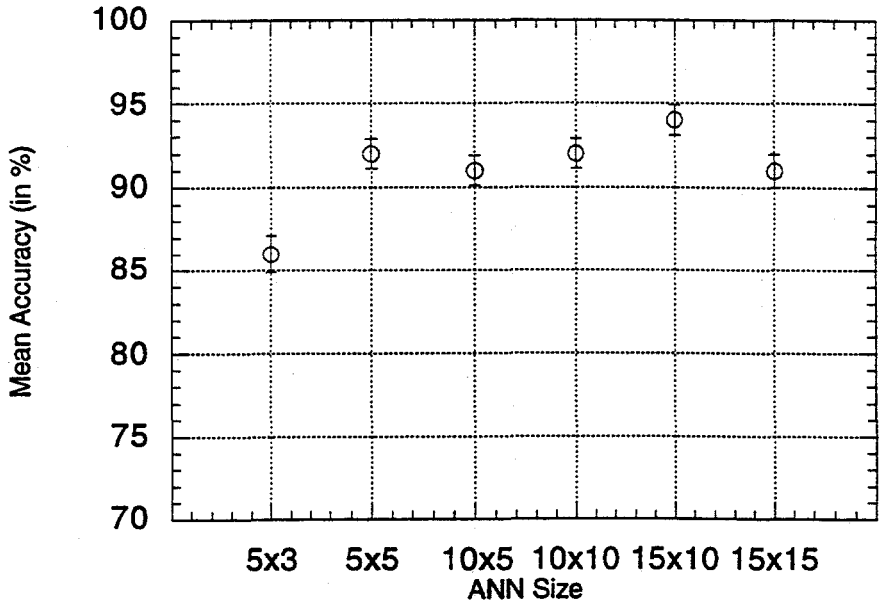

Figure 5
Mean accuracy and confidence intervals for ANNs with two hidden layers and where the input data were transformed into the eigenspace

i.e., one sample per trace. Furthermore, we will need only a small network to do the classification, which in turn results in a fast training time.

To train a network to classify the water saturation, we have selected a three layer feed forward network. The input layer consist of 12 inputs, i.e., it DEPTH, it 0-OFFSET, *AVO-SLOPE*, *GREF-3*, *SLOPE-3*, *SLOPE-4*, *SLOPE-7*, P&S Velocities, Density. The hidden layer had 6 neurons while there is only one output neuron. The output values can be between -1 and 1. However, for classification purposes we threshold the value at zero, i.e., if the network output is less than zero the saturation level is at 40% level while an output greater than zero indicated saturation level of 100%.

The input data consisted 26 samples that were randomly selected from the pool of 152 samples. All the data values were normalized to be between -1 and 1. The network was tested on all 152 samples. The following figures show the network output vs. the desired value, and the cases that network misclassified the saturation level. Figures 7 and 8 show that only 6 out of 152 were misclassified, i.e., success rate of over 96%.

7.5 Collaboration with Industry

Our collaboration with Unocal has been educational on both sides. Unocal generated the data used in this work. Their guidance (in particular Dr. F. Aminzadeh) has been invaluable in the analysis of our results and in the planning of further mutually cooperative experiments. These experiments are outlined in the next section.

7.6 Planned Work for Second Year of Task

The second year of this research (if funding is available) will be most interesting. The ORNL, Unocal, and JPL team will use ANNs to estimate properties of a reservoir that has been fully measured. The ANN will use a model to generate the training data. The test data will be obtained from well logs. Well log data will be available at several locations and seismic data will be available over the entire region. Once the ANN is trained, we will predict reservoir parameters at the well locations, based solely on the seismic data for the locations. These predictions will then be compared with parameters measured (well log data) at the corresponding locations. This experiment will directly address the specific objective stated at the beginning of this report. The results of this experiment will indicate to DOE and the oil companies how valuable a tool ANNs can be in extrapolating well log data into other regions where only seismic data exists.

7.7 Conclusions

Industry representatives have analyzed the ANN results presented here. It is their feeling that this work demonstrates that ANNs produce surprisingly accurate estimates of reservoir parameters. They deemed this aspect of the experiment to estimate reservoir parameters from seismic data a success. Our work indicates that ANNs can be used to capture, based solely on data, the same information of a reservoir as a model.

Additional tests of the ANN method for predicting reservoir parameters will be performed during the forthcoming year.

References

1. N.B. Toomarian, and J. Barhen, "Fast Temporal Neural Learning Using Teacher Forcing", *U.S. Patent No. 5,428,710* (June 27, 1995).
2. N.B. Toomarian, and J. Barhen, "Learning a Trajectory Using Adjoint Functions and Teacher Forcing", *Neural Networks*, **5**, 473-484 (1992).
3. J. Barhen, N.B. Toomarian, and S. Gulati, "Application of Adjoint Operators to Neural Learning", *Appl. Math Lett.*, **3**(3), 13-18 (1990).
4. This section follows the notation of Keinosuke Fukunaga, Introduction to Statistical Pattern Recognition, Academic Press, San Diego, 1990.
5. R. Kohavi, "A Study of Cross-Validation and Bootstrap for Accuracy Estimation and Model Selection," *14th International Joint Conference on Artificial Intelligence*, Montreal, CA, 1137 (1995).

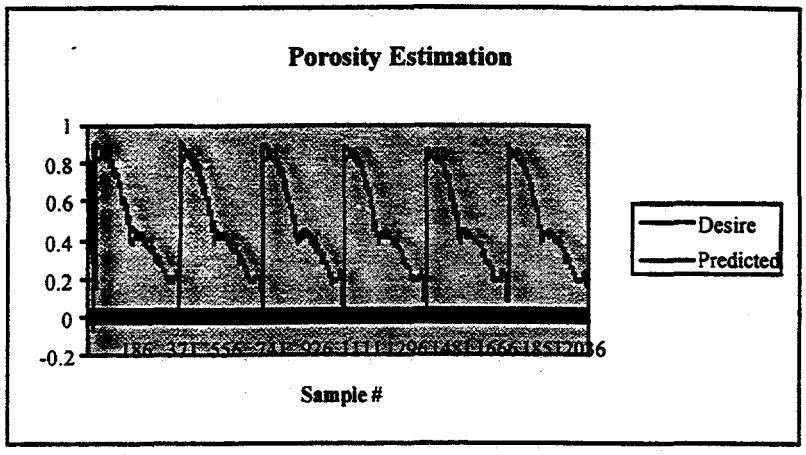

Figure 6
Effective porosity shown with the ANN

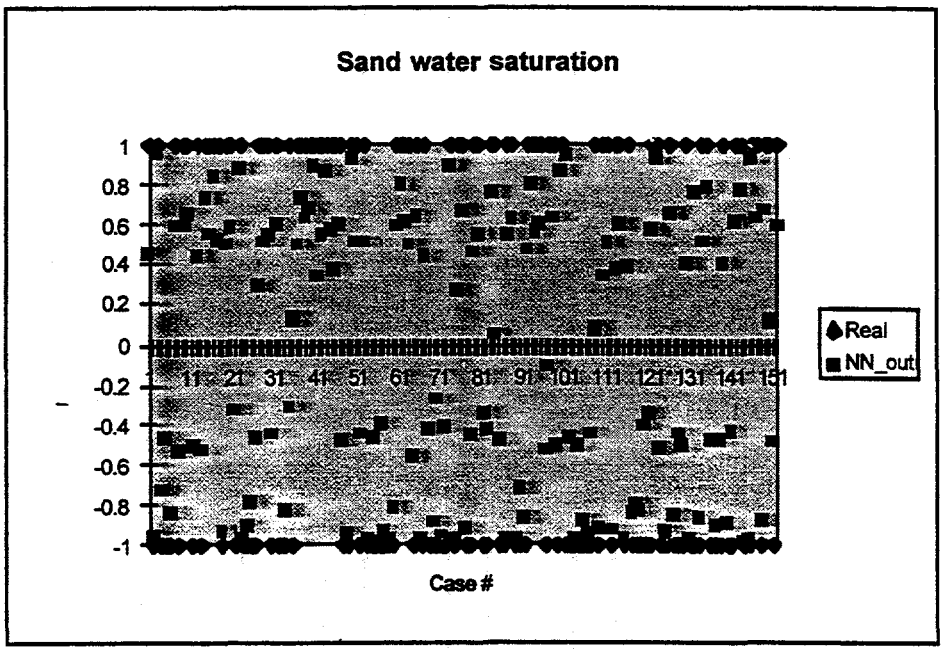

Figure 7
ANNs output for sand water saturation for each of the 152 traces

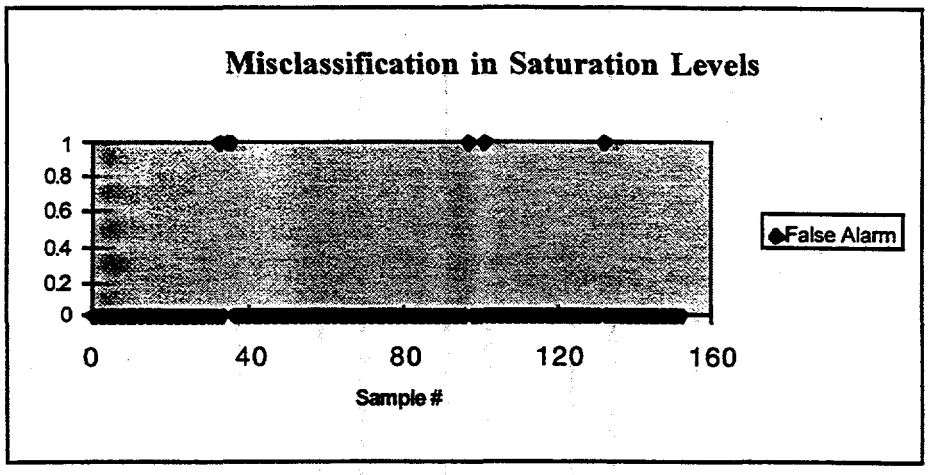

Figure 8
Graph of misclassification in sand water saturation

8 Seismic Holography (H.K. Liu, Y. Jin, and J. Barhen)

8.1 Technical Performance and Achievements

In the experimental process for the 3-D holographic visualization of seismic data, we have discovered that a new photo polymer recording material may be used to record high efficiency holograms. Conventional holographic recording using silver halide film needs dark-room wet chemical processing which requires at least one hour to process and is time-consuming. The new material can be processed by illuminating the film with ultra-violet light. This discovery makes the display results much brighter because of the volume holographic effect and the significant modulation depth achievable on the index of refraction of the film. The new discovery makes the demonstration of the display of the seismic holography much more efficient and results greatly improved.

In addition, a new approach of electronically capturing 3-D data via grating projection and digital reconstruction has been developed. The unique technique is based on the projection of variable gratings onto a 3-D "object". Effective data reduction is achieved. The hologram is generated by using an opto-electronic hybrid system in which the Fourier transform is calculated optically to avoid the slow computer calculations.

The hologram is displayed on a spatial light modulator (SLM) for 3-D reconstruction. We have demonstrated that computer-generated holograms can be written on a commercially available spatial light modulator. A diffraction grating which can diffract light into an 8×8 equal beam patterns has been found, which will be used in our new system. Hence, we can selectively store the 8×8 subcells of a computer generated hologram for the display of the seismic hologram. The device will increase the spatial bandwidth product by two orders of magnitude, and therefore improve the resolution of the project display.

8.2 Technical Meetings and Publications

A project status report and an experimental demonstration of a rotating platform and a rotating vase were presented at the *ACTI Progress Meeting* on October 17, 1995 in Houston, Texas. The platform represents an opaque object and the vase represents a translucent object. The experimental results demonstrated the feasibility of the use of holography for the visualization of the underground structures.

A invited paper entitled "Optoelectronic Seismic Holographic Data Storage and Visualization" by H.K. Liu, Y. Jin, and J. Barhen was presented in the *Holography Session at the Society of Engineering Science 32nd Annual Technical Meeting*, October 29-November 2, 1995 and published in the Proceedings of the meeting.

A comprehensive invited paper on the topic of 3-D display both using holograms and not using holograms was presented in the *International Conference on Display* in Tienjin, China. The paper was well-received. Dr. Hua-Kuang Liu served on the program committee of the SPIE Photonics West Conference 2695B *"Functional Photonics Integrated Circuits"*, January 30, 1996, San Jose, California and collected information on the state-of-the-art of optics equipment for the lab demo of the project.

A seminar entitled "Smart Optical RAM for Fast Information Management and Analysis" was presented on April 19, 1996 at the Oak Ridge National Laboratory.

9 National Laboratory Role

ORNL is one of the worlds leading centers for the application of high performance computing to problems in science and engineering. Several methodologies required to regain U.S. leadership in computational techniques for exploratory seismic analysis are *uniquely* available from CESAR / ORNL. They include:

- novel unconditionally stable algorithms, that will enable, for the first time, a massively parallel solution of partial differential equations such as the acoustic wave equation and the elastic wave equation using novel absorbing boundary conditions;

- a global optimization algorithm (TRUST), which has outperformed, by one to three orders of magnitudes (on standard nonconvex optimization benchmarks), the fastest competing techniques published in the open literature. Global optimization is considered by industry experts as the most promising approach for solving the very complex residual statics estimation problem, which has enormous economic impact.

- internationally recognized expertise in neural networks technology, including unique contributions to the field in areas such as fast learning, finite sample theory and multisensor fusion.

A national laboratory such as ORNL is uniquely positioned to help transition these complex technologies to an industry working level. Through successful demonstration of the computational power and data handling capabilities of parallel computers, a national laboratory can help accelerate the adoption of 3-D seismic processing advances by U.S. oil companies.

10 Benefits to DOE Missions and ORNL Core Competencies

10.1 Support of DOE Missions

Since 1974, a core mission for DOE has been to reduce dependence on imported oil. In the "1995 National Assessment of United States Oil and Gas Resources" (USGS Circular 1118) by the U.S. Geological Survey, the total remaining oil in the onshore areas and State waters of the U.S. were estimated at 112.6 BB (Billion Barrels). Of this total, 20 BB are proved reserves, 60 BB are reserve growth in known fields, and 30 BB are undiscovered conventional resources.

The key to oil discovery is to use scientific techniques to find oil structures without having to drill expensive exploratory oil wells. The primary scientific technique used to find oil structures is 3-D seismic analysis. The goal of this project is to develop advanced computational tools that reduce the cost and increase the precision of 3-D seismic analysis. Thus, this project is directly focused on the DOE mission to reduce oil imports.

This task will also significantly contribute to the strategic plan issued by the Secretary of Energy (see, e.g., "Fueling a Competitive Economy", April 1994) in the area of Science and Technology.

10.2 Support of ORNL Core Competencies

This project supports three ORNL core competencies. Its primary relevance is to the Laboratory's Computational Science and Advanced Computing competency. In particular, CESAR/ORNL Task 1 corresponds to the programmatic goal of developing and deploying "numerical algorithms for solving large-scale scientific and engineering problems" (see, e.g., ORNL R&D Strategic Plan, page 37). Our approach is perfectly aligned with the first strategy, i.e., "develop new and innovative techniques to solve systems of partial differential equations using both serial and parallel computer architectures" (*ibid*). Our efforts will also contribute to the programmatic goal of building a world-class program in computational sciences.

Energy Production (e.g., oil exploration and recovery) and Advanced Material Synthesis (because of the importance of modeling material processes by partial differential equations) are the two other core competencies which are supported by this project.

11 Economic Considerations and Partner Commitment

The operational framework of this project is an ensemble of collaborative efforts between three national laboratories, universities and the oil industry. The SEG acts as coordinator of the industry efforts, and fourteen U.S. oil companies are participating. *Because of the fundamental nature of this research task, and the underlying need for free flow of information, the establishment of a formal CRADA was not deemed appropriate by the participating laboratories, the oil industry and DOE.* However, ORNL (through Lockheed

Martin Energy Research Corp.) has executed a memorandum of understanding (statement of work and cost-sharing) with the SEG. Note that LANL and LLNL were *not* required to carry out such a signed agreement.

11.1 Partners

Majors, independents and service contractors in the oil and computer industry have expressed strong support for this project. Companies that are involved at this time include Amoco, Chevron, CogniSeis, Conoco, Cray Research, Exxon, Louisiana Land and Exploration, Marathon, Paradigm Geophysical, Shell, Standard International, Teledyne, Texaco, Total Minatom, Western Geophysical, and Unocal.

11.2 Partners Cost Share

The combined industry commitments to all tasks in the umbrella proposal include manpower support (aggregate of $600K), computer time ($1140K), and seismic data ($1400K). Furthermore, the SEG will assist in coordinating the dissemination of the information generated in this project through the SEG Research Committee, and the organization of workshops and symposia.

11.3 Partners' Commitments

Partner commitment comes in various forms. For example, Dr. M. Zeitlin and Dr. Y. Cheung of Texaco, who are interested in the holographic projection display, are planning to send us data for demonstration. They are interested in actively participating in the research, and have offered to help solicit additional industrial participation. Marathon, on the other hand, has agreed to make available a preprocessed version of the physical model dataset being processed at the University of Houston. As a final example, J. DuBose from CogniSeis has offered both manpower (computer code development), expertise and data in support of the global optimization task.

11.4 Commercialization Potential

The CESAR / ORNL tasks have an *outstanding potential* for commercialization in the oil and gas sector. Even at this early stage, industrial partners have indicated (May 95 ACTI Working Group Meeting) strong interests in the underlying technologies. Their recommendation is to transfer technology in stages, i.e., first to a "service company", then to the actual producers.

More important, however, is the broader commercialization potential of the CESAR/ORNL technology. Because of the strong fundamental research component of our approach, innovative results obtained, e.g., for the unconditional stability and massive parallelization of the acoustic wave equation, can be adapted, with little effort, to partial differential equations arising in other challenging application areas such as material sciences.

11.5 Work Characterization

The CESAR / ORNL work can best be described as *technology research*, in which we combine basic and applied methods to overcome major computational challenges facing the oil industry through the design of long range innovative solutions.

11.6 Industry and CRADAs

Industry is lacking the expertise to perform this work alone. This is best illustrated by the fact that when a need for an advanced 3-D acoustic wave seismic code arose in connection with the GONII SEG/EAEG modeling project in 1994, the chosen recourse was to turn to the Institut Français du Petrole, and use a French code. DOE support is essential, if advanced computational techniques for 3-D seismic analysis are to become a practical tool used by U.S. oil companies.

11.7 Potential for Private Sector Investment

A serious assessment of the potential for private sector investment is *premature* at this early stage of work. However, through its already substantial contributions (manpower, in kind) to our tasks, the private sector has already cast a strong vote of confidence.

12 Summary

The development of advanced computational tools for 3-D seismic analysis along the lines proposed by CESAR / ORNL involves a major element of high-risk long-term fundamental research. If successful, it should result in a revolutionary advance in processing technology for seismic exploration, an area that has strategic importance to DOE's mission, and high potential impact on society (through the availability and ultimately price of oil and natural gas).

7. ADVANCED TURBINE SYSTEMS

7.1 MATERIALS/MANUFACTURING ELEMENT OF THE ADVANCED TURBINE SYSTEMS PROGRAM

M. A. Karnitz

INTRODUCTION

The DOE Offices of Fossil Energy and Energy Efficiency and Renewable Energy have initiated a program to develop advanced turbine systems for power generation. The objective of the Advanced Turbine Systems (ATS) Program is to develop ultra-high efficiency, environmentally superior, and cost competitive gas turbine systems for utility and industrial applications. One of the supporting elements of the ATS Program is the Materials/Manufacturing Technologies Task. The objective of this element is to address the critical materials and manufacturing issues for both industrial and utility gas turbines.

DISCUSSION OF CURRENT ACTIVITIES

No contribution was received for work performed during this reporting period.

ORNL-6902

INTERNAL DISTRIBUTION

J. Barhen
R. A. Bradley
K. Breder
T. D. Burchell
P. T. Carlson (4)
N. C. Cole
D. F. Craig
C. S. Daw
G. M. Goodwin
E. Greenbaum
M. A. Janney
R. R. Judkins (5)
E. N. Kaufman
P. N. Leiby
C. T. Liu
C. G. McKamey
R. L. Miller
T. W. Schmidt
J. Sheffield
V. K. Sikka
A. J. Stewart
J. O. Stiegler
D. P. Stinton
R. W. Swindeman
P. F. Tortorelli
I. G. Wright
Central Research Library (2)
Document Reference Section
Laboratory Records Department (2)
Laboratory Records, ORNL - RC
M&C Records Office (3)
ORNL Patent Section

EXTERNAL DISTRIBUTION

W. T. Bakker
ELECTRIC POWER RESEARCH INSTITUTE
P.O. Box 10412
3412 Hillview Avenue
Palo Alto, CA 94303

A. L. Baldwin
DEPARTMENT OF ENERGY
Pittsburgh Energy Technology Center
P.O. Box 10940
Pittsburgh, PA 15236

R. C. Bedick
DEPARTMENT OF ENERGY
Morgantown Energy Technology Center
P.O. Box 880
Morgantown, WV 26505

D. J. Beecy
DEPARTMENT OF ENERGY
FE-72
19901 Germantown Road
Germantown, MD 20874-1290

J. L. Beeson
DEPARTMENT OF ENERGY
Morgantown Energy Technology Center
P.O. Box 880
Morgantown, WV 26505

R. G. Bidwell, Jr.
DEPARTMENT OF ENERGY
FE-431, 3G-043/FORS
Washington, DC 20545

R. J. Braitsch
DEPARTMENT OF ENERGY
FE-4, 4G-055/FORS
Washington, DC 20545

J. P. Carr
DEPARTMENT OF ENERGY
FE-72
19901 Germantown Road
Germantown, MD 20874-1290

D. C. Cicero
DEPARTMENT OF ENERGY
Morgantown Energy Technology Center
P.O. Box 880
Morgantown, WV 26505

A. B. Crawley
DEPARTMENT OF ENERGY
Bartlesville Project Office
220 North Virginia Avenue
P.O. Box 1398
Bartlesville, OK 74003

F. W. Crouse, Jr.
DEPARTMENT OF ENERGY
Morgantown Energy Technology Center
P.O. Box 880
Morgantown, WV 26505

J. B. Darby
DEPARTMENT OF ENERGY
Office of Basic Energy Sciences
ER-131
19901 Germantown Road
Germantown, MD 20874-1290

R. A. Dennis
DEPARTMENT OF ENERGY
Morgantown Energy Technology Center
P.O. Box 880
Morgantown, WV 26505

DEPARTMENT OF ENERGY
Office of Scientific and Technical Information
P.O. Box 62
Oak Ridge, TN 37831

DEPARTMENT OF ENERGY
Deputy Assistant Manager for Energy Research and Development
Oak Ridge Operations Office
P.O. Box 2008
Oak Ridge, TN 37831-6269

DEPARTMENT OF ENERGY
Assistant Manager for
Energy Research and Development
Oak Ridge Operations
P.O. Box 2001
Oak Ridge, TN 37831

L. W. R. Dicks
SHELL DEVELOPMENT COMPANY
P.O. Box 1380
Houston, TX 77251-1380

H. Feibus
DEPARTMENT OF ENERGY
FE-232
19901 Germantown Road
Germantown, MD 20874-1290

S. G. Fishman
OFFICE OF NAVAL RESEARCH
Code 431, 800 N. Quincy Street
Arlington, VA 22217

R. D. Furiga
DEPARTMENT OF ENERGY
FE-40, 3G-024/FORS
Washington, DC 20545

D. W. Geiling
DEPARTMENT OF ENERGY
Morgantown Energy Technology Center
P.O. Box 880
Morgantown, WV 26505

F. M. Glaser
DEPARTMENT OF ENERGY
FE-72, 3037/270
Washington, DC 20545

P. M. Goldberg
DEPARTMENT OF ENERGY
Pittsburgh Energy Technology Center
P.O. Box 10940
Pittsburgh, PA 15236

L. E. Graham
DEPARTMENT OF ENERGY
Morgantown Energy Technology Center
P.O. Box 880
Morgantown, WV 26505

L. G. S. Gray
ALBERTA RESEARCH COUNCIL
Oil Sands Research Department
P.O. Box 8330
Postal Station F
Edmonton, Alberta
Canada T6H5X2

H. D. Guthrie
DEPARTMENT OF ENERGY
Morgantown Energy Technology Center
P.O. Box 880
Morgantown, WV 26505

J. S. Halow
DEPARTMENT OF ENERGY
Morgantown Energy Technology Center
P.O. Box 880
Morgantown, WV 26505

S. Harding
CONSOLIDATION COAL COMPANY
4000 Brownsville Road
Library, PA 15129

A. M. Hartstein
DEPARTMENT OF ENERGY
FE-32, 4067/270
Washington, DC 20545

J. L. Hebb
DEPARTMENT OF ENERGY
Pittsburgh Energy Technology Center
P.O. Box 10940
Pittsburgh, PA 15236

J. D. Hickerson
DEPARTMENT OF ENERGY
Pittsburgh Energy Technology Center
P.O. Box 10940
Pittsburgh, PA 15236

J. M. Hobday
DEPARTMENT OF ENERGY
Morgantown Energy Technology Center
P.O. Box 880
Morgantown, WV 26505

N. T. Holcombe
DEPARTMENT OF ENERGY
Morgantown Energy Technology Center
P.O. Box 880
Morgantown, WV 26505

C. M. Huang
TENNESSEE VALLEY AUTHORITY
Energy Demonstration & Technology
MR 2N58A
Chattanooga, TN 37402-2801

W. J. Huber
DEPARTMENT OF ENERGY
Morgantown Energy Technology Center
P.O. Box 880
Morgantown, WV 26505

R. A. Johnson
DEPARTMENT OF ENERGY
Morgantown Energy Technology Center
P.O. Box 880
Morgantown, WV 26505

S. S. Kim
DEPARTMENT OF ENERGY
Pittsburgh Energy Technology Center
P.O. Box 10940
Pittsburgh, PA 15236

S. L. Lai
DEPARTMENT OF ENERGY
Morgantown Energy Technology Center
P.O. Box 880
Morgantown, WV 26505

S. R. Lee
DEPARTMENT OF ENERGY
Pittsburgh Energy Technology Center
P.O. Box 10940
Pittsburgh, PA 15236

A. M. Manaker
TENNESSEE VALLEY AUTHORITY
1101 Market Street
3A Missionary Ridge
Chattanooga, TN 37402-2801

G. V. McGurl
DEPARTMENT OF ENERGY
Pittsburgh Energy Technology Center
P.O. Box 10940
Pittsburgh, PA 15236

T. J. McMahon
DEPARTMENT OF ENERGY
Morgantown Energy Technology Center
P.O. Box 880
Morgantown, WV 26505

D. R. Messier
ARMY MATERIALS TECHNOLOGY
LABORATORY SLCMT-MCC
Watertown, MA 02172-0001

H. S. Meyer
GAS RESEARCH INSTITUTE
8600 West Bryn Mawr Avenue
Chicago, IL 60631

C. L. Miller
DEPARTMENT OF ENERGY
FE-22, 3111/270
Washington, DC 20545

W. R. Miller
DEPARTMENT OF ENERGY
Morgantown Energy Technology Center
P.O. Box 880
Morgantown, WV 26505

H. M. Ness
DEPARTMENT OF ENERGY
Morgantown Energy Technology Center
P.O. Box 880
Morgantown, WV 26505

J. E. Notestein
DEPARTMENT OF ENERGY
Morgantown Energy Technology Center
P.O. Box 880
Morgantown, WV 26505

J. Oakey
BRITISH COAL CORPORATION
Coal Technology Development Division
Stoke Orchard, Cheltenham
Glocestershire, England GL52 4ZG

Aksel Olsen
RISOE NATIONAL LABORATORY
P.O. Box 49
DK-4000
Roskilde, Denmark

M. H. Rawlins
DEPARTMENT OF ENERGY
Oak Ridge Operations
P.O. Box 2008
Building 4500N, MS 6269
Oak Ridge, TN 37831

S. E. Rogers
DEPARTMENT OF ENERGY
Pittsburgh Energy Technology Center
P.O. Box 10940
Pittsburgh, PA 15236

L. A. Ruth
DEPARTMENT OF ENERGY
Pittsburgh Energy Technology Center
P.O. Box 10940
Pittsburgh, PA 15236

T. A. Sarkus
DEPARTMENT OF ENERGY
Pittsburgh Energy Technology Center
P.O. Box 10940
Pittsburgh, PA 15236

C. E. Schmidt
DEPARTMENT OF ENERGY
Pittsburgh Energy Technology Center
P.O. Box 10940
Pittsburgh, PA 15236

D. K. Schmidt
DEPARTMENT OF ENERGY
Morgantown Energy Technology Center
P.O. Box 880
Morgantown, WV 26505

R. C. Searles
MOBIL RESEARCH & DEVELOPMENT CORPORATION
P.O. Box 1026
Princeton, NJ 08540

T. B. Simpson
DEPARTMENT OF ENERGY
FE-231, 3003/270
Washington, DC 20545

M. I. Singer
DEPARTMENT OF ENERGY
FE-70, 4G-052/FORS
Washington, DC 20545

J. Stringer
ELECTRIC POWER RESEARCH INSTITUTE
P.O. Box 10412
3412 Hillview Avenue
Palo Alto, CA 94303

D. F. Swink
DEPARTMENT OF ENERGY
EE-20, 6B-052/FORS
Washington, DC 20545

T. M. Torkos
DEPARTMENT OF ENERGY
Pittsburgh Energy Technology Center
P.O. Box 10940
Pittsburgh, PA 15236

D. B. Uthus
DEPARTMENT OF ENERGY
FE-221, 3113/270
Washington, DC 20545

M. Van de Voorde
EUROPEAN COMMUNITIES JOINT RESEARCH CENTRE
Petten Establishment
P.O. Box 2
1755 ZG Petten
The Netherlands

J. K. Wachter
DEPARTMENT OF ENERGY
Morgantown Energy Technology Center
P.O. Box 880
Morgantown, WV 26505

W. L. Warnick
DEPARTMENT OF ENERGY
ER-412
19901 Germantown Road
Germantown, MD 20874-1290

T. C. Wesson
DEPARTMENT OF ENERGY
Bartlesville Project Office
220 North Virginia Avenue
P.O. Box 1398
Bartlesville, OK 74003

C. M. Zeh
DEPARTMENT OF ENERGY
Morgantown Energy Technology Center
P.O. Box 880
Morgantown, WV 26505

E. A. Zuech
DEPARTMENT OF ENERGY
Bartlesville Project Office
220 North Virginia Avenue
P.O. Box 1398
Bartlesville, OK 74003